EFFECT OF UNCONVENTIONAL SHAPES ON RESPONSE OF TALL BUILDINGS UNDER WIND LOAD

A thesis

Submitted in partial fulfilment of the requirements for the award of the degree of

DOCTOR OF PHILOSOPHY

In

CIVIL ENGINEERING

By

SURESH KUMAR NAGAR

(2K18/PHD/CE/28)

Under the supervision of

Dr. Ritu Raj & Prof. Nirendra Dev

DEPARTMENT OF CIVIL ENGINEERING

DELHI TECHNOLOGICAL UNIVERSITY

SHAHBAD DAULATPUR, BAWANA ROAD, DELHI - 110042 (INDIA).

February, 2022

DELHI TECHNOLOGICAL UNIVERSITY

(Formerly Delhi College of Engineering, Since 1941)

Shahbad Daulatpur, bawana road, Delhi- 110042

CANDIDATE DECLARATION

I hereby declare that the research work presented in this thesis entitled "**Effect of Unconventional Shapes on Response of Tall Buildings Under Wind Load**" for the award of the degree of Doctor of Philosophy in the Department of Civil Engineering (CE), Delhi Technological University, Delhi, India is original and carried out by me under the supervision of Dr. Ritu Raj and Prof. Nirendra Dev, Department of Civil Engineering, Delhi Technological University, Delhi. The content of this thesis has not been submitted either in part or whole to any other university or institute for the award of any degree or diploma.

Date: 14 / 02/2022 (Suresh Kumar Nagar)

Place: DTU, Delhi

DELHI TECHNOLOGICAL UNIVERSITY

(Formerly Delhi College of Engineering, Since 1941)
Shahbad Daulatpur, bawana road, Delhi- 110042

Date: - 14 / 02 /2022

CERTIFICATE

This is to certify that the Ph.D thesis entitled, " **Effect of Unconventional Shapes on Response of Tall Buildings Under Wind Load** ", being submitted by Mr. Suresh Kumar Nagar for the partial fulfilment of the requirements for the award of the degree of Doctor of Philosophy in Civil Engineering, to the Department of Civil Engineering, Delhi Technological University, Delhi, India, is a bonafide record of original research work carried out by her under our guidance and supervision. It is further certified that the work embodied in this thesis is neither partially nor fully submitted to any other university or institution for the award of any other degree or diploma.

(Dr. Ritu Raj)
Supervisor
Department of Civil Engineering
Delhi Technological University
Delhi – 110042.

(Prof. Nirendra Dev)
Co-Supervisor
Department of Civil Engineering
Delhi Technological University
Delhi – 110042.

ACKNOWLEDGMENT

I would like to express my gratitude to all those people who have helped me most during my research work and work as the driving force to make this thesis possible. I would like to express my feeling of gratefulness and submit my acknowledgment for them further in the following lines.

First and foremost, I wish to express my deepest gratitude to my research supervisors, Prof. Nirendra Dev, Professor and DRC Chairman, and Dr. Ritu Raj, Assistant Professor in the Department of Civil Engineering, Delhi Technological University, Delhi for their invaluable guidance, enduring patience, and nurturing support throughout this research without which successful completion would not have been possible. The knowledge and wisdom I have gained from them will forever guide me in education and life.

I would like to extend my sincere gratitude to the SRC members; Prof. H.K Sharma, Dept. of Civil Engineering, NIT, Kurukshetra, Prof. Khalid Moin, Dept. of Civil Engineering, JMI, Delhi, Prof. V.K. Minocha, Head, Department of Civil Engineering DTU, Prof. S. Anbu Kumar, Department of Civil Engineering, DTU, Prof S. Sivaprasad Kumar, Department of Applied Mathematics, DTU for generously sharing their knowledge and time.

My sincere thanks with deepest gratitude to Dr. P. Harikrishna chief scientist and head, and G. Ramesh Babu senior principal scientist, wind engineering lab CSIR-SERC, Chennai, for their numerous valuable suggestions.

I sincerely acknowledge the staff members of Wind Engineering Laboratory at IIT Roorkee, Roorkee, Earthquake Engineering lab, and CAD lab at DTU for providing supports and all possible help in the completion of my work.

I would like to thank all my colleagues, Ms. Supriya Pal, Mr. Arun Kumar, Ms. Arti Raha, Mr. Rahul Meena, Mr. Deepak Singh, Mr. Indrajeet Singh, Mr. Manvendra Verma,

Mr. Sushant, and Mr. Dinesh Reddy, for providing me with critical comments and suggestions and help whenever they were approached and all those who interacted and exchanged ideas with me in completing the research.

Words cannot completely express my love and gratitude to my family members who have supported and encouraged me through this journey. I want to extend special thanks from the core of my heart to my reverend parents for their blessing. I have no word to express the support of my wife Ms. Kavita Nagar, for her enormous patience during this process and taking all the pains of loneliness during my absence and beard all the troubles in her day-to-day life. I am really and sincerely thankful to my loving daughter Krisha Nagar. She has been a constant source of strength and inspiration during my work. I am also grateful to my brother Mr. Dwarika Prasad and My sister Ms. Shimla and Ashoka Nagar, and all other family members for their moral and emotional support.

I express my gratefulness to all those names that are not quoted above but always remained a driving force in my day-to-day life.

At the end, I am thankful and grateful to the almighty for bringing this day in my life.

SURESH KUMAR NAGAR

ABSTRACT

With the advances in construction methods, materials, and technologies, more high-rise buildings with unconventional shapes have been continuously built. A large number of tall buildings with irregular shapes have been built in past years in urban areas due to a shortage of land and demand for good architectural design. As the wind velocity increase with height, the top of the building may experience a higher wind. Tall buildings are the structures that are more sensitive to wind loads, and thus the response to the wind load is the main concern of designers while designing tall buildings. Most of the tall buildings are bluff bodies. As flow separates and reattaches around bluff bodies, the external shape of tall buildings plays an influential role in the generation of wind load on high-rise buildings.

High-rise residential buildings are commonly built as twin towers. Twin tall buildings are subjected to the proximity effects due to small gaps between them. Under the influence of proximity, the wind load on tall buildings may differ from that on the isolated buildings. The codes and standards related to the wind loads are generally do not consider these proximity effects. Further, no analytical formula is available to evaluate the wind effect on irregular shape tall buildings and proximity effects between twin towers, which necessitates more experimental or analytical study for irregular shape tall buildings.

In the present study, four different plan shapes, namely square, plus-1, plus-2, and H-plan, are considered. The floor area and height of all four models are kept the same. The plus-1 and plus-2 plan shapes are prepared by providing the large-sized recessed corners in the rectangular plans of different sizes, whereas the H-plan shape is prepared by providing recessed cavities on the two opposite faces of a rectangular plan shape. The study has been conducted in three phases, namely (i) pressure measurements through wind tunnel study in isolated and interference conditions, (ii) force evaluation through pressure integration technique, and (iii) study of the response of prototype buildings to wind loads calculated on scaled models.

In the first phase, to investigate the wind-induced pressure at the surfaces of the building, four rigid models scaled at 1:300 as described earlier are tested in an open circuit layer

wind tunnel having a working section of 2 m x 2 m cross-section and 15m length. The wind flow characteristics inside the tunnel are simulated similar to the Indian sub-urban terrain with well-scattered objects with a height between 1.5 to 10 m according to the Indian standard IS 875 (part 3): 2015. The mean wind speed and turbulence intensity profile with a power-law index of 0.22 is simulated in the tunnel. The turbulence intensity near the floor of the wind tunnel and wind velocity at building height is 12% and 9.87 m/sec, respectively. The pressure models are prepared with a 4 mm thick transparent Perspex sheet with stiff faces to ensure sufficient rigidity and strength of the model. The pressure measurement study is conducted in two parts. In the first part, the pressure models are tested in isolated conditions for wind directions of 0, 30^0, 60^0, and 90^0 angles at an interval of 30^0 to assess the effects of wind direction on the surface wind pressure. In the second part, the pressure models are tested with an interfering building model present upstream of the pressure model at different locations. The interfering building models are made of wooden material with dimensions similar to the pressure models. Interference effects are assessed for three different positions of interfering building, such as full blockage, half blockage, and no blockage. From the time history of fluctuating pressure data, the mean, maximum, minimum and r.m.s pressure coefficients are evaluated at each pressure point on the surface of the model in isolated and interference conditions.

In the second phase of the study, local wind force coefficients at various levels of the models and the overall base forces have been evaluated through the pressure integration technique. The local forces at each level of the model are calculated by integrating the local forces of each pressure tap at that particular level. The overall base forces and moments are calculated by integrating the force and moment of all levels. The forces in along-wind and across wind directions are presented as mean and r.m.s coefficients.

In the third phase of the study, the responses of prototype buildings of the four models to the wind load calculated through wind tunnel study on the scaled models are studied through analytical study. The effects of various wind directions and various interference conditions have been assessed on the response of four buildings through stress parameters, including axial forces, the moment in X and Y directions, and twisting moments. At last,

the effects of the various plan shapes on the response of tall buildings under wind loads have been investigated.

The results show that wind flow direction has significant effects on the pressure distribution on the surfaces of the models. For the square model, the wind directions normal to the surfaces are critical direction. The wind direction of 60^0 generates the most critical positive and negative mean pressure on the plus-1 model. The effects of wind direction on the pressure on the plus-2 model are not as much severe as the plus-1 model. Pressure distribution on the front faces of all models is completely different in interference conditions from those in isolated conditions. The influence of interference on the square and H-plan model are beneficial, while it has negative effects on some face of the plus-1 model. The along-wind mean local wind forces at normal wind incidence are higher than those at oblique wind incidence. The along-wind forces in all interference conditions decreased significantly from those in isolated condition. The values of along-wind forces: drag and moment at normal wind incidence of 0^0 and 90^0 angles are larger than those at oblique wind incidence in isolated condition. The C_{FD} and C_{MD} values are likely to be reduced significantly in interference conditions. The effects of change in cross-sectional shape are significant on the across-wind forces. The effects of cross-sectional shape are dominant for wind flow at oblique angles in isolated condition while more at half blockage condition of interference. The axial force is independent of the building cross-section. All the buildings have the same axial force in central columns. The maximum twisting moment is observed in PL-2 Building in isolated as well as in interference conditions. The H-building show the best performance in isolated condition.

PUBLICATIONS

Published

1. Nagar, S.K., Raj, R. and Dev, N (2020), "Experimental study of wind-induced pressures on tall buildings of different shapes," Wind and Structure, an international journal, Vol. 31 (5), pp. 431-443 DOI: https://doi.org/10.12989/was.2020.31.5.431. **(SCIE)**
2. Nagar, S.K., Raj, R. and Dev, N (2020), "Proximity effects between two plus-plan shaped high-rise buildings on mean and RMS pressure coefficients," SCIENTIA IRANICA, International Journal of Science and Technology, DOI: https://doi.org/10.24200/SCI.2021.55928.4484 **(SCIE)**
3. Nagar, S.K., Raj, R. and Dev, N (2021), "Effect of interference between twin tall buildings with recessed corners on wind-induced pressure," International Review of Civil Engineering (I.RE.C.E.) (Accepted) **(Scopus)**

Conference Paper

1. Nagar, S.K., Raj, R. and Dev, N (2020), "Effect of proximity between two plus plan shaped tall buildings on wind-induced pressure," The Second ASCE India Conference on Challenges of Resilient and sustainable infrastructure development in emerging economies (CRSIDE-2020) held on 2-4 March 2020, Kolkata.
2. Nagar, S.K., Raj, R. and Dev, N (2020), "Interference Effects between Twin Tall Buildings under Wind Excitation," International Conference on Recent Developments in Sustainable Infrastructure (Research & Practices). (ICRDSI-2020) held on December 19 - 21, 2020.

TABLE OF CONTENTS

LIST OF FIGURES

Fig. No. **Description** **Page No.**

LIST OF TABLES

LIST OF PHOTOGRAPHS

1. CHAPTER-1

INTRODUCTION

1.1. GENERAL

The biggest wave that the world is undergoing in development is the construction of taller buildings (photo 1.1). As the buildings become higher, wind loads become more dominant than the earthquake load regarding safety and serviceability. Wind actions are crucial regarding construction and safety as wind is the most devastating natural phenomenon [1]. Tall buildings are more flexible and hence very sensitive to dynamic wind loads.

Most of the tall buildings are bluff bodies. These bluff bodies create separated flow regions that become the source of vortex shedding, which can create problems in wind engineering contexts [2]. As flow separates and reattaches around bluff bodies, the external shape of tall buildings plays an influential role in the generation of wind load on high-rise buildings. The square or rectangular buildings are susceptible to aeroelastic instabilities because of flow separation at the windward corners of the building. Hence, there is the formation of strong vortices by rolling up the separated shear layer. An attentive study of wind flow around the tall buildings is of great importance in the design process of tall buildings, which may be performed experimentally in the wind tunnel or numerically using computational fluid

dynamics (CFD) or using an uncoupled fluid-structure interaction (FSI) approach [3], [4]. Shape optimization of the cross-section is put forward to improve its wind resistance [5]. Changing the characteristics of the separated shear layer through modification of the corner helps in the reduction of drag and fluctuating lift. Focusing more on the shape during the design stage will minimize the wind-induced vibrations of tall buildings [6]. Using various types of passive and active control devices and by adopting different kinds of aerodynamics modifications to the geometry of buildings could help in reduced wind effects.

(a) Burj Khalifa

(b) Taipei 101,

(c) Abenobashi Terminal

(d) Incheon Tower

(e) Huntington Center

(f) Sky City Tower

(g) Willis Tower Chicago

(h) Nakheel Tower

(i) Doha Convention Center

(j) Shanghai Tower

(k) Pentominium Tower

(l) Petronas Tower

Photo 1.1 Typical tall buildings in the world

The crosswind excitation is caused by wake excitation associated with vortex shedding and inflow turbulence [7]. The crosswind load and effects for super high-rise buildings have been a problem of great concern as the crosswind dynamic response is usually higher than the along-wind response in super-tall buildings and an important factor in the structural design of tall buildings [8], [9]. Appropriate horizontal (chamfer, recession, roundness etc.) and vertical (tapering, setback, twisting and opening etc.) aerodynamic treatments for external shapes of tall buildings can reduce the wind loads on tall buildings significantly. Corner modification in the form of a small corner cut and recession is very effective in reducing drag and lift [10]. The Irregular and unconventional shapes of recent tall buildings effectively suppress crosswind response, which helps while designing tall buildings regarding safety and habitability [11]. However, modification of building corners is not always effective and may have an adverse effect. Vertical aerodynamic modification through tapering could reduce the crosswind response of tall buildings [12].

With the rapid urbanization and shortage of land in urban areas, modern high-rise buildings are often constructed in groups. When two or more tall buildings are situated in the near vicinity, flow patterns surrounding the building are quite intricate than isolated buildings due to interaction effects. This may have an adverse effect upon wind conditions in such areas depending on the shape of the building, as the external shape of tall buildings plays an influential role in the generation of wind load on high-rise buildings. This problem is likely to increase significantly in the future due to the increasingly dense arrangement of buildings in cities caused by the shortage of land. Guidelines for estimating the wind loads on tall buildings in current design codes and standards [13]–[17] are only available for regular and symmetric shapes. Also, codes and standards offer little guidance regarding the proximity effect for unconventional plan-shaped buildings. Since a large number of variables that include the shape and size of buildings, their relative positions, wind direction, etc., are involved [18], it is challenging to provide the compendious and generalized set of guidelines for modification in wind load due to the presence of adjacent buildings. Further, no analytical formula is available to evaluate the wind effect on irregular shape tall buildings, which necessitates more experimental or analytical study for irregular shape tall buildings.

1.2. TYPES OF BUILDINGS

1.2.1. Based on Height

Buildings may be classified as low-rise or high-rise (tall) buildings according to the number of stories or height of the building. Indian standard IS 875 (part 3)- 2015 [16] describes the low-rise building with less than 20 m. A building with a height more than or equal to 50 m or a building with a height to smaller dimension ratio less than 6 is described as a high-rise building according to the code.

From the structural design point of view, it is simpler to define a building as tall when its structural analyses and design are in some way affected by the lateral loads, particularly by sway caused by such loads [19]. According to the CTBUH Height Criteria, a tall building is further classified in two categories as “supertall” building and “megatall” building. A tall building is considered as “supertall” building with a height more than 300 meter (984 feet) or taller and a tall building with height more than 600 meter (1968 feet) or more is considered a megatall building.

1.2.2. Based on their primary use

On the basis of their primary use, tall buildings may be further classified as office building, hotel building, residential and apartment building, or mixed-use building. One more category of building may also be defined as an industrial building, but this category buildings are essentially low-rise buildings.

1.3. LOADS ON TALL BUILDINGS

Design loads for tall buildings are not similar to that of low-rise buildings. Because of gravity load accumulate on floors from top to bottom and the increased significance of lateral loads like wind and earthquake. As wind and earthquake loads are random in nature, prediction of these loads is difficult. Wind load becomes more dominant than earthquake load for tall buildings. Hence wind loads should be appropriately evaluated for the realistic wind load design of buildings.

1.3.1. Wind Load

The wind is a complex phenomenon in respect of wind-load on the structures because of the wind-structure interaction. Wind loads are generated on the exterior of the building,

which is affected by a large number of parameters. These parameters can be divided into (i) Flow parameters and (ii) Structural parameters. Flow parameters include velocity, the direction of wind flow, local ground roughness, or turbulence intensity. Structural parameters include the shape, side ratio, aspect ratio, or height of the building, opening, position of other structures, etc.

1.4. DETERMINATION OF WIND LOADS

Wind loads on the buildings can be determined either theoretically according to the procedure given in codes and standards or numerically or experimentally using a wind tunnel. However, the majority of codes provide data for the calculation of wind load for regular shapes only. Wind loads on a structure need to be calculated for the design of the building, the design of the main wind-force-resisting system, and for the design of components and cladding. There are two methods of wind load evaluation given by the Indian Standard on wind load [IS: 875 (part- 3)- 2015] as (i) pressure coefficients method and (ii) force coefficients method.

The design wind load or force on a structure is determined according to IS code using the formula given below.

$$F = A \times P \quad \text{(1.1)}$$

Where,

F = wind force

P = wind pressure acting uniformly on area A, given by

$$P = C_p \times P_d \quad \text{(1.2)}$$

Where,

C_p = pressure coefficient, given in code

P_d = design wind pressure given by

$$P_d = K_d K_a K_c p_z \quad \text{(1.3)}$$

p_z = wind pressure at height z given by

$$p_z = 0.5 \times \rho \times V_z^2 \quad \text{(1.4)}$$

V_z = design wind speed at height z

ρ = density of air = 1.2 N-Sec^2/ m^4

C_p for the building with opening is given by-

$C_p = C_{pe} - C_{pi}$ ……..…..... (1.5)

Where,

C_{pe} = external pressure coefficient,

C_{pi} = internal pressure coefficient.

Therefore, $P = (C_{pe} - C_{pi}). P_d{}^2$ ……...……. (1.6)

As per IS: 875 (part-3) -2015 design wind speed, V_z is the function of basic wind speed V_b and It can be mathematically expressed as follows:

$V_z = V_b \times k_1 \times k_2 \times k_3 \times k_4$ ……... (1.7)

Where,

V_b = basic wind speed

k_1 = probability factor (risk coefficient)

k_2 = terrain roughness and height factor

k_3 = topography factor and,

k_4 = importance factor for the cyclonic region

If the force coefficient method is used, the total wind load (F) on that particular building or structure is given by-

$F = C_f A_e P_d$ ……... (1.8)

Where,

C_f = The value of force coefficients apply to a building or structure as a whole

A_e = effective frontal area of the building or structure, and

P_d = design wind pressure

1.4.1. Experimental Technique (Wind Tunnel Method)

As the guidelines for estimating the wind loads on tall buildings in current design codes and standards are generally available for regular and symmetric shapes only. It is important to have the information of correct values of wind forces on structures for its safe and economical design. Most of the structures present are bluff bodies, making it difficult to ascertain the wind forces accurately. Further, no analytical formula is available to evaluate the wind effect correctly on irregular shape tall buildings, necessitating more experimental or analytical study for irregular shape tall buildings. The geometries of typical structures, terrain characteristics, and other nearby structures introduce the complexity of wind flow, which necessitates the determination of wind forces experimentally using wind tunnel study on the scaled model and simulated wind.

An experimental study with the Boundary Layer Wind Tunnel (BLWT) is a reliable method to determine the wind effects on tall buildings. Wind tunnel studies are adopted alternatives to codes when more precise information is sought. Wind tunnel studies of structures improve the reliability of performance and economy of design. It also ensures an adequate measure of safety against aerodynamic instabilities for tall, slender, and flexible buildings. BLWT model study is important to increase human comfort and safety through information on sway and twist acceleration and torsional velocities.

1.5. NEED OF THE STUDY

As stated earlier, code and standards do not provide sufficient data to evaluate the wind forces accurately for tall buildings with unconventional plans. Also, available data are for isolated building conditions only. Although there have been many research works conducted to investigate the wind forces on buildings with unconventional plans, there is still a need to fill some research gaps.

The present study is conducted to address the various research gaps identified through an extensive literature survey. Following are the research gaps that have been identified for the present study to bridge with the previous ones.

i. Past studies related to the model with large recessed corners mainly focused on the overall wind loads [8], [10], [20]–[27]. Detailed investigations of characteristics of local surface pressure and forces have not yet been conducted for the model with large recessed corners.

ii. Past studies on interference effects generally focused on square or rectangular tall buildings [6], [28]–[40]. Interference effects between closely spaced buildings with large recessed corners are yet to investigate.

iii. Comparative study of wind forces between square model and model with large recessed corners keeping the plan area and height equals for both models is rarely conducted.

iv. Past studies related to models with recessed cavities have been conducted mainly for the isolated condition [41]–[43]. Detailed investigation of local wind pressure and forces for various interference conditions is yet to be conducted for the model with recessed cavities.

v. A comparative study of wind forces between a base square model and a model with recessed cavities of equal plan area and height is not performed.

vi. Response studies of building models with large recessed corners and models with recessed cavities under wind excitation are to be done at various wind incidence angles.

1.6. RESEARCH OBJECTIVES

Following are the objectives that have been drawn from the research gaps of existing literature:

i. To simulate the wind flow parameters like velocity, turbulence intensity, etc., through Atmospheric Boundary Layer (ASL) inside the wind tunnel for required terrain conditions.

ii. To validate the experimental data and evaluation procedure used in the present study. The experimental parameters of the base square building model have been compared with the experimental parameter for CAARC standard tall building model tested at several research institutions for validation.

iii. To evaluate local pressure in terms of mean, maximum, r.m.s and minimum pressure coefficients from the fluctuating wind pressure records at all pressure points of rigid models considered in this study at various wind incidence angles.

iv. To determine local forces in terms of mean and r.m.s. local force coefficients at the different height levels of all building models using pressure integration technique at different wind incidence angles.

v. To evaluate the overall base moments in terms of mean and r.m.s. force coefficients and to compare the values of all building models to assess the effect of unconventional shapes at different wind incidence angles.

vi. To study the interference/ shielding effects between closely spaced twin tall building models for different positions of interfering building present at windward.

vii. To evaluate the response of the prototype buildings of all models selected at various wind incidence angles in isolated conditions and in different interference conditions.

1.7. ORGANISATION OF THE THESIS

The present research work is organized into **8 chapters**.

Chapter-1 deals with the introduction part, which discusses about wind effects on tall buildings, followed by methods to evaluate the wind loads. The last section discuss about the research gaps identified, followed by the objectives of the present research work.

Chapter-2 describes the summary of the reviewed literature to find out the research gaps. Firstly the literature related to pressure and force measurement in the wind tunnel and force measurement using pressure integration method are discussed. This is followed by a review of literature related to interference effects between buildings. The last section presents the summary of reviewed literature about CFD and full-scale measurements.

Chapter-3 describes the wind tunnel details and characteristics of the approach wind flow. Also, the details about building models tested, the material used for models, and their geometric properties are described in this chapter.

Chapter-4 deals with experimental results of pressure measurement on tall building models tested in the wind tunnel in isolated conditions at various wind incidence angles. The effect of change in wind direction is also described in this chapter.

Chapter-5 presents the results of the experimental study related to the pressure measurements on tall building models tested in different interference conditions.

Chapter-6 deals with the evaluation of local wind forces in along-wind and crosswind directions at different height levels of building models and overall base moments using pressure integration techniques.

Chapter-7 describes the effect of unconventional shape and wind incidence angle on the response of prototype building of models tested in an isolated condition. The effect of the interfering building at different positions on the response of the prototype is also presented at last.

Chapter-8 presents the conclusions drawn from the present study. Contributions made by the author and some directions for future research are also included in this chapter.

2. CHAPTER-2
LITERATURE REVIEW

2.1. GENERAL

This chapter discusses the relevant literature to address the research gaps and to develop a theoretical framework and methodology for the present research study. As the present study concentrates on the pressure and force measurement for unconventional plan models through wind tunnel testing, the research contributions directly related to this area are described in detail. Firstly the literature related to the pressure and force measurement study in the isolated condition is discussed. Which is followed by literature review related to the interference effects on buildings. Subsequent sections discuss the literature related to CFD and full-scale measurement.

2.2. PRESSURE AND RESPONSE MEASUREMENT IN ISOLATED CONDITION

Characteristics of wind-induced vibration become an important factor for the structural design and comfort of its occupant in high-rise buildings. Square or rectangular buildings are susceptible to aeroelastic instabilities because of flow separation at the windward corners of the building. Hence, there is the formation of strong vortices by rolling up the separated shear layer. Tall buildings vibrate simultaneously in the along-wind, across-wind, and torsional directions under wind action [44]. Changing the characteristics of the separated shear layer through modification of the corner helps in the reduction of drag and fluctuating lift. Focusing more on the shape during the design stage will minimize the wind-induced vibrations of tall buildings [6]. The torsional response is greatly affected by the building cross-section [45].

Architects and designers are designing complicated sectional shapes to provide novel and unconventional expressions, which are basically good regarding reducing the crosswind excitations [6]. The Irregular and unconventional shapes of recent tall buildings effectively suppress crosswind response, which helps while designing tall buildings regarding safety and habitability [11]. Many researchers have studied wind effects on buildings with unconventional plans. [6], [9], [46]–[48]. The codes and standards do not

provide useful data regarding these modified buildings. Indian standard IS 875 (part-3): 2015 [[16]] first time reported the across-wind provisions but are too high compared to other standards [49]. However, modification of building corners is not always effective and may have an adverse effect.

Corner modification as horizontal slots, slotted corners, Corner cut, recession, and chamfered corners are effective in a significant reduction of both along-wind and crosswind response [8]–[10], [24], [26], [27], [50]–[53], Changing section, along with height through tapering or setback, could also be useful in reducing the across-wind response of the tall buildings [12], [54]–[59]. Tall tapered buildings along height might spread the vortex-shedding over a broad range of frequencies as they show better aerodynamic performance in the along-wind direction [6], [60]. Helical twist, opening and their combination [6], [61] and change of aspect ratio, side ratio [62]–[66] are effective in causing a significant reduction in both along-wind and crosswind response.

Davenport (1971) [20] studied the response of six building shapes through boundary layer wind tunnel. Extreme response required in the design is also determined through different aerodynamic and structural properties. The results showed that peak deflection was highest for the rectangular and triangular buildings while lowest for circular building.

Kwok and Bailey (1987) [52] investigated the effect of aerodynamic devices as small fins or vented fins on the response of a square tower through wind tunnel tests. It was found that along-wind response increased while cross wind response was reduced for a limited range of reduced velocities.

Dutton and Isyumov (1990) [67] studied the aerodynamically modified square cross-section by introducing openings or gaps in the upper half of the building to reduce the tall building motion. It was concluded that across-wind excitation can be reduced by providing through-building gaps. The reduction was maximum with small gaps of 4%.

Hayashida and Iwasa (1990) [22] studied the effects of different building plan shapes on the response of high-rise buildings. Total eight models were tested, four were basic shapes, and the other were their deformed shapes with corner modification. Results showed that the square model shows the maximum cross wind response while the ‘Y’ plan model with recessed corner shows the least response.

Beneke and Kwok (1993) [45] tested four different models with rectangular, diamond, triangular, and D-shaped plan in the wind tunnel to investigate the effects on wind-induced torsion. Results revealed that the dynamic torsional response of the triangular model was much higher than other models.

Cooper *et al.* (1997) [68] measured the unsteady wind loads on the tall building having tapered cross-section and beveled corners as a function of reduced velocity and motion amplitude.

Kawai (1998) [10] performed wind tunnel tests on corner modified square and rectangular models to investigate the effects of corner cut, recession and roundness on vortex-induced excitation and galloping oscillation. Results indicate that small corner cuts and recession are beneficial in preventing the aeroelastic instabilities, but large corner cut and recession promote instability at low velocity.

Kim and You (2002) [12] conducted HFFB tests on models with different tapering ratios of 5%, 10%, 15%, and a basic square cross-section model. The effect of tapering for reducing the wind-induced response of tapered tall building was investigated. It was concluded that the tapering effect is more significant in the reduction of cross-wind response than along wind. Also tapering effect is more efficient in suburban flow conditions than that in urban flow conditions.

Liang *et al.* (2002) [62] investigated across-wind forces on the rectangular tall building models with various side ratios in boundary layer wind tunnel. Based on the test results, empirical formulas were presented for across-wind force spectra, r.m.s lift coefficients, and Strouhal number. Results indicated that r.m.s lift coefficient increased with the increase of side ratio while Strouhal number decreases with increase in side ratio.

Zhou et al. (2003) [44] conducted HFFB measurements in the wind tunnel on a typical tall building model. The influence of the side ratio, aspect ratio and turbulence characteristics are analyzed, and an interactive database of aerodynamic loads was presented.

Gu and Quan (2004) [8] generated formulas for the across-wind force spectra, base moment coefficients, and shear force coefficients on the basis of the results of wind tunnel study with the HFFB technique. Total 15 tall building models of square, rectangular and

corner modified cross-sections with different aspect ratios and side ratios were tested to generate the formula.

Lin *et al.* (2005) [63] conducted a pressure measurement study and base forces measurement by HFFB technique on a rectangular cross-section model with various side ratios and aspect ratios. Local wind forces in terms of force coefficients, power spectral density and span-wise correlation were investigated. Results of base moment obtained by HFFB and integration of local forces were compared.

Gomes *et al.* (2005) [69] conducted a pressure measurement study on the L-plan and U-plan shaped model to assess the effect of different model shapes. A numerical study was also conducted for a better understanding of the flow pattern around these models.

Liang *et al.* (2005) [70] conducted a series of wind tunnel tests on tall building models with various side and aspect ratios in boundary layer wind tunnel. Simplified empirical formulas were proposed to estimate the crosswind dynamic response of tall rectangular building based on the results obtained. Across-wind response determined by proposed formulas and codes were compared with the results of wind tunnel tests.

Huang and Chen (2007) [71] conducted a wind tunnel study through synchronous pressure measurement on square tall building models of different heights to study the variation of the gust response factor with different along-wind responses.

You *et al*. (2008) [56] conducted HFFB tests to investigate the tapering effect on the reduction of wind-induced response of a tapered tall building model with tapering ratios of 2.5%. 5%, 7.5%, 10%, and 15%. It was concluded that the tapering ratio of 2.5 -5% has no significant effect on changing the peak characteristics of wind spectra. At the same time, the peak showed a significant increase for tapering ratio 7.5-10%.

Kim *et al.* (2008) [55] investigated the effect of tapering on reducing the RMS (root mean square) across-wind response of a square tall building with various tapering ratios. It was observed that increase tapering could have an adverse effect with a low structural damping ratio.

Zhang and Gu (2009) [64] analyzed the distribution of the along-wind and cross-wind fluctuating loads along the height of tall building models through simultaneous pressure measurements.

Tse et al. (2009) [24] proposed the empirical formulas for cross-wind response in terms of building dimension and dynamic properties based on the test results of wind tunnel study using HFFB technique for tall building models with various corner modifications as corner recession and corner chamfered. The construction cost and financial returns were compared for all models. It was concluded that corner recessed are more efficient in the reduction of base moments.

Gu (2009) [72] analyzed the characteristics of the wind pressure and forces acting on different typical tall building models through wind pressure scanning and HFFB techniques in the wind tunnel.

Tamura *et al.* (2010) [73] determined wind pressure and forces acting on 31 different tall building models with various configurations of basic plan shapes, and their aerodynamically modified models with corner cut, chamfered, tilted, tapered, helical, setback, opening etc through a series of wind tunnel tests. The relationship of aerodynamic force characteristics with structural properties and aerodynamic modifications was investigated based on these tests results.

Kim and Kanda (2010a) [57] investigated the mechanism of aerodynamic force reduction, using wind tunnel tests for pressure and force due to fluctuating wind component. Two tapered, one setback, and one prototype square experimental model was used for the study. It was concluded that mean drag and fluctuating lift force could be effectively reduced through tapering or setback. The setback model reduced fluctuating lift force more efficiently than a tapered model.

Kim and Kanda (2010b) [74] analyzed the wind-induced response and characteristics of OTMs of tall building square models with modification along the height. It was concluded that mean along-wind OTM and fluctuating across-wind OTM decreases greatly through tapering and setback.

Lou *et al.* (2010) [75] investigated the wind load effects on an X-shape tall building model through synchronous surface pressures measurements in a wind tunnel. The mean and r.m.s force coefficients at storey levels in along-wind, across-wind, and torsional directions were presented. Results indicate that mean drag coefficients were higher than rectangular building.

Amin and Ahuja (2011) [76] investigate the wind pressure distribution on two L-shaped and two T-shaped models. It was observed that pressure distributions were greatly affected by the plan shape and dimensions of building models.

Cluni *et al.* (2011) [77] performed wind tunnel tests through the HFFB method and synchronous multi-pressure sensing system on a regular square model and two irregular shape similar to the bank of China Tower in Hong Kong. The results of the two methods used were compared through statistical analysis of the test results.

Kim *et al.* (2011) [54] tested 13 super tall building models of square plan with height variations under an urban area flow to find the wind-induced response of these super tall buildings. The total acceleration of the various building shapes was compared. Results showed that along-wind and torsional accelerations are smaller for setback and tapered models. However, across-wind acceleration is higher than the square model.

Tanaka *et al.* (2012) [6] investigated the aerodynamic characteristics of various aerodynamically modified tall building models with corner cut, setback, helical etc., to propose the most significant structural shape of the tall building in the wind-resistant design of tall buildings. It was observed that tapered and setback models show batter aerodynamic behaviors in along-wind direction while helical and model with cross opening show batter behaviors in across-wind directions for maximum mean OTM coefficients.

Yoshida *et al.* (2012) [47] investigated the aerodynamic characteristics of various configurations of a triangular section model. Variation of OTM coefficients, PSDs, and trajectories of various wind force coefficients were analyzed.

Kim and Kanda (2013) [60] investigated the spatio-temporal features of pressure fluctuations in tapered and setback tall buildings. The difference in pressure coefficients at leeward surfaces was reported compare to the square model. It was observed that mean

pressure on the windward side was almost similar for all models, but on leeward surface are quite different.

Wong and lam (2013) [42] investigated modification in the wind-induced loading and the dynamic response of H-shapes tall buildings due to the presence of recessed cavities with a variation in the ratio of breadths and depths of the recessed cavities systematically. Wind pressure at all surfaces was measured with a multi-point pressure scanning system. The most important observation was the significant reduction in the across-wind excitation and response building.

Amin and Ahuja (2013) [78] conducted a pressure measurement study in boundary layer wind tunnel on rectangular building models with various side ratios of 0.25 to 4. Mean and r.m.s values of surface pressure coefficients were evaluated. It was concluded that pressure distribution on leeward and side surfaces is significantly affected by the change in side ratio of the building model.

Bandi *et al.* (2013) [79] investigated the variation of OTM coefficients, PSDs, and the trajectories of various wind force coefficients for triangular cross-section model with various modifications as corner cut, Helical and straight triangle. Effects of aerodynamic modification and helical angle on mean and r.m.s of local wind force and OTM coefficients and peak PSDs were investigated.

Ha (2013) [80] conducted wind tunnel tests on an aeroelastic rectangular model with various aspect and side ratios. Empirical formulas were formulated for across-wind fluctuating OTM coefficients and PSDs as a function of the side ratio of building. Results showed that fluctuating OTM coefficients are mainly affected by the change in side ratio.

Mukherjee *et al.* (2014) [81] studied pressure developed on different faces of a 'Y' plan-shaped tall building through wind tunnel study, and results were compared with numerical results.

Chakraborty *et al.* (2014) [82] presented the results of comparative experimental (wind tunnel) and numerical (CFD) studies on '+' plan-shaped tall building.

Holmes (2014) [83] compared wind tunnel data for along-wind and crosswind base moments of a benchmark building studied in the recent international study with the Hong Kong code, Australian code and ASCE Code.

Amin and Ahuja (2014) [65] presented the results of a wind tunnel study on a rectangular building with various side ratios of 1, 1.56, 2.25, 3.06, and 4. Pressure distribution and mean response of all models were evaluated through pressure measurements.

Bhattacharyya *et al.* (2014), Bhattacharyya and Dalui (2018), [84], [85] analyzed the pressure distribution on the surfaces of an 'E' plan shape tall building at wind direction from 0 to 180 degree through numerical study and the results were compared with the results obtained from an experimental study in the wind tunnel.

Deng *et al.* (2015) [86] investigated the effects of tapering and chamfered modification on the aerodynamic loads through synchronous pressure measurement techniques in the wind tunnel. Results revealed that tapering leads to a reduction of crosswind aerodynamic loads

Bhattacharyya and Dalui (2015) [87] studied the force and pressure coefficient for an unsymmetrical 'E' plan building experimentally and numerically.

Kim *et al.* (2015) [88] investigated the effect of tapering on the fundamental aeroelastic behavior of conventional tapered super tall buildings through aeroelastic wind tunnel study. The suppression of response through tapering was the main finding of the study.

Cheng *et al.* (2015) [43] analyzed the effect of recessed cavities on wind pressure distribution at the side faces of an H-section tall building model. The characteristics of fluctuating wind pressure at side faces were compared with the square building model.

Hu *et al.* (2015) [89] performed a pressure measurement study of an inclined square prism through a series of inclinations in windward and leeward sides. Effects of inclination on the aerodynamic characteristics of the square prism were assessed based on the pressure data.

Kim *et al.* (2015) [90] investigated the effect of the number of sides on the response characteristics of polygon cross-section. The results showed that OTM coefficients, PSDs, and response decrease with the increasing number of sides. The largest OTM coefficients were observed for the straight triangular model.

Li and Li (2016) [91] performed wind tunnel experiments to study the along-wind and across-wind loads on an L-shaped tall building with different dimensions. Empirical formulas were proposed to estimate the crosswind dynamic loads as a function of side ratio and terrain category. The effects of the side ratio and aspect ratio on the lift force coefficient were discussed. It was concluded that the lift coefficient affected more by side ratio rather than aspect ratio.

Quan *et al.* (2016) [92] investigated the effect of different flow and structural parameters like turbulence intensity, side and aspect ratio on the aerodynamic damping ratios determined from the wind-induced response of the 15 aeroelastic models of the rectangular tall building tested in various simulate wind conditions. The results revealed that turbulence intensity and side ratio are the main factors that affect the crosswind damping ratio.

Guan *et al.* (2016) [93] conducted wind tunnel model tests and numerical analysis on a typical high-rise building to investigate the distribution characteristics of wind pressure coefficients of the air flow around open-window and enclosed buildings. It was concluded from the results that the opening of a window has little influence on the wind pressure distribution.

Elshaer *et al.* (2017) [94] proposed an aerodynamic optimization procedure (AOP) in building corners to reduce the wind loads using large eddy simulation and an artificial neural network.

Li *et al.* (2017) [48] studied the characteristics of wind-induced torque acting on L-shaped rigid models with different geometric parameters in boundary layer wind tunnel. RMS force coefficients, PSDs, and vertical correlation functions of wind-induced torques were analyzed. It was concluded that mean torque increases gradually with an increase in side ratio.

Zhao and He (2017) [95] analyzed the characteristics of the surface pressure distribution of an oval-shaped tall building model to assess the effect of different height-width and height-thickness ratios on mean wind pressure coefficients (C_m). Results indicated that the absolute value of C_m increased with a decrease in height-width ratio.

Zhang and Li (2017) [96] assessed the wind effects on the supertall building of Ping a Finance Center in China having unconventional plan configuration. Characteristics of wind forces in terms of mean and r.m.s coefficients, PSDs, correlations, wind-induced displacement, and acceleration response were discussed.

Zheng *et al.* (2018) [5] studied the characteristics of the response of tall buildings due to the wind load under combined aerodynamic control, which includes the shape optimization and air suction on tall building models with different cross-sections.

Yuan *et al.* (2018) [97] WAS 89 investigated the effect of the presence of rectangular groves on a circular cylinder using wind tunnel tests and full-scale large-eddy simulations. It was found that deeper groves reduce mean and fluctuating wind pressure. When two or more tall buildings are constructed in the near vicinity, flow patterns surrounding the building are of a much more complex nature than isolated buildings due to the presence of interaction effects.

Li *et al.* (2018) [26] investigated the effects of building corner modification in the form of recessed, chamfered and rounded corners and compare the results with a benchmark square model. The authors concluded that corner rounded is not too effective as corners recessed and chamfered to reduce these wind loads.

Deng *et al.* (2018) [98] studied the effects of aerodynamic shapes on the distribution of peak negative wind pressure and wind force coefficients on super tall building through tapering, chamfering, and opening ventilation slots. It was found that the force coefficient increased with increase in tapering ratio. Peak negative pressure decreased slightly with increased tapering ratio while increased near the chamfered location and at the area of opening ventilation slots.

Sheng *et al.* (2018) [99] investigated the wind effects on the overall and local wind forces on a square-plan tall building through HFFB and Multi-point unsteady pressure measurement techniques. The results showed that wall-pressure forces were influenced by the upstream flow or shear layer formed at the upstream corners of the building.

Mallick *et al.* (2018) [100] conducted experimental and numerical studies to investigate the wind effects on C-shaped building models with different aspect ratios.

Li *et al.* 2019 [27] reported that corner recessed, corner chamfer and corner rounded can reduce wind loads on square tall buildings. Corner chamfered is more effective for reducing along-wind loads, while the model with recessed corner is the best among these three corner-modified models for the reduction of across-wind loads.

Liu *et al.* (2019) [101] investigated the distribution of surface pressure in terms of mean, r.m.s and peak coefficients for rectangular-plan tall buildings with various plan ratios ranging between 0.11 to 9. Pressure measurements were carried out on scaled models in the wind tunnel. Results showed that pressure coefficients on the leeward and side surfaces were affected significantly by plan ratios between 0.11 to 4. Peak values of base shear coefficients occur for a plan ratio of about 0.67.

Liu *et al.* (2019) [102] investigated the wind pressure and aerodynamic forces acting on a square megatall building under the effect of two types of twisted wind flows with twist angles of 15 and 25 degree. It was revealed that twisted wind flow significantly affects the wind pressure distribution. Sharp peaks of the PSDs of lateral wind forces were notices in twisted wind flows.

Li *et al.* (2019) [103] proposed a new transiting test method to evaluate the wind pressure through theoretical derivation and field testing. Proposed test method was adopted for evaluation of mean pressure coefficients of the CAARC standard tall building model at different vehicle driving wind speeds. Results of the mean pressure coefficients at typical measuring point through proposed method agreed well with wind tunnel test results.

Hu *et al.* (2019) [104] investigate the effect of double-skin façade (DSF) system on the cladding pressure of building fitted with a DSF with vertical openings. Effects of vertical openings in external skin at windward face were investigated on the surface pressure through pressure measurement study in the wind tunnel. It was revealed through test results that the DSF with openings can be efficient in the reduction of wind pressure on side and leeward surfaces.

Li *et al.* (2020) [51] investigated the effect of corner chamfers on the aerodynamic performance of CAARC standard tall buildings with different modification rates from 5% to 20%. Based on the test results, wind pressure, local forces, and base moments and their PSDs were calculated and compared for all models. It was revealed through test results that

increase in corner chamfer rate can improve the aerodynamic performance of the tall building model.

Guzmán-Solís *et al.* (2020) [66] investigated the effects of change in aspect ratio and terrain category on the wind-induced torsional load. Each model was built with identical plan dimensions. Shear force coefficient, bending moment coefficient and torsional moment at the base of each building model were calculated through synchronous pressure measurements. It was concluded that mean base shear and moment coefficients increases with decrease in aspect ratio.

Khodaie (2020) [105] computed the wind-induced response of a super tall building using a combination of structural and aerodynamic modification. Tapering of cross-section is used in combination with TMD system to control the wind-induced vibrations of super tall buildings. The response of building in along-wind and crosswind were computed using the frequency domain analysis for different combination of varying tapering ratio and TMD ratio. Results indicated that by using combination of two control methods, displacement and acceleration response can be effectively reduced.

Lamberti *et al.* (2020) [106] investigated the characteristics of the mean and r.m.s peak pressure coefficients at each pressure point of a high-rise building through high-resolution pressures measurement in the wind tunnel. Experiments were performed and the data were compared for two different wind tunnels: the open circuit wind tunnel and, the closed circuit wind tunnel. Probability density function of local and face average pressure coefficients were presented and their relevance in the cladding design was investigated.

Li *et al.* (2020) [107] investigated the effects of various turbulence intensities on the pressure distribution on the surfaces of CAARC standard tall building. Experiment were performed with wind tunnel with two group of turbulent intensities. In the first group a constant turbulent intensity but with different integral scale was used. The second group had different turbulent intensities with a constant integral length. The results showed that the r.m.s and peak of pressure coefficients increased with the increase in turbulent integral scale and intensity. Effect of increase in length scale is more significant on leeward face while effect of intensity is more significant on side faces of the building model.

Gu et al.(2020) [50] tested sixteen 2D prisms with various chamfered corners and side ratios in the wind tunnel at low-turbulence flow. Wind pressure on the surfaces of models was measured to assess the effects of chamfered corners on the pressure coefficients and correlation coefficients on the side face with different side ratios. It was observed that separated flow does not reattach to the side face due to the presence of chamfered corners and hence affects the pressure correlations at the side faces. Mean and r.m.s drag and r.m.s lift coefficients significantly decrease due to the presence of chamfered corners.

Li et al. (2021) [108] presented the effects of area extreme pressure (AEP) reduction on large-scale cladding based on wind tunnel test data. Wind tunnel tests were conducted and based on the tests data, the effects of AEP reduction on the large-scale cladding were determined using area average and moving average methods. It was revealed that the AEP reduction at the edges and corners is more significant than the interior of the roof.

2.3. INTERFERENCE EFFECTS

Since wind effects depend on the shape and size of buildings, their relative positions, wind direction, etc., [18], [109], it is challenging to provide the compendious and generalized set of recommendations for modification in wind load due to the presence of adjacent buildings. Therefore, the proximity effect due to nearby structures should be appropriately investigated for the realistic design of buildings for wind [110]. Many researchers have studied proximity effects between tall buildings.

Bailey and Kwok (1985) [111] conducted a series of wind-tunnel models tests in low-turbulence normal strong wind conditions. Response of a tall square building under interference due to neighboring tall buildings. It was reported that dynamic load might increase by a factor of up to 4.4 at upstream and up to 3.2 at downstream buildings.

Yahyai *et al.* (1992) [112] studied the response of an aeroelastic rectangular plan model in along-wind and crosswind in the presence of an interfering building placed at different locations upstream and downstream. It was concluded that the interference effects were more prominent for the upstream location of the interfering building.

Taniike (1992) [113] studied the proximity effects on a typical square building in the presence of interfering buildings of different sizes. It was revealed that fluctuating

component of wind force on the principal building was generally increased for all sizes of interfering buildings.

Zhang *et al.* (1995) [114] investigated the effects of proximity on the torsional response of a square tall building model. Tests were performed for two different sizes of interfering buildings present at upstream and downstream of principal building. The results indicated that mean and rms of torsional response can be enhance significantly.

Khanduri *et al.* (2000) [115] investigated the modification in wind loads under the interference effects due to the presence of interfering building of different heights. It was concluded that mean loads were reduced due to shielding, when two buildings were arranged in tandem while fluctuating loads were increased.

Thepmongkorn *et al.* (2002) [116] investigate the interference effects on the CAARC standard tall building model in the presence of a square building of similar height at upstream and downstream. The results showed that base moments were significantly increased for diagonally upstream location of interfering building.

Xie and Gu (2004) [33] performed a series of wind tunnel tests to study the mean interference effects between two and among three tall buildings arranged in tandem, staggered and side by side arrangement. It was found that mean wind load on the principal building at downstream decreases due to the presence of the interfering buildings due to shielding effect. However, mean wind loads increased due to the channeling effects.

Xie and Gu (2005) [117] studied the wind-induced mean and dynamic interference effects on tall buildings in the presence of a interfering building of different sizes. Two type of interfering buildings were used. The first type of buildings had height similar to the principal building with different breadths of 0.5 to 2.0 time the breadth of principal building. In the second group buildings with same cross section as the principal building but with the different height of 0.5 to 1.5 times the height were used. Comprehensive analysis of the interference effects were done by using artificial neural network and correlation analysis.

Xie and Gu (2007) [28] performed a series of wind tunnel tests using HFFB technique to asses the interference effects between a group of three tall buildings on the base-bending

moments response of tall buildings. Interference effects on the principal building were analyzed in the presence of two upwind interfering building of different heights. The interference effects were presented as envelope interference factor (EIF) between three tall building. The results showed that dynamic effects of two interfering buildings were more adverse than a single interfering building. Author found a good correlation in the distribution of EIF of different configuration and upwind terrains.

Lim and Bienkiewicz (2007) [118] studied the wind-induced response of twin-tall buildings connected by a skybridge through HFFB technique. The effects of structural coupling were analyzed on the building response. The results indicated that the adverse dynamic interference effects can be reduced by using structural coupling of twin building in close proximity. It was suggested by the authors that structural coupling should be considered in the design of twin tall buildings for wind loads.

Lam *et al.* (2008) [34] studied the proximity effects on closely spaced square buildings arranged in line under different wind angles and gap distances between buildings. They concluded that strong channeling through the building gaps exists due to the close proximity. The buildings inside the row experienced much reduced wind load in the direction of row for most of the wind directions. While wind load on the buildings at upwind for wind direction at oblique angle to the row of buildings. Much smaller fluctuation in the across-wind loads to that of isolated building were observed.

Zhao and Lam (2008) [119] investigated the interference effects between five square tall buildings in the wind tunnel, arranging them in L- and T-shaped patterns. Mean and fluctuating components of shear force, OTM and torsional moments measuring through HFFB technique were considered. It was observed that a strong interference effect exists on all member buildings, which significantly modifies wind loads as compared to the isolated building. Sheltering effects on wind load in the direction of arm of the "T" or "L" were observed on the inner buildings.

Tavakol and Yaghoubi (2010) [120] investigated the flow around a surface-mounted hemisphere. The study was done experimentally and numerically, and flow patterns were studied for different flow velocities at various sections.

Kim *et al.* (2011) [36] studied the Interference effects on local peak pressures for different wind incidence angles, various locations and height ratios of interfering building. Interference factors for two peak values at top and bottom of fluctuating pressure data at each measurement point were presented and discussed. The results showed that the peak suction enlarged with higher height ratio. Oblique arrangement generates more severe peak suction compare to tandem configuration.

Hui *et al.* (2013, 2013a, 2012) [34], [35], [121] investigated the mutual interference effects on local peak pressure coefficients between two high-rise building models of different shapes. Interference effects on local peak pressures were investigated. It was observed that proximity effects depend much on building shapes, configuration and wind angles. The smallest minimum peak pressure at the face increased up to 40%. Unfavorable positions w.r.t the peak pressure interference factors are normally concentrated at the corners and the edges of the building surfaces.

Mara *et al.* (2014) [40] performed wind tunnel tests to assess the proximity effects among two buildings having similar heights and geometries associated with square plan building under consideration. Data were presented in form of IFs of wind loading and response of principal building under interference. The aerodynamic interference factors greater than unity were observed for RMS cross-wind forces for the direct upstream location of the interfering building. The mean and r.m.s moments in along-wind direction were generally reduced in presence of twin single upstream building.

Yu et al. (2015) [29] developed a relationship between interference factor and spacing through high precision regression equations for interference effects between two buildings with different arrangements. The tests were conducted using synchronous pressure measurement technique. The results showed that the interference effect was beneficial for mean pressure, but the peak pressure at the lateral façade near the interfering building was amplified. With increase in heigh and breadth ratio, the shielding effects becomes more astonishing.

Yan and Li (2016) [122] investigated the interference effects between a pair of aerodynamically modified super-tall buildings. The results were presented as contour plots of local pressure, global aerodynamic loads and response of tall buildings to assess the

interference effects. Results showed that the dynamic response has substantially enlarged in a critical arrangement. The bottom peak of fluctuating pressure was increased up to 30% of isolated building case.

Dongmei *et al.* (2017) [123] assessed the Interference factors of global aerodynamics & local wind pressure and lift spectra of a square building due to a lower height building of the same cross-section at different positions. Based on wind tunnel testing results, related spectra and parameters for evaluating these wind loads were proposed. It was observed that fluctuating aerodynamic forces on the principal building were increased significantly for the oblique upstream position of the interfering building.

Kim and Tse (2018) and Kim *et al.* (2018) [124], [125] analyzed the effect of a structural link and different gap distances on the lateral wind response of two square-linked buildings. Results showed that for 0 degree wind angle at a small gap between buildings, channeling is strong, and the linked building system acts as a single bluff body. A good correlation of 1st POD mode with along-wind forces at both small and large gap distances. Correlation of 2nd and 3rd POD modes with cross-wind forces was associated at small and large gap distances, respectively.

Zu and Lam (2018) [126] studied the shielding effect on the square tall building due to a row of low rise or medium-rise buildings. The various parameter like spacing between buildings in row, height of upstream buddings, and their position relative to the target building were considered. It was concluded that the mean along wind load on the principal tall building at the normal incidence angle is always reduced. For small separation distance channeling and blocking arrangement lead to evidently different pressure distribution.

Flaga *et al.* (2018) [127] studied the effect of interference between closely spaced irregular shaped tall buildings on mean pressure distribution, global forces and pedestrian comfort for wind. It was discovered that the close proximity between buildings generates high negative peak pressure on the surfaces facing the gap.

Zhang *et al.* (2018) [128] analyzed the interference effects between two linked “H” type twin-tower structures. It was concluded that the surrounding building's channeling effect is the main source of the maximum cross-bridge displacement. The correlation effects on along-bridge displacement between the two towers can be ignored.

Kim *et al.* (2019) [129] studied the effect of gap distance on wind flow around linked buildings. The results showed that for a parallel arrangement of buildings, the single vortex street and biased flow is observed for a small gap between buildings at 0-degree wind incidence.

Li and Li (2019) [130] investigated the interference effect on the irregular shaped twin-tall tapered buildings with recessed corners. It was observed that the proximity effects between tapered buildings were considerably different from that of the square building. Shielding effects were noticeable in tandem arrangement but significantly weaker than those on square buildings for similar separation distance. Fluctuations in the across-wind response were likely to be increased for oblique arrangement at 2.5B at wind direction of 22.5^0.

Jing et al. (2019) [131] analyzed the proximity effects between two oil storage tanks on wind fields and dynamic response due to the wind effects. Results revealed that the pressure acting on the tank under interference is notably higher compared to the single one.

Sharma *et al.* (2019) [59] analyzed the mean and fluctuating forces for aerodynamically modified tall buildings by changing the section along with the height through tapering. Study was conducted in two parts: in first part effects of height ratio of interfering building were examined and in the second part the effects of tapering were analyzed. It was concluded that shielding effects decreases with increase in the height of interfering building.

Chen *et al.* (2020) and **Quan *et al.* (2020)** [132], [133] studied the proximity effects on an existing target tall building with existence of a proposed super tall building and a pair of adjacent buildings of similar height. The wind pressure, response data and aerodynamic forces of existing tall building were analyzed. The results showed that the aerodynamic response of the target building was considerably increased when the proposed super-tall building existed upstream, the vortex shedding and the deflection of induced air flow was the main reasons. It was proposed that buildings facing the side of the proposed building need to pay more attention.

Liang *et al.* (2020) [134] examined the interference effects on the wind pressure at the windward facade of the principal building through wind tunnel tests. The bimodal

probability distribution was presented. It was observed that by varying the relative position of the secondary building, the bimodal distribution could be altered to a unimodal form.

Sun *et al.* (2020) [135] conducted pressure measurement tests to study the proximity effects between two chimneys with various distances and wind angles. IF contour were presented for pressure coefficients. It was concluded that the interference effects were significantly higher on across-wind load compare to those of along-wind load. The wind directions of 105^0 and 30^0 was most unfavorable for extreme response in along-wind and across-wind directions, respectively. The maximum interference factor of 1.3 and 1.9 was observed for the extreme along-wind and across-wind responses, respectively.

Behera *et al.* (2020) [136] studied the proximity effect between high-rise buildings with different plan ratios and interfering building positions. The local peak pressure coefficients were plotted as contours and the interference effects were presented in from of interference zone charts. It was observed that interference effects were beneficial with respect to the maximum positive pressure, but minimum negative pressure significantly increased. The interference zones enlarged with increased plan ratios.

Chauhan (2021) [137] presented the alteration in wind forces caused by the change in the relative orientation of a closely spaced interfering building. Results of forces were presented as 2-D plots with change in wind direction. The pressure measurement data were pictured as mean and r.m.s pressure contours. The negative drag was observed and the reason was that the target building was completely shielded by the upstream building when presents in line of the wind direction.

2.4. COMPUTATIONAL WIND ENGINEERING

Revuz *et al.* (2012) [138] Used RNG k-ε turbulence model in a series of steady-state solutions using different domain sizes, with the mesh resolution in the building/wake region left unchanged to suggested the size of flow domain that should be used around a building of height, h.

Kar and Dalui (2016) [139] investigated the wind interference effects on mean pressure coefficients on an irregular shape building due to a group of three square plan buildings of the equal heights at different locations in along-wind and across-wind directions.

Roy and Bairagi (2016) [140] analyzed a stepped unsymmetrical plan shape tall building for velocity and force coefficient and flow patterns around the building using CFD simulation..

Paul and Dalui (2016) [141] presented a case study of wind effects on 'Z' plan shaped tall building under varying wind angles.

Mukherjee and Bairagi (2017) [142] used numerical simulation with CFD to determine the wind pressure coefficients and wind velocity analysis of 'N' plan shape tall buildings for wind angles varying from 0° to 180° at 30° interval and a scale of 1:300 and terrain category 2.

Xing and Qian (2018)[143] numerically studied the flow around a group of three circular cylinders arranged in equilateral-triangle arrangements. It was observed that the wake in the back of two parallel cylinders downstream of the three was asymmetrical at small spacing, which disappeared with an increase in spacing ratios.

Chen *et al.* (2018) [144] conducted simulation of the wind environment around a square building. The three dimensional flow fields around a single building were analyzed and the simulating approach is validated with experimental data.

Sanyal and Dalui (2020) [145] investigated the effect of corner modification on reducing wind effects on various corner modified (chamfered and rounded) Y plan-shaped buildings. It was observed that corner rounded is more efficient in comparison to corner chamfered

3. CHAPTER-3
EXPERIMENTAL SETUP

3.1. GENERAL

As described earlier, an experimental study through wind tunnel testing is carried out in the proposed research work to evaluate the wind pressure at the surfaces of building models having different unconventional plan shapes. This chapter deals with the details of wind tunnel used to test models and wind flow characteristics like velocity profile and turbulence intensity profile. Furthermore, details of the instruments used for simulation of Atmospheric Boundary Layer and pressure measurement are described in this chapter, in addition to the details of building models tested.

3.2. WIND TUNNEL DESCRIPTION

The experiments were carried out by Raj, R. (2015) [146] in an open circuit boundary layer wind tunnel (BLWT) at the Civil Department of the Indian Institute of Technology Roorkee, Roorkee, India. The tunnel had a single fan to generate uninterrupted flow, which was operated by a 125 HP motor. The working section of the tunnel was 15m long with a 2 m X 2 m cross-section, and the total length of the tunnel was 38 m long (Fig. 3.1). The sufficient length of the test section allows the placement of roughness elements and turbulence generators to adequately characterize the atmospheric boundary layer and turbulence intensity profile for a particular terrain category. It is possible to develop a boundary layer with a thickness of approximately 1 m at the test section. A dyno drive attached to the diffuser or fan at the outlet of the tunnel has been utilized to vary the wind speed in the tunnel with a maximum speed of 25 m/s. Models have been placed at the center of the turntable, which was located at 12.21m from elliptical effuse, and which can be rotated to set the angle of wind incidence.

3.3. WIND FLOW CHARACTERISTICS

The approach wind flow characteristics with a power-law index (α) of 0.22 are simulated according to Indian standard IS 875-part 3: 2015 (IS 875 (part 3), 2015) for wind loads by placing vortex generators, cubical blocks, and barrier walls at the inlet region.

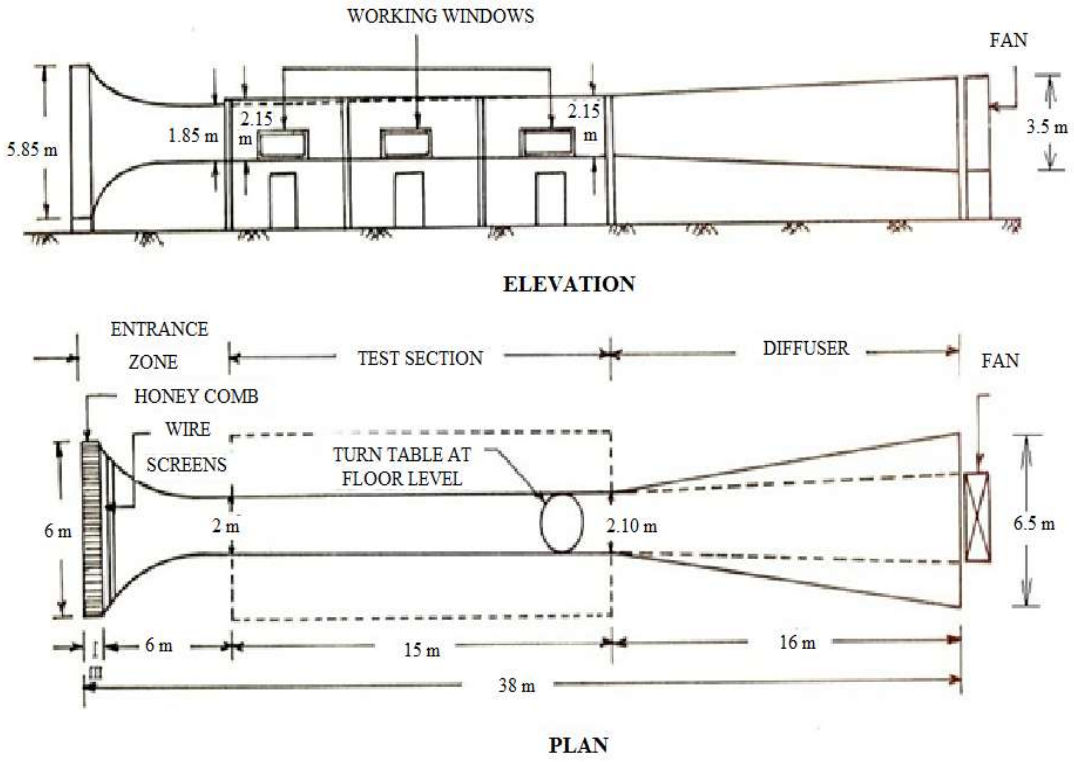

Fig. 3.1 Line diagram of the wind tunnel

The final arrangement of the roughness elements was determined by trial and error to achieve suitable wind flow characteristics. The wind velocity profile measured at the downstream end of the wind tunnel on the top of the turntable and the variation of the turbulence intensity of flow is shown in Fig. 3.2. The mean wind speed at the top of the test models is about 9.87m/s, and the turbulence intensity at the floor level is about 12%, respectively. The reference velocity V_0 is 10.80 m/sec at reference height Z_0 (900 mm).

The power-law used to represent the variation of wind speed with height is an empirical relation given by-

$$\frac{V}{V_0} = \left(\frac{Z}{Z_0}\right)^{\alpha} \quad \text{.....(3.1)}$$

Where, V_0 is the velocity at reference height Z_0, V is the velocity at any height Z and α is the power law index.

Power law index (α) is calculated from the curve between (V/V_0) and (Z/Z_0) plotted on a log-log scale as shown in Fig. 3.3. The slope of the straight line gives the value of the power law index, which is 0.22 for the current study. Turbulence intensity is defined as

$$I_u = \frac{\sigma_z}{V_z} \quad \text{..... (3.2)}$$

Where, V_z is the mean wind speed at height Z, and σ_z is the standard deviation of the fluctuating velocity

The wind pressure on the models is measured using a "Baratron Pressure Transducer," which is capable of measuring extremely low differential heads.

3.4. INSTRUMENTS USED

The salient features of the instruments used for the determination of various quantities are described here.

3.4.1. TESTO-480

Wind velocity inside the wind tunnel is measured with the help of an instrument called "TESTO-480" . A probe has connected to this instrument to measure the wind velocity at a different height, which has a length of 1 m. Further, this instrument is connected to and operated through a computer.

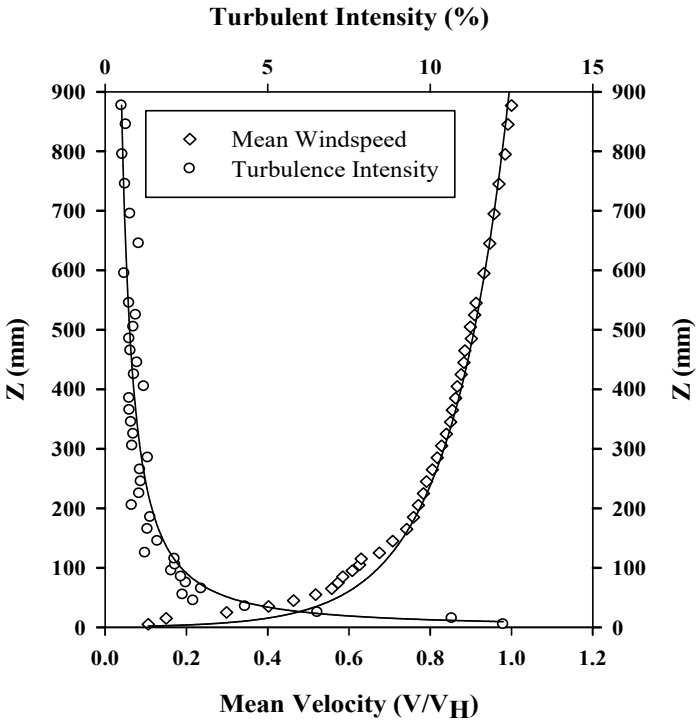

Fig. 3.2 Simulated mean wind speed and turbulence intensity profile in wind tunnel

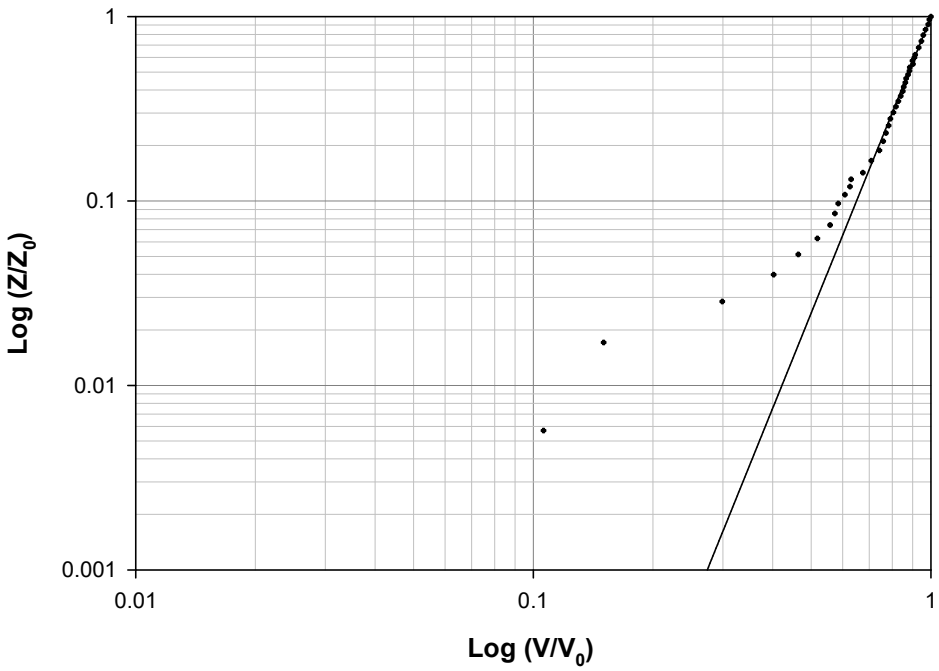

Fig. 3.3 Non dimensional mean wind speed profile on log-log scale

3.4.2. Pressure Transducer

Wind pressure at the surface of the building model is measured with the help of an MKS-made “Baratron Pressure Transducer”. This instrument is a capacitance type pressure transducer which is capable of measuring very low differential heads. The pressure transducer comprises of a pressure head and a display unit where the surface pressure measured is directly displayed in terms of mmHg, which can be converted into N/m^2. The output from the display unit is stored in a computer with the help of Data Acquisition System. The pressure on the surface of a model in the wind tunnel is measured with respect to a reference pressure. The reference pressure is the pressure at a point on the inner surface of the wall of the test section, which is not affected by the obstacles on the upstream side. One end of the pressure head is connected to pressure taping on the surface of the model, and another end is connected to the reference point.

3.4.3. Data Acquisition System

The Data Acquisition System is an electronic instrument that receives the electronic signals from the measuring devices like pressure transducer, load cell, etc. and transfer them to a computer.

3.5. DETAILS OF MODELS

In the present study, two types of building models are prepared. One is the principal building models made of transparent Perspex sheet, which are tested in the wind tunnel for pressure measurement, and the other are made from plywood of similar dimensions used as interfering building models. A total 4 number of models are prepared for both principal and interfering building models. Plan area (40,000 mm^2) and the height (600 mm) of all four models are kept similar to assess the effect of shape modification on wind loads through comparative analysis of all models. The length scale is set as 1:300 so that the models represent the full-scale building of height 180 m. The plan and isometric views of the building models are shown in Fig. 3.4 and Fig. 3.5, respectively.

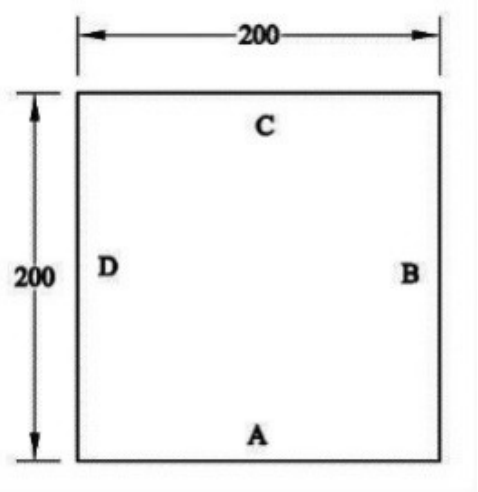

Model-1 (Sq model)

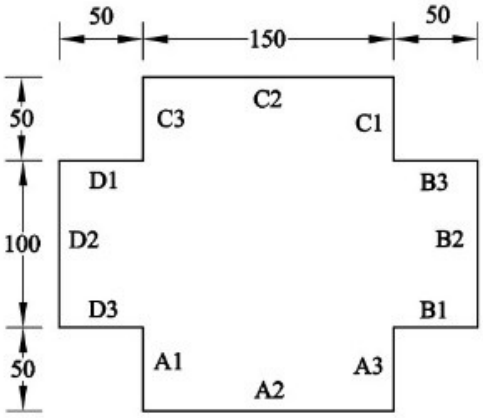

Model-2 (Pl-1 model)

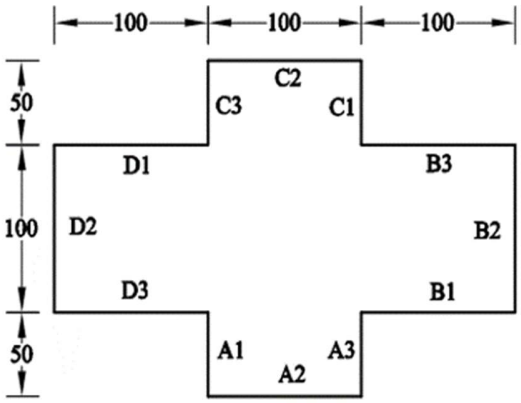

Model-1 (Pl-2 model)

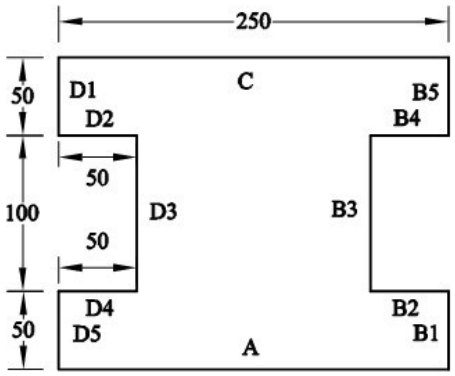

Model-1 (H- model)

Fig. 3.4 Plan view of buildings models

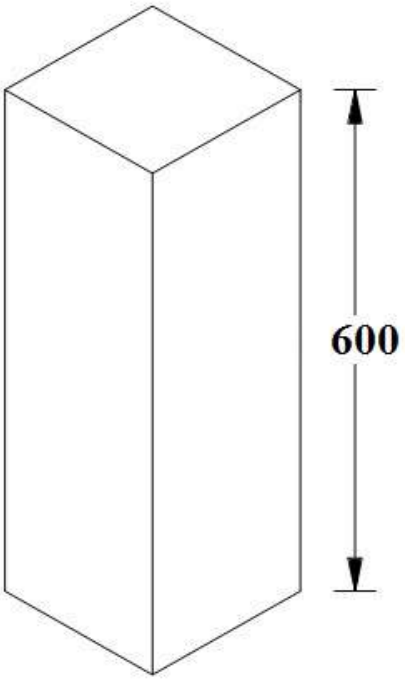

Model-1 (Sq model)

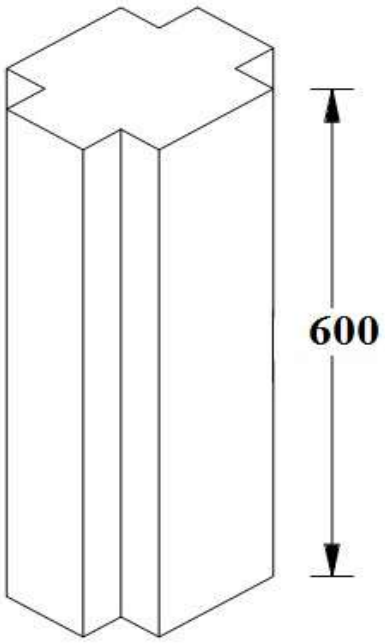

Model-2 (Pl-1 model)

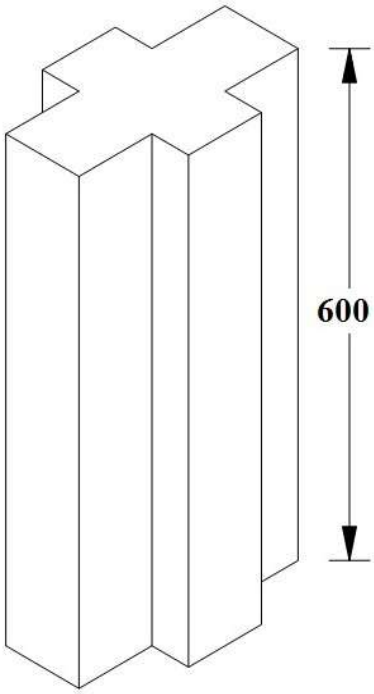

Model-1 (Pl-2 model)

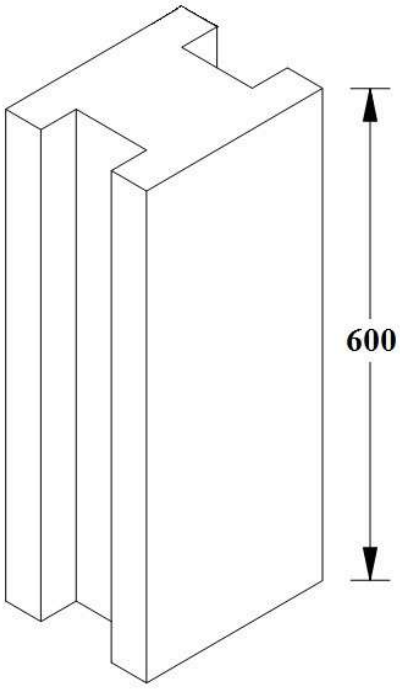

Model-1 (H- model)

Fig. 3.5 Isometric view of buildings models

Models are made with a 4 mm Perspex sheet with stiff faces to ensure the sufficient rigidity and strength of the models. All the Perspex sheet models are provided with closely spaced pressure taps located at seven different heights levels of 10, 60, 180, 300, 420, 540, and 590 mm (Level A-G from top) to obtain a good distribution of pressure at all the faces of the models. Plan and isometric view of pressure taping distribution at models are shown in Fig. 3.6 to Fig. 3.9. The pressure taps have been made of steel tubes with an internal diameter of 1 mm and 15-20 mm in length.

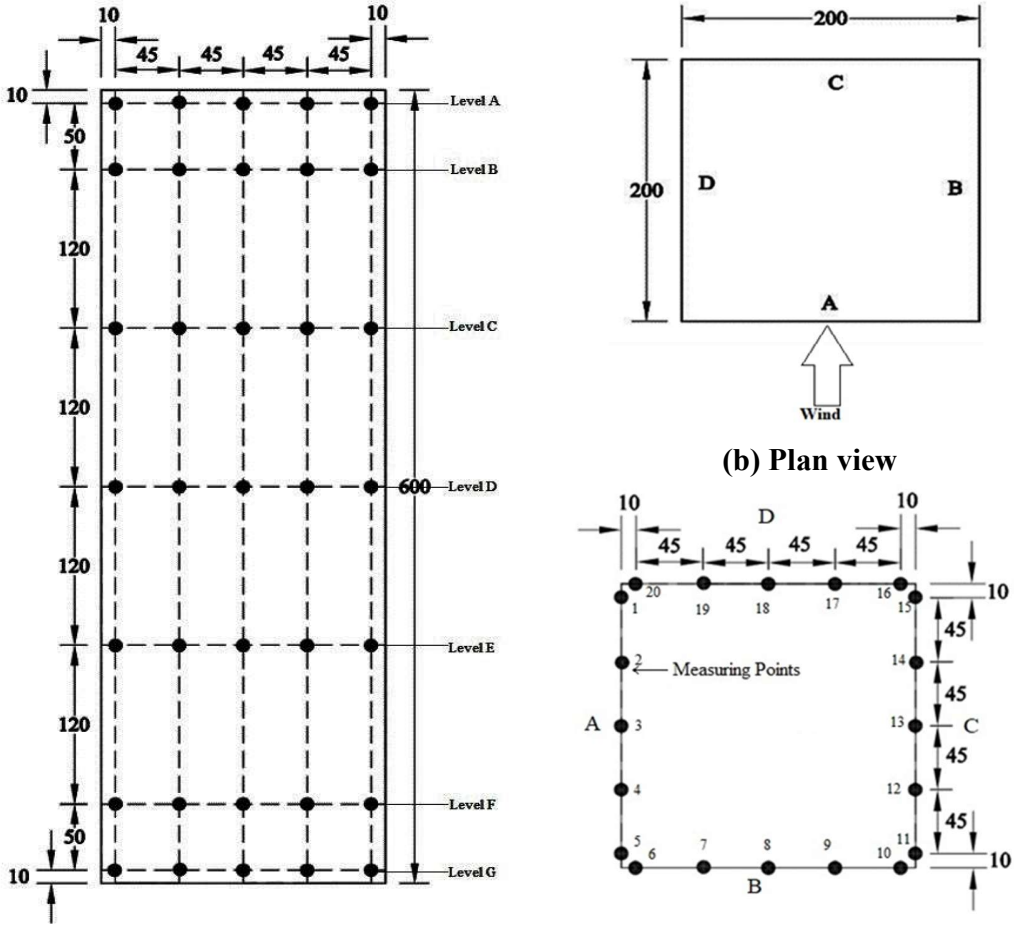

(a) Front face elevation

(b) Plan view

(c) Pressure taping along perimeter

Fig. 3.6 Pressure tapping details of model-1 (Sq model) (All dimensions in mm**)**

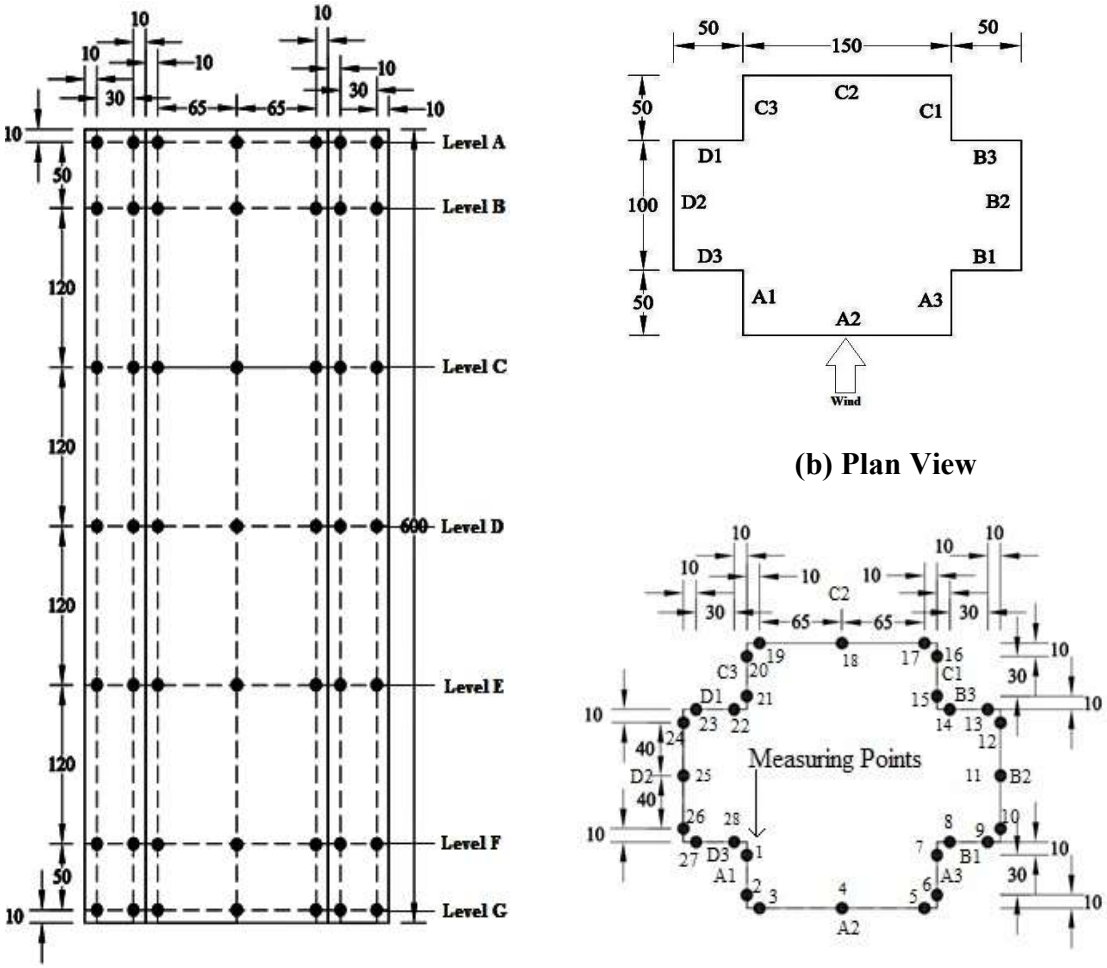

(a) Front face elevation

(b) Plan View

(c) Pressure taping along perimeter

Fig. 3.7 Pressure tapping details of model-2 (Pl-1 model) (All dimensions in mm**)**

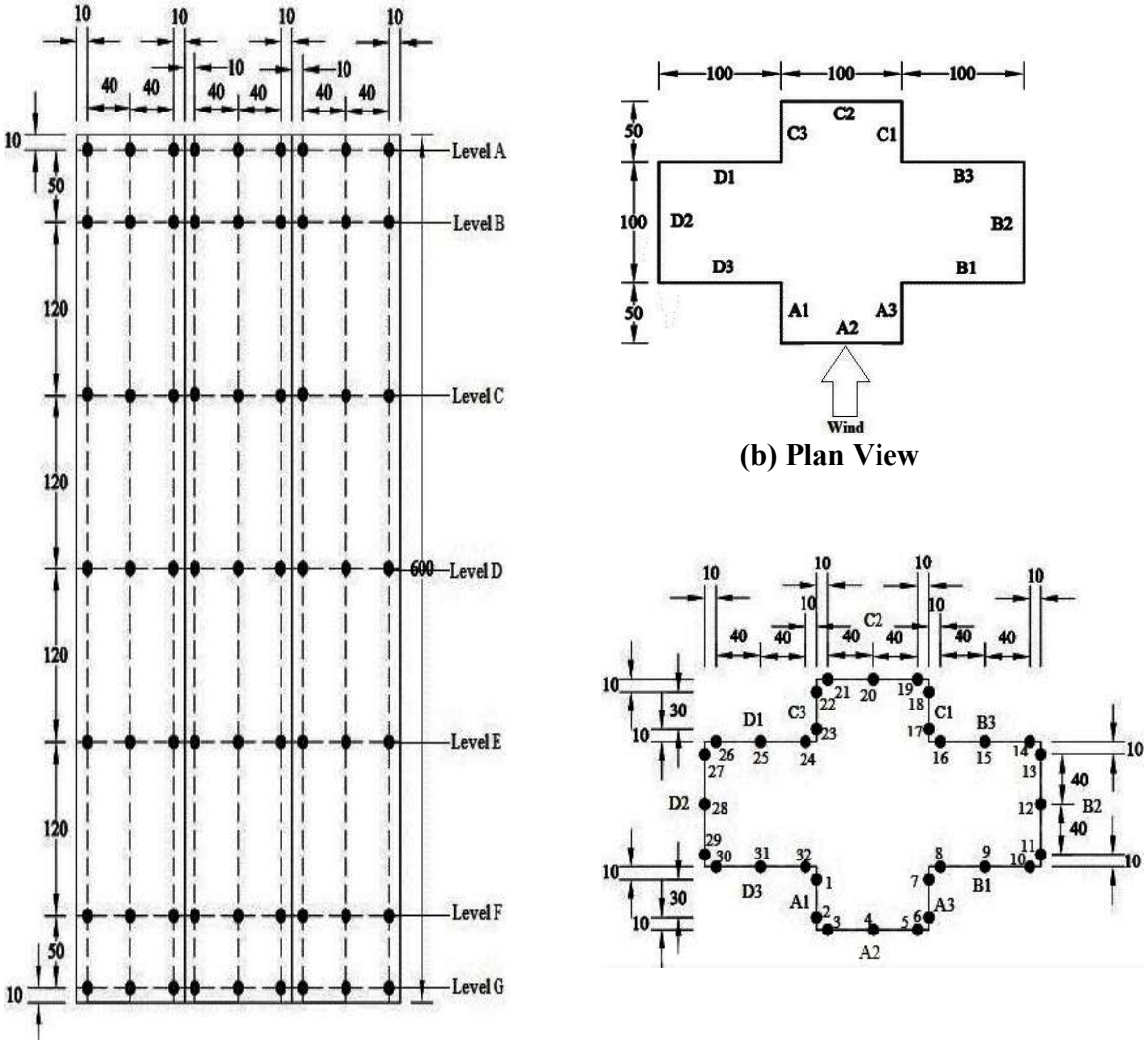

(a) Front face elevation

(b) Plan View

(c) Pressure taping along perimeter

Fig. 3.8 Pressure tapping details of model-3 (Pl-2 model) (All dimensions in mm**)**

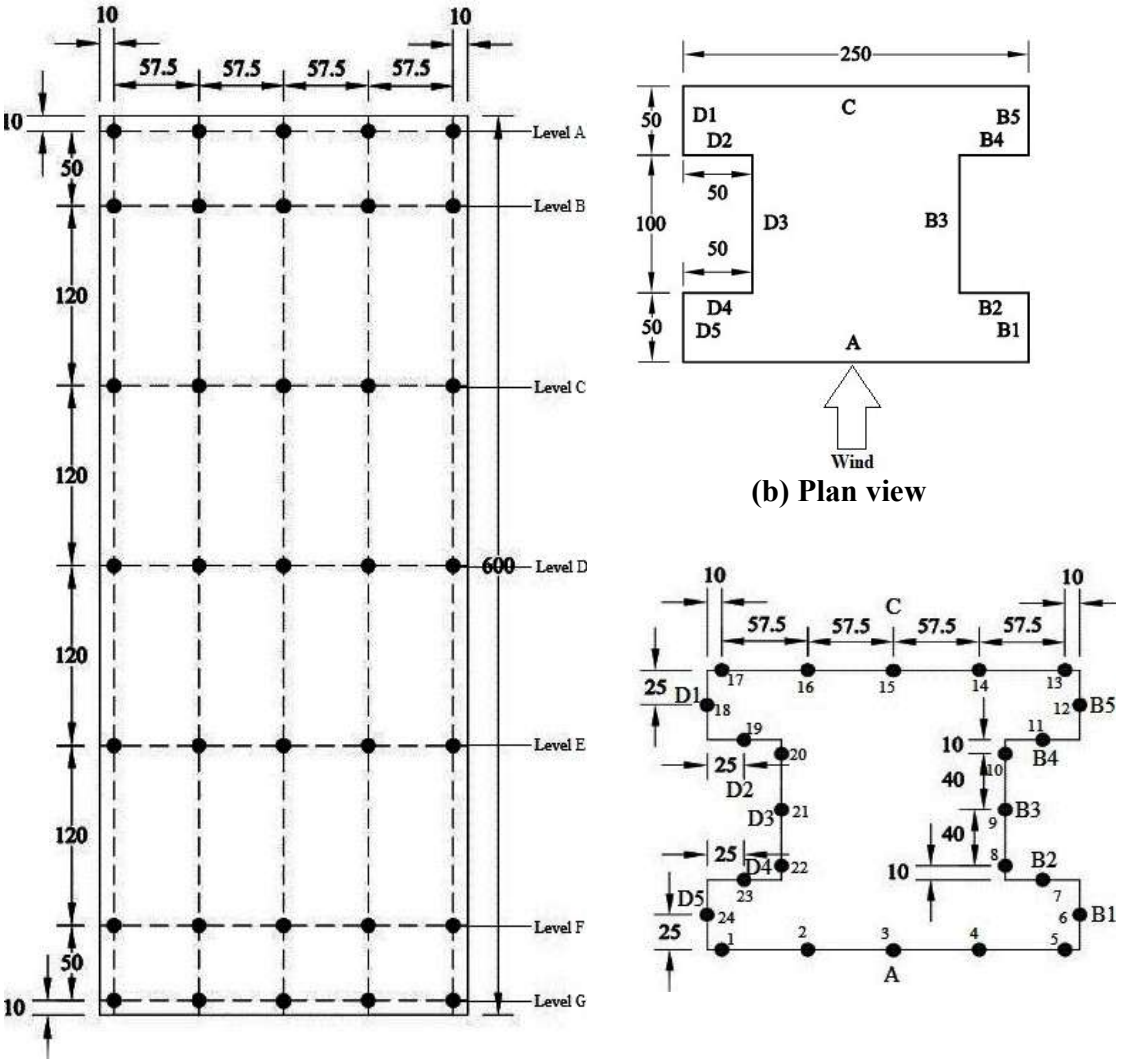

(a) Front face elevation

(b) Plan view

(c) Pressure taping along perimeter

Fig. 3.9 Pressure tapping details of model-4 (H model) (All dimensions in mm**)**

3.6. DATA PROCESSING

3.6.1. Wind Pressure Coefficients

The pressure p at any pressure point on the building is generally expressed by a non-dimensional pressure coefficient C_p, which is calculated by normalizing the measuring wind pressure at the corresponding measuring point given by the following equations [147], [148]:

$$C_{P,mean} = \frac{\bar{p} - p_0}{\frac{1}{2}\rho_a {U_H}^2} \quad \text{..... (3.3)}$$

$$C_{P,max} = \frac{p_{max} - p_0}{\frac{1}{2}\rho_a {U_H}^2} \quad \text{..... (3.4)}$$

$$C_{P,min} = \frac{p_{min} - p_0}{\frac{1}{2}\rho_a {U_H}^2} \quad \text{..... (3.5)}$$

$$C_{P,rms} == \sigma_{cp} = \frac{p_{rms}}{\frac{1}{2}\rho_a {U_H}^2} \quad \text{..... (3.6)}$$

p_{rms} is determined as [51], [110]

$$p_{rms} = \sqrt{\sum_{K=1}^{N} (p_k - p_{mean})^2 / (N-1)} \quad \text{.....(3.7)}$$

Where $\bar{p}$ is the local mean pressure, p_0 is the reference static pressure or atmospheric pressure, p_{max} is the highest peak pressure of the fluctuating pressure, p_{min} is the lowest peak pressure, p_{rms} is the root-mean square of the fluctuating components of time history data, p_k is the time history of pressure measuring point; N is the total number of samples, ρ_a is the density of air, and U_H is the mean wind velocity at the model's height equal to 9.87 m/sec in the current study. Local Force Coefficients are calculated for wind incidence angles of 0^0 to 90^0 at an interval of 30^0.

3.6.2. Local wind force Coefficients

The force coefficients are described similar to wind pressure coefficients in the form of non-dimensional coefficients. The aerodynamic forces may conveniently be resolved into two orthogonal directions considering wind axes or geometry axes of the body (body axes). In the present work, forces are resolved in two orthogonal directions based on wind axes for all wind directions of 0 to 90 degrees.

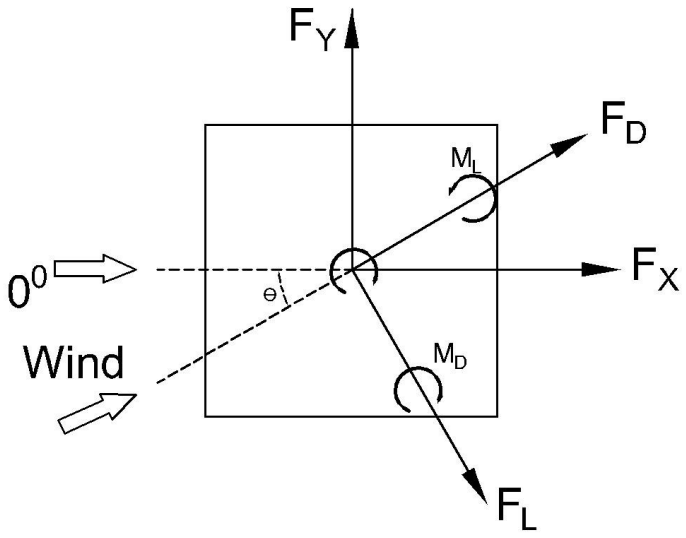

Fig. 3.10 Wind force direction

The forces in the direction of the axis, parallel to the wind direction are considered as along-wind force and termed as 'drag,' and forces in orthogonal direction are considered as crosswind force and termed as 'lift' as in Fig. 3.10. The mean local wind force coefficients are calculated using the local wind pressure coefficients at each pressure tap, and the mean wind velocity pressure q_H at the top of the model. The mean and r.m.s. local wind force coefficients in along-wind and crosswind directions are calculated for all models for wind directions of 0 to 90 degree. The wind forces at each measurement layer of building models can be calculated using the pressure integration method. Researchers have adopted wind pressure integration technique to obtain the along-wind and crosswind dynamic forces on tall buildings and structures [10], [25], [27], [72], [95], [130]. The local mean wind force coefficients are defined as follows:

$$F_{x(z_i)} = \text{mean} \left(\sum_{i=1}^{N} p_{xi} A_i\right) \quad \text{..... (3.8)}$$

$$F_{y(z_i)} = \text{mean} \left(\sum_{i=1}^{N} p_{yi} A_i\right) \quad \text{..... (3.9)}$$

$$F^*_{x(z_i)} = \text{rms} \left(\sum_{i=1}^{N} p_{xi} A_i\right) \quad \text{..... (3.10)}$$

$$F^*_{y(z_i)} = \text{rms} \left(\sum_{i=1}^{N} p_{yi} A_i\right) \quad \text{.....(3.11)}$$

$$F_{D(z_i)} = F_{x(z_i)} \cos\theta + F_{y(z_i)} \sin\theta \quad \text{..... (3.12)}$$

$$F_{L(z_i)} = F_{x(z_i)} \sin\theta - F_{y(z_i)} \cos\theta \quad \text{..... (3.13)}$$

$$\sigma_{D(z_i)} = F^*_{x(z_i)} \cos\theta + F^*_{y(z_i)} \sin\theta \quad \text{..... (3.14)}$$

$$\sigma_{L(z_i))} = F^*_{x(z_i)} \sin\theta - F^*_{y(z_i)} \cos\theta \quad \text{..... (3.15)}$$

$$C_{D(z_i)} = \frac{F_{D(z_i)}}{q_H B H_i} \quad \text{..... (3.16)}$$

$$C_L(z_i) = \frac{F_{L(z_i)}}{q_H B H_i} \quad \text{..... (3.17)}$$

$$C^*_{D(z_i)} = \frac{\sigma_{D(z_i)}}{q_H B H_i} \quad \text{..... (3.18)}$$

$$C^*_L(z_i) = \frac{\sigma_{L(z_i)}}{q_H B H_i} \quad \text{..... (3.19)}$$

Where $C_{D(z_i)}$ and $C_{L(z_i)}$ are mean local wind force coefficients of the i[th] level in along-wind and crosswind directions, respectively; $F_{D(z_i)}$ and $F_{L(z_i)}$ are mean local wind forces in along-wind and crosswind directions, respectively; $C^*_{D(z_i)}$ and $C^*_L(z_i)$ are r.m.s. local wind force coefficients of the i[th] level in along-wind and crosswind directions, respectively; $\sigma_{D(z_i)}$ and $\sigma_{L(z_i)}$ are r.m.s. local wind forces in along-wind and crosswind directions, respectively; $F_{x(z_i)}$ and $F_{y(z_i)}$ are mean local wind forces along-parallel (x) and perpendicular(y) axis related to the geometry of the body; $F^*_{x(z_i)}$ and $F^*_{y(z_i)}$ are the corresponding r.m.s. local wind forces in x and y-axis; q_H is the mean wind velocity pressure at the top of model height; p_i and A_i are the wind pressure and tributary area of each pressure tap; B is the projected model width; θ is wind direction; Hi represents the occupied height of different levels, where i=1, 2,……7

3.6.3. Base Wind Forces

The base forces have been calculated by integrating all the forces at different height levels. The base moments have been calculated by multiplying the time series of local wind forces at each measurement layer and their corresponding heights. The mean and RMS overturning moment coefficients of the three models are expressed as follows;

$$M_D = mean \sum_{i=1}^{N} F_{D(z_i)}\, h_i \quad \text{..... (3.20)}$$

$$M_L = mean \sum_{i=1}^{N} F_{L(z_i)}\, h_i \quad \text{.....(3.21)}$$

$$\sigma_{MD} = \sum_{i=1}^{N} \sigma_{D(z_i)} h_i \quad \text{.....} \quad (3.22)$$

$$\sigma_{ML} = \sum_{i=1}^{N} \sigma_{L(z_i)} h_i \quad \text{.....} \quad (3.23)$$

$$C_{FD} = \frac{\sum_{i=1}^{7} F_{D(z_i)}}{q_H BH} \qquad C_{FL} = \frac{\sum_{i=1}^{7} F_{L(z_i)}}{q_H BH} \quad \text{.....} \quad (3.24)$$

$$C^*_{FD} = \frac{\sum_{i=1}^{7} \sigma_{D(z_i)}}{q_H BH} \qquad C^*_{FL} = \frac{\sum_{i=1}^{7} \sigma_{L(z_i)}}{q_H BH} \quad \text{.....} \quad (3.25)$$

$$C_{MD} = \frac{M_D}{q_H BH^2} \qquad C_{ML} = \frac{M_L}{q_H BH^2} \quad \text{.....} \quad (3.26)$$

$$C^*_{MD} = \frac{\sigma_{MD}}{q_H BH^2} \qquad C^*_{ML} = \frac{\sigma_{ML}}{q_H BH^2} \quad \text{.....} \quad (3.27)$$

In which, C_{FD} and C_{FL} are the mean along-wind base force coefficient and mean across-wind base force coefficient, respectively; C^*_{FD} and C^*_{FL} are the corresponding RMS coefficients; C_{MD} and C_{ML} are the mean components of overturning moment coefficients in along-wind and cross-wind directions, respectively; C^*_{MD} and C^*_{ML} are corresponding RMS coefficients; M_D and M_L are mean components of overturning moments (OTM) in along-wind and cross-wind directions, respectively; σ_{MD} and σ_{ML} are RMS overturning moments; H is the model height

4. CHAPTER-4

EXPERIMENTAL STUDY- PRESSURE MEASUREMENT (ISOLATED)

4.1. GENERAL

As discussed earlier, the codes and standards do not provide useful data regarding irregular tall buildings. Further, no analytical formula is available to evaluate the wind effect on irregular shape tall buildings, which necessitates more experimental or analytical study for irregular shape tall buildings.

In the proposed research work, wind tunnel testing of four tall buildings models, as shown in Fig. 3.5, has been carried out to measure the fluctuating values of wind pressure distribution at pressure points on the various surfaces of building models. Mean ($C_{p,mean}$), Maximum ($C_{p,max}$), Minimum ($C_{p,min}$), and r.m.s. ($C_{p,rms}$) values of pressure coefficients are evaluated by normalizing the measured fluctuated wind pressure as discussed in the previous chapter. To assess the effect of wind direction, all the building models are tested at wind direction of 0 to 90 degree at an interval of 30 degree. The range of wind direction is kept up to 90 degree due to symmetry about both the axes. The fluctuating pressure at each pressure point is measured using a Baratron pressure gauge for a duration of 60 seconds. The readings recorded at each pressure point in the **mmHg** unit are converted into the pressure unit N/m^2 by multiplying with Baratron range and multiplying factor as-

Pressure (N/m^2) = Multiplying factor x Baratron range x Baratron reading …… (4.1)

The results of the present study are presented in four parts. In the first part, the results of the pressure measurement on all building models tested in the isolated condition at various wind directions are presented in chapter four. The second part is presented in chapter five, in which results of the pressure measurements of all building models in the different interfering conditions are presented. The third part covers the results of the local wind force, and base forces and base moments evaluated using the pressure integration

method in chapter six. The seventh chapter presents the fourth part of test results related to the response study of all the models.

As mentioned above, test results of pressure measurement in isolated conditions are presented in this chapter.

4.2. DATA VALIDATION

Since experimental data may also be affected by a range of factors, it is necessary to verify the calculation method used for wind loading measurements. For the validation of the experimental procedure, the experimental data of the square model have been compared with the various international codes and with data of the Commonwealth Advisory Aeronautical Research Council (CAARC) model.

4.2.1. Validation with international codes

The comparison of the area average values of mean pressure coefficients at various surfaces of the square model is presented in table 4.1. It has been observed that average mean pressure coefficients at the front surface, side surface, and leeward surface of isolating square model have appreciable results with the international codes [13]–[17].

Table 4.1 Comparison average $C_{p,mean}$ of the Square tall building

International Code	**Wind angle**	**Front Surface**		**Leeward surface**		**Side surface**	
Experimental results	0° 90°	**0.68** **0.68**	**Variation %**	**-0.42** **-0.42**	**Variation %**	**-0.67** **-0.66**	**Variation %**
AS/NZS: 1170.2:2002	0° 90°	0.80 0.80	15 15	-0.50 -0.50	16 16	-0.65 -0.65	3 2
ASCE/SEI 7-10	0° 90°	0.80 0.80	15 15	-0.50 -0.50	16 16	-0.70 -0.70	4 5
EN: 1991-1-4	0° 90°	0.80 0.80	15 15	-0.55 -0.55	23 23	-0.80 -0.80	16 17
BS: 6399-2	0° 90°	0.76 0.76	10 10	-0.50 -0.50	16 16	-0.80 -0.80	16 17
IS 875 (part 3)	0° 90°	0.80 0.80	15 15	-0.25 -0.25	40 40	-0.80 -0.80	16 17

4.2.2. Validation with CAARC data

The experimental parameters of a base square building model tested at 0-degree wind incidence in this study have been compared with the experimental parameter [95], [103], [149], [150] of the classical model of the Commonwealth Advisory Aeronautical Research Council (CAARC) standard tall building model tested at several research institutions, including the University of Bristol (BU), Monash University (MU), National Aeronautical Establishment (NAE) and National Physical Laboratory. Fig. 4.1 presents the comparison of $C_{p,mean}$ at 0.7H height of the square building model with the $C_{p,mean}$ of the CAARC standard tall building model at 2/3H. The mean wind pressure coefficients obtained from this study for the reference square building model are consistent with those of the CAARC model.

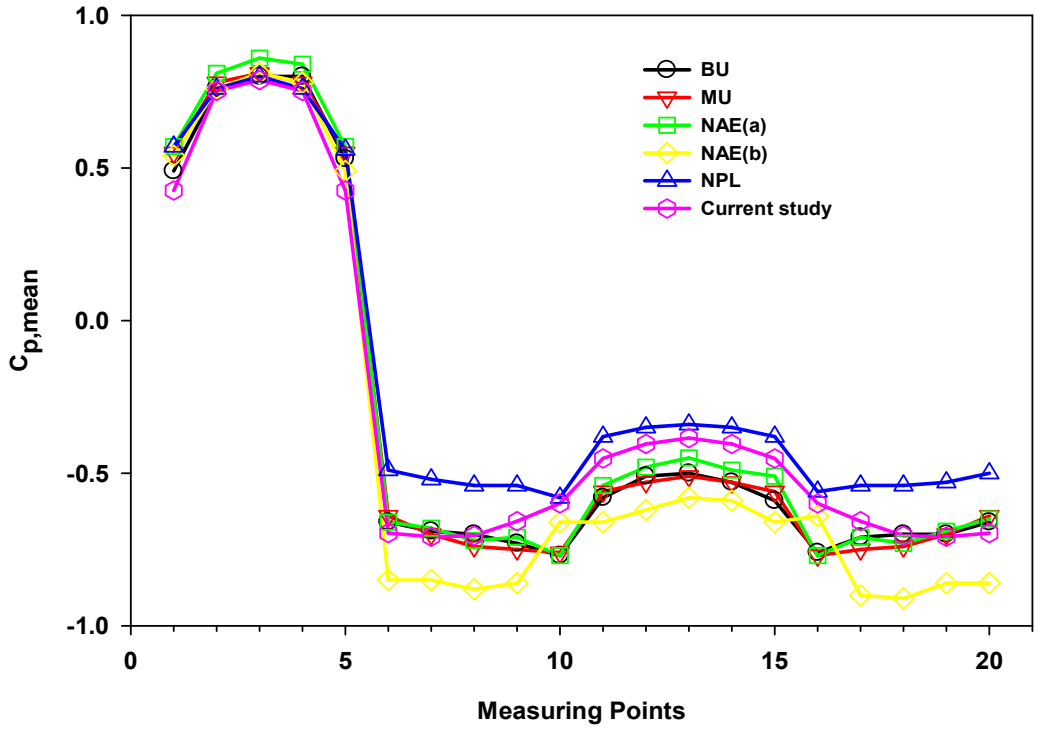

Fig. 4.1 Comparison of $C_{p,\,mean}$ of square model with CAARC standard models

4.3. PRESSURE MEASUREMENT PLAN

The detailed study of variation of pressure coefficients for different wind incidence angles is an essential task before designing the elements of tall buildings for wind load. The local pressure coefficients on the surfaces of the tall buildings can be very useful in the design of cladding. In this aspect, a detailed investigation of pressure variation as mean and r.m.s coefficients at different faces of all four building models has been carried out for wind direction between 0^0 to 90^0 at an interval of 30^0. The variation of mean pressure coefficients is presented in the form of contours at different faces and along the perimeter at different height levels for all models at all wind directions, as mentioned. The distribution of r.m.s pressure coefficients is presented in the form of contours at different surfaces of all models. Peak maximum and peak minimum off fluctuating pressure data are presented in tabular form at different pressure points. Area average values of mean pressure coefficients of the different surfaces are also presented in tabular form for all models for wind direction of 0^0 to 90^0.

4.4. RESULTS AND DISCUSSION

4.4.1. Square Model (Sq-model)

As mentioned earlier, the Perspex sheet model of the square cross-section is tested in a wind tunnel under four different wind directions from 0^0 to 90^0 as shown in Figure 4.2.

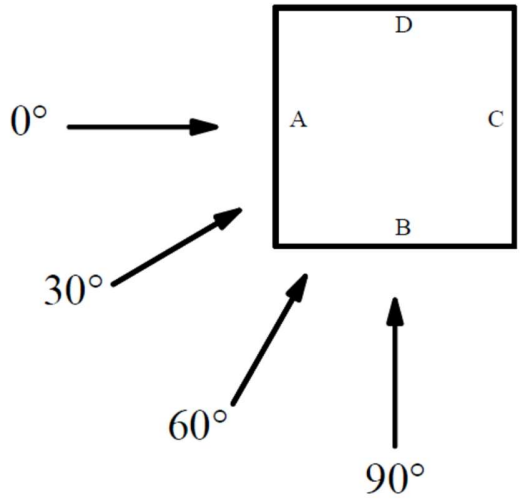

Fig. 4.2 Wind direction on Sq-model in isolated condition

Values of $C_{p,\ mean}$ depend on the wind direction, shape of the building, and flow conditions. It is observed from the mean pressure variation shown in Fig. 4.3 that for wind incidence at 0^0, the front face A is subjected to appositive pressure throughout the area. Pressure distribution is symmetric about the vertical central line. Pressure increases with height at the front face due to an increase in velocity. The zone of high pressure concentrates at the central part of width at 0.7H from the bottom. The side faces experience suction due to flow separation at the edges, and leeward faces experience suction due to flow recirculation. Mean pressure coefficients at the front face varies from a very low pressure coefficient of 0.23 near the ground at edges to a high pressure coefficient of 0.87 at 0.7H from the bottom. Suction at side faces decreases from wind ward edge to leeward edge. A maximum suction coefficient of -0.87 occurs at the side face near the top corner at the windward side. Suction at the leeward surface increases toward the outer edges.

When the angle of attack (AOA) increases to 30^0, the maximum value of $C_{p,\ mean}$ shifted from the central line to the right edge of the windward face. The pressure coefficient at the left edge is reduced to almost zero. The maximum positive pressure coefficient is still found at face A, but the magnitude is reduced to 0.66. Face B is subjected to positive pressure at the center, whereas suction near the edges. The maximum value of the overall negative $C_{p,mean}$ appears at the leeward edge of the left side face D equal to -0.63 and decreases near the windward edge. The variation of mean wind pressure coefficients at all faces for 30^0 wind are shown in Fig. 4.4.

As shown in Fig. 4.5, the $C_{p,\ mean}$ for the wind flow at 60^0 angle is negative at the left edge of the windward face, which turns positive towards the right edge. Pressure at face A varies between 0.13 to -0.27. The $C_{p,\ mean}$ reaches up to the value of 0.63 near the windward edge of the side face B, while the maximum suction coefficient (-0.65) occurs near the peripheral edge of the leeward face C. Leeward face is still under suction similar to 0^0 wind, but the suction intensity is slightly higher than 0^0 wind.

The distribution of wind pressure coefficient at 90^0 AOA is similar to 0^0 wind angle due to symmetry. Mean wind pressure distribution along perimeter for 90 degree angle of attack is shown in Fig. 4.6.

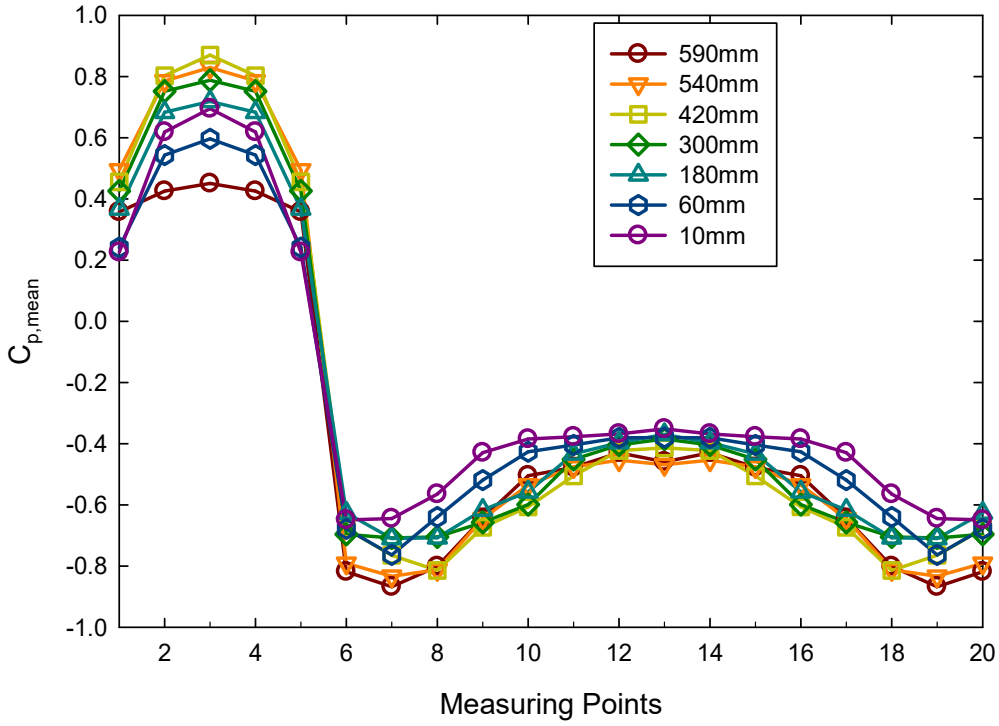

Fig. 4.3 $C_{p,\,mean}$ along perimeter-Sq model (0 degree)

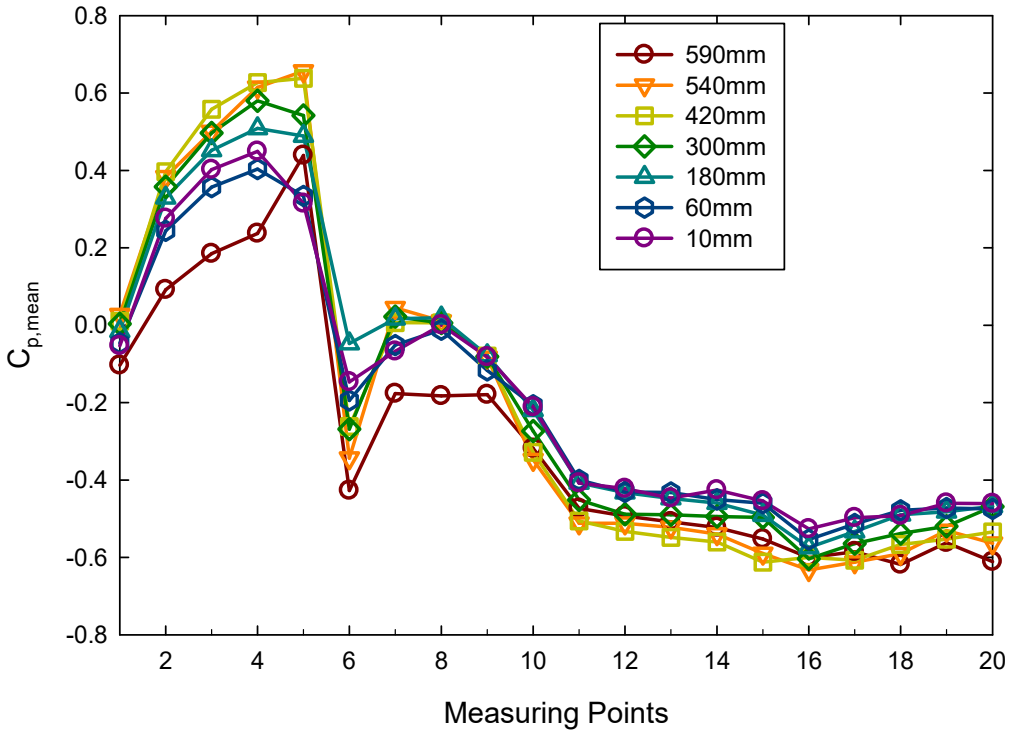

Fig. 4.4 $C_{p,\,mean}$ along perimeter-Sq model (30 degree)

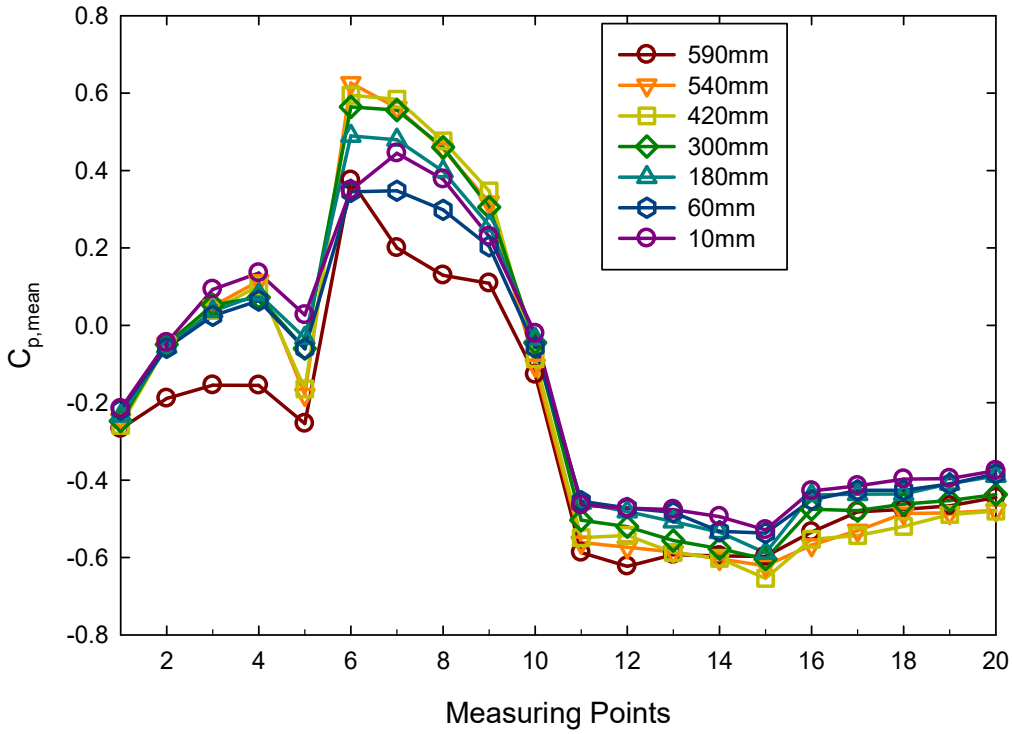

Fig. 4.5 $C_{p,\,mean}$ along perimeter-Sq model (60 degree)

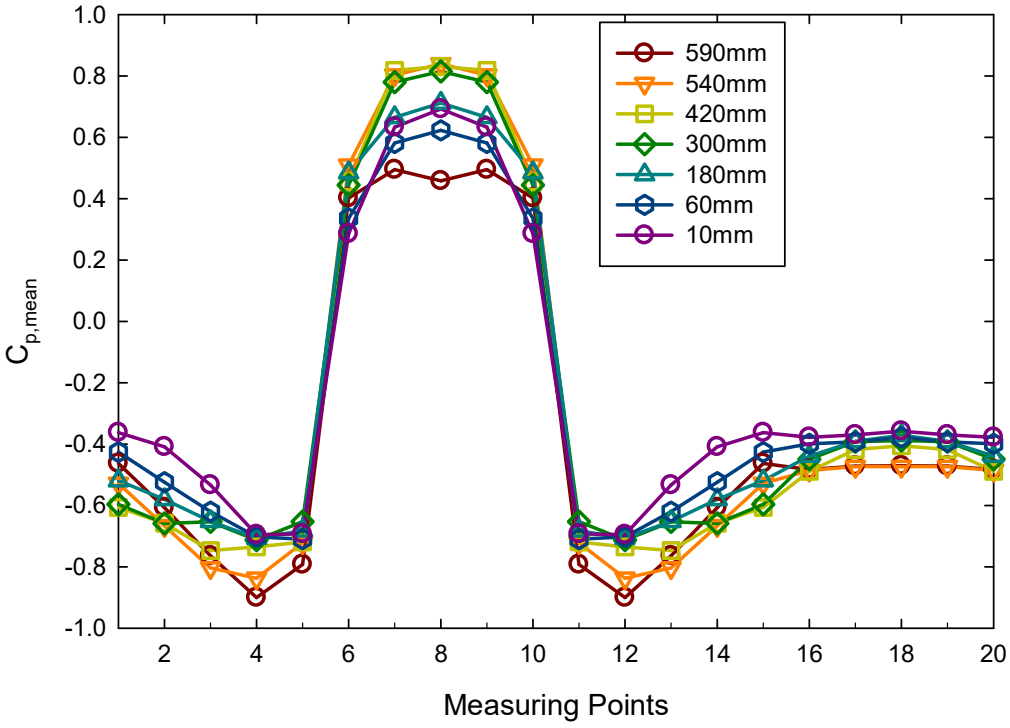

Fig. 4.6 $C_{p,\,mean}$ along perimeter-Sq model (90 degree)

The area-averaged values of mean pressure coefficients at different faces are shown in table 4.2. The pressure at face A is maximum for 0^0 wind while suction is highest for 90^0 wind. Face B has the reverse situation of face A due to perpendicular wind directions. Face C and D are subjected to suction for all wind directions. Maximum suction at face C is observed for 90^0 wind, whereas at face D for 0^0 wind.

Table 4.2 Area averaged mean pressure coefficients- Sq model

Wind Angle	Face A	Face B	Face C	Face D
0 degree	0.68	-0.67	-0.42	-0.67
30 degree	0.38	-0.10	-0.49	-0.54
60 degree	-0.04	0.33	-0.55	-0.46
90 degree	-0.66	0.68	-0.66	-0.42

The distribution of r.m.s pressure coefficients ($C_{p,rms}$) is shown in Fig. 4.7 to 4.10 for wind directions of 0^0 to 90^0, respectively. A smaller value of r.m.s wind coefficients at windward and leeward surfaces indicates the lower level of turbulence in the flow at these faces at 0 and 90 degree wind. The distribution of r.m.s coefficients at the back face is more complicated, which indicates the irregular and disorders vortices in the flow. The values of fluctuating pressure coefficients are higher on the side face compare to windward and leeward faces, which may be due to the existence of a strong and coherent vortex motion due to the flow separation, especially at the windward edges. The values of r.m.s pressure at the lower part are higher than those at the upper part, which indicates the presence of obstruction and interaction effects at the lower part. For wind at skew angles 30^0 and 60^0, r.m.s values are smaller because flow remains attached after separating at edges of face A and B.

Maximum and minimum peak pressure coefficients (($C_{p,max}$ and ($C_{p,min}$)) at each pressure point are calculated from the fluctuating time history of the pressure data recorded. The values of peak pressure coefficients of square models are shown in table 4.3 to 4.6 for wind direction of 0 to 90 degree, respectively. The maximum value of $C_{p,max}$ and $C_{p,min}$ at face A is 1.05 for 0 degree wind and -1.23 for 90 wind direction, respectively. The maximum values of peak max. and peak min. observed at face B are 0.91 for 60^0 and -1.26 for 0^0, at face C are 0.49 for 0^0 and -1.22 for 90^0 wind, and at face D values are 0.00 for 0^0 and -1.37 for 0^0 wind angles.

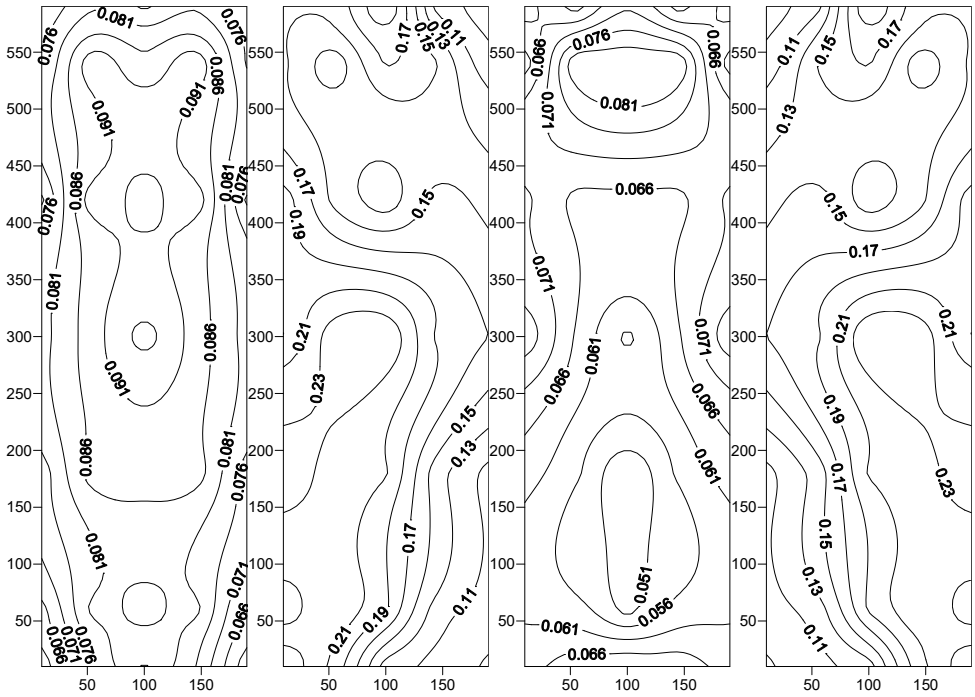

Fig. 4.7 Contour of r.m.s wind pressure coefficient - Sq model (0 degree)

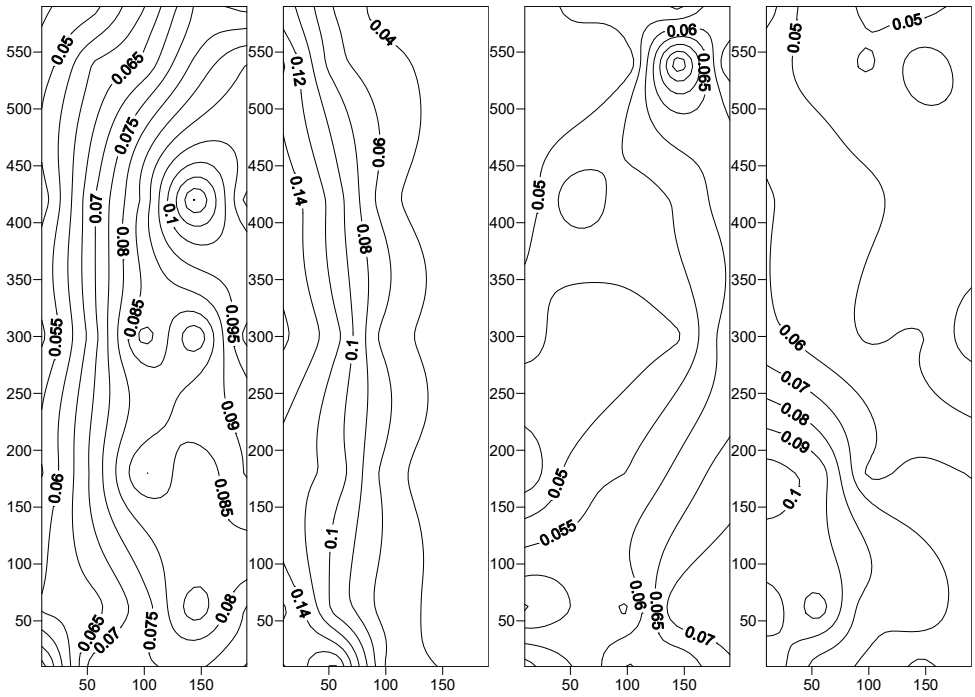

Fig. 4.8 Contour of r.m.s wind pressure coefficient - Sq model (30 degree)

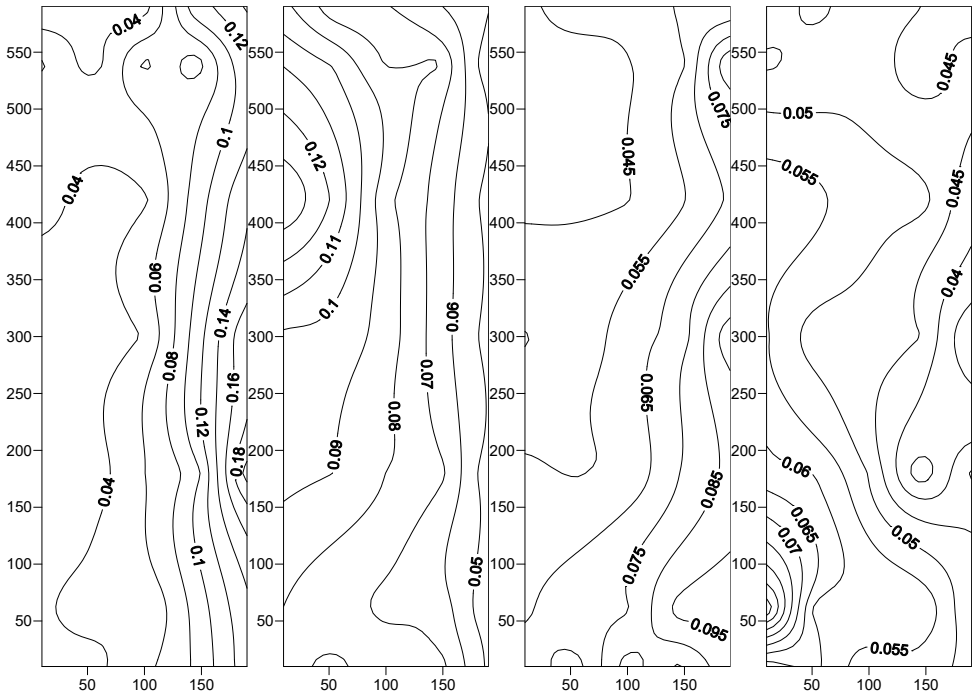

Fig. 4.9 Contour of r.m.s wind pressure coefficient - Sq model (60 degree)

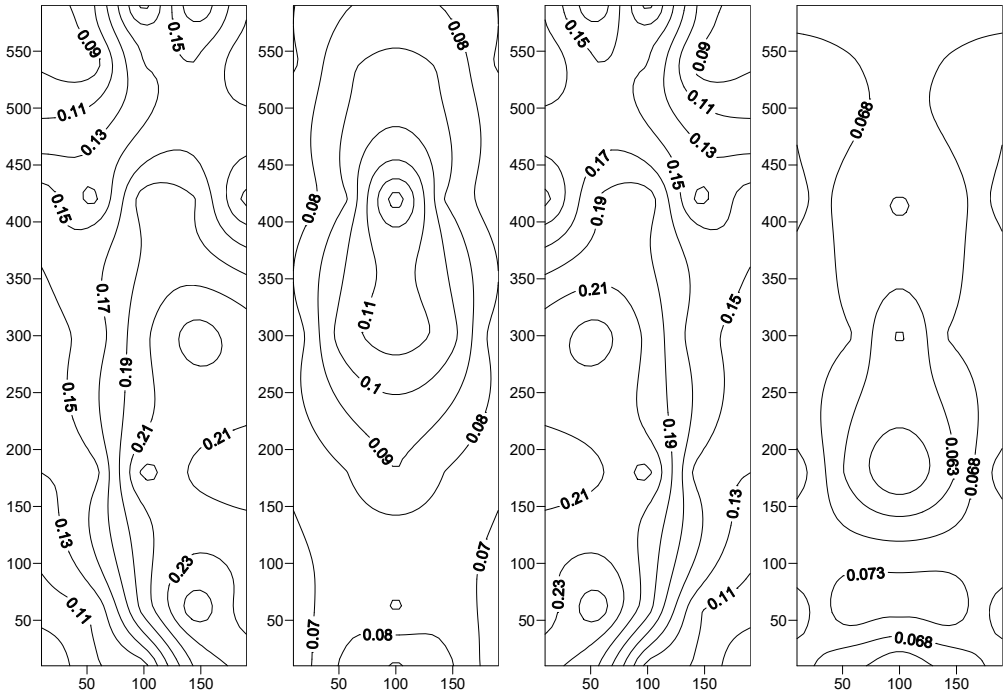

Fig. 4.10 Contour of r.m.s wind pressure coefficient - Sq model (90 degree)

Table 4.3 Peak pressure coefficients at pressure points of Sq model (0 degree)

Pressure Point	Face A		Face B		Face C		Face D	
	Max. Peak	Min. Peak	Max. Peak	Min. Peak	Max. Peak	Min. Peak	Max. Peak	Min. Peak
1	0.44	0.00	-0.07	-1.07	-0.33	-0.64	-0.36	-0.70
2	0.60	0.03	-0.08	-1.16	0.07	-0.27	-0.26	-0.83
3	0.59	0.06	-0.07	-1.10	-0.34	-0.62	-0.07	-1.10
4	0.58	0.03	-0.26	-0.83	0.07	-0.27	-0.08	-1.16
5	0.57	0.00	-0.36	-0.70	-0.33	-0.64	-0.07	-1.07
6	0.60	0.14	-0.34	-1.05	-0.35	-0.64	-0.16	-0.73
7	0.96	0.34	-0.34	-1.07	0.00	-0.59	-0.07	-0.84
8	1.02	0.41	-0.08	-1.10	0.00	-0.63	-0.08	-1.10
9	0.97	0.34	-0.07	-0.84	0.00	-0.59	-0.34	-1.07
10	0.69	0.14	-0.16	-0.73	-0.35	-0.64	-0.34	-1.05
11	0.63	0.09	-0.07	-0.99	-0.37	-0.71	-0.03	-0.87
12	0.98	0.24	-0.29	-1.06	-0.31	-0.59	-0.07	-0.90
13	1.05	0.40	-0.58	-1.11	-0.31	-0.56	-0.58	-1.11
14	0.99	0.24	-0.07	-0.90	-0.31	-0.59	-0.29	-1.06
15	0.58	0.09	-0.03	-0.87	-0.37	-0.71	-0.07	-0.99
16	0.62	0.06	-0.07	-1.05	-0.32	-0.74	-0.07	-1.02
17	0.98	0.37	-0.03	-1.11	-0.28	-0.55	-0.06	-0.98
18	1.01	0.41	-0.06	-1.20	-0.30	-0.50	-0.06	-1.20
19	0.99	0.37	-0.06	-0.98	-0.28	-0.55	-0.03	-1.11
20	0.61	0.06	-0.07	-1.02	-0.32	-0.74	-0.07	-1.05
21	0.53	0.00	-0.07	-1.03	-0.31	-0.61	-0.38	-0.76
22	0.90	0.32	-0.07	-1.19	-0.29	-0.55	-0.07	-0.91
23	0.92	0.37	-0.07	-1.09	-0.30	-0.52	-0.07	-1.09
24	0.91	0.32	-0.07	-0.91	-0.29	-0.55	-0.07	-1.19
25	0.60	0.00	-0.38	-0.76	-0.31	-0.61	-0.07	-1.03
26	0.39	-0.08	-0.07	-1.01	-0.30	-0.55	-0.15	-0.75
27	0.80	0.18	-0.07	-1.19	-0.26	-0.55	-0.26	-0.79
28	0.73	0.24	-0.07	-0.95	-0.27	-0.50	-0.07	-0.95
29	0.71	0.18	-0.26	-0.79	-0.26	-0.55	-0.07	-1.19
30	0.49	-0.08	-0.15	-0.75	-0.30	-0.55	-0.07	-1.01
31	0.32	-0.09	-0.06	-1.22	-0.29	-0.53	-0.24	-0.63
32	0.82	0.27	-0.07	-0.98	-0.24	-0.57	-0.26	-0.73
33	0.86	0.34	-0.19	-0.85	-0.26	-0.66	-0.19	-0.85
34	0.80	0.27	-0.26	-0.73	-0.24	-0.57	-0.07	-0.98
35	0.43	-0.09	-0.24	-0.63	-0.29	-0.53	-0.06	-1.22

Table 4.4 Peak pressure coefficients at pressure points of Sq model (30 degree)

Pressure Point	Face A		Face B		Face C		Face D	
	Max. Peak	Min. Peak	Max. Peak	Min. Peak	Max. Peak	Min. Peak	Max. Peak	Min. Peak
1	0.00	-0.21	-0.12	-0.72	-0.37	-0.58	-0.49	-0.81
2	0.19	-0.02	-0.08	-0.37	-0.37	-0.60	-0.50	-0.68
3	0.29	0.04	-0.12	-0.25	-0.39	-0.69	-0.50	-0.74
4	0.39	0.06	-0.10	-0.28	-0.43	-0.64	-0.46	-0.69
5	0.59	0.29	-0.24	-0.37	-0.43	-0.74	-0.48	-0.72
6	0.13	-0.07	0.04	-0.67	-0.43	-0.60	-0.54	-0.80
7	0.50	0.24	0.19	-0.20	-0.42	-0.61	-0.53	-0.71
8	0.63	0.36	0.11	-0.12	-0.43	-0.66	-0.49	-0.72
9	0.81	0.41	-0.02	-0.14	0.00	-0.65	-0.47	-0.62
10	0.83	0.49	-0.28	-0.41	-0.52	-0.72	-0.48	-0.65
11	0.12	-0.13	0.26	-0.55	-0.42	-0.65	-0.44	-0.79
12	0.52	0.23	0.18	-0.40	-0.43	-0.65	-0.49	-0.73
13	0.76	0.38	0.09	-0.14	-0.41	-0.65	-0.44	-0.72
14	0.81	0.07	-0.03	-0.13	-0.44	-0.71	-0.46	-0.66
15	0.81	0.46	-0.25	-0.40	-0.44	-0.77	-0.45	-0.66
16	0.14	-0.09	0.13	-0.51	-0.34	-0.61	-0.49	-0.80
17	0.53	0.23	0.24	-0.32	-0.41	-0.59	-0.44	-0.71
18	0.69	0.32	0.17	-0.08	-0.39	-0.60	-0.43	-0.67
19	0.72	0.40	0.03	-0.19	-0.40	-0.62	-0.40	-0.71
20	0.73	0.27	-0.21	-0.32	-0.36	-0.66	-0.40	-0.54
21	0.13	-0.13	0.25	-0.28	-0.33	-0.52	-0.08	-0.81
22	0.46	0.18	0.24	-0.31	-0.32	-0.54	-0.07	-0.72
23	0.69	0.27	0.12	-0.17	-0.35	-0.58	-0.38	-0.64
24	0.71	0.35	0.00	-0.13	-0.36	-0.63	-0.35	-0.66
25	0.80	0.31	-0.14	-0.30	-0.37	-0.70	-0.35	-0.62
26	0.07	-0.17	0.12	-0.49	-0.24	-0.54	-0.44	-0.82
27	0.37	0.09	0.16	-0.29	-0.29	-0.57	-0.07	-0.82
28	0.53	0.23	0.12	-0.15	-0.32	-0.58	-0.36	-0.73
29	0.58	0.25	-0.03	-0.22	-0.29	-0.64	-0.35	-0.76
30	0.51	0.18	-0.14	-0.30	-0.33	-0.68	-0.36	-0.65
31	0.07	-0.16	0.14	-0.61	-0.30	-0.55	-0.39	-0.76
32	0.47	0.15	0.52	-0.17	-0.33	-0.60	-0.36	-0.76
33	0.57	0.21	0.13	-0.13	-0.31	-0.61	-0.34	-0.71
34	0.66	0.29	0.01	-0.16	-0.28	-0.56	-0.37	-0.59
35	0.50	0.18	-0.14	-0.28	-0.32	-0.68	-0.31	-0.65

Table 4.5 Peak pressure coefficients at pressure points of Sq model (60 degree)

Pressure Point	Face A		Face B		Face C		Face D	
	Max. Peak	Min. Peak	Max. Peak	Min. Peak	Max. Peak	Min. Peak	Max. Peak	Min. Peak
1	-0.20	-0.33	0.60	0.17	-0.50	-0.71	-0.44	-0.62
2	-0.12	-0.26	0.39	0.06	-0.51	-0.72	-0.40	-0.59
3	-0.09	-0.23	0.30	-0.01	-0.47	-0.71	-0.35	-0.67
4	0.30	-0.51	0.23	-0.01	-0.47	-0.80	-0.38	-0.56
5	0.03	-0.55	-0.03	-0.24	-0.48	-0.75	-0.37	-0.57
6	0.00	-0.52	0.81	0.08	-0.46	-0.64	-0.48	-0.64
7	0.02	-0.11	0.82	0.30	-0.50	-0.70	-0.44	-0.65
8	0.32	-0.43	0.63	0.29	-0.49	-0.71	-0.38	-0.60
9	0.25	0.00	0.53	0.15	-0.50	-0.76	-0.40	-0.59
10	0.05	-0.45	-0.03	-0.20	-0.07	-0.81	-0.39	-0.64
11	0.00	-0.32	0.86	0.07	-0.46	-0.64	-0.45	-0.74
12	0.04	-0.12	0.91	0.34	-0.46	-0.70	-0.42	-0.71
13	0.11	-0.04	0.65	0.29	-0.50	-0.70	-0.42	-0.65
14	0.27	-0.12	0.50	0.17	-0.51	-0.74	-0.39	-0.66
15	0.18	-0.41	0.00	-0.18	-0.50	-0.81	-0.40	-0.62
16	-0.05	-0.33	0.80	0.39	-0.41	-0.64	-0.39	-0.68
17	0.03	-0.12	0.76	0.33	-0.45	-0.67	-0.38	-0.60
18	0.14	-0.05	0.66	0.28	-0.43	-0.70	-0.32	-0.60
19	0.26	-0.26	0.52	0.19	-0.45	-0.81	-0.37	-0.61
20	0.28	-0.43	0.07	-0.16	-0.07	-0.82	-0.37	-0.51
21	-0.14	-0.29	0.66	0.28	-0.32	-0.67	-0.33	-0.66
22	0.02	-0.11	0.67	0.31	-0.38	-0.61	-0.33	-0.63
23	0.18	-0.10	0.60	0.22	-0.40	-0.73	-0.35	-0.56
24	0.24	-0.17	0.42	0.12	-0.42	-0.79	-0.36	-0.48
25	0.42	-0.48	0.06	-0.11	-0.43	-0.81	-0.30	-0.50
26	-0.16	-0.33	0.63	0.21	-0.33	-0.66	-0.32	-0.91
27	0.04	-0.21	0.51	0.21	-0.31	-0.74	-0.32	-0.59
28	0.12	-0.07	0.46	0.17	-0.34	-0.76	-0.30	-0.58
29	0.25	-0.14	0.35	0.06	-0.40	-0.93	-0.23	-0.59
30	0.25	-0.35	0.03	-0.16	-0.07	-0.78	-0.29	-0.50
31	-0.07	-0.29	0.53	0.19	-0.35	-0.64	-0.31	-0.55
32	0.02	-0.15	0.62	0.26	-0.36	-0.62	-0.29	-0.61
33	0.27	0.00	0.54	0.23	-0.07	-0.67	-0.31	-0.53
34	0.34	-0.16	0.38	0.06	-0.35	-0.73	-0.28	-0.59
35	0.29	-0.36	0.11	-0.11	-0.37	-0.76	-0.29	-0.47

Table 4.6 Peak pressure coefficients at pressure points of **Sq model (90 degree)**

Pressure Point	Face A		Face B		Face C		Face D	
	Max. Peak	Min. Peak	Max. Peak	Min. Peak	Max. Peak	Min. Peak	Max. Peak	Min. Peak
1	-0.32	-0.71	0.39	0.08	-0.62	-1.22	-0.38	-0.60
2	-0.07	-0.77	0.43	0.11	-0.70	-1.18	-0.36	-0.64
3	-0.07	-1.04	0.41	0.00	-0.07	-1.02	-0.33	-0.63
4	-0.71	-1.20	0.56	0.16	-0.41	-0.80	-0.34	-0.61
5	-0.08	-1.12	0.35	-0.01	-0.31	-0.67	-0.29	-0.69
6	-0.35	-0.73	0.51	0.16	-0.07	-0.95	-0.33	-0.67
7	-0.50	-0.80	0.81	0.41	-0.07	-1.14	-0.37	-0.63
8	-0.07	-1.04	0.84	0.40	-0.08	-1.09	-0.32	-0.61
9	-0.08	-1.12	0.78	0.39	-0.50	-0.87	-0.31	-0.61
10	-0.07	-1.04	0.42	0.15	-0.33	-0.78	-0.34	-0.72
11	-0.07	-1.07	0.44	0.15	-0.07	-0.90	-0.37	-0.69
12	-0.07	-0.95	0.80	0.46	-0.08	-1.09	-0.29	-0.58
13	-0.10	-1.14	0.82	0.07	-0.07	-1.06	-0.26	-0.55
14	-0.07	-1.07	0.82	0.40	-0.08	-0.90	-0.31	-0.62
15	-0.52	-1.00	0.43	0.06	-0.05	-0.86	-0.35	-0.66
16	-0.08	-0.79	0.43	0.12	-0.07	-0.98	-0.31	-0.62
17	-0.07	-0.89	0.82	0.07	-0.06	-1.14	-0.29	-0.58
18	-0.06	-1.15	0.81	0.08	-0.07	-1.00	-0.29	-0.62
19	-0.07	-1.14	0.73	0.38	-0.06	-0.92	-0.25	-0.66
20	-0.07	-1.04	0.37	0.05	-0.08	-0.91	-0.32	-0.60
21	-0.08	-0.73	0.59	0.22	-0.07	-0.98	-0.29	-0.58
22	-0.06	-0.82	0.65	0.32	-0.06	-0.97	-0.28	-0.57
23	-0.06	-1.03	0.73	0.33	-0.06	-1.12	-0.28	-0.52
24	-0.07	-1.05	0.68	0.24	-0.07	-0.89	-0.27	-0.56
25	-0.06	-1.21	0.41	0.03	-0.06	-0.77	-0.28	-0.66
26	-0.23	-0.66	0.33	0.08	-0.06	-1.05	-0.25	-0.61
27	-0.31	-0.77	0.59	0.21	-0.06	-1.16	-0.25	-0.65
28	-0.08	-0.97	0.61	0.29	-0.07	-1.07	-0.25	-0.62
29	-0.06	-1.05	0.61	0.26	-0.33	-0.75	-0.28	-0.66
30	-0.09	-1.13	0.26	-0.07	-0.27	-0.79	-0.27	-0.61
31	-0.25	-0.58	0.30	-0.07	-0.06	-1.11	-0.19	-0.62
32	-0.26	-0.75	0.75	0.25	-0.06	-1.08	-0.25	-0.61
33	-0.07	-0.78	0.71	0.27	-0.29	-0.78	-0.23	-0.56
34	-0.06	-1.20	0.57	0.26	-0.06	-0.63	-0.25	-0.58
35	-0.07	-1.23	0.15	-0.09	-0.24	-0.52	-0.21	-0.58

4.4.2. Plus-1 Model (Pl-1 model)

Similar to the square model, tests have been performed on a Perspex sheet model for wind directions of 0^0 to 90^0 at an interval of 30^0 with 0^0 wind perpendicular to the face A2 and 90^0 perpendicular to face B2 as shown in Fig. 4.11.

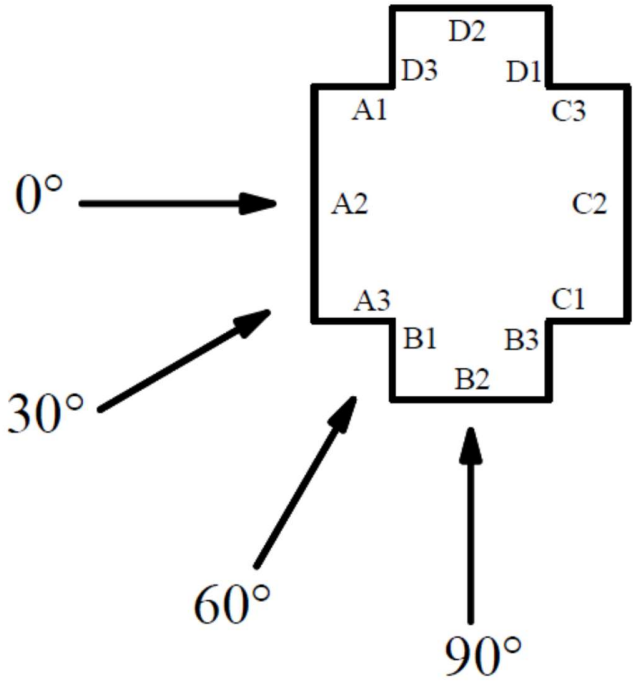

Fig. 4.11 Wind direction on Sq-model in isolated condition

The variation of Cp,mean along the perimeter is shown in Fig. 4.12 to 4.15, respectively for wind angles of 0 to 90 degree, respectively. The wind pressure distribution at symmetric faces is symmetric due to symmetry in the flow around the building model at the wind direction of 0^0. The wind pressure is positive on front face A2 and negative, i.e., suction on all other surfaces. The symmetric side faces B2 and D2 are subjected to maximum suction coefficient among all surfaces with a mean suction coefficient of -0.69 at 0^0 wind angle. The suction at these faces decreases from windward to leeward edge. The mean wind pressure at windward surfaces B1 and D3, which are attached to re-entrant corners, is negligible because the wind pressure at opposite edges of these surfaces is of the opposite nature due to the presence of re-entrant corners. The area near the outer edge

is subjected to positive wind pressure similar to front surface A2, but wind pressure near to inner edge is negative because of flow stagnation and the formation of eddies in re-entrant corners. Although the surfaces A1 and A3 are parallel to side face B2 and D2, suction at face A1 and A3 is very small compared to side face B2 and D2 because of the presence of re-entrant corners at leeward edges of these surfaces.

When the wind incidence angle increases to 30^0, the absolute value of mean wind pressure coefficients at all surfaces from D3 to B1 anticlockwise has increased significantly except at face A2 and reduces slightly on the surfaces from B2 to D2. The symmetry about the along-axis is vanished due to non-symmetric flow. The suction at surfaces A1 and D3 near re-entrant corners on the front-left side has increased significantly due to the flow separation at the edge of face A2 and thus the formation of eddies in the wake created in this region. Further, the suction coefficient increases from -0.20 to -0.82 for surface A1 while it increases from -0.05 to -0.85 for surface D3. The intensity of positive wind pressure is reduced on face A2; wind pressure is positive on the right edge towards wind incidence while negative on opposite edges, and due to which average of the surface is reduced. The mean wind pressure coefficients at face A3 and B1 are changed to positive, and the absolute value is also increased because of an increased region of stagnant air formed in the re-entrant corner near these surfaces. The suction coefficient on side face B2 is reduced to almost half, whereas the reduction in suction for all other surfaces is up to 20%.

As the wind incidence angle increases to 60^0, negative wind pressure intensity reduces on the surfaces from D3 to A2 at the front side toward 0- degree wind incidence between D3 to A2 but still higher than the wind pressure in the case of 0^0 wind incidence whereas, negative wind pressure intensity increase on the surfaces between B3 to C2 compare to wind pressure in case of 0^0 and 30^0 wind incidence angles. The wind pressure intensity does not change as much at faces between C3 to D2. Face A2, which experiences positive wind pressure at 0^0 and 30^0 wind flow, changes to suction, but the absolute value is almost the same as 30^0 wind flow. Suction at face A1 and D3 reduces to almost half compared to 30^0 wind flow. The wind pressure at surfaces A3 and B1 near the re-entrant corner does not change, and similar to 30^0 wind flow, these surfaces experience a higher intensity of mean wind pressure near the corner edge. The wind pressure at side face B2 is positive, which was suction in case of 0 and 30-degree wind flow, but the absolute value is reduced

by 60%. The suction at surfaces B3 and C1 increase up to 130% due to increased flow in the re-entrant corner.

Now, when wind flow at an incidence angle of 90^0, flow hits directly at face A3, B2, and C1, which are side faces for 0^0 wind flow and are subjected to suction. It is quite interesting to note that wind pressure coefficient values at face A3 and B1 are very low compared to other faces. The symmetric faces A3 and C1 experience almost negligible average wind pressure because of re-entrant corners even though wind hits directly at these faces. The suction at surface A2 increases when the wind angle change from 60^0 to 90^0. The wind pressure on windward face B2 has also increased with a change of wind incidence angle.

The above discussion represents the overall distribution of $C_{p,mean}$ on the face of the model for all wind directions. However, these cannot illustrate the concrete information for the variation of pressure coefficient with the perimeter of the model. To overcome this problem and to investigate the effect of distance from the leading edge on the mean pressure, the pressure coefficients are presented along the measuring points at each measurement level for all wind directions. The influence of flow separation at the edges is observed to be significant on $C_{p,mean}$ distribution of the square building model for all wind directions. The deviation between the pressure coefficients at pressure points along the perimeter is higher at windward side pressure points for each respective wind direction, where the wind hits directly. The values of $C_{p,mean}$ are almost similar to each other for pressure points at other locations.

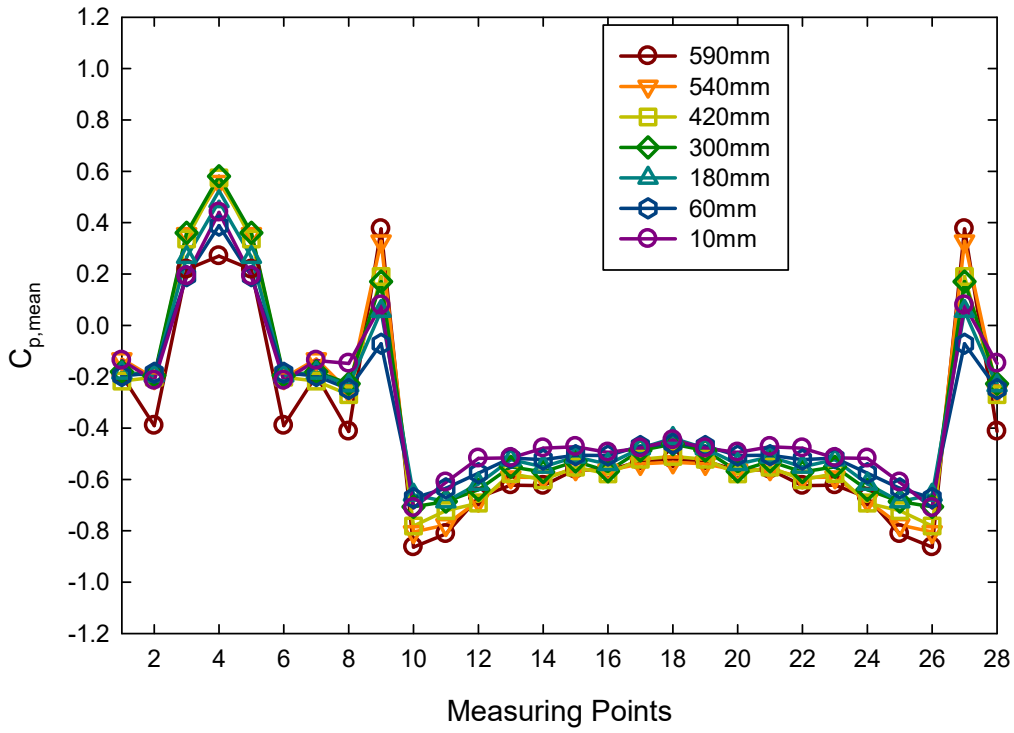

Fig. 4.12 $C_{p,\,mean}$ along perimeter-PL-1 model (0 degree)

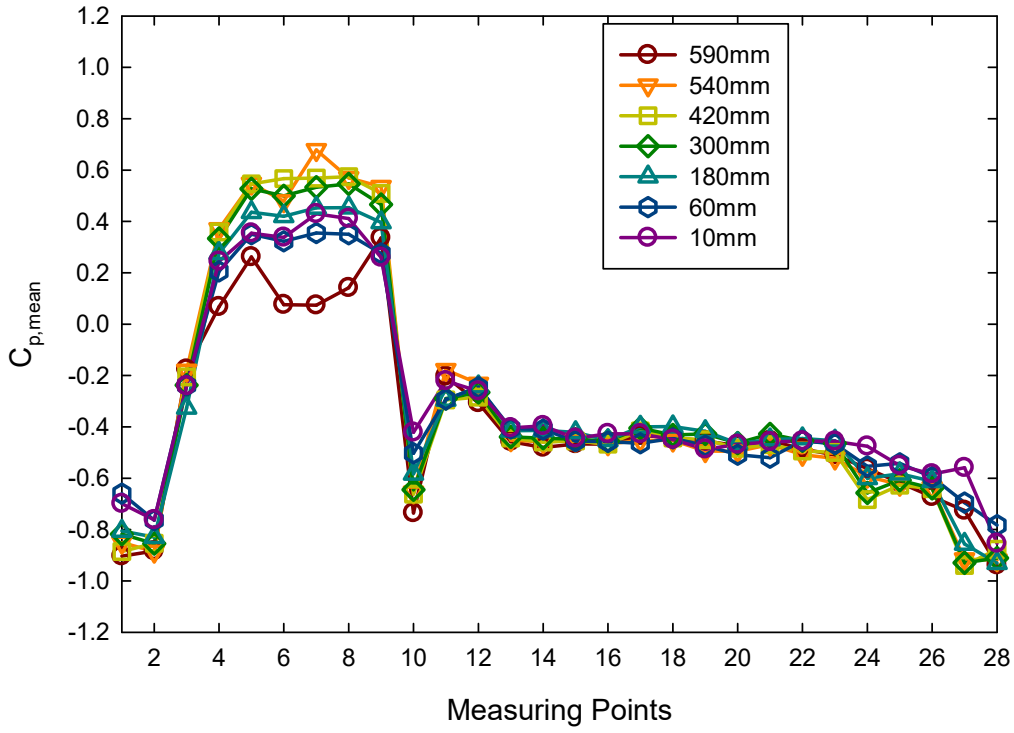

Fig. 4.13 $C_{p,\,mean}$ along perimeter-PL-1 model (30 degree)

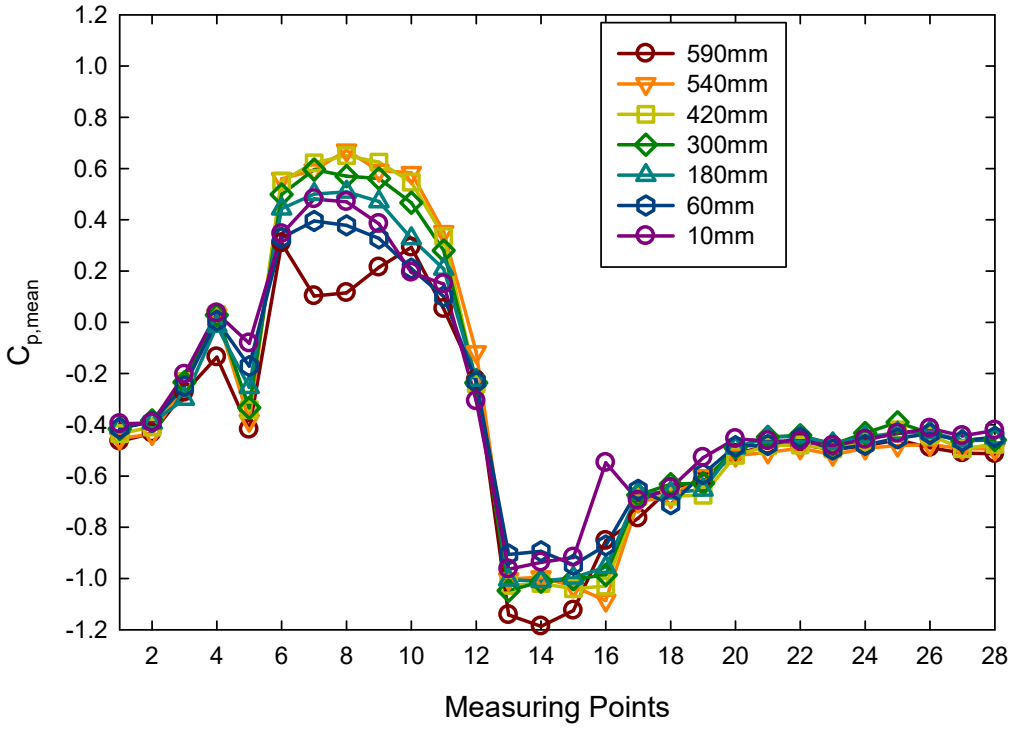

Fig. 4.14 $C_{p,\,mean}$ along perimeter-PL-1 model (60 degree)

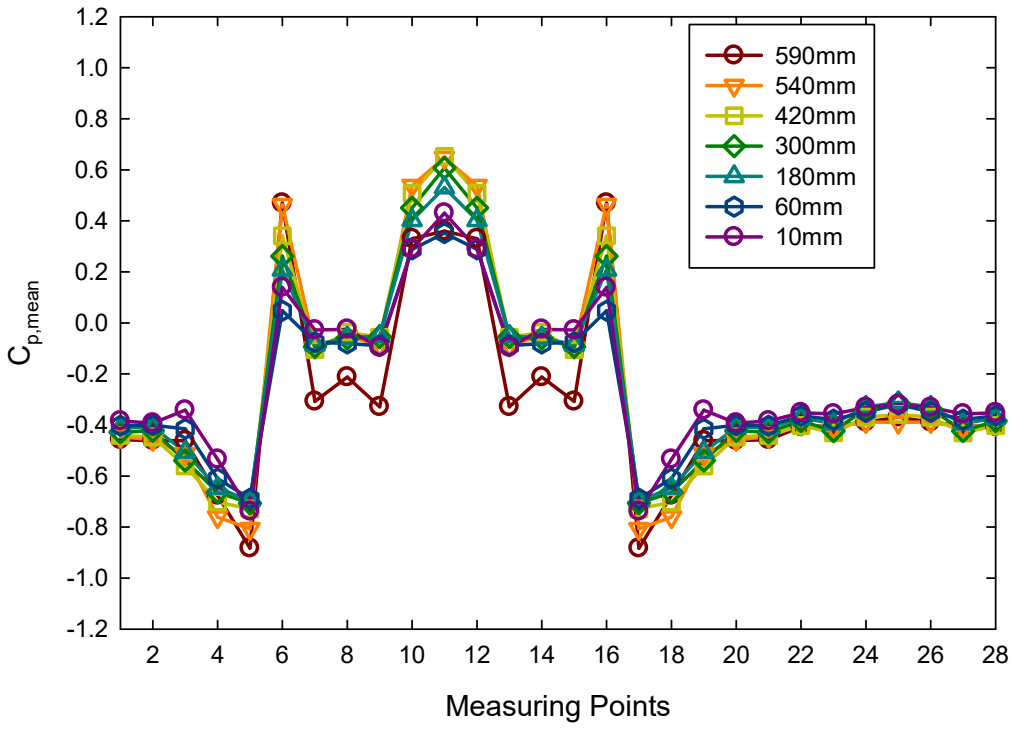

Fig. 4.15 $C_{p,\,mean}$ along perimeter-PL-1 model (90 degree)

The area average values of mean pressure coefficients at different faces are shown in table 4.7. Face A1 is subjected to suction for all wind directions with the maximum at 30^0 wind direction. Face A2 is subjected to positive pressure for 0 and 30 degree wind while suction for wind directions of 60 and 90 degree. Face A3 is subjected to positive pressure for all wind directions except 0 degree wind. Pressure at face B2 changes from positive to negative as wind direction changes from 0 to 90 degree. All the faces between C1 to D3 are under suction because they lie in the wake region.

Table 4.7 Area averaged mean pressure coefficients at faces of- Pl-1 model

Wind Angle	A1	A2	A3	B1	B2	B3	C1	C2	C3	D1	D2	D3
0 degree	-0.20	0.38	-0.20	-0.05	-0.69	-0.56	-0.54	-0.49	-0.54	-0.56	-0.69	-0.05
30 degree	-0.82	0.19	0.49	0.45	-0.37	-0.43	-0.45	-0.44	-0.47	-0.48	-0.61	-0.87
60 degree	-0.41	-0.15	0.49	0.51	0.15	-1.0	-0.98	-0.66	-0.48	-0.47	-0.44	-0.47
90 degree	-0.43	-0.64	0.08	-0.07	0.47	-0.07	0.08	-0.64	-0.43	-0.39	-0.35	-0.39

The distribution of r.m.s pressure coefficients ($C_{p,rms}$) is shown in the Fig. 4.16 to 4.19 for wind directions of 0 to 90 degree, respectively. The smaller value of r.m.s wind coefficients at windward and leeward surfaces perpendicular to the wind direction at 0 degree wind indicates the lower level of turbulence in the flow at these faces. Fluctuating values at different pressure points at front face A2 are mostly similar, which shows that flow at the front face is relatively stable. The values of fluctuating pressure coefficients are higher on the side faces and face near to front corners compare to other faces, which may be due to the existence of a strong and coherent vortex motion due to the flow separation at side faces and formation of eddies in the corner region. Fluctuating r.m.s values of pressure coefficients at faces near the left corner (face A1 and D3) increase significantly for 30 degree wind; the reason is that irregular vortices are generated in the wake flow after separating at the edges of face A2. A similar type of change in the r.m.s pressure is observed at face C1 and C2 for 60 wind.

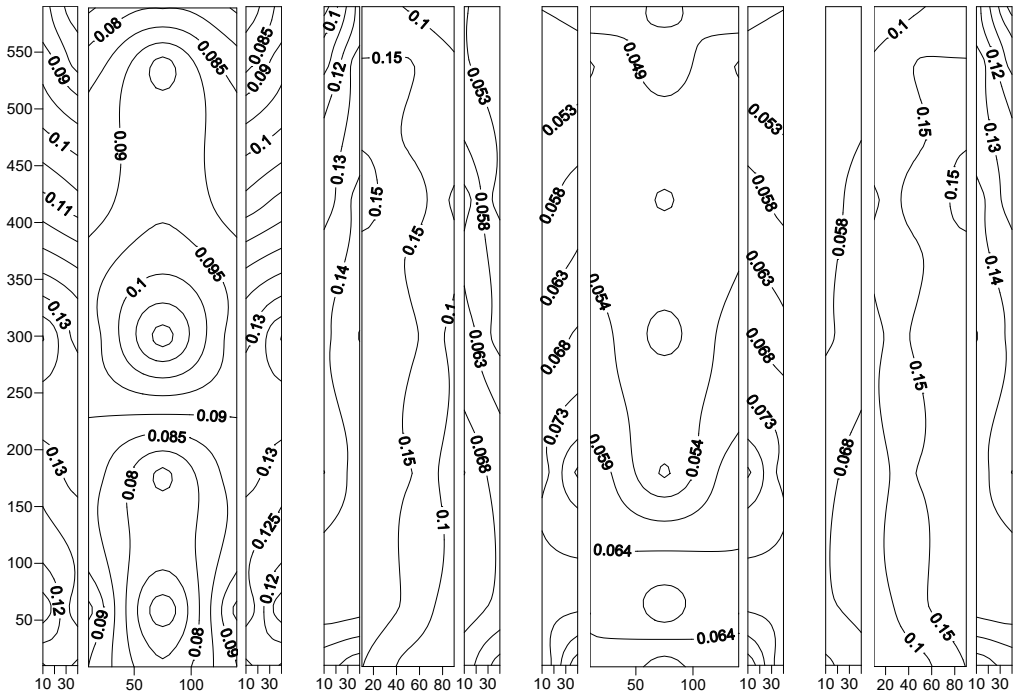

Fig. 4.16 Contour of r.m.s wind pressure coefficient-Pl-1 model (0 degree)

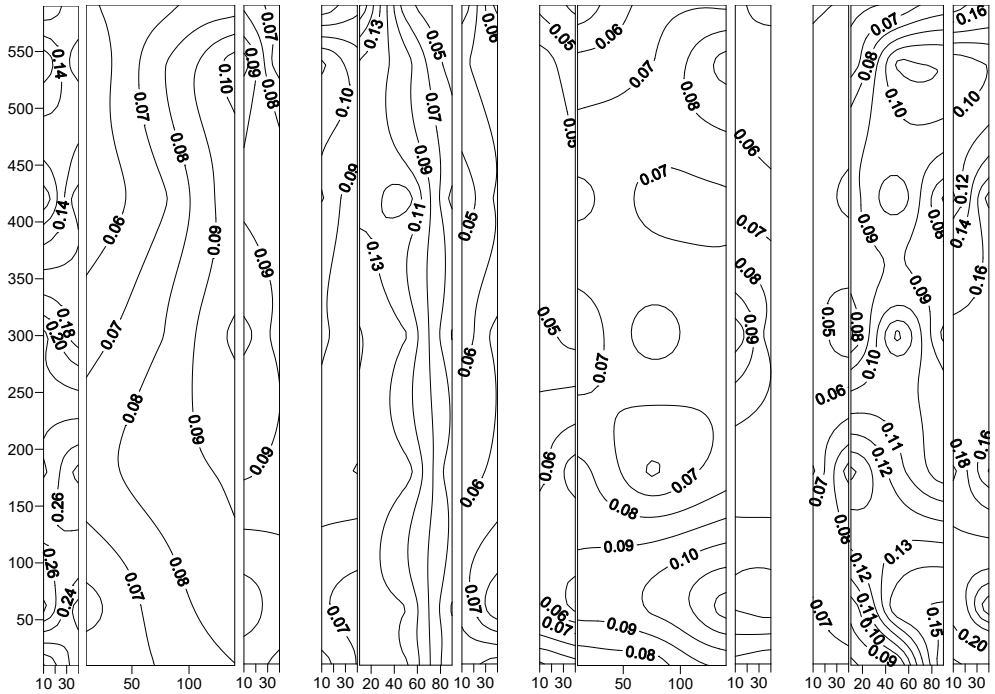

Fig. 4.17 Contour of r.m.s wind pressure coefficient-Pl-1 model (30 degree)

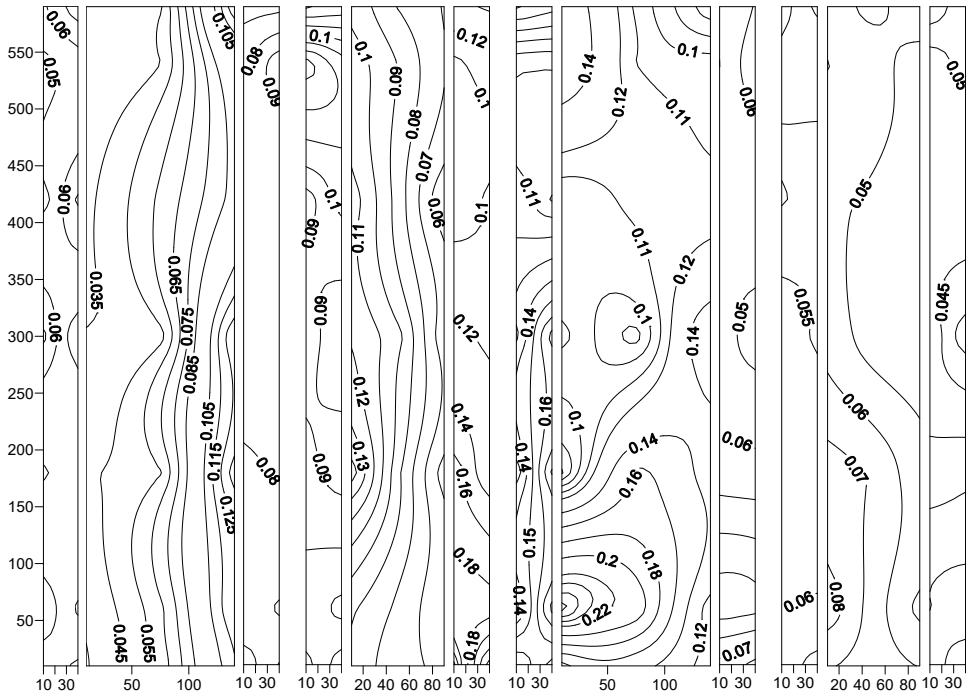

Fig. 4.18 Contour of r.m.s wind pressure coefficient-Pl-1 model (60 degree)

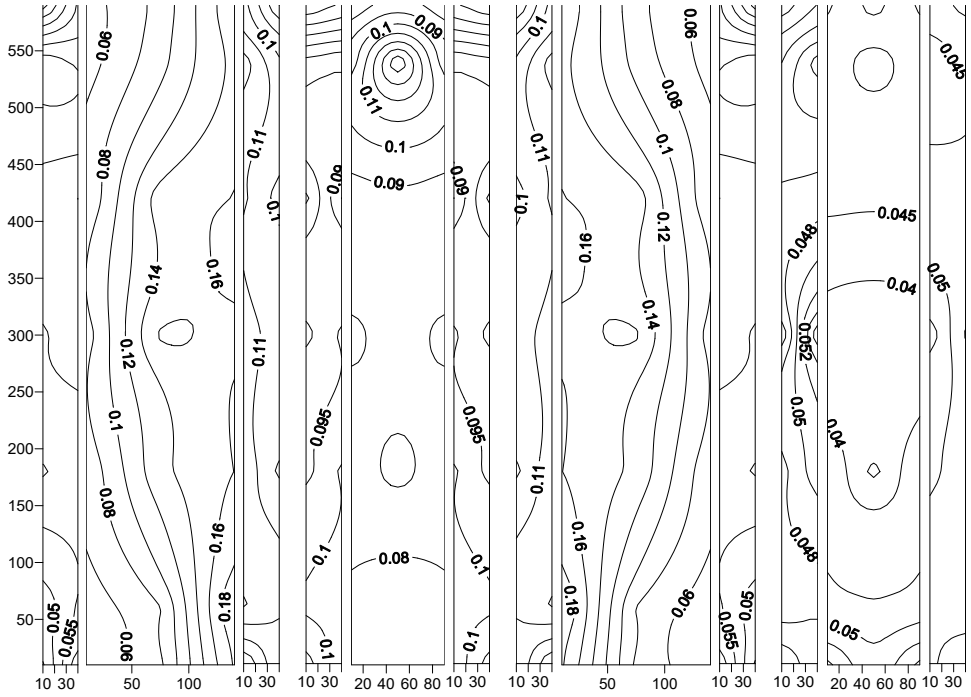

Fig. 4.19 Contour of r.m.s wind pressure coefficient-Pl-1 model (90 degree)

Maximum and minimum peak pressure coefficients at each pressure point are calculated similar to the square model. The values of peak pressure coefficients of Pl-1 models are shown in table 4.8 to 4.11 for wind direction of 0 to 90 degree, respectively. The average of $C_{p,max}$ is positive at all windward surfaces while it is negative at all surfaces at the side and leeward position for 0^0 wind. The largest positive value of $C_{p,max}$ is observed at face A2 while face B3 has the negative highest value. For wind direction of 30^0, peak pressure at face A1 turn to negative. The largest value increased slightly and shifted to face A3. The highest value of positive $C_{p,max}$ is still similar for 60^0 and 90^0 wind directions. Suction is maximum for 60 degree wind at face B3.

The average value of $C_{p,min}$ is positive at face A2 and negative at all other surfaces for 0^0 wind angle. The symmetric side faces B2 and D2 are subjected to the highest suction of -0.95. The $C_{p,min}$ Value at face A2 is reduced to almost zero while at faces of the windward right corner, it changes to positive for wind direction of 30^0. The highest suction value (-1.14) of $C_{p,min}$ for 30^0 wind angle is observed at face A1. The face B3 is subjected to the overall highest peak suction of -1.29 at 60^0 wind direction. For wind direction of 90 degree, the B2 is the only face that is subjected to positive $C_{p,min}$.

Table 4.8 Peak pressure coefficients at pressure points of Sq model (0 degree)

Pressure Point	Face A		Face B		Face C		Face D	
	Max. Peak	Min. Peak	Max. Peak	Min. Peak	Max. Peak	Min. Peak	Max. Peak	Min. Peak
1	0.01	-0.41	-0.24	-0.63	-0.45	-0.68	-0.52	-0.76
2	-0.24	-0.57	0.64	0.08	-0.46	-0.66	-0.51	-0.76
3	0.38	0.01	-0.39	-1.18	-0.44	-0.62	-0.55	-0.88
4	0.44	0.00	-0.37	-0.99	-0.41	-0.70	-0.37	-0.99
5	0.38	0.01	-0.55	-0.88	-0.44	-0.62	-0.39	-1.18
6	-0.24	-0.57	-0.51	-0.76	-0.46	-0.66	0.64	0.08
7	0.01	-0.41	-0.52	-0.76	-0.45	-0.68	-0.24	-0.63
8	0.03	-0.39	-0.03	-0.50	-0.45	-0.68	-0.47	-0.73
9	-0.02	-0.40	0.62	0.02	-0.47	-0.72	-0.47	-0.72
10	0.53	0.18	-0.08	-1.14	-0.42	-0.68	-0.07	-0.87
11	0.76	0.34	-0.08	-1.03	-0.43	-0.65	-0.08	-1.03
12	0.53	0.18	-0.07	-0.87	-0.42	-0.68	-0.08	-1.14
13	-0.02	-0.40	-0.47	-0.72	-0.47	-0.72	0.62	0.02
14	0.03	-0.39	-0.47	-0.73	-0.45	-0.68	-0.03	-0.50
15	0.01	-0.49	-0.01	-0.55	-0.44	-0.71	-0.50	-0.71
16	0.05	-0.47	0.52	-0.12	-0.45	-0.74	-0.46	-0.71
17	0.55	0.16	-0.29	-1.02	-0.42	-0.67	-0.31	-0.82
18	0.81	0.39	-0.07	-1.04	-0.42	-0.67	-0.07	-1.04
19	0.55	0.16	-0.31	-0.82	-0.42	-0.67	-0.29	-1.02
20	0.05	-0.47	-0.46	-0.71	-0.45	-0.74	0.52	-0.12
21	0.01	-0.49	-0.50	-0.71	-0.44	-0.71	-0.01	-0.55
22	0.13	-0.55	0.04	-0.55	-0.41	-0.68	-0.47	-0.72
23	0.13	-0.50	0.47	-0.22	-0.43	-0.75	-0.43	-0.75
24	0.55	0.11	-0.07	-1.09	-0.38	-0.64	-0.28	-0.78
25	0.81	0.27	-0.08	-0.92	-0.35	-0.56	-0.08	-0.92
26	0.55	0.11	-0.28	-0.78	-0.38	-0.64	-0.07	-1.09
27	0.13	-0.50	-0.43	-0.75	-0.43	-0.75	0.47	-0.22
28	0.13	-0.55	-0.47	-0.72	-0.41	-0.68	0.04	-0.55
29	0.05	-0.48	0.05	-0.50	-0.38	-0.70	-0.45	-0.73
30	0.07	-0.57	0.37	-0.28	-0.20	-0.73	-0.26	-0.65
31	0.50	0.05	-0.07	-1.03	-0.37	-0.73	-0.47	-0.78
32	0.67	0.27	-0.07	-0.99	-0.35	-0.54	-0.07	-0.99
33	0.50	0.05	-0.47	-0.78	-0.37	-0.73	-0.07	-1.03
34	0.07	-0.57	-0.26	-0.65	-0.20	-0.73	0.37	-0.28
35	0.05	-0.48	-0.45	-0.73	-0.38	-0.70	0.05	-0.50
36	0.06	-0.50	0.10	-0.56	-0.37	-0.71	-0.40	-0.72
37	0.08	-0.47	0.26	-0.44	-0.39	-0.67	-0.37	-0.70
38	0.45	0.01	-0.07	-1.07	-0.33	-0.61	-0.42	-0.79
39	0.53	0.28	-0.07	-0.90	-0.31	-0.65	-0.07	-0.90
40	0.45	0.01	-0.42	-0.79	-0.33	-0.61	-0.07	-1.07
41	0.08	-0.47	-0.37	-0.70	-0.39	-0.67	0.26	-0.44
42	0.06	-0.50	-0.40	-0.72	-0.37	-0.71	0.10	-0.56
43	0.18	-0.37	0.14	-0.40	-0.19	-0.66	-0.37	-0.61
44	0.02	-0.52	0.32	-0.23	-0.39	-0.64	-0.39	-0.70
45	0.39	-0.01	-0.07	-1.02	-0.35	-0.62	-0.41	-0.72
46	0.60	0.29	-0.47	-0.81	-0.32	-0.58	-0.47	-0.81
47	0.39	-0.01	-0.41	-0.72	-0.35	-0.62	-0.07	-1.02
48	0.02	-0.52	-0.39	-0.70	-0.39	-0.64	0.32	-0.23
49	0.18	-0.37	-0.37	-0.61	-0.19	-0.66	0.14	-0.40

Table 4.9 Peak pressure coefficients at pressure points of Sq model (30 degree)

Pressure Point	Face A		Face B		Face C		Face D	
	Max. Peak	Min. Peak	Max. Peak	Min. Peak	Max. Peak	Min. Peak	Max. Peak	Min. Peak
1	-0.70	-1.13	0.25	0.00	-0.35	-0.56	-0.35	-0.63
2	-0.10	-1.09	0.51	0.12	-0.33	-0.63	-0.40	-0.67
3	-0.05	-0.27	-0.07	-1.14	-0.36	-0.52	-0.47	-0.68
4	0.24	-0.07	-0.09	-0.37	-0.33	-0.59	-0.52	-0.75
5	0.42	0.10	-0.23	-0.38	-0.35	-0.60	-0.53	-0.82
6	0.24	-0.09	-0.36	-0.62	-0.37	-0.67	-0.07	-0.91
7	0.20	-0.10	-0.36	-0.72	-0.32	-0.61	-0.10	-1.22
8	0.00	-1.09	0.82	0.32	-0.36	-0.55	-0.39	-0.64
9	-0.71	-1.18	0.77	0.30	-0.36	-0.57	-0.40	-0.62
10	-0.08	-0.27	-0.08	-0.88	-0.37	-0.64	-0.45	-0.73
11	0.48	0.20	0.00	-0.50	-0.35	-0.72	-0.07	-0.82
12	0.74	0.32	-0.16	-0.34	-0.37	-0.74	-0.07	-0.79
13	0.70	0.27	-0.32	-0.62	-0.34	-0.64	-0.72	-1.13
14	1.21	0.95	-0.36	-0.70	-0.36	-0.56	-0.72	-1.24
15	-0.72	-1.05	0.81	0.37	-0.37	-0.59	-0.35	-0.59
16	-0.09	-1.18	0.72	0.32	-0.38	-0.58	-0.37	-0.67
17	-0.11	-0.33	-0.07	-0.82	0.00	-0.55	-0.52	-0.94
18	0.48	0.20	-0.06	-0.65	-0.34	-0.65	-0.07	-0.83
19	0.75	0.33	-0.19	-0.36	-0.33	-0.62	-0.51	-0.79
20	0.77	0.32	-0.35	-0.58	-0.36	-0.61	-0.73	-1.15
21	0.76	0.41	-0.33	-0.60	-0.31	-0.61	-0.08	-1.12
22	-0.10	-1.24	0.78	0.36	-0.34	-0.56	-0.34	-0.57
23	-0.08	-1.26	0.61	0.27	-0.37	-0.59	-0.35	-0.57
24	-0.14	-0.41	-0.07	-0.91	-0.31	-0.63	-0.47	-0.78
25	0.49	0.15	0.01	-0.58	-0.31	-0.80	-0.07	-1.04
26	0.76	0.29	-0.17	-0.43	-0.33	-0.63	-0.51	-0.87
27	0.76	0.27	-0.34	-0.57	0.00	-0.74	-0.10	-1.26
28	0.74	0.35	-0.33	-0.68	-0.30	-0.66	-0.09	-1.19
29	-0.07	-1.16	0.71	0.27	-0.32	-0.64	-0.30	-0.56
30	-0.08	-1.32	0.58	0.21	-0.34	-0.65	0.00	-0.66
31	-0.19	-0.48	-0.07	-0.83	0.00	-0.53	-0.07	-0.86
32	0.46	0.09	-0.03	-0.58	-0.29	-0.53	-0.07	-0.79
33	0.64	0.23	-0.13	-0.36	-0.28	-0.60	-0.44	-0.82
34	0.61	0.19	-0.32	-0.58	-0.34	-0.63	-0.07	-1.17
35	0.61	0.22	-0.31	-0.65	-0.33	-0.67	-0.55	-1.18
36	-0.07	-1.09	0.54	0.19	-0.35	-0.59	-0.31	-0.60
37	-0.09	-1.13	0.45	0.16	-0.36	-0.63	-0.33	-0.75
38	-0.13	-0.38	-0.20	-0.82	-0.28	-0.76	-0.37	-0.76
39	0.42	0.06	-0.04	-0.60	0.00	-0.66	-0.06	-0.79
40	0.52	0.21	-0.16	-0.37	0.00	-0.76	-0.07	-1.02
41	0.47	0.18	-0.25	-0.56	-0.35	-0.78	-0.06	-0.94
42	0.57	0.20	0.00	-0.57	-0.33	-0.80	-0.06	-1.28
43	-0.07	-0.93	0.63	0.24	0.00	-0.69	-0.31	-0.60
44	-0.07	-1.06	0.40	0.00	0.00	-0.58	-0.29	-0.67
45	-0.08	-0.39	-0.18	-0.80	-0.31	-0.65	-0.29	-0.65
46	0.47	0.11	0.04	-0.51	-0.31	-0.64	-0.37	-0.78
47	0.49	0.18	-0.17	-0.42	-0.31	-0.74	-0.07	-0.84
48	0.55	0.19	-0.29	-0.58	-0.36	-0.63	-0.06	-0.81
49	0.67	0.26	-0.29	-0.54	-0.36	-0.61	-0.10	-1.16

Table 4.10 Peak pressure coefficients at pressure points of Sq model (60 degree)

Pressure Point	Face A		Face B		Face C		Face D	
	Max. Peak	Min. Peak	Max. Peak	Min. Peak	Max. Peak	Min. Peak	Max. Peak	Min. Peak
1	-0.36	-0.63	0.24	-0.02	-0.85	-1.55	-0.38	-0.61
2	0.00	-0.54	0.33	0.05	-0.08	-1.03	-0.41	-0.59
3	-0.21	-0.33	0.50	0.13	-0.08	-1.23	-0.39	-0.64
4	-0.05	-0.22	0.27	-0.14	-0.07	-0.81	-0.37	-0.57
5	-0.13	-0.78	-0.09	-0.37	-0.48	-0.76	-0.40	-0.64
6	0.45	0.19	-0.90	-1.63	-0.43	-0.64	-0.40	-0.68
7	0.28	-0.04	-0.87	-1.45	-0.34	-0.62	-0.42	-0.64
8	-0.38	-0.58	0.97	0.08	-0.83	-1.30	-0.39	-0.64
9	-0.33	-0.57	0.80	0.08	-0.80	-1.33	-0.40	-0.62
10	-0.19	-0.31	0.81	0.32	-0.07	-0.98	-0.37	-0.66
11	0.11	-0.08	0.57	0.17	-0.07	-0.82	-0.40	-0.64
12	-0.10	-0.57	0.01	-0.27	0.00	-0.78	-0.38	-0.61
13	0.70	0.31	-0.76	-1.19	-0.37	-0.63	-0.40	-0.60
14	0.74	0.31	-0.79	-1.27	-0.39	-0.67	-0.38	-0.64
15	-0.34	-0.56	0.82	0.44	-0.82	-1.41	-0.35	-0.60
16	0.00	-0.54	0.87	0.43	-0.82	-1.21	-0.35	-0.64
17	-0.17	-0.30	0.76	0.24	-0.08	-0.82	-0.36	-0.60
18	0.13	-0.12	0.49	0.18	-0.07	-0.84	-0.33	-0.55
19	-0.15	-0.56	-0.15	-0.39	-0.08	-0.89	-0.35	-0.59
20	0.73	0.34	-0.86	-1.19	-0.43	-0.65	-0.40	-0.60
21	0.78	0.48	-0.81	-1.29	-0.37	-0.64	-0.40	-0.61
22	0.00	-0.55	0.86	0.40	-0.73	-1.24	-0.33	-0.62
23	-0.32	-0.49	0.70	0.41	-0.10	-1.38	-0.34	-0.58
24	-0.13	-0.33	0.73	0.19	-0.08	-0.82	-0.35	-0.64
25	0.11	-0.08	0.55	0.07	0.12	-0.28	-0.32	-0.51
26	0.01	-0.60	0.00	-0.35	-0.07	-0.84	-0.34	-0.52
27	0.68	0.27	-0.72	-1.28	-0.37	-0.65	-0.35	-0.58
28	0.76	0.30	-0.81	-1.33	-0.35	-0.56	-0.39	-0.55
29	-0.33	-0.65	0.78	0.30	-0.79	-1.22	-0.33	-0.58
30	-0.29	-0.63	0.74	0.28	-0.10	-1.34	-0.34	-0.68
31	-0.22	-0.42	0.68	-0.11	-0.52	-0.82	-0.27	-0.65
32	0.10	-0.23	0.44	0.04	-0.07	-1.00	-0.34	-0.77
33	0.10	-0.55	-0.11	-0.35	-0.07	-0.87	-0.29	-0.60
34	0.60	0.29	-0.11	-1.34	-0.37	-0.62	-0.38	-0.60
35	0.76	0.38	-0.79	-1.39	-0.32	-0.61	-0.35	-0.68
36	-0.29	-0.61	0.56	0.23	-0.63	-1.24	-0.34	-0.67
37	-0.29	-0.54	0.48	0.17	-0.10	-1.18	-0.37	-0.62
38	-0.19	-0.34	0.41	-0.03	-0.07	-1.12	-0.32	-0.77
39	0.11	-0.20	0.31	-0.01	-0.07	-1.19	-0.34	-0.63
40	0.19	-0.40	-0.07	-0.36	-0.07	-0.81	-0.33	-0.56
41	0.50	0.20	-0.10	-1.14	0.00	-0.68	-0.32	-0.67
42	0.53	0.24	-0.09	-1.13	0.00	-0.63	-0.33	-0.63
43	-0.30	-0.65	0.62	0.32	-0.10	-1.18	-0.34	-0.63
44	-0.27	-0.51	0.54	0.24	-0.21	-0.77	-0.29	-0.61
45	-0.12	-0.27	0.38	0.01	-0.07	-1.07	-0.33	-0.62
46	0.17	-0.13	0.39	0.03	-0.08	-0.82	-0.33	-0.63
47	0.15	-0.32	-0.14	-0.46	-0.06	-0.75	-0.29	-0.54
48	0.49	0.20	-0.08	-1.30	-0.25	-0.62	-0.31	-0.63
49	0.62	0.31	-0.66	-1.15	-0.37	-0.57	-0.33	-0.57

Table 4.11 Peak pressure coefficients at pressure points of Sq model (90 degree)

Pressure Point	Face A		Face B		Face C		Face D	
	Max. Peak	Min. Peak	Max. Peak	Min. Peak	Max. Peak	Min. Peak	Max. Peak	Min. Peak
1	-0.19	-0.64	-0.08	-0.37	-0.10	-0.46	-0.31	-0.56
2	-0.36	-0.63	-0.11	-0.45	0.68	0.19	-0.30	-0.52
3	-0.35	-0.57	0.51	0.16	-0.10	-1.23	-0.29	-0.51
4	-0.30	-0.80	0.54	0.17	-0.30	-0.80	-0.26	-0.48
5	-0.10	-1.23	0.51	0.16	-0.35	-0.57	-0.29	-0.51
6	0.68	0.19	-0.11	-0.45	-0.36	-0.63	-0.30	-0.52
7	-0.10	-0.46	-0.08	-0.37	-0.19	-0.64	-0.31	-0.56
8	-0.36	-0.56	0.15	-0.24	0.20	-0.31	-0.31	-0.52
9	-0.35	-0.57	0.12	-0.27	0.75	0.18	-0.32	-0.53
10	-0.42	-0.65	0.75	0.35	-0.32	-1.13	-0.28	-0.50
11	-0.35	-0.93	0.88	0.07	-0.35	-0.93	-0.28	-0.51
12	-0.32	-1.13	0.75	0.35	-0.42	-0.65	-0.28	-0.50
13	0.75	0.18	0.12	-0.27	-0.35	-0.57	-0.32	-0.53
14	0.20	-0.31	0.15	-0.24	-0.36	-0.56	-0.31	-0.52
15	-0.35	-0.58	0.18	-0.29	0.14	-0.31	-0.31	-0.50
16	-0.34	-0.59	0.17	-0.24	0.57	0.06	-0.33	-0.53
17	-0.44	-0.70	0.72	0.32	-0.30	-1.06	-0.28	-0.50
18	-0.07	-0.89	0.80	0.46	-0.07	-0.89	-0.27	-0.48
19	-0.30	-1.06	0.72	0.32	-0.44	-0.70	-0.28	-0.50
20	0.57	0.06	0.17	-0.24	-0.34	-0.59	-0.33	-0.53
21	0.14	-0.31	0.18	-0.29	-0.35	-0.58	-0.31	-0.50
22	-0.31	-0.57	0.16	-0.24	0.13	-0.33	-0.30	-0.48
23	-0.33	-0.55	0.12	-0.28	0.55	0.03	-0.30	-0.58
24	-0.39	-0.72	0.67	0.25	-0.33	-0.99	-0.26	-0.41
25	-0.07	-0.85	0.78	0.47	-0.07	-0.85	-0.26	-0.40
26	-0.33	-0.99	0.67	0.25	-0.39	-0.72	-0.26	-0.41
27	0.55	0.03	0.12	-0.28	-0.33	-0.55	-0.30	-0.58
28	0.13	-0.33	0.16	-0.24	-0.31	-0.57	-0.30	-0.48
29	-0.15	-0.58	0.20	-0.25	0.13	-0.28	-0.29	-0.50
30	-0.31	-0.57	0.15	-0.29	0.52	-0.04	-0.29	-0.53
31	-0.36	-0.65	0.56	0.21	-0.07	-1.07	-0.25	-0.47
32	-0.07	-0.82	0.71	0.35	-0.07	-0.82	-0.25	-0.38
33	-0.07	-1.07	0.56	0.21	-0.36	-0.65	-0.25	-0.47
34	0.52	-0.04	0.15	-0.29	-0.31	-0.57	-0.29	-0.53
35	0.13	-0.28	0.20	-0.25	-0.15	-0.58	-0.29	-0.50
36	-0.29	-0.52	0.14	-0.32	0.16	-0.35	-0.28	-0.49
37	-0.30	-0.59	0.12	-0.31	0.34	-0.22	-0.29	-0.53
38	-0.31	-0.52	0.46	0.11	-0.07	-1.06	-0.26	-0.46
39	-0.46	-0.78	0.61	0.19	-0.46	-0.78	-0.22	-0.42
40	-0.07	-1.06	0.46	0.11	-0.31	-0.52	-0.26	-0.46
41	0.34	-0.22	0.12	-0.31	-0.30	-0.59	-0.29	-0.53
42	0.16	-0.35	0.14	-0.32	-0.29	-0.52	-0.28	-0.49
43	-0.30	-0.52	0.15	-0.24	0.25	-0.28	-0.26	-0.46
44	-0.27	-0.63	0.14	-0.33	0.35	-0.02	-0.27	-0.47
45	-0.24	-0.48	0.46	0.14	-0.07	-1.03	-0.23	-0.49
46	-0.39	-0.73	0.56	0.26	-0.39	-0.73	-0.21	-0.47
47	-0.07	-1.03	0.46	0.14	-0.24	-0.48	-0.23	-0.49
48	0.35	-0.02	0.14	-0.33	-0.27	-0.63	-0.27	-0.47
49	0.25	-0.28	0.15	-0.24	-0.30	-0.52	-0.26	-0.46

4.4.3. Plus-2 Model (Pl-2)

The direction of wind incidence is kept similar to the plus-1 model with face A2 is perpendicular to the wind for 0^0 wind and face B2 perpendicular for 90 degree wind as shown in Figure 4.20.

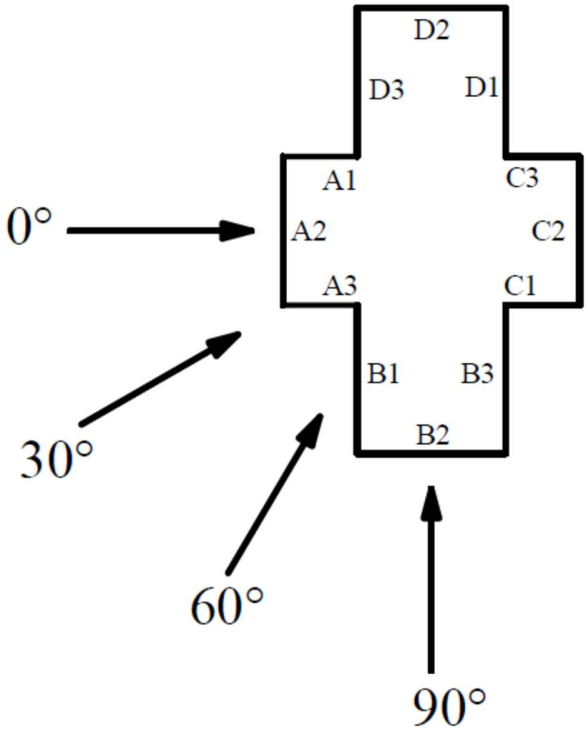

Fig. 4.20 Wind direction on Sq-model in isolated condition

Fig. 4.21 to 4.24 illustrates the distribution of the $C_{p,\,mean}$ at the various measuring levels of plus-2 model. The $C_{p,\,mean}$ values are consistent with each other at various levels. The pressure at all the faces on the windward side is positive, unlike the plus-1 model, even if the face is parallel to wind direction due to deceleration of wind flow by the large size of faces B1 and D3. The maximum positive $C_{p,\,mean}$ has been increased from 0.58 (plus-1 model) to 0.70 for the plus-2 model. Due to the decelerated separation, smaller negative coefficients appears at the leading edge of the side face compared to the plus-1 model. At 30 degree angle of attack, the absolute value of the negative pressure reduces at the corner faces A1 and D3 compare to those of the plus-1 model. The maximum value of negative $C_{p,mean}$ can reach up to -0.88. The maximum positive wind pressure coefficient still has a

higher value when compared to the square and plus-1 model. The absolute value of the negative $C_{p,\,mean}$ has a smaller value than the plus-1 model but higher than the square model at 60-degree wind incidence angle. The maximum suction coefficients turnup at the right edge of the front central face. For the leeward, the negative wind pressure coefficients reduce compare to the plus-1 model. For the wind direction of 90^0, except the central windward, all the walls have negative pressure coefficients, unlike wind flow at 0-degree angle. The maximum value of 0.77 of the mean wind pressure coefficients emerges at the central windward face. The absolute value of negative C_p can reach to 0.86 or more, and which appears at the front edge of the side central wall.

Compare to the base model, the positive pressure at windward reduces slightly but the negative wind pressure coefficient at leeward increases slightly and thus along-wind force almost similar at wind direction of 0 degree. At the wind direction of 90^0, the positive pressure at the windward and the negative pressure at leeward have decreased significantly, which results in the reduced along-wind forces at 90^0 wind compare to the square model.

Deviation between the pressure coefficients of the pressure points at different level along the height is higher near the corners of windward side faces, where wind separates . The values of $C_{p,mean}$ are almost similar to each other for pressure point at other faces. Deviation is higher for pressure points at top level.

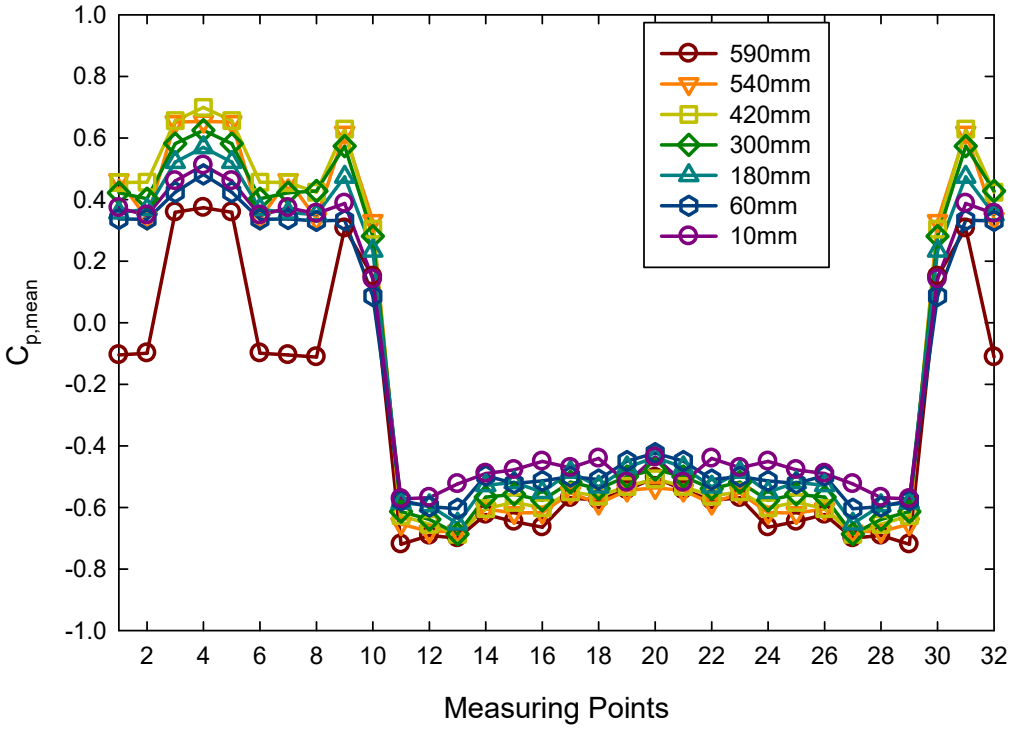

Fig. 4.21 $C_{p,\,mean}$ along perimeter-PL-2 model (0 degree)

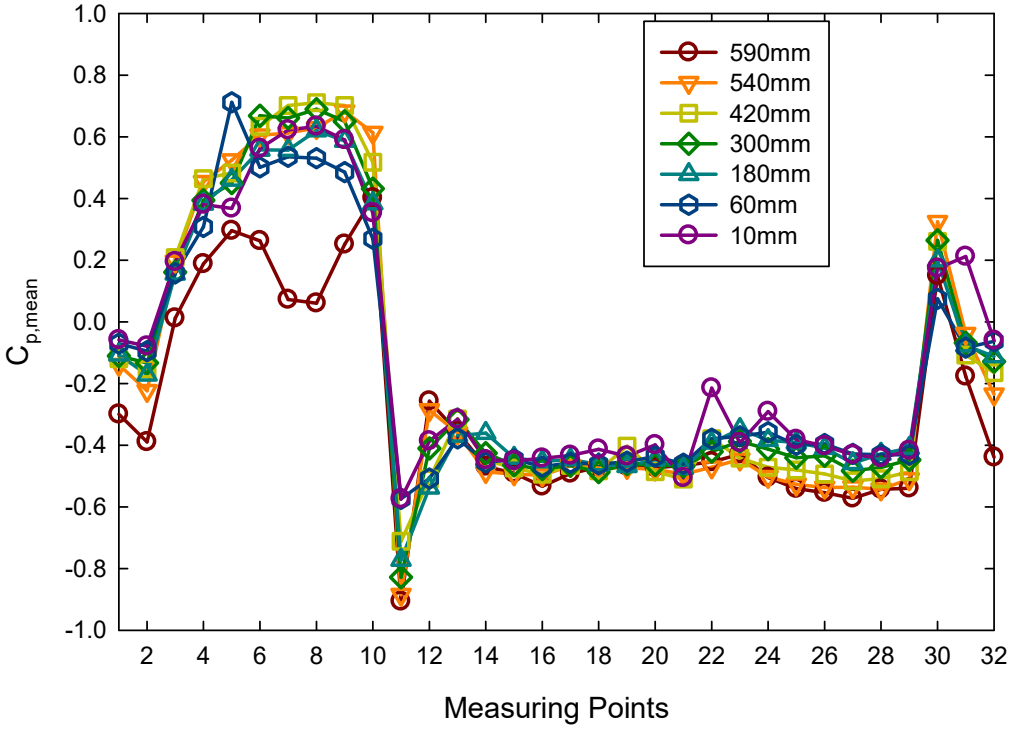

Fig. 4.22 $C_{p,\,mean}$ along perimeter-PL-2 model (30 degree)

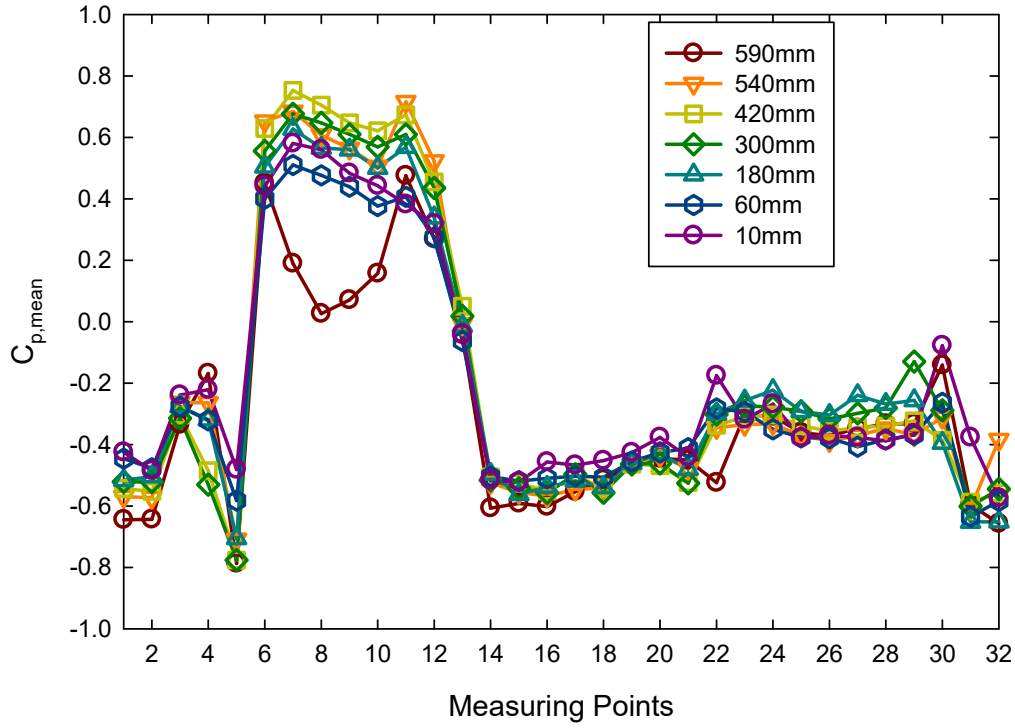

Fig. 4.23 $C_{p,\,mean}$ along perimeter-PL-2 model (60 degree)

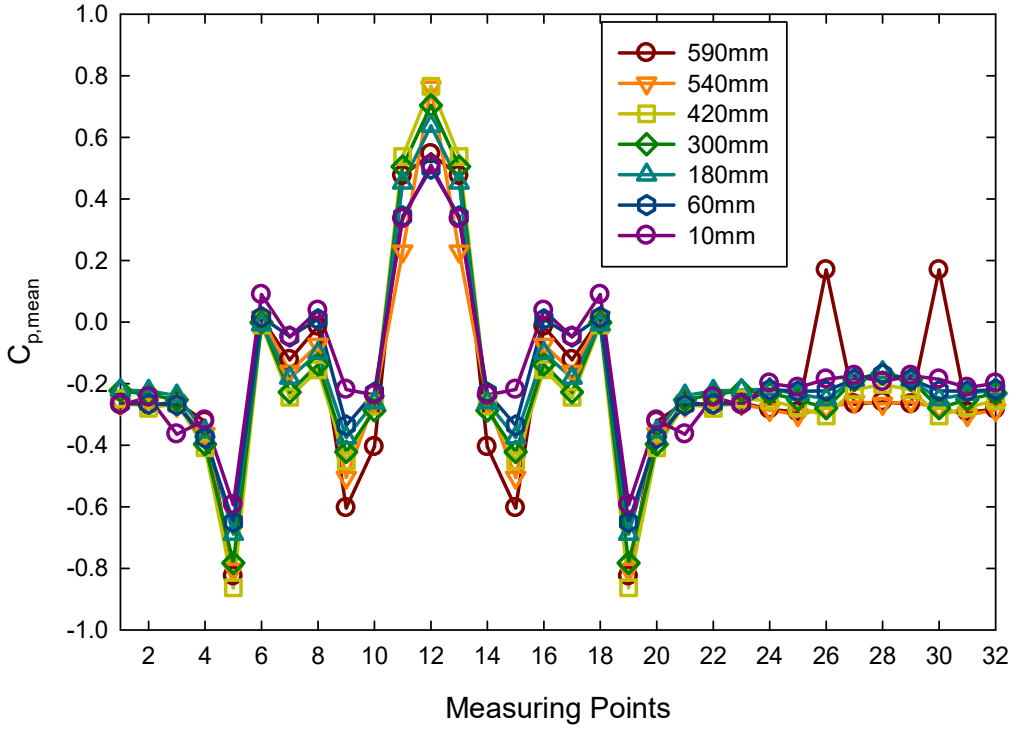

Fig. 4.24 $C_{p,\,mean}$ along perimeter-PL-2 model (90 degree)

Table 4.12 Area averaged mean pressure coefficients at faces of- Pl-2 model

Wind Angle	A1	A2	A3	B1	B2	B3	C1	C2	C3	D1	D2	D3
0 degree	0.37	0.57	0.37	0.38	-0.63	-0.56	-0.53	-0.49	-0.53	-0.56	-0.63	0.38
30 degree	-0.14	0.35	0.58	0.55	-0.51	-0.46	-0.47	-0.46	-0.40	-0.44	-0.47	-0.006
60 degree	-0.53	-0.45	0.59	0.54	0.33	-0.54	-0.52	-0.46	-0.31	-0.33	-0.33	-0.50
90 degree	-0.25	-0.46	-0.08	-0.25	0.52	-0.27	-0.08	-0.46	-0.25	-0.25	-0.20	-0.25

The area average values of $C_{p,mean}$ at different faces of the PL-2 model are shown in table 4.12. Unlike the PL-1 model, Face A1 of the PL-2 model is subjected to positive pressure at 0 degree wind due to the blockage of flow through face D3, even though it is a side face. Face A2 is subjected to positive pressure for 0^0 and 30^0 wind similar to plus-1 model. $C_{p,mean}$ at face B1 is significantly higher than those of Plus-1 model for normal wind incidence. Suction at face D3 is greatly reduced to almost zero for 30^0 wind compare to Plus-1 model.

The distribution of r.m.s pressure coefficients ($C_{p,rms}$) is shown in the Fig. 4.25 to 4.28 for wind directions of 0^0 to 90^0 , respectively. Similar to the plus-1 model, $C_{p,rms}$ values are higher at side faces. Unlike P-1 model, r.m.s of fluctuating pressure is higher at front face A2. Side face B2 and D2 still have higher value of r.m.s pressure similar to Pl-1 model. For wind direction at skew angles, r.m.s pressure slightly higher than those for perpendicular wind directions.

The values of peak pressure coefficients ($C_{p,max}$ and $C_{p,min}$) of Pl-2 models are shown in table 4.13 to 4.16. The average of $C_{p,max}$ at face A is positive for 0 degree wind and decreases to almost zero for 30^0 wind. Suction is observed for wind at 60^0 and 90^0. Peak minimum is also positive for 0^0 wind which show that fluctuating pressure is have both peaks positive. For higher wind angles minimum peak values are negative. Suction increase till 60^0 wind and then decreases. Maximum and minimum peaks at face A2 have positive values till 30^0 wind and change to negative after that. Face A3 and B1 have both the peaks positive till 60^0 wind. The peak maximum and peak minimum at face B2 creates suction for wind directions of 0 and 30 degree, and then change to positive pressure. The peak maximum and peak minimum at all the face on leeward side shows their both peaks as suction. The highest value of $C_{p,max}$ is observed at face A3 for 30 degree wind, whereas highest value of $C_{p,min}$ is observed at face B2 for 0 degree wind direction.

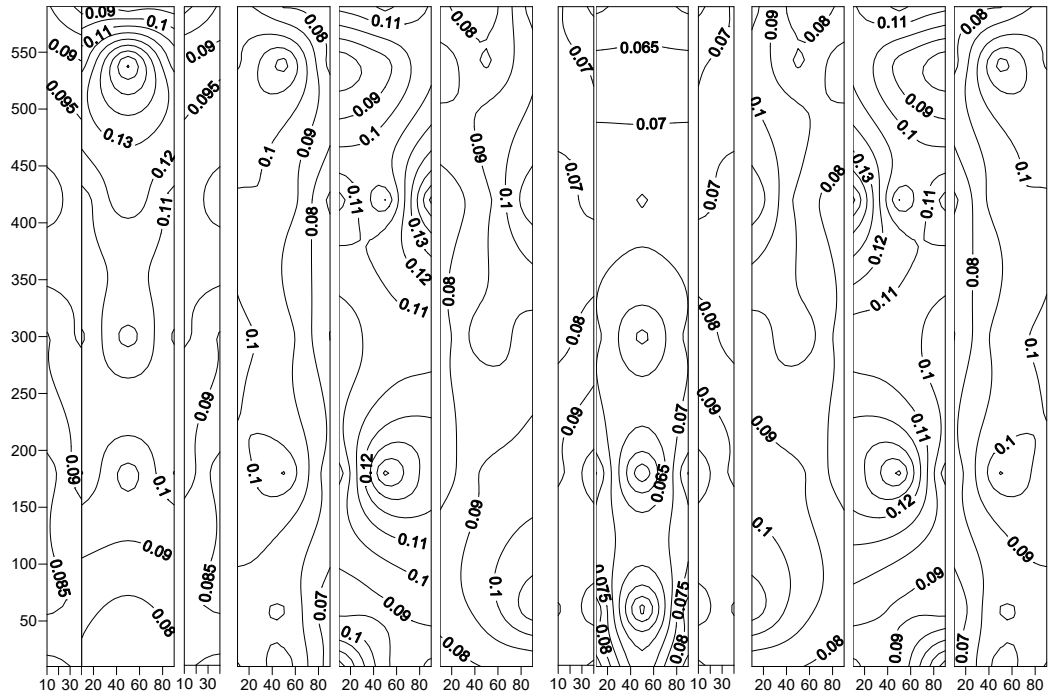

Fig. 4.25 Contour of r.m.s wind pressure coefficient – Pl-2 model (0 degree)

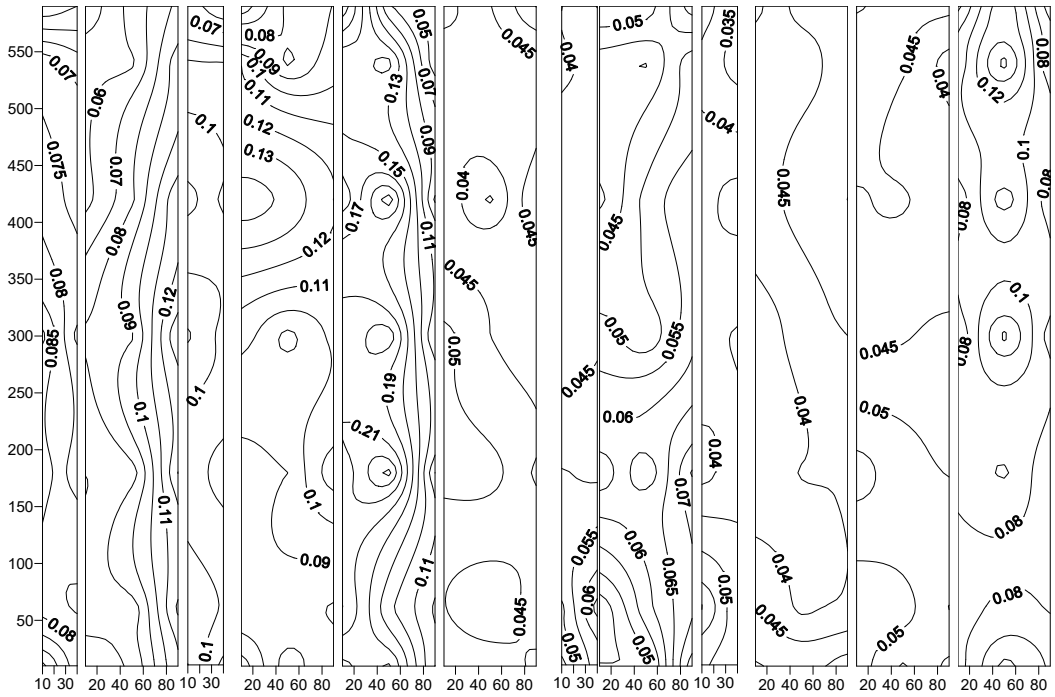

Fig. 4.26 Contour of r.ms wind pressure coefficient – Pl-2 model (30 degree)

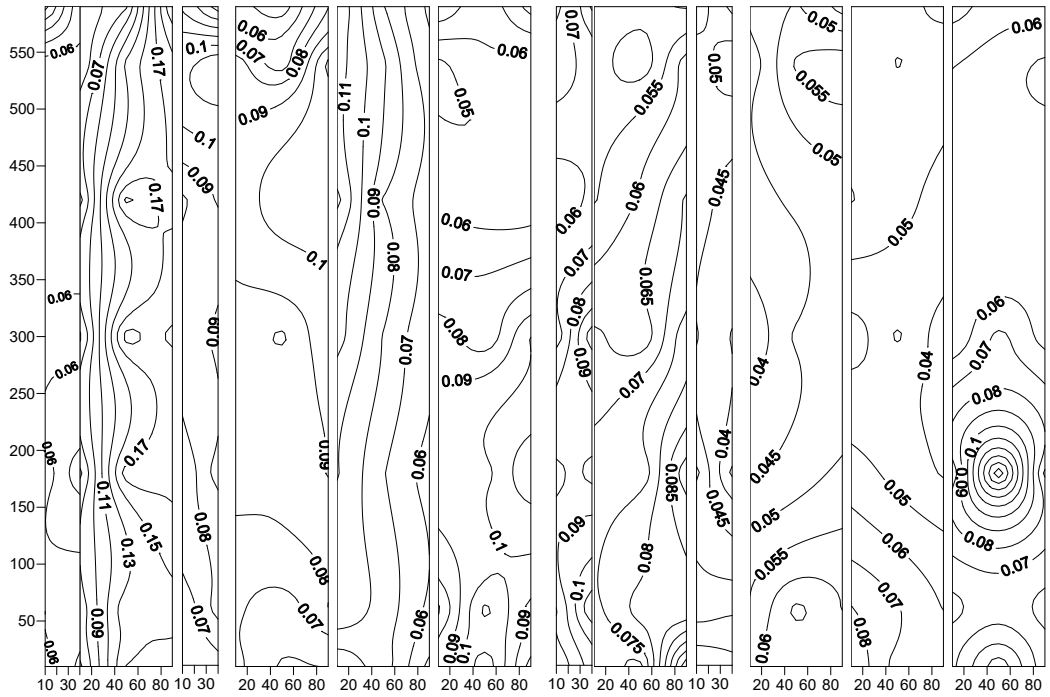

Fig. 4.27 Contour of r.m.s wind pressure coefficient – Pl-2 model (60 degree)

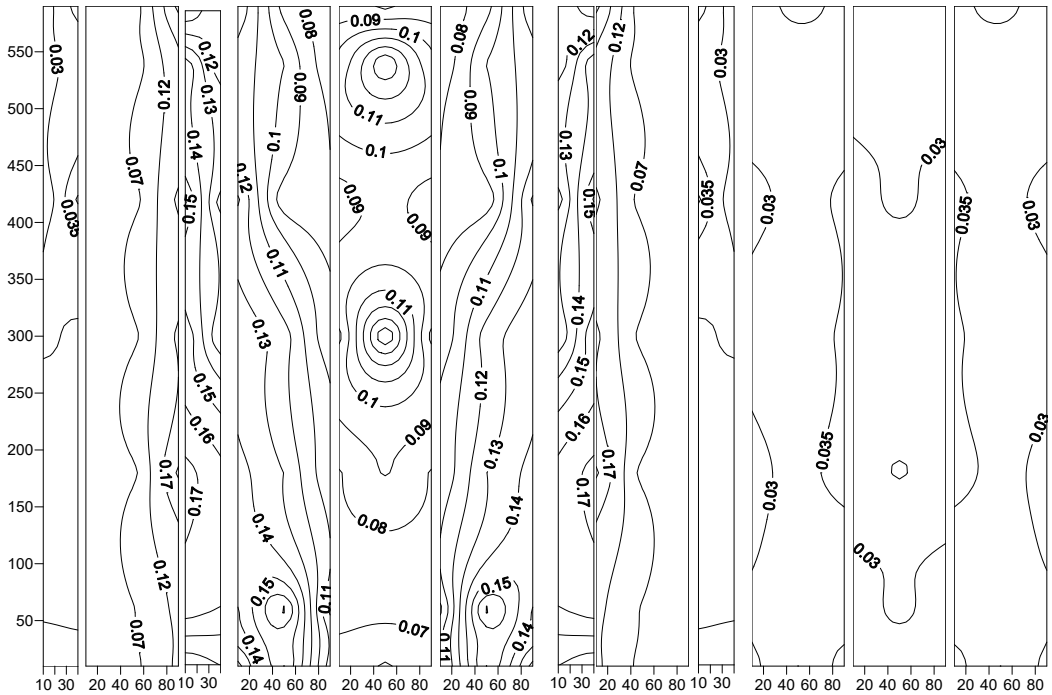

Fig. 4.28 Contour of r.m.s wind pressure coefficient – Pl-2 model (90 degree)

Table 4.13 Peak pressure coefficients at pressure points of Pl-2 model (Face A)

Pressure Point	0 degree		30 degree		60 degree		90 degree	
	Max.	Min.	Max.	Min.	Max.	Min.	Max.	Min.
1	0.02	-0.25	-0.19	-0.41	-0.08	-0.81	-0.24	-0.36
2	0.03	-0.30	-0.29	-0.52	-0.46	-0.77	-0.23	-0.40
3	0.05	0.23	0.11	-0.09	-0.27	-0.43	-0.23	-0.36
4	0.07	0.16	0.32	0.02	-0.06	-0.41	-0.30	-0.47
5	0.09	0.13	0.43	0.08	-0.06	-1.13	-0.10	-1.25
6	0.10	-0.32	0.43	0.10	0.57	0.26	-0.25	-0.37
7	0.12	-0.14	0.18	-0.05	0.31	0.07	0.06	-0.44
8	0.14	0.28	0.02	-0.30	-0.46	-0.68	-0.24	-0.36
9	0.15	0.14	-0.10	-0.40	-0.41	-0.73	-0.25	-0.38
10	0.17	0.45	0.33	0.01	-0.21	-0.36	-0.25	-0.38
11	0.19	0.00	0.58	0.32	0.00	-0.64	-0.32	-0.49
12	0.21	0.08	0.75	0.27	-0.07	-1.03	-0.07	-1.07
13	0.22	0.12	0.84	0.44	0.83	0.07	0.33	-0.44
14	0.24	0.16	0.80	0.37	0.96	0.08	0.05	-0.36
15	0.26	0.23	0.03	-0.32	-0.42	-0.70	-0.24	-0.38
16	0.27	0.24	-0.01	-0.31	-0.44	-0.71	-0.24	-0.43
17	0.29	0.44	0.35	0.07	-0.22	-0.41	-0.22	-0.37
18	0.31	0.08	0.65	0.25	-0.06	-0.79	-0.38	-0.60
19	0.33	0.07	0.71	0.17	-0.07	-1.04	-0.07	-1.20
20	0.34	0.25	0.80	0.08	0.82	0.43	0.29	-0.45
21	0.36	0.20	0.97	0.49	0.97	0.56	-0.05	-0.52
22	0.38	0.22	0.13	-0.32	-0.40	-0.64	-0.19	-0.37
23	0.39	0.19	0.05	-0.26	-0.38	-0.69	-0.21	-0.31
24	0.41	0.33	0.38	0.00	-0.24	-0.41	-0.24	-0.37
25	0.43	0.08	0.60	0.22	-0.08	-0.96	-0.34	-0.57
26	0.44	0.40	0.71	0.11	-0.07	-1.05	-0.07	-1.12
27	0.46	0.17	0.82	0.49	0.73	0.33	0.37	-0.37
28	0.48	0.26	0.95	0.45	0.93	0.50	-0.04	-0.52
29	0.50	0.17	0.14	-0.29	-0.38	-0.66	-0.19	-0.32
30	0.51	0.22	-0.04	-0.35	-0.42	-0.61	-0.22	-0.34
31	0.53	0.28	0.27	0.01	-0.18	-0.38	-0.22	-0.35
32	0.55	0.40	0.64	0.23	0.01	-0.76	-0.30	-0.57
33	0.56	0.25	0.67	0.07	-0.06	-1.09	-0.08	-1.15
34	0.58	0.16	0.86	0.32	0.65	0.37	0.39	-0.37
35	0.60	0.19	0.77	0.07	0.81	0.45	0.21	-0.51
36	0.62	0.17	0.14	-0.28	-0.34	-0.58	-0.18	-0.30
37	0.63	0.14	0.05	-0.28	-0.35	-0.66	-0.20	-0.32
38	0.65	0.29	0.38	0.03	-0.18	-0.41	-0.18	-0.39
39	0.67	0.34	0.52	0.16	-0.03	-0.65	-0.24	-0.56
40	0.68	0.00	0.89	0.08	-0.08	-0.85	-0.08	-0.94
41	0.70	0.12	0.75	0.32	0.53	0.27	0.38	-0.32
42	0.72	0.20	0.75	0.37	0.73	0.35	0.30	-0.44
43	0.74	0.23	0.10	-0.23	-0.32	-0.54	-0.15	-0.35
44	0.75	0.17	0.12	-0.23	-0.35	-0.66	-0.21	-0.33
45	0.77	0.29	0.34	0.05	-0.15	-0.36	-0.17	-0.35
46	0.79	0.35	0.54	0.24	0.06	-0.70	0.38	0.10
47	0.80	0.30	0.65	0.17	-0.21	-0.82	-0.08	-0.81
48	0.82	0.15	0.80	0.38	0.59	0.34	0.48	-0.29
49	0.84	0.19	0.83	0.08	0.74	0.46	0.28	-0.32

Table 4.14 Peak pressure coefficients at pressure points of Pl-2 model (Face B)

Pressure Point	0 degree		30 degree		60 degree		90 degree	
	Max.	Min.	Max.	Min.	Max.	Min.	Max.	Min.
1	0.06	-0.40	0.17	-0.08	0.14	-0.08	0.34	-0.28
2	0.50	0.16	0.45	0.06	0.15	-0.04	-0.46	-0.90
3	0.30	-0.05	0.64	0.22	0.31	-0.04	-0.32	-0.60
4	-0.08	-0.99	-0.10	-1.35	0.69	0.19	0.70	0.35
5	-0.08	-0.95	-0.13	-0.43	0.42	0.10	0.73	0.34
6	-0.08	-0.89	-0.26	-0.49	0.07	-0.18	0.60	0.18
7	-0.08	-0.76	-0.39	-0.57	-0.42	-0.81	-0.23	-0.64
8	-0.48	-0.88	-0.37	-0.58	-0.49	-0.73	-0.42	-0.76
9	-0.56	-1.19	-0.44	-0.74	-0.45	-0.89	0.27	-0.21
10	0.58	0.13	0.84	0.38	0.76	0.44	0.20	-0.33
11	0.80	0.07	0.82	0.47	0.71	0.45	-0.36	-0.71
12	0.51	0.14	0.82	0.44	0.70	0.19	-0.11	-0.43
13	-0.53	-0.84	-0.49	-1.17	0.96	0.41	0.14	-0.30
14	-0.54	-1.05	-0.02	-0.80	0.73	0.27	0.97	0.08
15	-0.08	-0.94	-0.29	-0.48	0.14	-0.12	0.75	0.27
16	-0.08	-0.81	-0.40	-0.62	-0.42	-0.63	-0.11	-0.52
17	-0.47	-0.82	-0.43	-0.59	-0.47	-0.72	-0.31	-0.79
18	-0.46	-0.80	-0.42	-0.59	-0.46	-0.68	0.21	-0.33
19	0.71	0.18	0.97	0.07	0.90	0.50	0.12	-0.38
20	0.87	0.43	0.94	0.08	0.83	0.07	-0.24	-0.65
21	0.51	0.17	0.75	0.08	0.81	0.36	-0.09	-0.42
22	-0.07	-0.94	-0.07	-1.02	0.92	0.08	0.79	0.36
23	-0.08	-0.89	-0.07	-0.95	0.67	0.31	0.96	0.58
24	-0.07	-0.93	-0.20	-0.54	0.20	-0.08	0.78	0.38
25	-0.45	-0.79	-0.35	-0.56	-0.39	-0.63	-0.08	-0.47
26	-0.08	-0.80	-0.42	-0.56	-0.42	-0.66	-0.33	-0.66
27	-0.07	-0.96	-0.40	-0.62	-0.46	-0.68	0.17	-0.45
28	0.63	0.19	0.93	0.41	0.91	0.47	0.28	-0.42
29	0.81	0.37	0.85	0.46	0.78	0.47	-0.12	-0.68
30	0.43	0.11	0.61	0.17	0.76	0.39	-0.04	-0.50
31	-0.43	-0.97	-0.09	-1.10	0.90	0.36	0.75	0.36
32	-0.44	-0.94	-0.05	-0.91	0.59	0.26	0.94	0.07
33	-0.10	-1.00	-0.13	-0.60	0.13	-0.11	0.68	0.35
34	-0.45	-0.82	-0.29	-0.58	-0.39	-0.79	-0.15	-0.47
35	-0.40	-0.82	-0.39	-0.60	-0.40	-0.73	-0.15	-0.76
36	-0.39	-0.88	-0.40	-0.57	-0.07	-0.72	0.07	-0.39
37	0.62	0.19	0.84	0.45	0.76	0.40	0.24	-0.40
38	0.71	0.26	0.76	0.38	0.73	0.37	0.09	-0.61
39	0.35	0.06	0.73	0.22	0.74	0.32	-0.03	-0.46
40	-0.48	-0.82	-0.06	-1.13	0.76	0.40	0.63	0.30
41	-0.07	-0.96	-0.06	-1.00	0.50	0.19	0.91	0.44
42	-0.07	-1.04	-0.22	-0.68	0.12	-0.16	0.63	0.27
43	-0.37	-0.76	-0.27	-0.54	-0.34	-0.76	-0.02	-0.55
44	-0.36	-0.79	-0.33	-0.56	-0.43	-0.80	-0.13	-0.64
45	-0.36	-0.76	-0.38	-0.56	-0.07	-0.90	0.18	-0.48
46	0.52	0.18	0.81	0.38	0.63	0.34	0.34	-0.27
47	0.57	0.09	0.67	0.33	0.59	0.32	0.06	-0.70
48	0.25	-0.02	0.45	0.14	0.55	0.18	-0.03	-0.43
49	-0.38	-0.77	-0.07	-0.93	0.61	0.22	0.57	0.19
50	-0.40	-0.82	-0.23	-0.77	0.51	0.15	0.68	0.30
51	-0.08	-0.81	-0.23	-0.64	0.06	-0.21	0.47	0.21
52	-0.30	-0.67	-0.35	-0.61	-0.35	-0.67	-0.05	-0.43
53	-0.35	-0.73	-0.38	-0.55	-0.07	-0.80	0.08	-0.69
54	-0.07	-1.02	-0.38	-0.62	-0.37	-0.72	0.24	-0.26
55	0.54	0.20	0.76	0.51	0.71	0.39	0.19	-0.21
56	0.67	0.22	0.82	0.39	0.64	0.37	0.10	-0.45
57	0.31	0.02	0.61	0.23	0.56	0.33	-0.02	-0.43
58	-0.38	-0.84	-0.24	-0.93	0.57	0.27	0.50	0.25
59	-0.38	-0.85	0.02	-0.79	0.51	0.15	0.65	0.34
60	-0.38	-0.74	-0.18	-0.51	0.10	-0.13	0.44	0.15
61	-0.33	-0.70	-0.36	-0.60	-0.39	-0.72	0.01	-0.49
62	-0.34	-0.67	-0.36	-0.54	-0.06	-0.76	0.12	-0.58
63	-0.33	-0.68	-0.35	-0.56	-0.31	-0.66	0.36	-0.27

Table 4.15 Peak pressure coefficients at pressure points of Pl-2 model (Face C)

Pressure Point	0 degree		30 degree		60 degree		90 degree	
	Max.	Min.	Max.	Min.	Max.	Min.	Max.	Min.
1	-0.45	-0.78	-0.42	-0.59	-0.44	-0.81	0.22	-0.34
2	-0.07	-0.77	-0.38	-0.56	-0.39	-0.66	0.73	-0.03
3	-0.42	-0.72	-0.34	-0.58	-0.37	-0.62	-0.07	-1.22
4	-0.37	-0.66	-0.38	-0.66	-0.35	-0.57	-0.20	-0.38
5	-0.44	-0.70	-0.39	-0.56	-0.36	-0.56	-0.16	-0.30
6	-0.46	-0.79	-0.35	-0.61	-0.44	-0.69	-0.17	-0.32
7	-0.43	-0.75	-0.36	-0.50	-0.20	-0.38	-0.18	-0.30
8	-0.42	-0.70	-0.40	-0.55	-0.43	-0.81	0.11	-0.36
9	-0.43	-0.82	-0.39	-0.55	-0.44	-0.73	0.42	-0.23
10	-0.39	-0.73	-0.38	-0.59	-0.38	-0.59	-0.08	-0.96
11	-0.42	-0.76	-0.39	-0.58	-0.34	-0.54	-0.21	-0.40
12	-0.43	-0.74	-0.37	-0.65	-0.37	-0.60	-0.18	-0.32
13	-0.46	-0.73	-0.39	-0.54	-0.25	-0.48	-0.16	-0.36
14	-0.38	-0.77	-0.37	-0.52	-0.22	-0.47	-0.17	-0.30
15	-0.40	-0.79	-0.37	-0.57	-0.40	-0.65	0.15	-0.43
16	-0.46	-0.72	-0.39	-0.63	-0.44	-0.71	0.34	-0.35
17	-0.40	-0.68	0.19	0.01	-0.34	-0.61	-0.07	-1.22
18	-0.40	-0.70	-0.39	-0.65	-0.34	-0.65	-0.27	-0.44
19	-0.41	-0.81	-0.40	-0.65	-0.39	-0.67	-0.16	-0.32
20	-0.43	-0.76	-0.27	-0.46	-0.25	-0.47	-0.17	-0.29
21	-0.45	-0.74	-0.31	-0.53	-0.22	-0.40	-0.15	-0.27
22	-0.35	-0.81	-0.38	-0.56	-0.34	-0.64	0.27	-0.41
23	-0.38	-0.74	-0.38	-0.61	-0.06	-0.78	0.27	-0.39
24	-0.37	-0.68	-0.38	-0.64	-0.35	-0.69	-0.07	-1.09
25	-0.36	-0.64	-0.38	-0.58	-0.33	-0.60	-0.23	-0.48
26	-0.32	-0.66	-0.36	-0.64	-0.37	-0.70	-0.15	-0.28
27	-0.07	-0.69	-0.33	-0.57	-0.19	-0.41	-0.14	-0.31
28	-0.40	-0.73	-0.32	-0.51	-0.17	-0.36	-0.15	-0.30
29	-0.34	-0.75	-0.36	-0.57	-0.33	-0.73	0.33	-0.50
30	-0.39	-0.74	-0.37	-0.58	-0.42	-0.74	0.37	-0.36
31	-0.30	-0.86	-0.37	-0.80	-0.28	-0.66	-0.07	-0.93
32	-0.31	-0.54	-0.31	-0.62	-0.29	-0.68	-0.19	-0.42
33	-0.34	-0.67	-0.38	-0.80	-0.31	-0.73	-0.13	-0.27
34	-0.07	-1.04	-0.30	-0.47	-0.17	-0.46	-0.13	-0.24
35	-0.33	-0.78	-0.26	-0.44	-0.19	-0.34	-0.13	-0.25
36	-0.30	-0.77	-0.35	-0.59	-0.34	-0.69	0.38	-0.36
37	-0.36	-0.85	-0.36	-0.71	-0.08	-0.82	0.35	-0.46
38	-0.07	-0.80	-0.36	-0.57	-0.32	-0.63	-0.43	-0.90
39	-0.30	-0.55	-0.33	-0.61	-0.27	-0.67	-0.27	-0.54
40	-0.31	-0.67	-0.33	-0.65	-0.27	-0.71	-0.21	-0.35
41	-0.33	-0.70	-0.15	-0.49	-0.19	-0.40	-0.22	-0.34
42	-0.34	-0.79	-0.26	-0.47	-0.15	-0.40	-0.22	-0.36
43	-0.36	-0.78	-0.36	-0.53	-0.33	-0.66	0.29	-0.33
44	-0.33	-0.74	-0.29	-0.59	-0.25	-0.69	0.48	-0.17
45	-0.29	-0.56	-0.36	-0.59	-0.28	-0.63	-0.31	-0.87
46	-0.30	-0.60	-0.28	-0.49	-0.23	-0.54	-0.22	-0.48
47	-0.36	-0.95	0.65	0.27	-0.07	-0.77	-0.37	-0.62
48	-0.19	-0.67	-0.11	-0.33	-0.06	-0.34	-0.18	-0.35
49	-0.30	-0.77	-0.26	-0.48	-0.19	-0.46	-0.24	-0.36

Table 4.16 Peak pressure coefficients at pressure points of Pl-2 model (Face D)

Pressure Point	0 degree		30 degree		60 degree		90 degree	
	Max.	Min.	Max.	Min.	Max.	Min.	Max.	Min.
1	-0.07	-0.82	-0.42	-0.60	-0.21	-0.41	-0.22	-0.40
2	-0.49	-0.77	-0.44	-0.65	-0.27	-0.52	-0.25	-0.42
3	-0.49	-0.80	-0.47	-0.66	-0.30	-0.47	0.69	0.53
4	-0.08	-0.86	-0.49	-0.67	-0.22	-0.49	-0.20	-0.35
5	-0.08	-0.85	-0.41	-0.66	-0.21	-0.45	-0.20	-0.33
6	-0.54	-0.86	-0.43	-0.68	-0.20	-0.47	-0.20	-0.33
7	0.33	-0.03	0.27	-0.02	0.04	-0.27	-0.20	-0.34
8	0.45	0.08	0.16	-0.51	-0.37	-0.75	-0.22	-0.35
9	0.05	-0.35	-0.34	-0.56	-0.52	-0.81	-0.23	-0.36
10	-0.07	-0.84	-0.40	-0.60	-0.24	-0.43	-0.20	-0.39
11	-0.48	-0.79	-0.40	-0.61	-0.26	-0.52	-0.23	-0.38
12	-0.46	-0.77	-0.43	-0.66	-0.27	-0.50	-0.21	-0.38
13	-0.08	-0.81	-0.43	-0.66	-0.28	-0.52	-0.21	-0.36
14	-0.52	-0.85	-0.45	-0.64	-0.22	-0.47	-0.20	-0.37
15	-0.52	-0.82	-0.40	-0.59	-0.26	-0.49	-0.19	-0.33
16	0.48	0.12	0.46	0.05	-0.18	-0.45	-0.22	-0.34
17	0.80	0.42	0.36	-0.28	-0.52	-0.79	-0.24	-0.37
18	0.46	0.16	-0.12	-0.37	-0.31	-0.50	-0.21	-0.39
19	-0.07	-0.80	-0.36	-0.58	-0.22	-0.39	-0.22	-0.35
20	-0.45	-0.80	-0.38	-0.62	-0.23	-0.43	-0.20	-0.39
21	-0.45	-0.87	-0.39	-0.60	-0.26	-0.46	-0.22	-0.39
22	-0.07	-0.95	-0.43	-0.59	-0.22	-0.56	-0.16	-0.29
23	-0.51	-0.81	-0.43	-0.60	-0.22	-0.46	-0.15	-0.27
24	-0.07	-0.81	-0.37	-0.58	-0.26	-0.42	-0.18	-0.28
25	0.44	0.17	0.38	0.08	-0.24	-0.54	-0.23	-0.38
26	0.81	0.42	0.31	-0.31	-0.48	-0.70	-0.22	-0.36
27	0.60	0.18	-0.03	-0.32	-0.43	-0.69	-0.17	-0.31
28	-0.38	-0.73	-0.33	-0.48	-0.20	-0.35	-0.17	-0.30
29	-0.07	-0.87	-0.33	-0.54	-0.20	-0.45	-0.19	-0.36
30	-0.42	-0.71	-0.33	-0.58	-0.22	-0.45	-0.19	-0.39
31	-0.56	-0.98	-0.41	-0.60	0.57	0.42	-0.14	-0.27
32	-0.07	-0.91	-0.40	-0.62	-0.18	-0.41	-0.11	-0.23
33	-0.49	-0.95	-0.34	-0.56	-0.05	-0.20	-0.14	-0.25
34	0.41	0.14	0.36	0.07	-0.19	-0.38	-0.21	-0.35
35	0.76	0.43	0.40	-0.34	-0.44	-0.74	-0.21	-0.34
36	0.76	0.24	0.01	-0.29	-0.39	-0.66	-0.17	-0.31
37	-0.41	-1.02	-0.30	-0.49	-0.13	-0.31	-0.15	-0.30
38	-0.37	-0.78	-0.30	-0.48	-0.18	-0.40	-0.15	-0.32
39	-0.41	-0.79	-0.34	-0.52	-0.20	-0.45	-0.16	-0.35
40	-0.07	-0.91	-0.34	-0.62	-0.10	-0.36	-0.14	-0.26
41	-0.07	-0.87	-0.33	-0.58	-0.16	-0.40	-0.11	-0.21
42	-0.42	-0.83	-0.27	-0.52	-0.17	-0.36	-0.14	-0.28
43	0.45	0.12	0.34	-0.01	-0.24	-0.58	-0.17	-0.33
44	0.71	0.24	0.20	-0.33	-0.07	-0.88	-0.18	-0.34
45	0.56	0.16	0.02	-0.25	-0.47	-0.77	-0.17	-0.28
46	-0.31	-0.77	-0.25	-0.45	-0.24	-0.46	-0.16	-0.31
47	-0.36	-0.79	-0.32	-0.49	-0.22	-0.54	-0.15	-0.28
48	-0.38	-0.84	-0.31	-0.47	-0.21	-0.55	-0.15	-0.28
49	-0.47	-0.82	-0.35	-0.60	-0.24	-0.68	-0.09	-0.27
50	-0.49	-0.82	-0.34	-0.55	-0.23	-0.60	-0.11	-0.23
51	-0.46	-0.79	-0.31	-0.54	-0.25	-0.56	-0.11	-0.29
52	0.23	-0.06	0.25	-0.04	-0.14	-0.39	-0.17	-0.30
53	0.49	0.12	0.07	-0.30	-0.50	-0.81	-0.17	-0.35
54	0.52	0.14	0.07	-0.32	-0.47	-0.68	-0.16	-0.29
55	-0.27	-0.74	-0.20	-0.41	-0.12	-0.42	-0.11	-0.27
56	-0.34	-0.77	-0.25	-0.49	-0.23	-0.57	-0.10	-0.31
57	-0.37	-0.70	-0.30	-0.56	-0.23	-0.57	-0.11	-0.21
58	-0.38	-0.78	-0.36	-0.57	-0.20	-0.62	-0.10	-0.23
59	-0.07	-0.86	-0.32	-0.58	-0.24	-0.52	-0.12	-0.28
60	-0.07	-0.81	-0.30	-0.55	-0.22	-0.55	-0.11	-0.29
61	0.25	-0.10	0.36	0.02	0.05	-0.22	-0.15	-0.28
62	0.57	0.18	0.51	-0.09	-0.11	-0.61	-0.16	-0.32
63	0.55	0.17	0.14	-0.27	-0.43	-0.71	-0.15	-0.30

4.4.4. H-Model

As mentioned earlier, all the models are tested for wind incidence angles of 0^0 to 90^0 at an interval of 30^0. For H-model, the larger face A is kept perpendicular to the 0^0 wind and changes to 90^0 wind angle towards the face B, as shown in Fig. 4.29

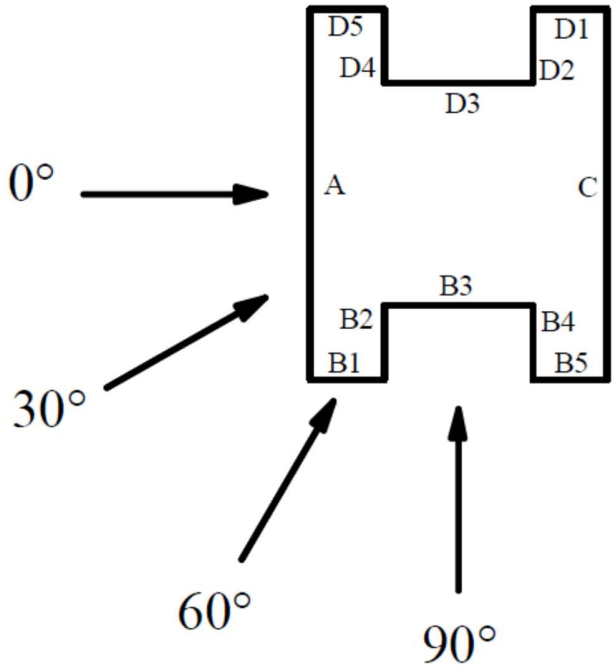

Fig. 4.29 Wind direction on Sq-model in isolated condition

The distribution of mean pressure coefficients along perimeters are shown in the figure 4.30 to 4.33, for wind directions of 0 to 90 degree, respectively. As this model is the modified version of the square model with the presence of recessed cavities, a comparative analysis of surface pressure has been provided. The variation of $C_{p,mean}$, is almost similar to the square models at front face for all wind incidence angles, but the H-plan model has a slightly higher pressure coefficient. Wind pressure coefficient distribution is symmetrical about the vertical centerline when the wind blows perpendicular to face A, i.e., at 0^0 wind incidence angle but does not remain symmetrical for other wind incidence angles. The face A is under positive pressure for wind incidence angle 0^0 and the values of $C_{p,mean}$ varies between 0.06 to 0.83. As expected, all the other surfaces are subjected to suction pressure, because of flow separation at the edges of side faces and wake flow at the leeward side.

The suction increases with height at all surfaces. The influence of recessed cavities on side faces is not observed for 0^0 wind direction.

At 30^0 wind incidence angle on face A, pressure remains positive except vertical leeward edges. The mean pressure coefficient decreases from windward to leeward edge because of the wind flow separation at the leeward edge. The value of the pressure coefficient varies between -0.03 to 0.81, with an average value of 0.44. The effect of the presence of cavities is observed in pressure at surfaces in the wake zone as the suction is reduced slightly. Pressure distribution at the side face in the middle (face B3) is of a complex nature where pressure from windward edge to leeward edge changes from higher negative to higher positive. The pressure at the middle is almost zero.

At 60^0 wind angle, the whole area of face A for beyond vertical centerline towards leeward side experiences suction, whereas part between the windward edge and vertical centerline is still subjected to positive pressure. The mean pressure coefficient varies between -0.17 to 0.32. The influence of recessed cavities is observed to be significant on the $C_{p,mean}$ of surface B and D at wind directions of 60^0 and 90^0. The mean pressure is positive at the complete area and significantly higher at surface B, while suction at surface D is significantly lower than those of the square model.

The area average values mean pressure coefficients at the surfaces are presented in table 4.17. The pressure at the front surface is positive till 60^0 wind and suction for 90^0 wind. Side face B is under suction for 0^0 wind and then changes to positive with a gradual increment from 30^0 wind to 90^0 wind direction. Leeward face C is always under suction with slightly lower values at skew wind angles. Side face is also subjected to suction for all wind with a gradual decrease with an increase in the wind angle.

Table 4.17 Area averaged mean pressure coefficients at faces of - H-model

Wind Angle	A	B1	B2	B3	B4	B5	C	D1	D2	D3	D4	D5
0^0	0.54	-0.67	-0.66	-0.65	-0.68	-0.57	-0.42	-0.57	-0.68	-0.65	-0.66	-0.67
30^0	0.49	0.00	0.09	0.08	0.20	-0.03	-0.34	-0.46	-0.41	-0.41	-0.40	-0.37
60^0	0.10	0.71	0.55	0.63	0.70	0.32	-0.39	-0.38	-0.38	-0.35	-0.34	-0.35
90^0	-0.51	0.61	0.80	0.81	0.80	0.61	-0.51	-0.18	-0.14	-0.14	-0.14	-0.18

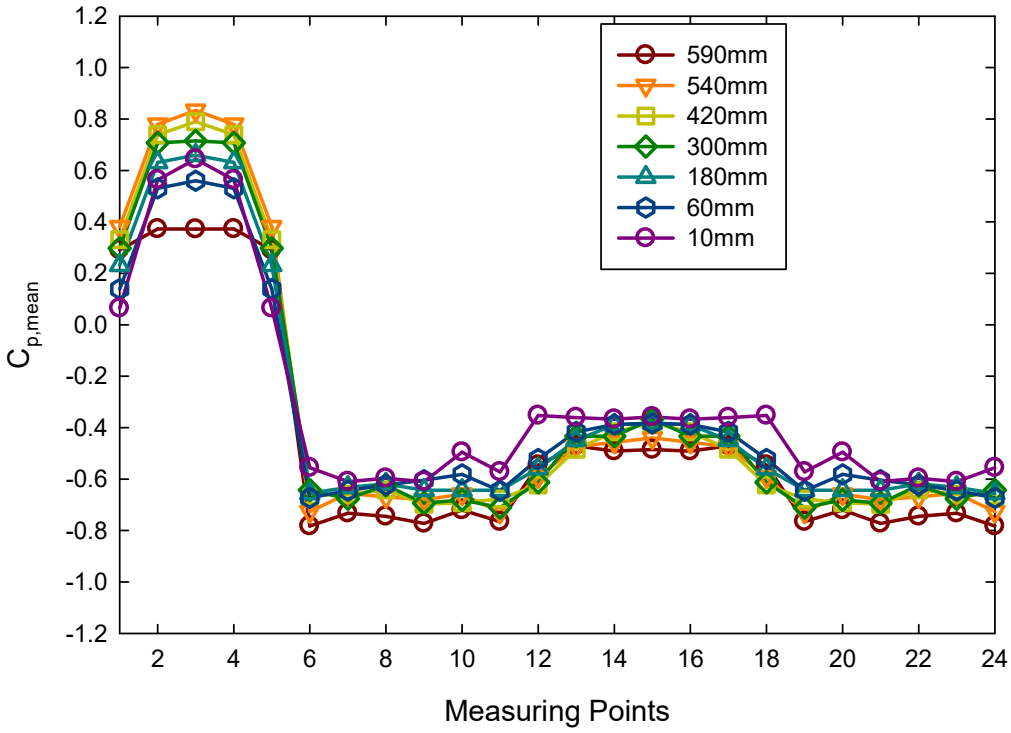

Fig. 4.30 $C_{p,\,mean}$ along perimeter-H- model (0 degree)

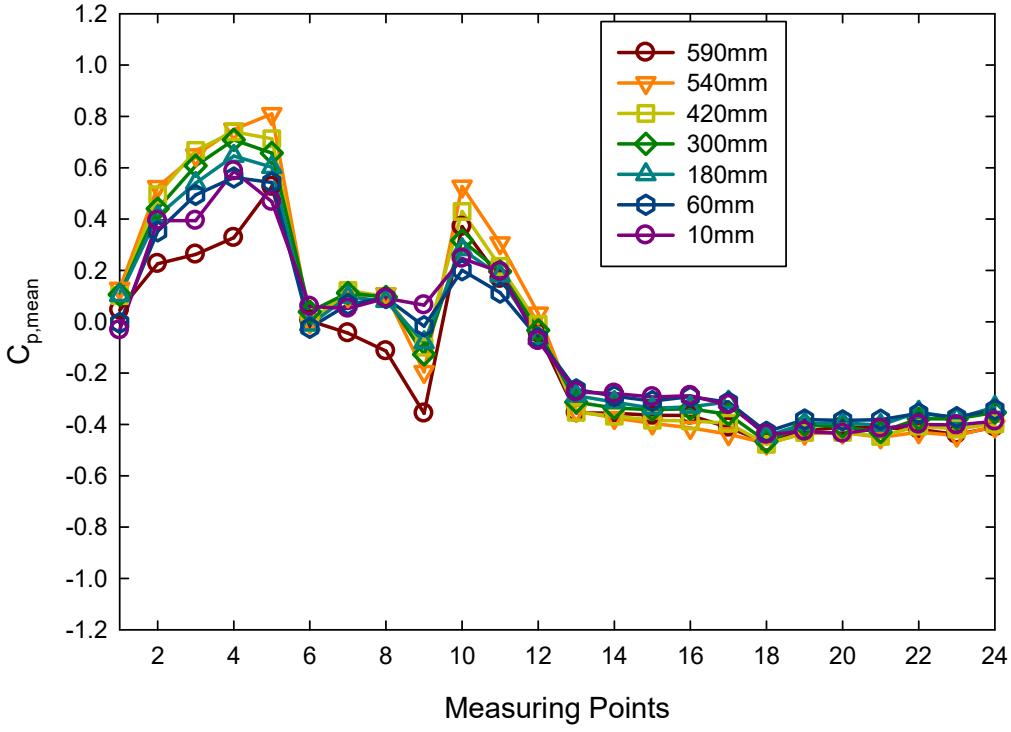

Fig. 4.31 $C_{p,\,mean}$ along perimeter-H- model (60 degree)

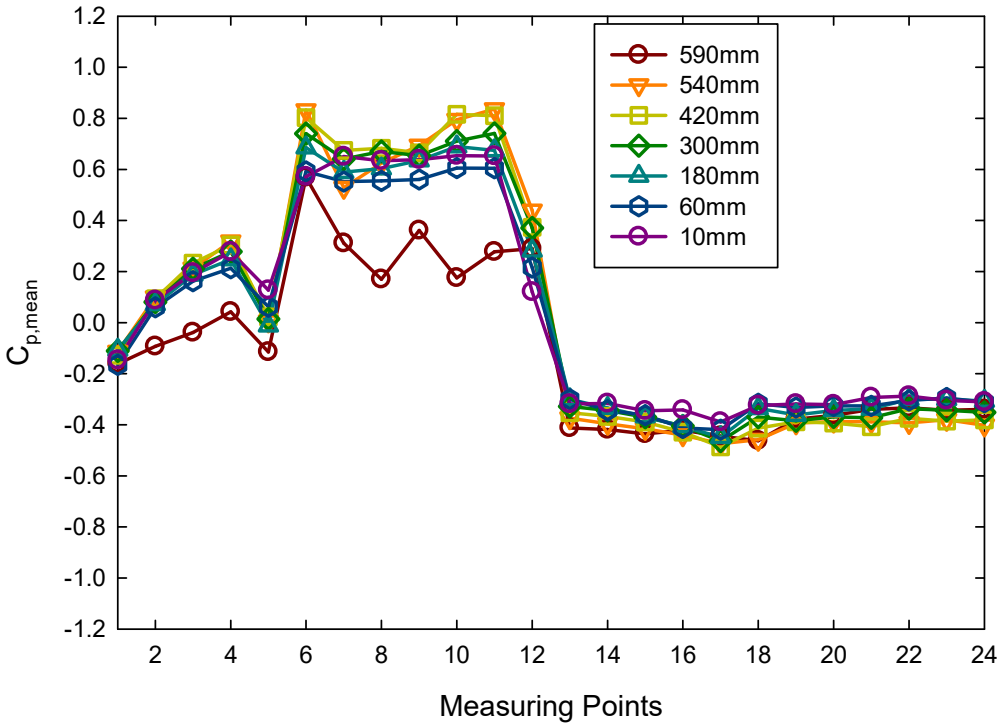

Fig. 4.32 $C_{p,\,mean}$ along perimeter-H- model (60 degree)

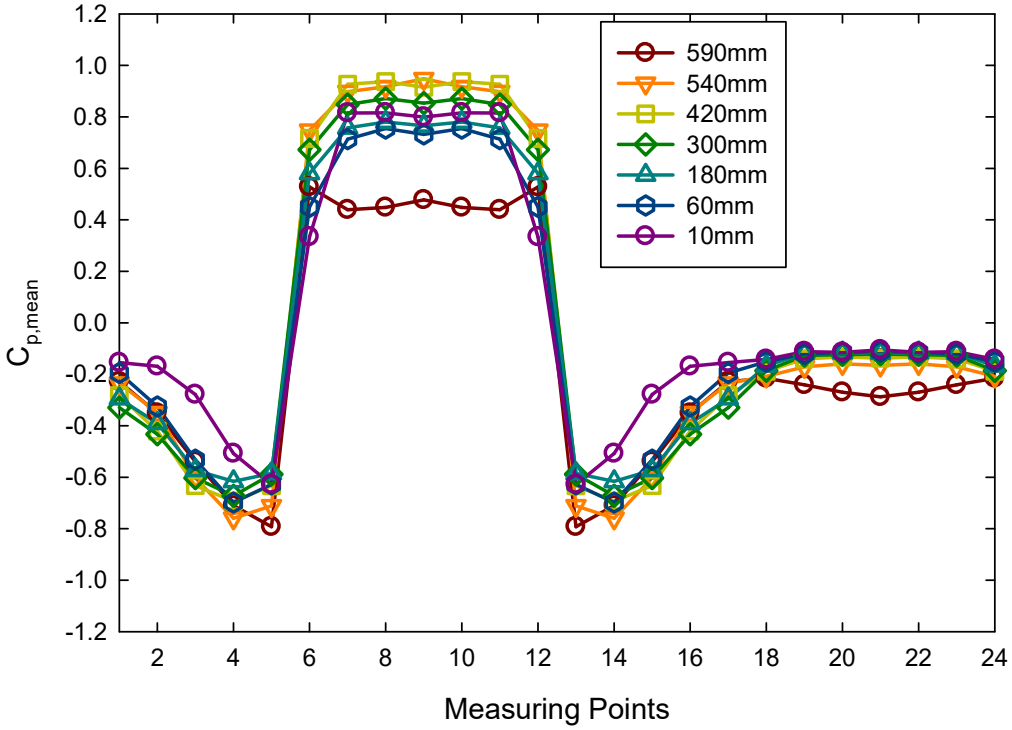

Fig. 4.33 $C_{p,\,mean}$ along perimeter-H- model (90 degree)

The distribution of r.m.s pressure coefficients ($C_{p,rms}$) is shown in the Fig. 4.34 to 4.37 for wind directions of 0^0 to 90^0, respectively. The values of $C_{p,rms}$ at different pressure points on the front face are almost similar, which indicates the stable flow similar to the square model. Higher values show a higher level of disturbance, which may indicate the disturbance of flow in recessed cavities on the side faces. Higher values with a complicated distribution at side faces show the strong irregular and disturbed vortex flow in the corners. Separation of flow at the trailing edges of the front face for skew wind angles generates a higher fluctuation in wind pressure.

The values of peak pressure coefficients ($C_{p,max}$ and $C_{p,min}$) of H-model are shown in table 4.18 to 4.21. The variation between two peaks at different faces generates higher level of fluctuations. The difference between two peaks is higher at side faces due to the disturbed flow. The averages of peak values $C_{p,max}$ and $C_{p,min}$ at front face are highest (0.64) at 0^0 wind and (-0.79) at 90^0 wind, respectively. The highest value (0.99) of $C_{p,max}$ at face B is for 90 degree wind while highest value (-1.11) of $C_{p,min}$ is for 0 degree wind. The difference between two peak values is comparatively low at leeward face. Side face D also have its highest value of $C_{p,max}$ for 0^0 wind direction. Face C and D have both the peak value as negative for all wind incidence angles.

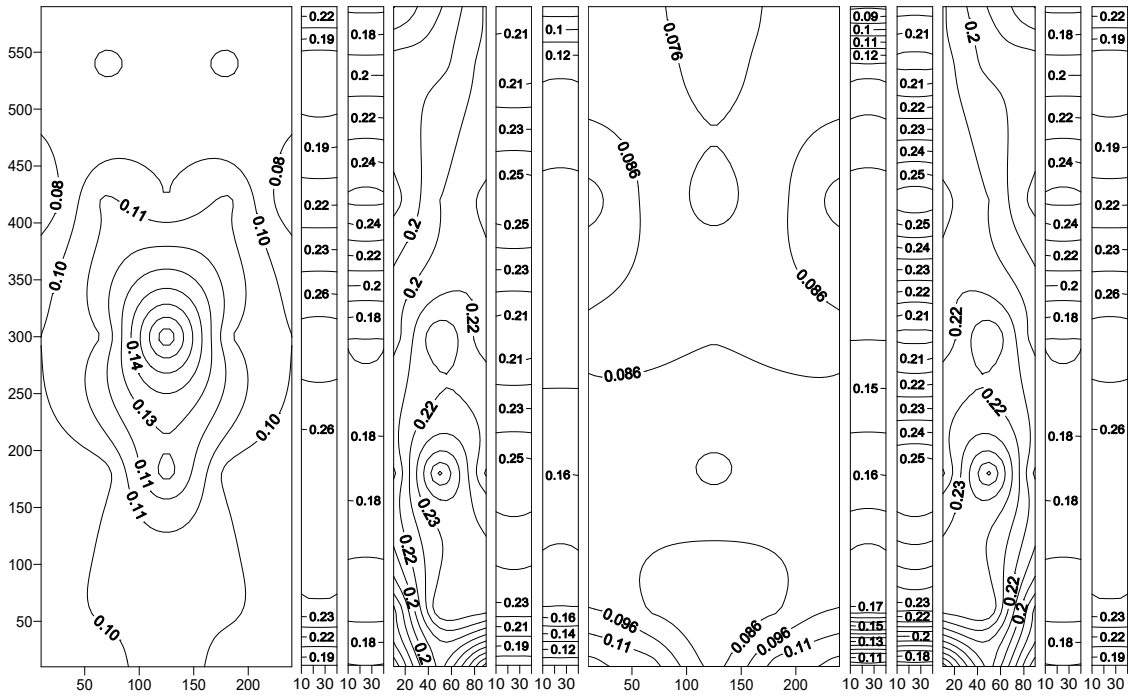

Fig. 4.34 Contour of r.m.s wind pressure coefficient – H- model (0 degree)

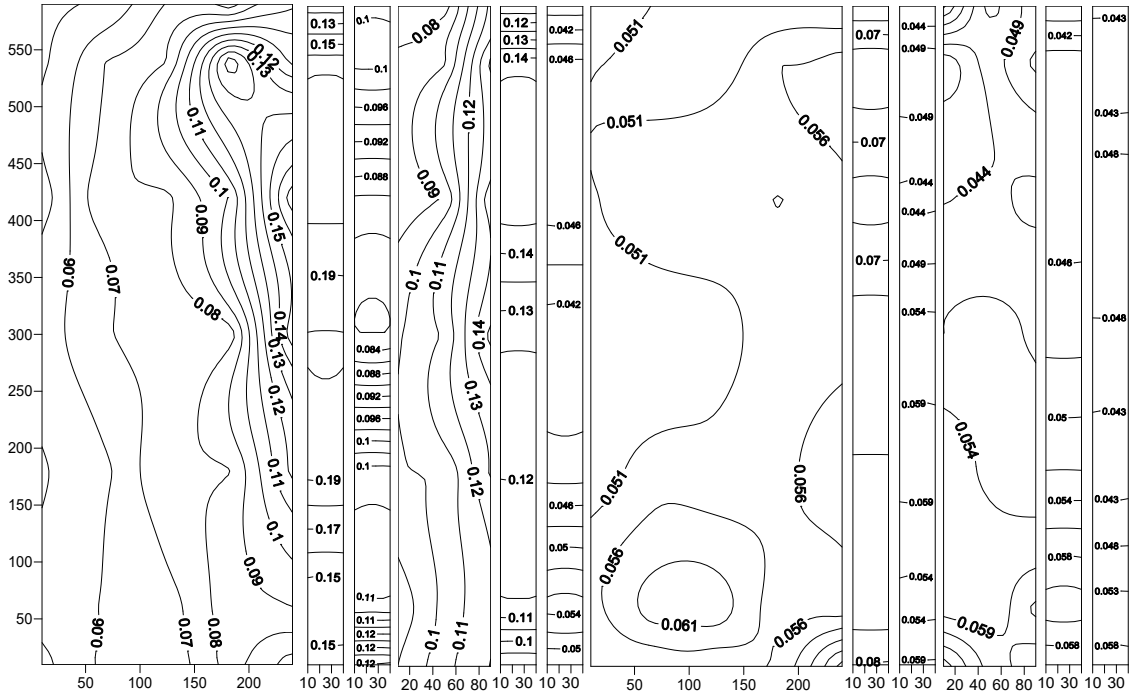

Fig. 4.35 Contour of r.m.s wind pressure coefficient – H- model (30 degree)

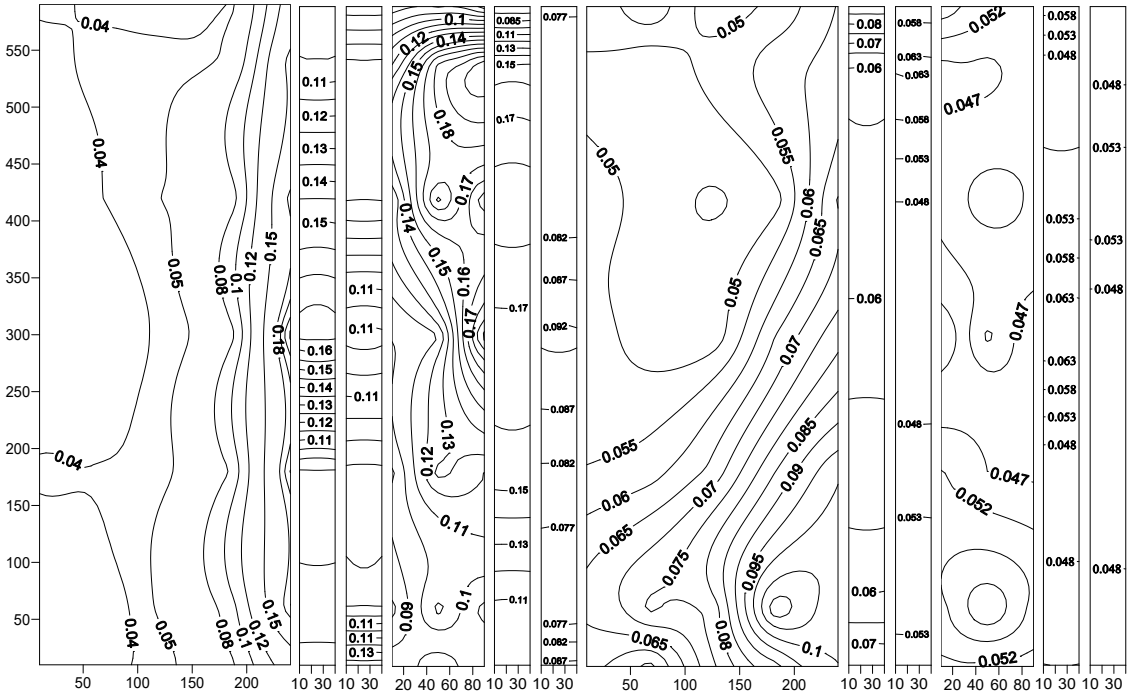

Fig. 4.36 Contour of r.m.s wind pressure coefficient – H- model (60 degree)

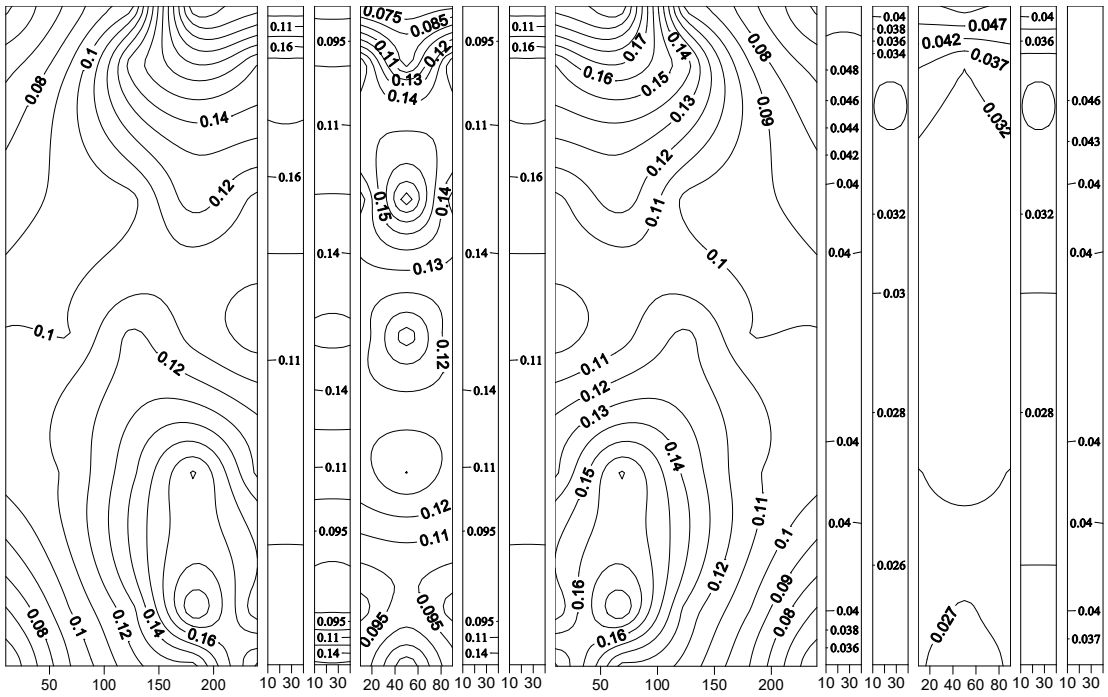

Fig. 4.37 Contour of r.m.s wind pressure coefficient - H- model (90 degree)

Table 4.18 Peak pressure coefficients at pressure points of H- model (Face A)

Pressure Point	0 degree		30 degree		60 degree		90 degree	
	Max.	Min.	Max.	Min.	Max.	Min.	Max.	Min.
1	0.53	0.08	0.15	-0.05	-0.10	-0.30	-0.13	-0.41
2	0.52	0.17	0.33	0.09	-0.01	-0.18	-0.26	-0.59
3	0.55	0.13	0.41	0.10	0.03	-0.12	-0.34	-0.78
4	0.52	0.17	0.46	0.19	0.12	-0.06	-0.07	-1.06
5	0.53	0.08	0.80	0.30	0.25	-0.40	-0.07	-1.39
6	0.61	0.10	0.27	0.03	-0.05	-0.20	-0.11	-0.60
7	0.55	0.28	0.66	0.33	0.20	0.00	-0.25	-0.61
8	0.55	0.22	0.82	0.42	0.30	0.13	-0.08	-0.81
9	0.55	0.13	0.94	0.07	0.48	0.21	-0.07	-1.00
10	0.61	0.15	1.06	0.59	0.39	-0.30	-0.07	-1.03
11	0.46	0.14	0.22	-0.01	-0.05	-0.20	-0.11	-0.53
12	0.89	0.56	0.69	0.36	0.20	0.02	-0.29	-0.68
13	1.03	0.60	0.85	0.51	0.39	0.13	-0.37	-0.82
14	0.97	0.07	1.01	0.57	0.46	0.04	-0.07	-0.99
15	0.54	0.14	1.09	0.07	0.33	-0.33	-0.08	-1.05
16	0.46	0.13	0.23	-0.02	-0.05	-0.19	-0.11	-0.68
17	0.94	0.07	0.65	0.28	0.16	0.00	-0.18	-0.68
18	0.97	0.07	0.78	0.42	0.33	0.13	-0.07	-0.82
19	0.98	0.55	0.82	0.55	0.40	0.11	-0.47	-0.82
20	0.62	0.10	0.89	0.08	0.54	-0.38	-0.32	-0.93
21	0.49	0.05	0.27	0.00	-0.01	-0.20	-0.11	-0.65
22	0.82	0.46	0.55	0.30	0.19	-0.04	-0.18	-0.66
23	0.89	0.07	0.70	0.36	0.28	0.09	-0.08	-0.82
24	0.83	0.43	0.82	0.48	0.40	0.02	-0.06	-0.99
25	0.40	0.03	0.80	0.07	0.50	-0.35	-0.07	-0.95
26	0.25	-0.11	0.15	-0.14	-0.08	-0.26	-0.09	-0.36
27	0.77	0.37	0.50	0.20	0.16	-0.01	-0.09	-0.55
28	0.78	0.39	0.62	0.36	0.31	0.00	-0.28	-0.76
29	0.80	0.36	0.80	0.41	0.41	-0.03	-0.06	-1.17
30	0.25	-0.10	0.73	0.33	0.45	-0.28	-0.07	-0.91
31	0.42	-0.01	0.08	-0.13	-0.09	-0.28	-0.07	-0.41
32	0.54	0.03	0.51	0.27	0.16	0.02	-0.06	-0.45
33	0.91	0.28	0.51	0.27	0.35	0.11	-0.10	-0.54
34	0.54	0.03	0.80	0.44	0.45	0.10	-0.20	-0.81
35	0.42	-0.02	0.63	0.34	0.44	-0.15	-0.06	-1.20

Table 4.19 Peak pressure coefficients at pressure points of H- model (Face B)

Pressure Point	0 degree		30 degree		60 degree		90 degree	
	Max.	Min.	Max.	Min.	Max.	Min.	Max.	Min.
1	-0.07	-1.20	0.23	-0.28	0.76	0.34	0.67	0.37
2	-0.07	-0.99	0.12	-0.31	-0.21	-0.49	0.45	-0.07
3	-0.07	-1.11	0.02	-0.35	-0.02	-0.34	0.28	0.01
4	-0.07	-1.09	-0.14	-0.51	0.54	0.20	0.48	0.18
5	-0.07	-1.04	0.71	0.10	0.39	0.02	0.39	-0.03
6	-0.07	-1.21	0.36	-0.09	0.44	0.15	0.37	0.02
7	-0.40	-0.72	0.08	-0.11	0.49	0.12	0.74	0.37
8	-0.07	-1.28	0.28	-0.44	1.07	0.59	0.93	0.07
9	-0.07	-0.94	0.29	-0.10	0.74	0.38	1.19	0.53
10	-0.07	-1.04	0.28	-0.14	0.82	0.07	1.15	0.08
11	-0.06	-1.08	0.00	-0.47	0.93	0.07	1.12	0.71
12	-0.07	-0.95	0.83	0.22	1.11	0.07	1.13	0.08
13	-0.07	-1.08	0.61	0.05	1.03	0.08	1.05	0.67
14	-0.33	-0.78	0.14	-0.08	0.60	0.22	1.07	0.07
15	-0.06	-0.99	0.36	-0.35	1.03	0.07	0.97	0.50
16	-0.06	-1.07	0.28	-0.23	0.82	0.50	1.18	0.08
17	-0.07	-0.94	0.23	-0.18	0.92	0.07	1.14	0.65
18	-0.07	-1.01	0.09	-0.31	0.97	0.07	1.20	0.09
19	-0.06	-1.10	0.80	0.10	1.07	0.07	1.23	0.63
20	-0.07	-1.08	0.53	-0.20	1.12	0.07	1.11	0.71
21	-0.06	-0.93	0.06	-0.18	0.57	0.20	1.05	0.07
22	-0.06	-1.15	0.37	-0.41	0.97	0.08	0.83	0.39
23	-0.07	-1.03	0.30	-0.06	0.81	0.08	1.11	0.08
24	-0.07	-1.08	0.27	-0.17	0.87	0.43	1.03	0.09
25	-0.06	-1.07	0.08	-0.32	0.91	0.38	1.02	0.65
26	-0.07	-1.07	0.64	-0.11	1.01	0.07	1.12	0.69
27	-0.07	-1.09	0.49	-0.35	0.99	0.08	1.03	0.08
28	-0.07	-0.82	0.05	-0.15	0.62	0.18	0.99	0.08
29	-0.05	-1.24	0.37	-0.45	0.94	0.45	0.75	0.36
30	-0.07	-1.01	0.28	-0.15	0.78	0.42	0.99	0.59
31	-0.06	-1.07	0.23	-0.25	0.85	0.42	1.03	0.08
32	0.00	-1.16	0.14	-0.36	0.93	0.07	1.00	0.08
33	-0.06	-1.04	0.65	-0.02	0.91	0.07	1.03	0.61
34	-0.06	-1.13	0.41	-0.09	0.89	0.07	1.00	0.08
35	-0.06	-0.80	0.05	-0.15	0.47	0.10	0.86	0.29
36	-0.05	-1.15	0.30	-0.36	0.81	0.42	0.66	0.22
37	-0.08	-1.14	0.29	-0.18	0.77	0.07	0.93	0.58
38	-0.06	-1.05	0.26	-0.11	0.75	0.34	0.90	0.59
39	-0.06	-1.07	0.20	-0.24	0.85	0.37	1.00	0.50
40	-0.06	-1.00	0.42	-0.03	0.81	0.45	0.93	0.55
41	-0.05	-1.14	0.44	-0.13	0.80	0.42	0.86	0.48
42	-0.06	-0.80	0.05	-0.19	0.39	0.08	0.67	0.32
43	-0.08	-0.76	0.40	-0.34	0.79	0.37	0.56	0.10
44	-0.07	-0.99	0.34	-0.29	0.97	0.07	1.05	0.07
45	-0.06	-0.81	0.33	-0.10	0.84	0.43	1.07	0.64
46	-0.05	-0.87	0.23	-0.28	0.82	0.47	1.09	0.08
47	-0.15	-0.75	0.64	0.03	0.81	0.45	1.02	0.64
48	-0.05	-0.94	0.43	0.01	1.01	0.47	1.41	0.59
49	-0.09	-0.58	0.03	-0.17	0.32	-0.15	0.50	0.19

Table 4.20 Peak pressure coefficients at pressure points of H- model (Face C)

Pressure Point	0 degree		30 degree		60 degree		90 degree	
	Max.	Min.	Max.	Min.	Max.	Min.	Max.	Min.
1	-0.33	-0.63	-0.26	-0.47	-0.31	-0.52	-0.07	-1.21
2	-0.35	-0.67	-0.24	-0.45	-0.31	-0.60	-0.07	-1.07
3	-0.33	-0.63	-0.27	-0.50	-0.36	-0.55	-0.32	-0.71
4	-0.31	-0.69	-0.28	-0.47	-0.31	-0.54	-0.16	-0.51
5	-0.31	-0.63	-0.32	-0.53	-0.35	-0.62	-0.12	-0.31
6	-0.30	-0.69	-0.25	-0.48	-0.28	-0.49	-0.07	-0.92
7	-0.32	-0.72	-0.28	-0.55	-0.31	-0.50	-0.07	-1.14
8	-0.30	-0.66	-0.29	-0.52	-0.33	-0.58	-0.08	-0.79
9	-0.30	-0.62	-0.29	-0.51	-0.35	-0.61	-0.09	-0.48
10	-0.35	-0.69	-0.34	-0.71	-0.33	-0.67	-0.10	-0.29
11	-0.31	-0.82	-0.25	-0.47	-0.25	-0.56	-0.47	-0.91
12	-0.24	-0.58	-0.26	-0.52	-0.25	-0.48	-0.52	-0.95
13	-0.23	-0.58	-0.29	-0.56	-0.29	-0.50	-0.34	-0.81
14	-0.23	-0.58	-0.25	-0.51	-0.34	-0.55	-0.21	-0.69
15	-0.28	-0.71	-0.25	-0.60	-0.33	-0.64	-0.16	-0.46
16	-0.26	-0.59	-0.20	-0.42	-0.20	-0.44	-0.34	-0.78
17	-0.24	-0.62	-0.20	-0.46	-0.25	-0.43	-0.07	-0.94
18	-0.24	-0.69	-0.25	-0.45	-0.26	-0.47	-0.41	-0.84
19	-0.30	-0.71	-0.22	-0.55	-0.30	-0.57	-0.27	-0.61
20	-0.30	-0.65	-0.23	-0.50	-0.32	-0.78	-0.12	-0.48
21	-0.27	-0.63	-0.17	-0.38	-0.17	-0.41	-0.33	-0.82
22	-0.22	-0.80	-0.23	-0.53	-0.24	-0.50	-0.07	-0.89
23	-0.23	-0.67	-0.23	-0.45	-0.24	-0.52	-0.08	-0.86
24	-0.23	-0.58	-0.20	-0.49	-0.23	-0.66	-0.20	-0.78
25	-0.29	-0.73	-0.21	-0.46	-0.27	-0.80	-0.14	-0.54
26	-0.22	-0.66	-0.16	-0.41	-0.19	-0.46	-0.44	-0.92
27	-0.24	-0.69	-0.16	-0.55	-0.07	-0.53	-0.07	-1.04
28	-0.25	-0.56	-0.15	-0.41	-0.24	-0.68	-0.28	-0.96
29	-0.22	-0.58	-0.17	-0.44	-0.24	-0.72	-0.09	-0.59
30	-0.26	-0.65	-0.20	-0.46	-0.25	-0.68	-0.06	-0.35
31	-0.07	-0.97	-0.16	-0.42	-0.20	-0.48	-0.07	-0.93
32	-0.20	-0.72	-0.18	-0.38	-0.20	-0.44	-0.20	-0.76
33	-0.21	-0.54	-0.20	-0.46	-0.19	-0.52	-0.10	-0.67
34	-0.18	-0.66	-0.18	-0.42	-0.21	-0.60	-0.02	-0.45
35	-0.06	-0.66	-0.16	-0.55	-0.24	-0.66	-0.07	-0.22

Table 4.21 Peak pressure coefficients at pressure points of H- model (Face D)

Pressure Point	0 degree		30 degree		60 degree		90 degree	
	Max.	Min.	Max.	Min.	Max.	Min.	Max.	Min.
1	-0.35	-0.74	-0.32	-0.62	0.00	-0.67	-0.12	-0.32
2	-0.07	-1.09	-0.34	-0.51	-0.24	-0.52	-0.14	-0.31
3	-0.08	-1.11	0.00	-0.52	-0.26	-0.49	-0.17	-0.37
4	-0.07	-0.93	-0.32	-0.50	-0.24	-0.47	-0.20	-0.45
5	-0.07	-0.93	-0.29	-0.59	-0.23	-0.47	-0.18	-0.46
6	-0.55	-0.97	-0.36	-0.54	-0.24	-0.54	-0.17	-0.42
7	-0.08	-1.02	-0.32	-0.53	-0.25	-0.43	-0.13	-0.36
8	-0.06	-0.81	0.00	-0.61	-0.31	-0.63	-0.12	-0.33
9	-0.07	-1.03	-0.34	-0.57	-0.30	-0.72	-0.10	-0.25
10	-0.07	-0.99	-0.37	-0.52	-0.29	-0.57	-0.06	-0.27
11	-0.07	-0.92	-0.38	-0.58	-0.30	-0.53	-0.10	-0.24
12	-0.07	-0.88	-0.30	-0.63	-0.29	-0.53	-0.09	-0.26
13	-0.07	-0.82	-0.35	-0.53	-0.27	-0.48	-0.11	-0.25
14	-0.06	-0.96	-0.34	-0.52	-0.31	-0.51	-0.12	-0.34
15	-0.07	-0.81	-0.39	-0.71	-0.27	-0.55	-0.12	-0.29
16	-0.07	-0.96	-0.35	-0.53	-0.30	-0.51	-0.07	-0.22
17	-0.06	-0.99	-0.34	-0.53	-0.30	-0.51	-0.06	-0.21
18	-0.07	-0.93	-0.35	-0.59	-0.32	-0.55	-0.07	-0.20
19	-0.06	-0.82	-0.27	-0.50	-0.28	-0.51	-0.06	-0.23
20	-0.07	-1.01	-0.30	-0.53	-0.26	-0.50	-0.07	-0.24
21	-0.07	-0.88	-0.26	-0.61	-0.24	-0.52	-0.11	-0.27
22	-0.07	-1.03	-0.33	-0.73	-0.22	-0.48	-0.09	-0.37
23	-0.07	-1.08	-0.30	-0.54	-0.26	-0.47	-0.06	-0.22
24	-0.07	-0.99	-0.33	-0.57	-0.29	-0.44	-0.07	-0.20
25	-0.07	-1.02	-0.31	-0.64	-0.24	-0.49	-0.07	-0.20
26	-0.07	-0.90	-0.24	-0.49	-0.26	-0.43	-0.06	-0.20
27	-0.09	-0.91	-0.24	-0.49	-0.24	-0.66	-0.08	-0.19
28	-0.07	-0.95	-0.26	-0.46	-0.26	-0.44	-0.12	-0.27
29	-0.06	-0.91	-0.31	-0.65	-0.21	-0.51	-0.07	-0.30
30	-0.06	-1.01	-0.27	-0.63	-0.27	-0.55	-0.06	-0.19
31	-0.06	-1.04	-0.30	-0.56	-0.24	-0.51	-0.06	-0.18
32	-0.07	-1.00	-0.29	-0.51	-0.25	-0.44	-0.06	-0.21
33	-0.06	-0.86	-0.25	-0.52	-0.20	-0.39	-0.07	-0.18
34	-0.06	-1.01	-0.27	-0.47	-0.19	-0.41	-0.08	-0.19
35	-0.06	-0.89	-0.24	-0.42	-0.20	-0.42	-0.07	-0.24
36	-0.25	-0.79	-0.26	-0.65	-0.22	-0.46	-0.04	-0.25
37	-0.06	-0.99	-0.28	-0.54	-0.25	-0.55	-0.07	-0.19
38	-0.06	-0.91	-0.22	-0.53	-0.24	-0.51	-0.07	-0.16
39	-0.06	-0.97	-0.27	-0.55	-0.19	-0.58	-0.05	-0.19
40	-0.06	-0.84	-0.25	-0.58	-0.21	-0.49	-0.06	-0.17
41	-0.07	-0.92	-0.27	-0.56	-0.20	-0.41	-0.08	-0.19
42	-0.06	-1.10	-0.25	-0.50	-0.22	-0.44	-0.06	-0.26
43	-0.19	-0.64	-0.29	-0.74	-0.17	-0.58	-0.06	-0.24
44	-0.08	-1.00	-0.32	-0.55	-0.21	-0.42	-0.06	-0.17
45	-0.06	-0.82	-0.27	-0.70	-0.20	-0.48	-0.07	-0.23
46	-0.06	-1.00	-0.29	-0.58	-0.21	-0.41	-0.04	-0.17
47	-0.08	-0.82	-0.27	-0.52	-0.18	-0.39	-0.06	-0.17
48	-0.07	-0.82	-0.28	-0.57	-0.23	-0.44	-0.07	-0.18
49	-0.05	-1.12	-0.24	-0.60	-0.21	-0.46	-0.03	-0.20

5. CHAPTER-5

EXPERIMENTAL STUDY- PRESSURE MEASUREMENT (INTERFERENCE)

5.1. GENERAL

The flow between two or more buildings involves interactions between shear layers, vortices, and wakes and thus complicated to understand [151]. The mean response of the principal building may reduce by the shielding effects, but the peak oscillatory response is increased significantly [152], [153]. The modification in the wind forces under interference depends on a large number of factors, including geometry and position of buildings, terrain conditions, Turbulence intensity etc. [154]. It is very difficult to cover the effects of all possible combinations to set the guidelines for interference. Therefore, it is worthy of understanding the actual mechanism of interference by wind tunnel study.

In the present research work, interference effects between twin building of models under consideration are investigated through wind tunnel tests. Experimental building models considered in this study comprised two buildings, out of which one is the pressure model referred to as principal building under consideration, and the second is the interfering building model. As mentioned earlier, the principal building model was made of a transparent Perspex sheet of 4 mm thickness with stiff faces to ensure sufficient rigidity and strength of the model, whereas the interfering building model was a wooden model of the similar shape and size without pressure taping.

Total three sets of test arrangements were made for the measurement of the pressure and interference effect between building models. Set-1 to set-3 are shown in Fig. 5.1, indicating the different positions of the interfering buildings with respect to the principal building. In set-1, the principal building is placed at the turntable, and the interfering building was placed in line with the principal building, causing full blockage of wind streams. Distance (x) between the principal building and the interfering building was kept equal to 60 mm ($1/10^{th}$ of height of the principal building) for all cases. In set-2 and set-3, the position of the principal building is kept the same as previous case, and the interfering building was

placed in oblique configuration, creating a half blockage of wind streams and no blockage conditions for the principal building, respectively.

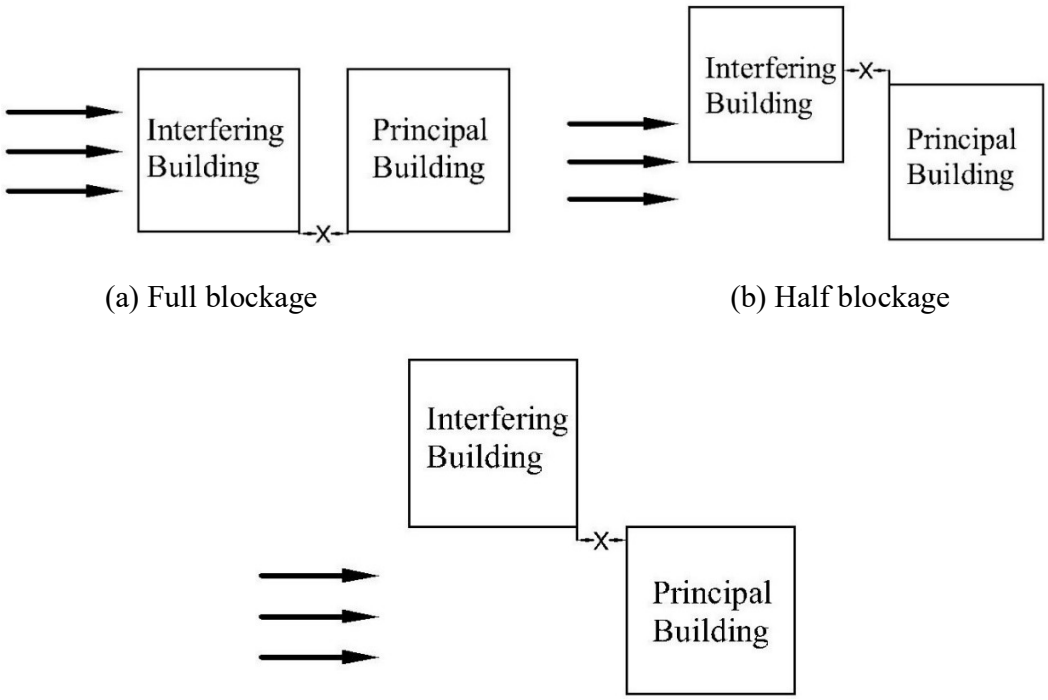

(a) Full blockage (b) Half blockage

(c) No blockage

Fig. 5.1 Various interference conditions - Sq model

5.2. SQUARE MODEL

5.2.1. Pressure Distribution

The prediction of wind load is a difficult task with interfering buildings present in the near vicinity. The relative location of these interfering buildings is an essential parameter that affects the characteristics of wind load on the principal building. The distribution of $C_{p,mean}$ corresponding to various interference conditions are presented in the Fig. 5.2 to 5.4. The influence of the presence of the interfering building in the close vicinity of the principal building is more stronger on the front face of target building in the full blockage condition, because it is shielded by the upstream building. Pressure distribution at the front face is completely different than those in case of isolated building. Windward face suffer higher negative wind pressure as it immerse in the wake of upstream building. The pressure

distribution on the side and leeward faces is similar to the isolated building case, but the suction intensity is likely to be reduced, especially on the side faces. The variation between the pressure at different points along the height is increased than those in the case of isolated building. An increase in the pressure variation is more significant for pressure points at the side and leeward faces. When the interfering building is present upstream of the target building with half blockage, the half of the windward face is shielded by the upstream building. The pressure changes from negative at the points on the half surface toward the interfering building to positive at points on the other side of the front face. The intensity of negative wind pressure at the front face is decreased from those in case of full blockage. The intensity of negative wind pressure at side and leeward side surfaces is likely to increase from those in case of full blockage, but still less than those in case of isolated building case. The presence of the interfering building in no blockage position is beneficial as positive and negative wind pressure at most unfavorable points on all the surfaces is likely to be decreased by the influence of the interfering building in full blockage position.

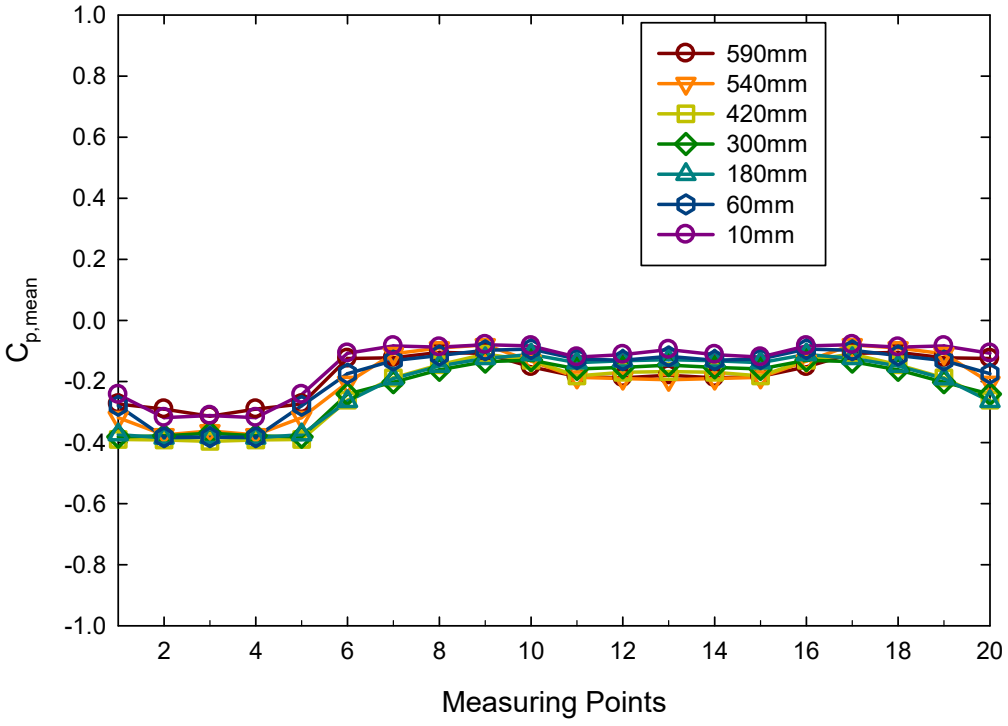

Fig. 5.2 $C_{p,\,mean}$ along perimeter-Sq-model (full blockage interference)

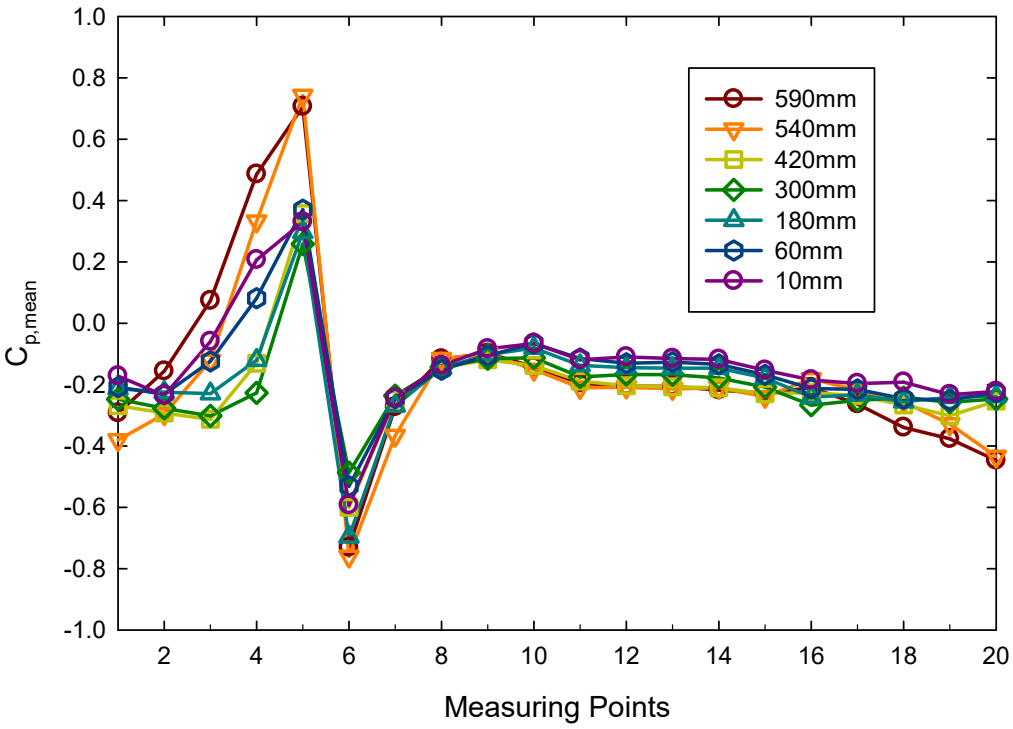

Fig. 5.3 $C_{p,\,mean}$ along perimeter-Sq-model (Half blockage interference)

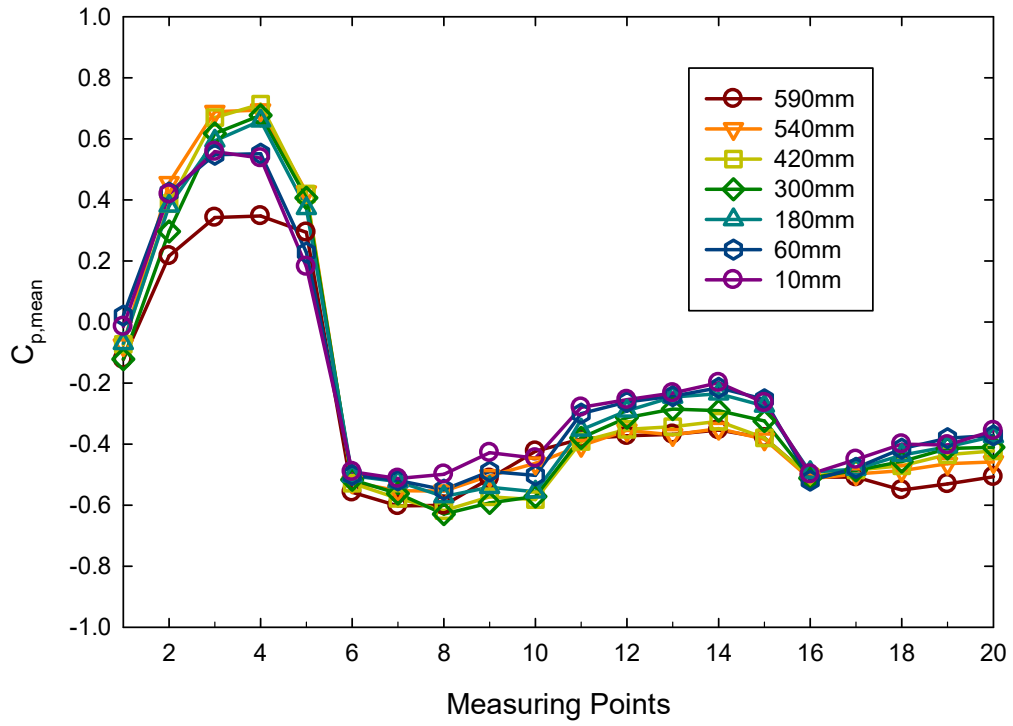

Fig. 5.4 $C_{p,\,mean}$ along perimeter-Sq-model (No blockage interference)

5.2.2. Interference Factor

The interference effects corresponding to different interference conditions on pressure coefficients (C_p) related to all measurement points are of composite nature and challenging to present for all. To clarify the intricacy and to scrutinize the interference effects on C_p in detail, interference factors (I.F.) for an average of $C_{p,mean}$ and $C_{p,rms}$ at each face are proposed as given by ***Khanduri et al.*** [18], to indicate the severity of interference effects on $C_{p,mean}$ and $C_{p,rms}$ as follows:

$$(\boldsymbol{MIF}) = \frac{C_{p,mean}\ with\ interfering\ building}{C_{p,mean}\ isolated\ building}$$

$$(\boldsymbol{RIF}) = \frac{C_{p,rms}\ with\ interfering\ building}{C_{p,rms}\ isolated\ building}$$

Where MIF and RIF are the interference factors for mean and RMS pressure coefficients, respectively.

Fig. 5.5 and 5.6, respectively, render the variation of MIF and RIF along the different faces of the principal building for all three interference conditions. From Fig. 5.5, the interference effects on mean pressure coefficients at all surfaces of square model are beneficial in full and half blockage interference conditions. The MIF values for area average of mean surface pressure are less than unity, which indicate the overall reduction in the mean pressure coefficients. The MIF values in no blockage condition are approximately equal to unity, which renders that there is no influence of the upstream interfering building on the mean surface pressure of the principal building.

Figure 5.6 show the RIF values for three interference conditions. It is quite evident from figure that the influence of the upstream building on the r.m.s pressure coefficients is not beneficial at front face in no blockage condition. The r.m.s pressure coefficients at front face have been increased slightly, the reason is the formation of disturbed and irregular vortices in the wake area of interfering building. The interference factor at side faces is always less than unity. Face C suffers very slight increase in $C_{p,rms}$ in no bocage condition. The upstream interfering building is always favorable to wind pressure of the principal building due to shielding, if present very near to the target building with full blockage condition.

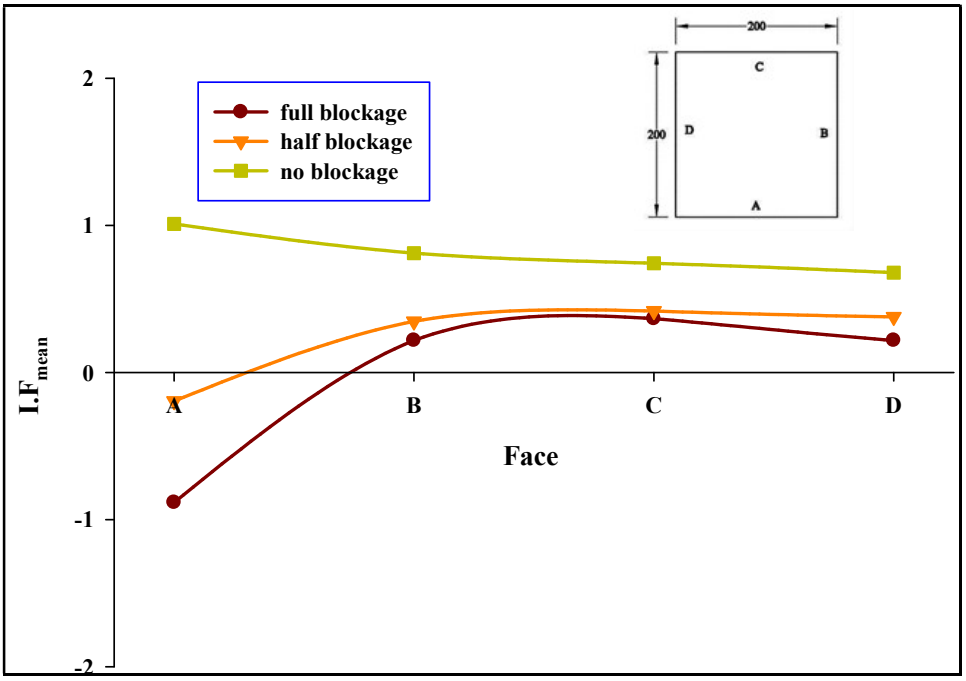

Fig. 5.5 MIF of area average values at faces-Sq- model

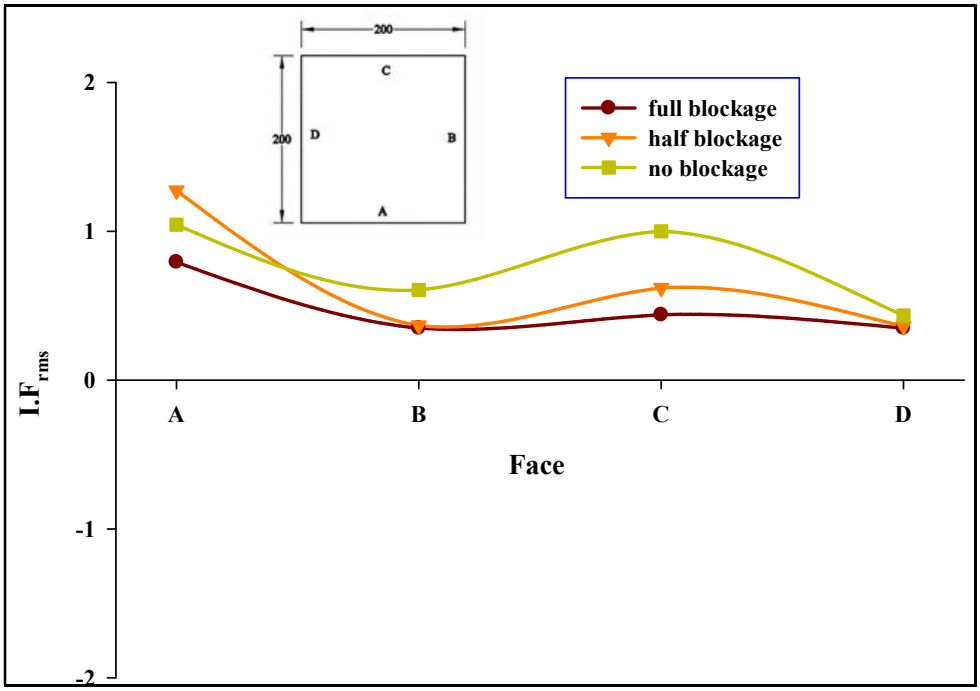

Fig. 5.6 RIF of area average values at faces- Sq model

The distribution of IFs for mean and r.m.s pressure coefficients is presented in the form of contours at different faces. In order to highlight the unfavorable positions related to interference effects at the surfaces, the lines of absolute IF ≥ 1 are retained in the contour plots. The contour plots of the faces having unfavorable locations are only presented here.

Fig. 5.7 shows the contour of MIFs on the faces of the square model for the three interference conditions. In the full blockage interference condition, only the front face has unfavorable locations. Most of the unfavorable locations are concentrate near bottom corners extended till the middle of the height. The complete half surface above the middle has favorable location as the absolute values of IF are less than unity. The negative values of IFs at all pressure points indicate the change in the nature of the pressure from positive to negative at all pressure points of the surface. The absolute maximum value of MIF in full blockage reaches up to 9.5 for the pressure points near the bottom corners. For the half blockage condition, the front face A and the side face B suffer the unfavorable locations. The unfavorable locations at the front face concentrate near the corners. The top and bottom corners toward the interfering buildings have negative IF values, whereas other side corners have positive IF values. The maximum absolute value of IF reaches up to 13 at the point near the bottom corner opposite to the interfering building. At face B, a very small portion near the windward edge shows the unfavorable location. The front face and both side faces have unfavorable locations for no blockage condition. The area on the opposite side to the interfering building on the front face has IF values more than unity. The side faces also have their unfavorable locations at bottom corners on the leeward side up to a very small height of 0.25H from the bottom.

The contour plot of RIF at critical surfaces is presented in the fig. 5.8 for the three conditions. Similar to MIF, only face A has unfavorable locations present near the corners. The variation between RIF values at different points is small, and the maximum value of RIF is less than 2. For half blockage condition, the front face A has an unfavorable location on the right side of the face. The RIF values increase from the middle to the right edge. The point at the middle height near the right edge has the maximum RIF value of 2.8. The face B has an unfavorable location in a very small area at the top windward corner. For the no blockage condition, all the four faces have unfavorable locations. The front face A and the leeward face C have RIF value more than unity at major areas.

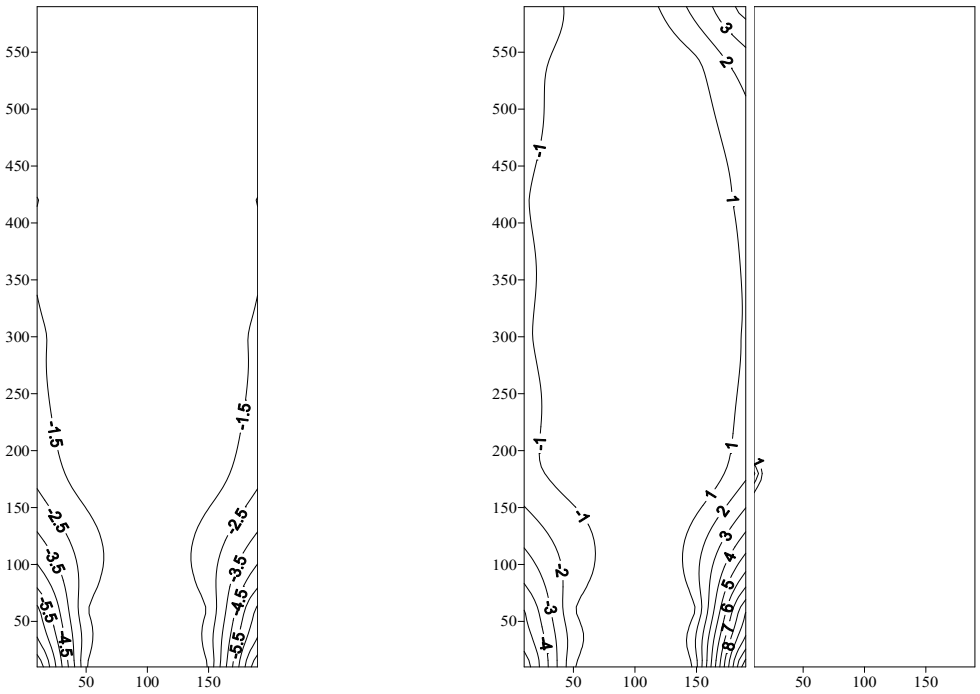

(a) Full blockage (Face A) (b) Half blockage (Face A, Face B)

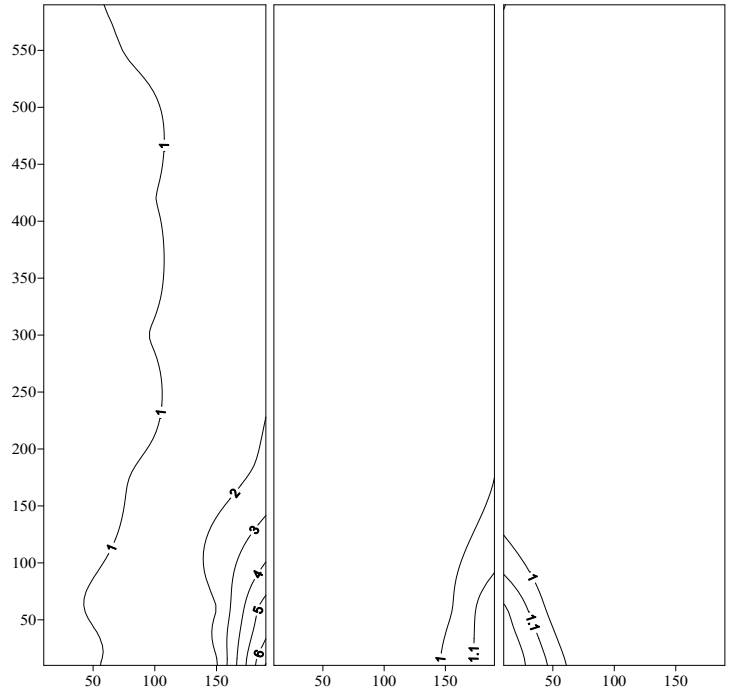

(c) No blockage (Face A, Face B, Face D)

Fig. 5.7 MIF (I.F ≥ 1) contour (a) Full (b) Half (c) No blockage- Sq model

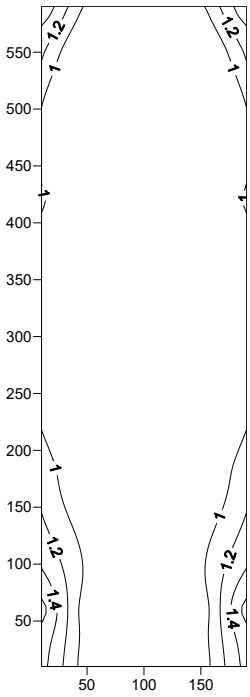

(a) Full blockage (Face A)

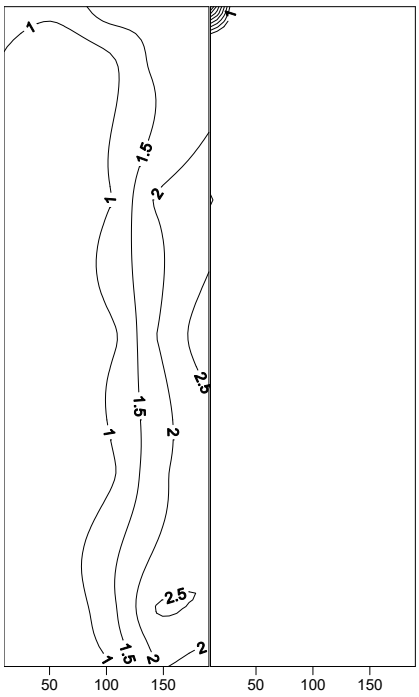

(b) Half blockage (Face A, Face B)

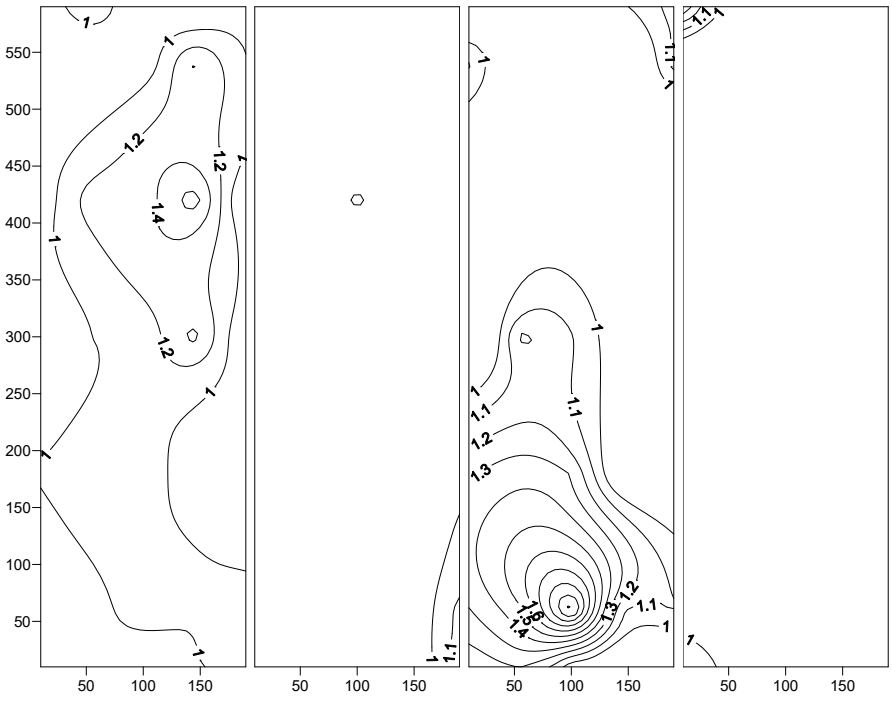

(c) No blockage (Face A, Face B, Face C, Face D)

Fig. 5.8 RIF (I.F ≥ 1) contour (a) Full (b) Half (c) No blockage- Sq model

5.3. PL-1 MODEL

5.3.1. Pressure Distribution

Pl-1 model is also tested in the wind tunnel for three interference conditions, as shown in Fig. 5.9. The distribution of $C_{p,mean}$ of PL-1 model corresponding to various interference conditions are presented in the Fig. 5.10 to 5.12. The distribution of $C_{p,mean}$ on all surfaces of the principal building in the presence of the interfering building, creating full blockage condition for the principal building is quite dissimilar from that of the isolated building. Pressure tends to increase with respect to height, like isolated building on the front face and reduces near the top edge. Strong interference effect is created on front faces because it immersed in the wake of interfering building, which causes suction on front face A2, unlike for isolated building and distribution of suction coefficient varies between -0.32 to -0.63. The high suction zone is located at a height between .75H to 0.85H. The absolute value is approximately 29% higher than those for isolated building. The mean suction coefficient for the wind-ward face (B1 and D3) at the side is significantly increased compared to an isolated building. The suction coefficient increased for windward side faces (A1 and A3) compared to the isolated building by 51%, corresponding to the average of the face; however suction decreases for leeward side faces (C1 and C3) with a small variation in suction coefficient between -0.21 to -0.24 on the surface. A considerable reduction (Approx. 65%) is noticed in suction on side faces (B2 and D2), and all leeward faces (B3, C1, C2, C3, and D1), and the percentage reduction is in the range of 55- 65 %. Suction coefficients on these side faces tend to decrease from windward to leeward edge, and maximum suction is at the middle height of the windward edge with $C_{p,mean}$. Distribution on windward face A2 and leeward face C2 is symmetric about the vertical centerline.

The interfering building creates unsymmetrical wind flow around the principal building in half blockage and thus creates different pressure distribution on the symmetric faces. The interference effect on all faces depends on the face position in the wake area and orientation concerning the flow of wind. Active shielding is created by interfering building. Unlike isolated and full blockage interference conditions, the distribution of pressure is not symmetrical about the vertical centerline on front face A2. Both sides are under the

opposite nature of pressure. The surfaces towards the interfering building, which come under the wake region of the interfering building, are under suction, whereas the opposite side has positive pressure. The high pressure zone is located near the right edge from bottom to top. Suction on the side face A1 at the center on the windward side increased, and the average $C_{p,mean}$ of the face is -0.47, which is 57% higher than isolated building. Front side face A3 has positive pressure, which was in suction for isolated as well as full blockage conditions. Wind ward face B1 at the side also experienced positive pressure, whereas face D3 is under increased suction compare to the isolated building and full blockage case. The effect of interference on all other faces is small, and the distribution of $C_{p,mean}$ is likely similar to that of isolated building case.

The distribution of $C_{p,mean}$ along the perimeter of the principal building for the no blockage interference condition is shown in Fig. 5.12. Interference effects for this location of interfering building are critical for faces in the left side of the centerline along the windward direction due to the fact that faces on this side are also affected by the wake generated due to the existence of the nearby building. Suction at the front side face A1 significantly increased and was maximum among isolated and all three interference conditions. The distribution of $C_{p,mean}$ varies from -0.68 to -0.86 with an average at the face is -0.76, which is 60% higher than half blockage condition. Pressure distribution on front face A2 is similar to that for half blockage interference condition. Maximum and face average values of $C_{p,mean}$ for front face D3 at the side toward the interfering building are also increased crucially as compared to isolated, and all other interference conditions and are -0.89 and -0.65, respectively. The face average value for face D3 is increased by 45% from half blockage condition. The interference effect on all other faces is favorable i.e. reduced.

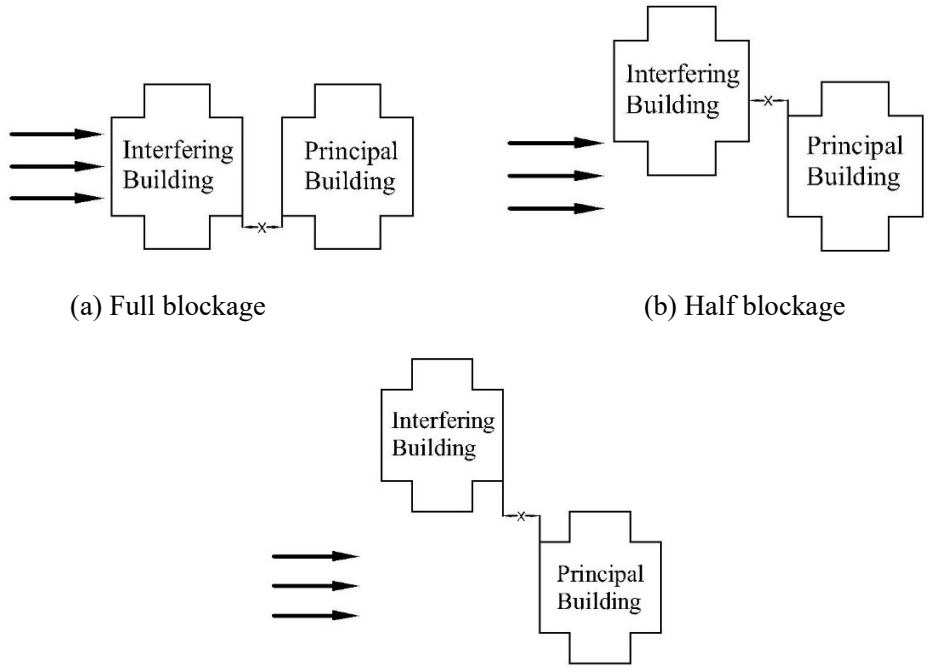

(a) Full blockage

(b) Half blockage

(c) No blockage

Fig. 5.9 Various interference conditions – PL-1 model

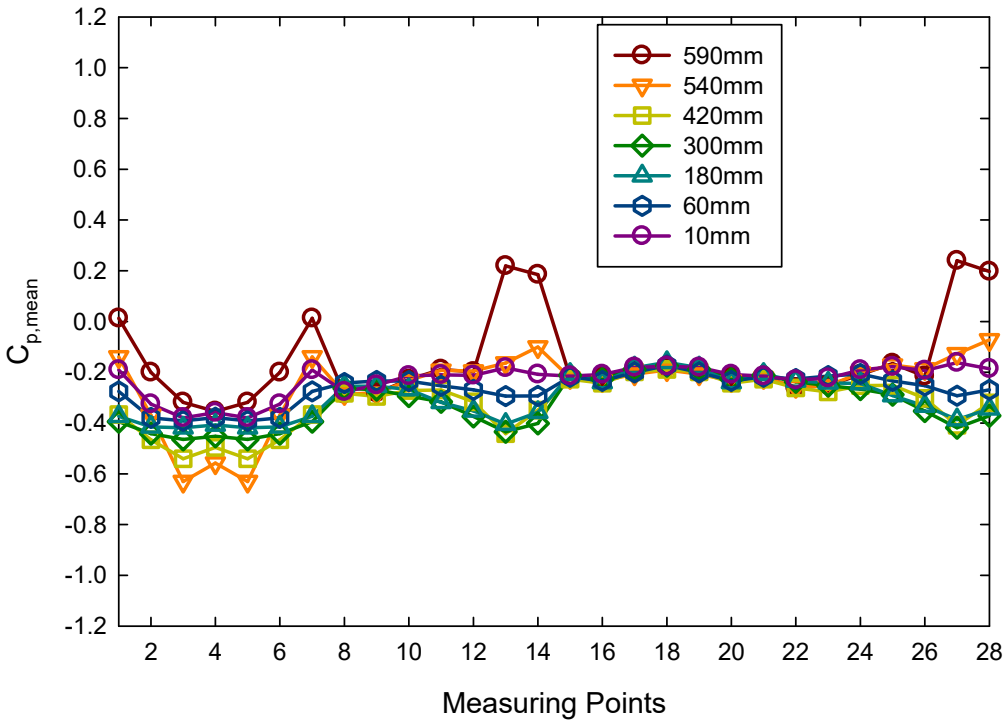

Fig. 5.10 $C_{p,\,mean}$ along perimeter-Pl-1-model (Full blockage interference)

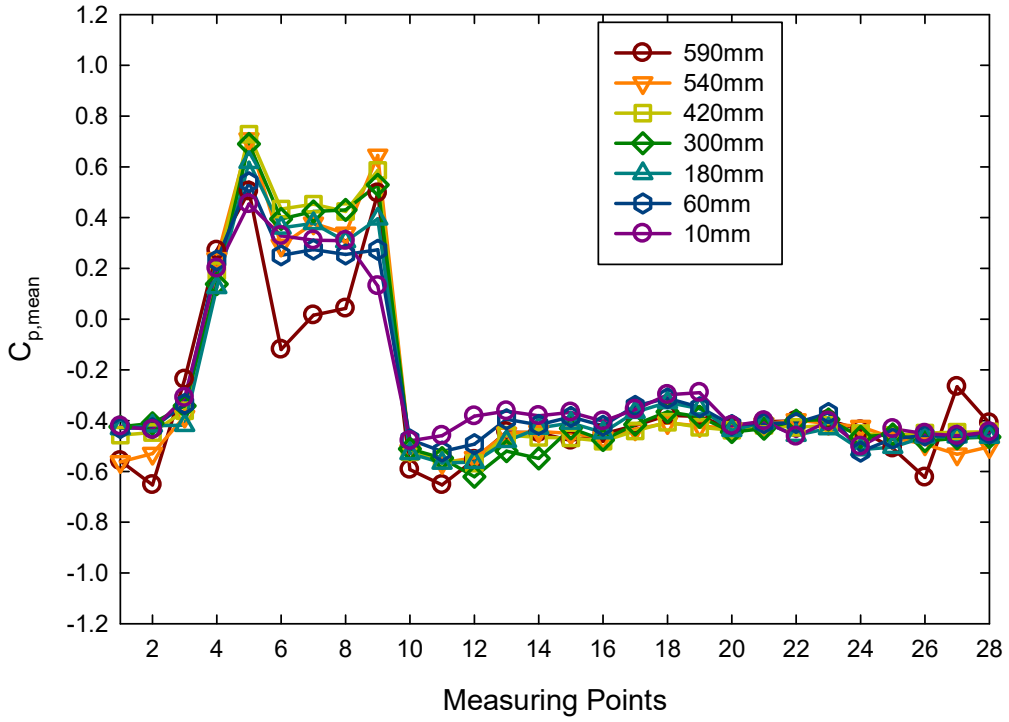

Fig. 5.11 $C_{p,\,mean}$ along perimeter-PL-1-model (Half blockage interference)

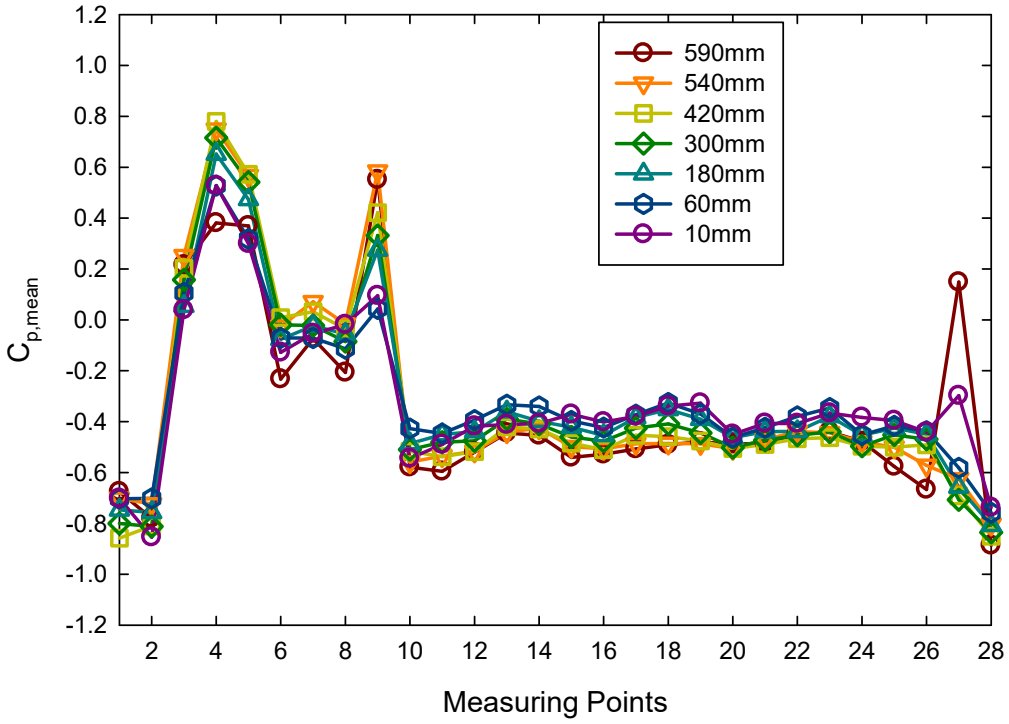

Fig. 5.12 $C_{p,\,mean}$ along perimeter-Pl-1-model (No blockage interference)

5.3.2. Interference Factor

The interference factors are calculated similar to that of square building model for mean and r.m.s wind pressure coefficients in the three interference conditions. Fig. 5.13 and 5.14 renders the variation of MIF and RIF along the different faces of the principal building starting from the front side face A1 to side front face D3 anticlockwise for all three interference conditions. From Fig. 5.13, interference effects are significant for face A1, B1, and D3 only. Interference effects for full blockage interference condition are critical at Face B1 and D3 only, for which MIF greater than 4. For half blockage condition, MIF is greater than 2, whereas for face B1, absolute MIF is greater than 7 with a negative sign, the significance of which is that the nature of pressure is changed due to interference. MIF for face D3 is greater than 9, which is maximum among all faces and signifies that effects of interference for full blockage condition are maximum for face D3, which is a side front face toward the interfering building and falls in the wake zone of interfering building.

Interference effects for no blockage condition are more severe for D3 among three critical faces. MIF for face D3 is greater than 13, which shows a large interference-effect. Interference effect on this face is most severe among all faces and all interference conditions, which can be explained by the fact that this face immerged in the wake region of interfering building corresponding to no blockage condition and the velocity of flow increased after separating from the upwind interfering building due to which suction is increased by a significant amount and results in a high value of interference factor. Form Fig. 5.14, the maximum value of RIF for surface average $C_{p,rms}$ is 1.03, which shows that the fluctuating component of pressure coefficient is not much affected due to the existence of an interfering building at three positions. Average of surface $C_{p,rms}$ for all surfaces are reduced due to the presence of the interfering building, but peak values at the top level for some surfaces have increased, which may be due to vortex shedding for half blockage and no blockage conditions. From Fig. 5.13, it is clear that interference effects are significant for three critical faces, namely A1, B1 and D3 for which I.Fs are very high, hence the distribution of I.Fs herein only deals with the results for these three faces of the principal building.

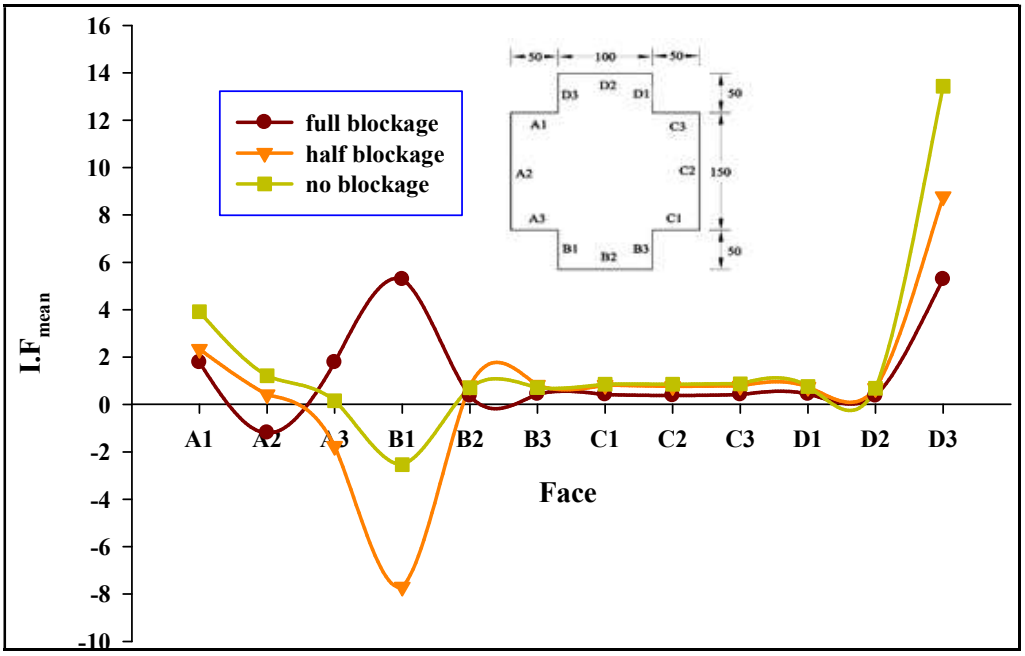

Fig. 5.13 MIF of area average values at faces-Pl -1 model

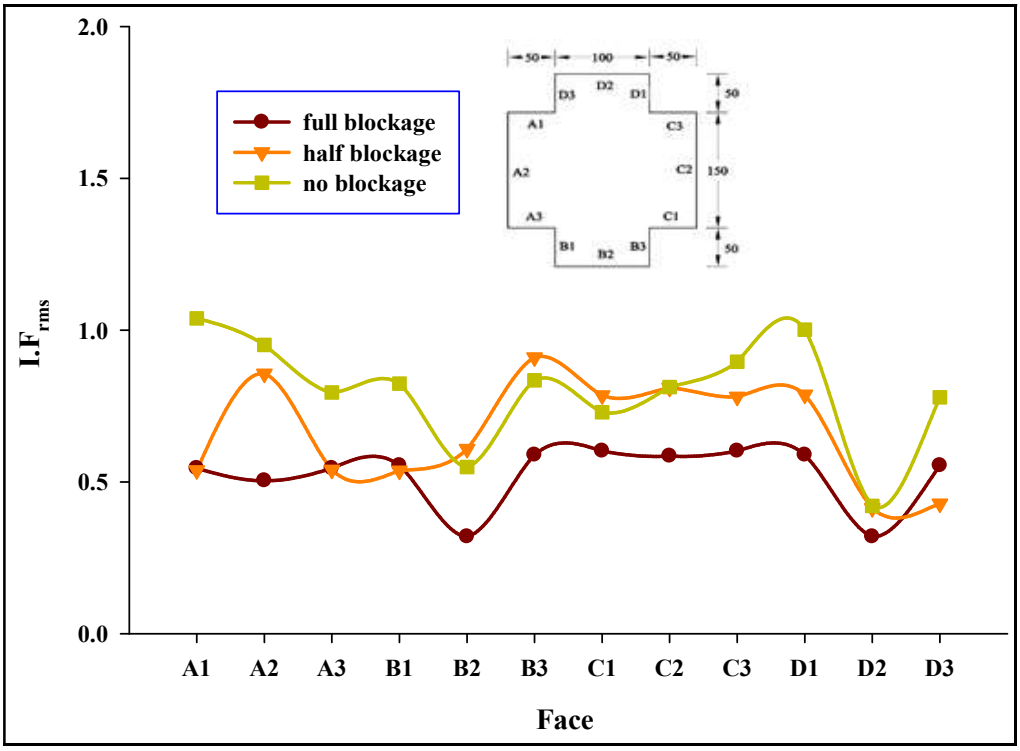

Fig. 5.14 RIF of area average values at faces-Pl -1 model

Fig. 5.15 represent the contours of *MIFs* on critical faces for three interference conditions, created due to different relative positions of the interfering building. In order to highlight the unfavorable positions of measuring points on the face, only those absolute I.F ≥ 1 are retained. For full blockage interference condition, on face A1 I.Fs distributed evenly on the surface from 0.51 to 2.31. Distribution on face B1 and D3 are similar due to symmetry in position and wind flow around. Outer edges are significantly affected by interference, and from Fig. 5.15(a) it is quite clear that positions above the middle of the inner edge are favorable, and regions of unfavorable locations concentrate on outer edges at 1/3 height from the bottom. MIF for half blockage condition on face A1 distributed on bottom 2/3 height with small variation, whereas variations at top 1/3 height are significant, and MIF varies from 1.67 to 4.27. For face B1 and D3 distribution is similar, but values are slightly different. MIF tends to increase near outer edges. The positions of favorable and unfavorable regions are similar as in the case of full blockage condition. For no blockage interference condition, the distribution of MIFs is quite different from previous conditions. A significantly large interference effect is noticed at face A1and D3. MIF on face A1 is distributed evenly throughout the face, and varies from 2.0 to 5.33, whereas at face D3 MIF varies between a large range from 0.39 to 11.83, and regions of unfavorable positions concentrate on the bottom half. Unfavorable measuring points at face B1 concentrates on the outer edge between a quarter to the half-height.

The distribution of RIFs is shown in Fig. 5.16 for critical faces and unfavorable positions are highlighted by retaining IF ≥ 1 only at surfaces. From the figure, it is evident that for full blockage regions of unfavorable are concentrate at the corner part of the building surfaces. The maximum value is 1.13. For half blockage distribution at central surface A2 is quite different than other because the boundary of the flow field at the back of interfering building lies at the center of this face. The maximum value reach up to 2.90 at face A1. For no blockage interfering condition, windward faces A1 and A2 and leeward face D1 are the most critical surfaces for which larger area is covered by unfavorable positions. The peak value of RIF is approximately equal to 2 at face A1.

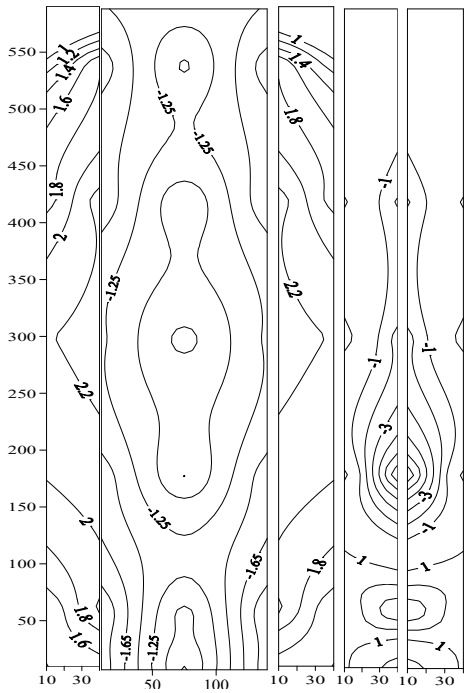

(a) Full blockage (A1, A2, A3, B1, D3)

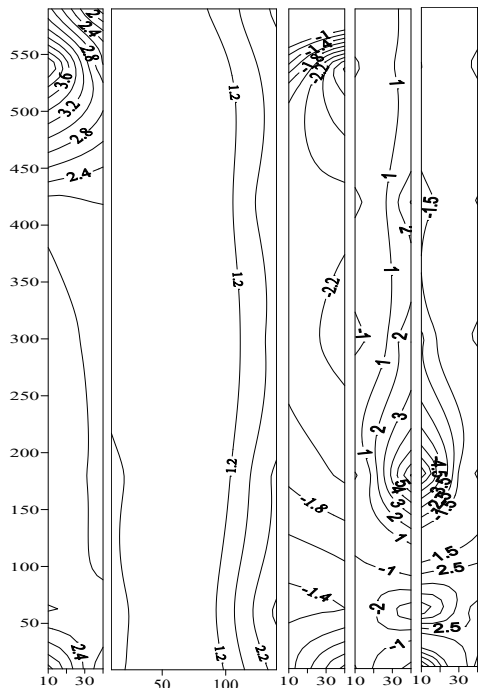

(b) Half blockage (A1, A2, A3, B1, D3)

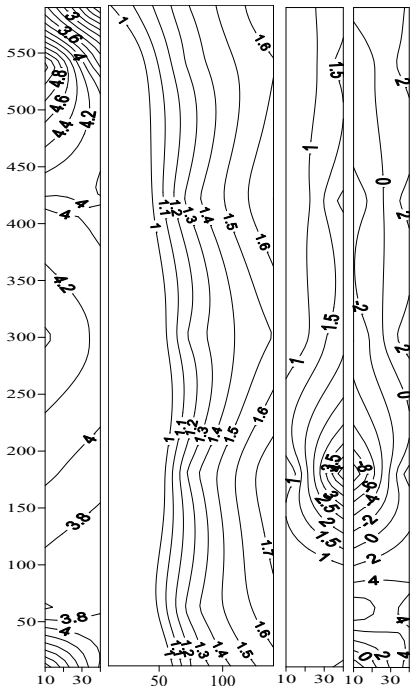

(c) No blockage (A1, A2, B1, D3)

Fig. 5.15 MIF (I.F ≥ 1) contour (a) Full (b) Half (c) No blockage- Pl-1 model

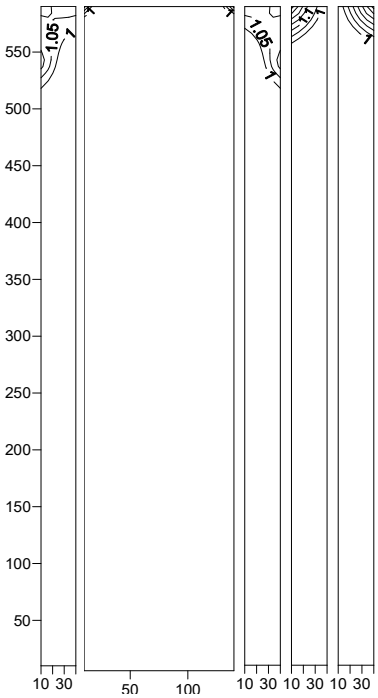

(a) Full blockage (A1, A2, A3, B1, D3)

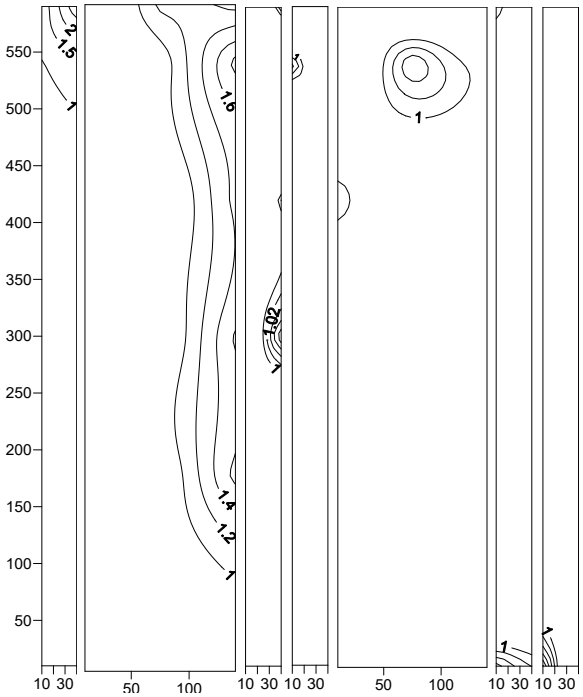

(b) Half blockage (A1, A2, B3, C1,C2, C3, D1)

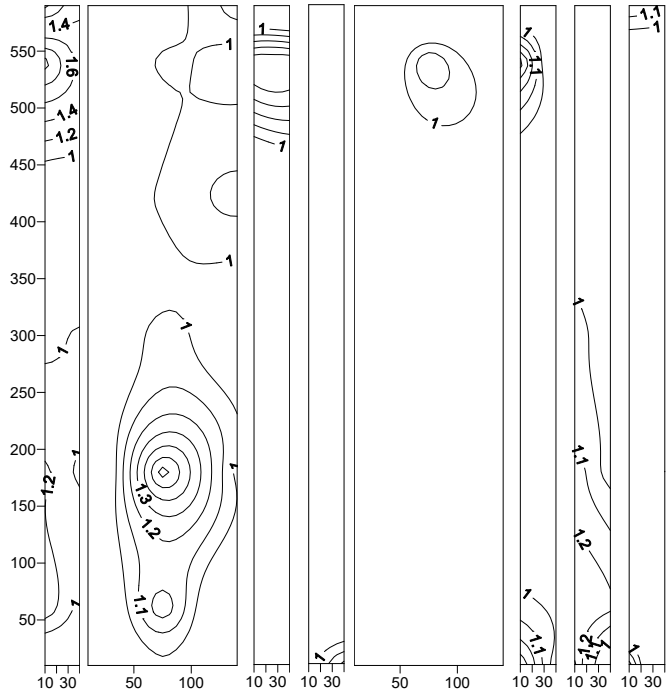

(c) No blockage (A1, A2, A3, B1, C2, C3, D1, D3)

Fig. 5.16 RIF (I.F ≥ 1) contour (a) Full (b) Half (c) No blockage- Pl-1 model

5.4. PL-2 MODEL

5.4.1. Pressure Distribution

The three interference positions of the upstream interfering building are shown in Fig. 5.17. The distribution of $C_{p,mean}$ along the perimeter of PL-2 model corresponding to various interference conditions are presented in the Fig. 5.18 to 5.20. From the Fig. 5.18, the pressure distribution at surfaces on windward side is found to be critically affected by the upstream interfering building, due to which wind pressure changes from positive to negative. It is evident from Figure that the peak negative pressure at windward side is increased than those on the Pl-1 model in similar flow conditions. Shielding effects at surfaces on windward side are clearly visible from pressure distribution. The intensity of negative pressure at other wall on side and leeward is also likely to be decreased than those on isolated building.

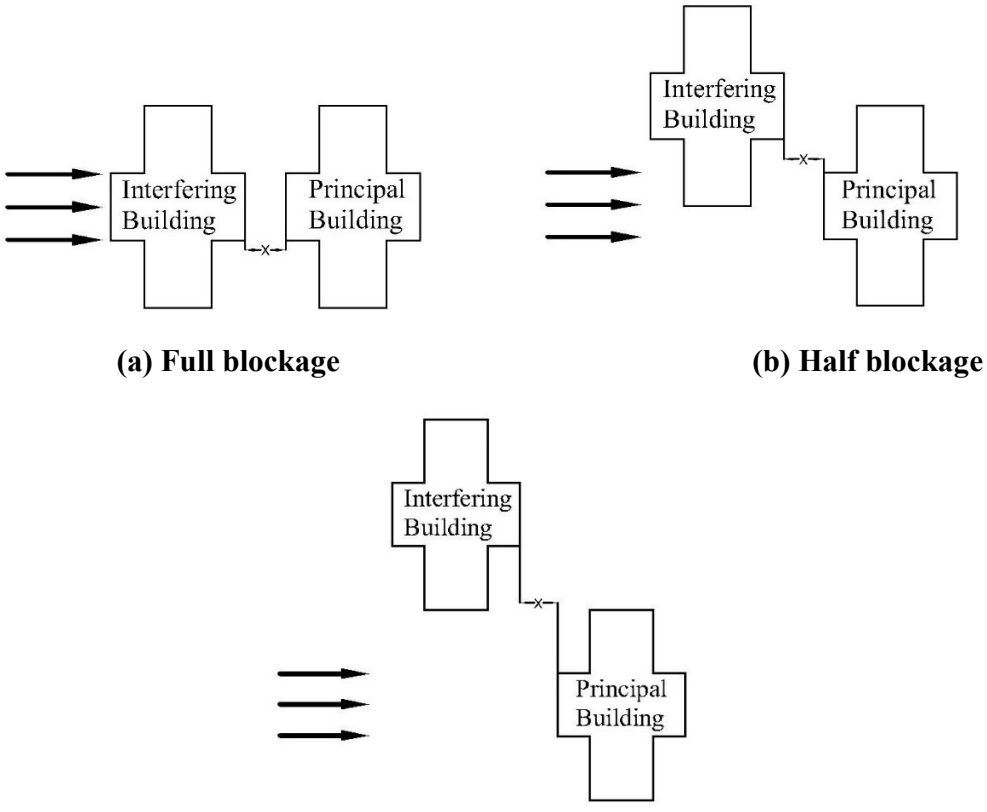

(a) Full blockage **(b) Half blockage**

(c) No blockage

Fig. 5.17 Various interference conditions – PL-2 model

In the half blockage interference condition, the shielding effects are more severe at half vertical area towards the interfering building of faces on windward side. The positive pressure at some windward faces toward the interfering building changes from positive to negative. The windward face at side away from the interfering building suffers the maximum positive pressure. The values of positive and negative pressure coefficients are increased from full blockage but still less than those in isolated case. In no blockage, the pressure points on the walls toward the interfering building are only affected by the upstream building, where the shielding is favorable. The distribution of mean pressure coefficients is almost similar to that of in isolated building case.

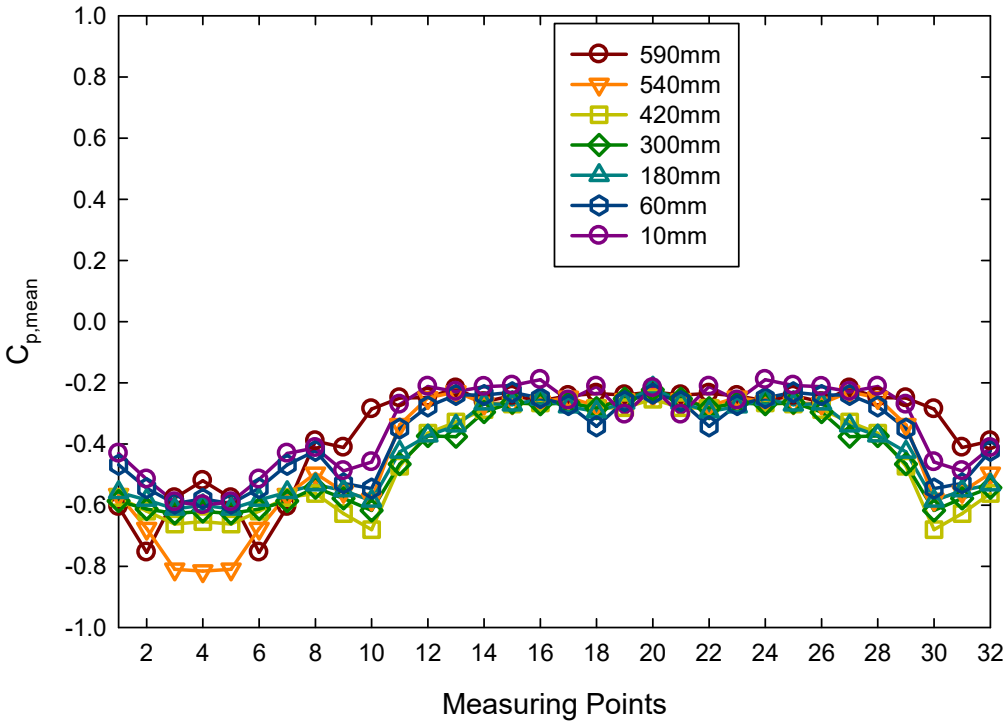

Fig. 5.18 $C_{p,\,mean}$ along perimeter-Pl-2-model (Full blockage interference)

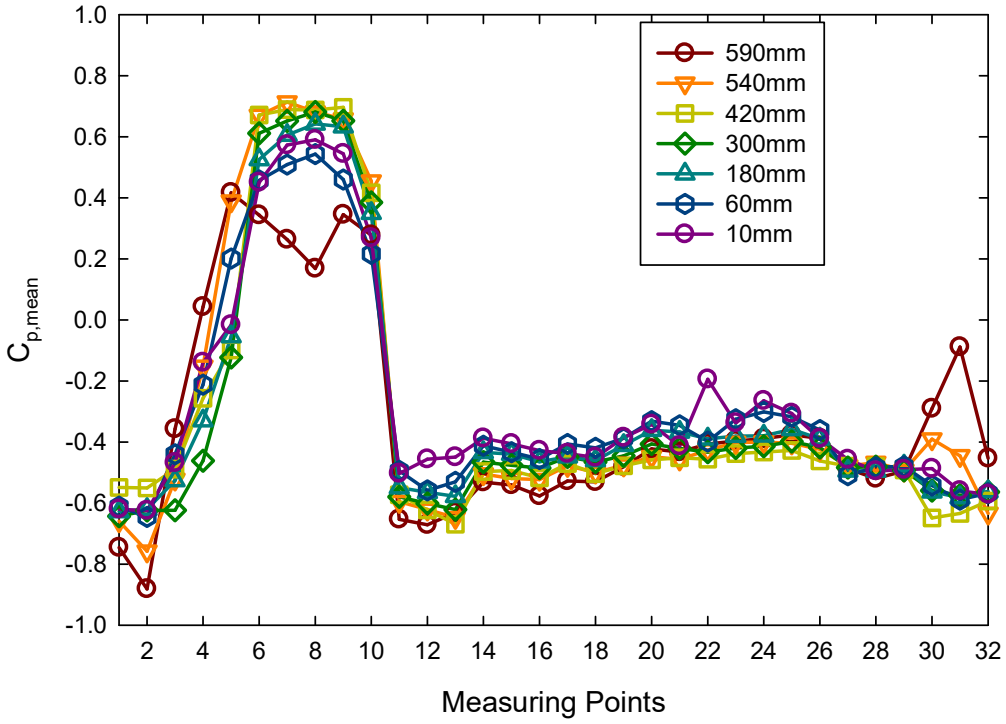

Fig. 5.19 $C_{p,\,mean}$ along perimeter-Pl-2-model (Half blockage interference)

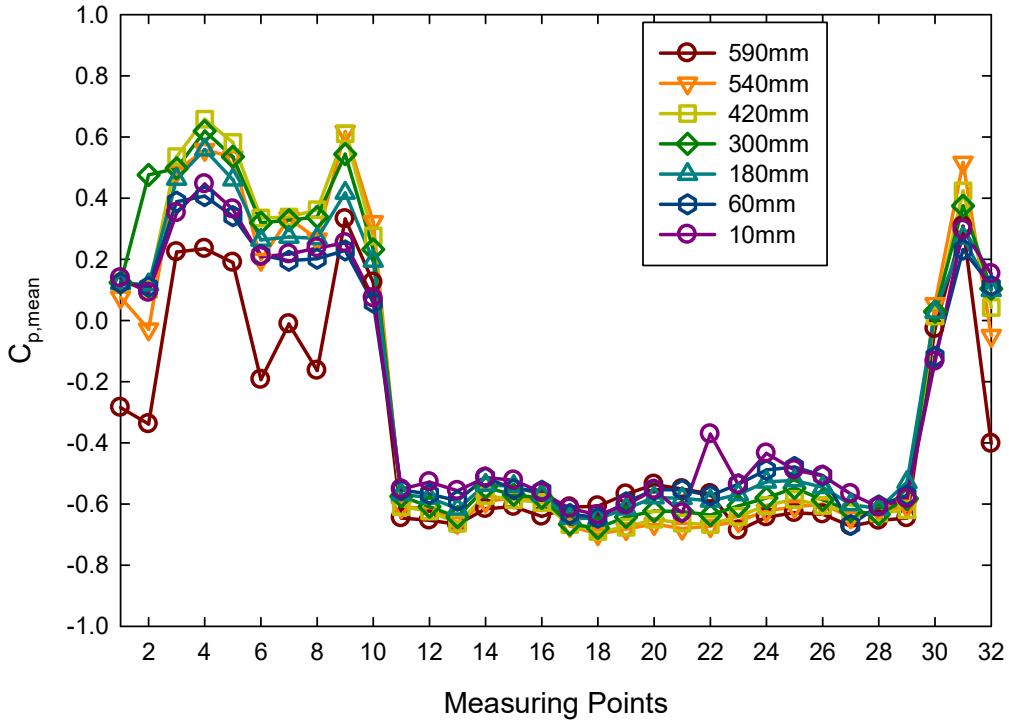

Fig. 5.20 $C_{p,\,mean}$ along perimeter-Pl-2-model (No blockage interference)

5.4.2. Interference Factor

The variation of interference factors for area average of mean and r.m.s pressure coefficients at various surfaces of the principal building is shown in the Fig. 5.21 and 5.22, respectively. The interference effects in full and half blockage are significant only at the surfaces on the windward side. The negative values of MIF at these faces in full blockage condition indicate the change in pressure from positive to negative due to the shielding. The maximum absolute value of MIF equal to 1.57 is observed at face A1. All the faces at side and at the leeward have MIF values less than unity, which show that shielding is favorable at these faces in full blockage. The presence of upstream building at half blockage position, turn the pressure from positive to negative at faces A1 and D3 which are under the wake of upstream interfering building. The absolute value of MIF is maximum at face A1 similar to the full blockage but higher. In the no blockage, all the faces at leeward side have MIF value larger than unity. The interference effects for all other faces at windward and at side are favorable.

The RIF distribution along the faces of principal building is presented in the Fig. 5.22. It is evident from the figure that the interference effects on the r.m.s pressure coefficients are favorable at all faces in the full blockage and no blockage. The RIF in full blockage and no blockage have their values less than 0.5 at all faces, which show that the $C_{p,rms}$ value at all the faces reduced to almost half of the values in isolated case. The higher values of RIF at central windward face A2 and at faces on windward side away from the upstream building indicate the increased turbulence level. The maximum value 1.25 of RIF is found to be for face A2.

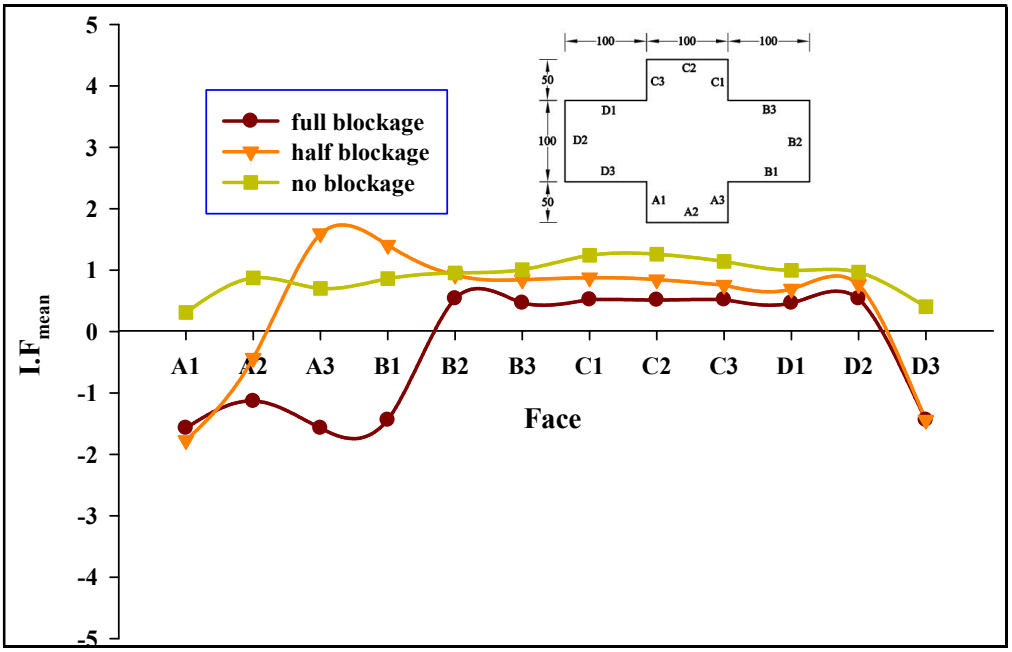

Fig. 5.21 MIF of area average values at faces-Pl -2 model

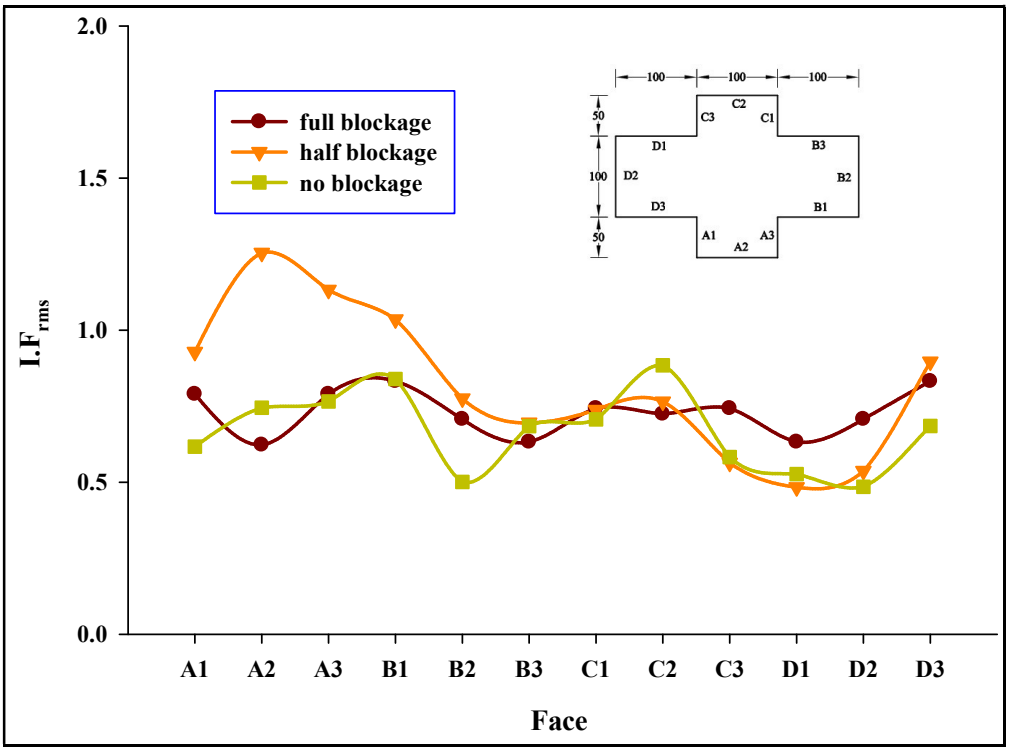

Fig. 5.22 RIF of area average values at faces-Pl -2 model

The contour plots of the IF greater than unity at various critical faces are shown in Fig. 5.23 for mean pressure. In the full blockage, the windward faces have unfavorable locations similar to that of Pl-1 model for MIF. The MIF value greater than unity concentrate at the top area above 0.9H of face A1. The MIF have their maximum value near top edge. Face A2 have negative values and the unfavorable location distributed evenly at full surface. Face B1 and D3 have symmetric distribution and have their unfavorable locations mostly at outer half area vertically. The interference effects increases from center vertical line to the outer edges of these faces. In half blockage, the again the faces at windward side suffers the unfavorable interference effects. Face A1 have both positive and negative values of MIF. The positive MIF concentrate at the area above 0.9H and below this negative value indicate the change of pressure nature. The peak absolute value of MIF have positive near top edge and reach up to 13. The face A2 have very small unfavorable area near the vertical edge towards the upstream building. All the other face at windward side have their unfavorable locations distributed at full surface. All the faces at leeward side have larger unfavorable area in no blockage. Although, all the surfaces have some unfavorable locations, but they have been distributes on a very small area near the corners.

The distribution of RIF greater than unity at various critical faces of the principal building is shown in Fig. 5.24 for r.m.s pressures coefficients. Most of the critical face have very small unfavorable locations. Face B3 and D1 on windward side and the side face B2 and D2 have larger critical area near the vertical edges. The distribution of RIF in half blockage condition is quite different from the previous one. The critical locations on the faces A2, A3 and B1 have been extended throughout the surface area. The interference effects are likely to be increased from the left edge near the upstream building to the opposite vertical edge of face A2. The RIF distribution is complex at face A3 and B1 which indicate the unstable flow at these faces. In no blockage condition, the leeward face suffers the unfavorable interference effects. The regions of unfavorable locations at leeward face C2 concentrates at the bottom part up to a height of H/3.

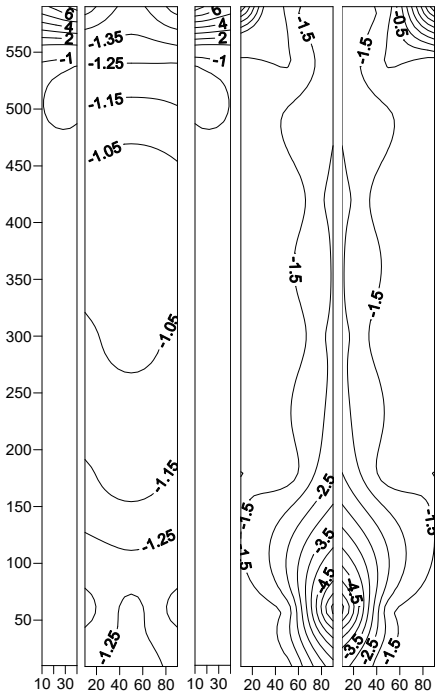

(a) Full blockage (A1, A2,A3, B1, D3)

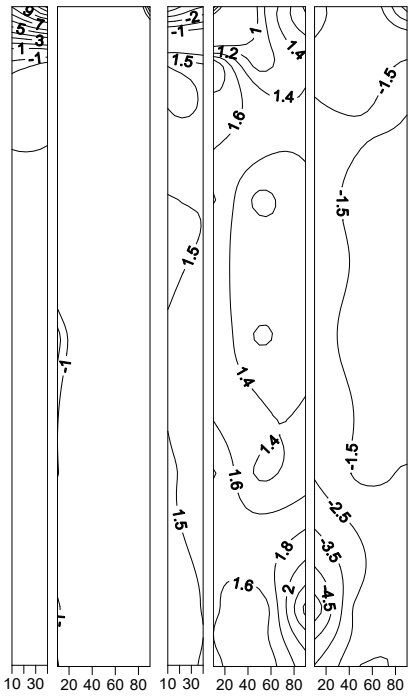

(b) Half blockage (A1, A2,A3, B1, D3)

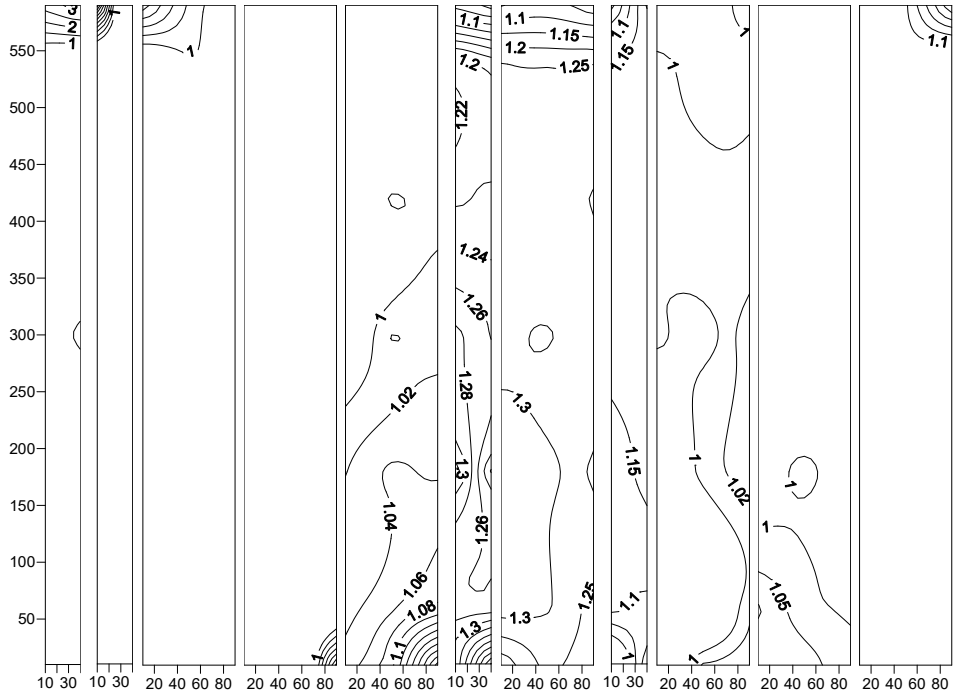

(c) Half blockage (A1,A3, B1, B2, B3, C1, C2, C3, D1, D2, D3)

Fig. 5.23 MIF (I.F ≥ 1) contour (a) Full (b) Half (c) No blockage- Pl-2 model

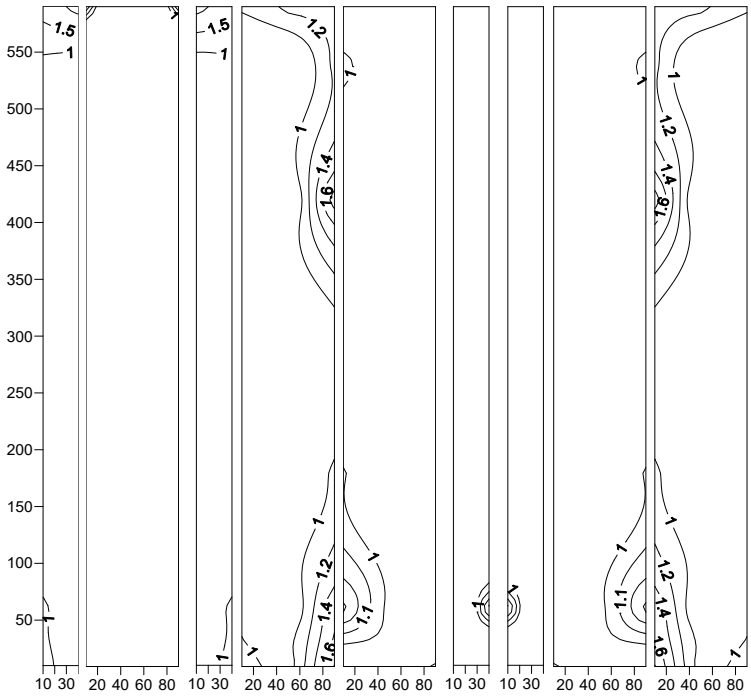

(a) Full blockage (A1, A2,A3, B1, B2, C1, C3, D2, D3)

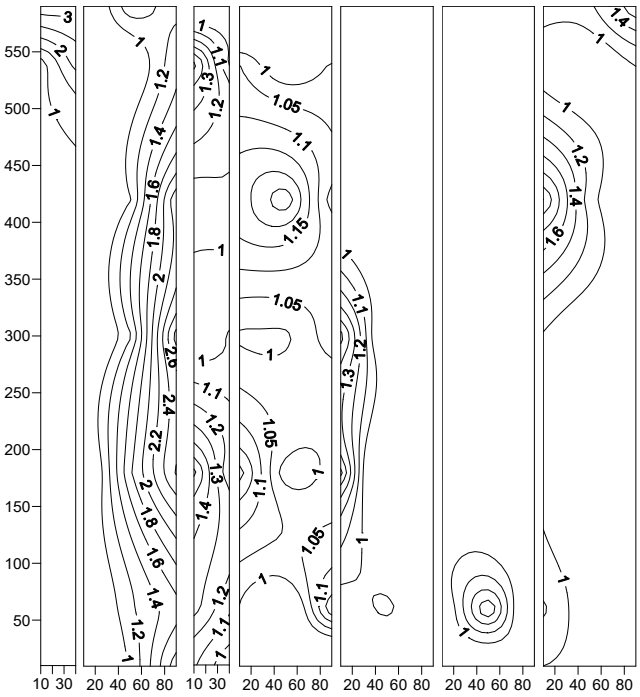

(b) Half blockage (A1, A2,A3, B1, B2, C2, D3)

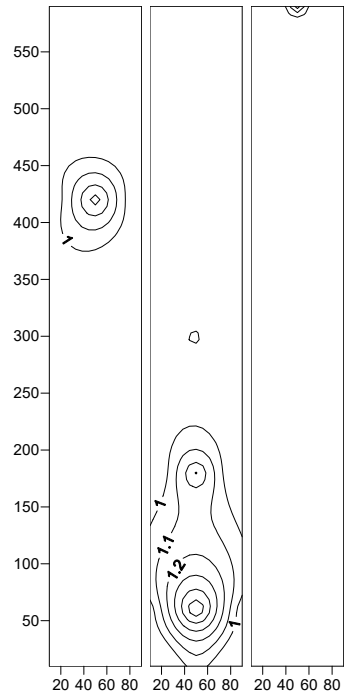

(c) No blockage (B1, C2, D3)

Fig. 5.24 RIF (I.F ≥ 1) contour (a) Full (b) Half (c) No blockage- Pl-2 model

5.5. H-MODEL

5.5.1. pressure distribution

It's a known fact that an interfering building might cause a very complex change in pressure distribution on different faces of the principal building. The three interference positions of interfering are shown in Fig. 5.25. The distribution of $C_{p,mean}$ along the perimeter of H-plan shape model for the three blockage conditions are shown in Fig. 5.26 to 5.28, respectively. For interference full blockage condition front face A experience suction and distribution is symmetric about the vertical centerline, whereas for other blockage conditions symmetry is lost, and higher variation of mean pressure coefficients is noticed. The mean suction coefficient variation is from -0.25 to -0.53 for the H-plan model. The absolute peak value of mean pressure coefficients is decreased significantly. The suction on other face at side and at leeward have also been reduced. A considerable variation of mean pressure coefficients between different pressure measurement points at face for half blockage and no blockage conditions is observed. In half blockage, the left half part to the vertical central line is immersed in the wake, and thus pressure is negative at this side and positive at other side of central line. The variation between the pressure coefficients at different pressure points along the perimeter at a particular height level is higher compare to that of other blockage conditions. At half blockage condition, the variation is in the range of -0.62 to 0.51 respectively, whereas for no blockage condition, the variation is in the range of -0.36 to 0.70. The distribution on no blockage is very similar to that of isolated conditions but the suction intensity at side and leeward faces is increased slightly.

5.5.2. Interference factor

The interference factor for mean and r.m.s pressure coefficients have been calculated and presented as MIF and RIF similar to other building models. The distribution of MIF and RIF along the faces of is shown in Fig. 5.29 and 5.30 respectively. In full blockage, the MIF at all faces is less than unity which represent the beneficial effects of interference through shielding by upstream building. The interference effects are also beneficial in half blockage at all other faces but face A suffers the some unfavorable effects.

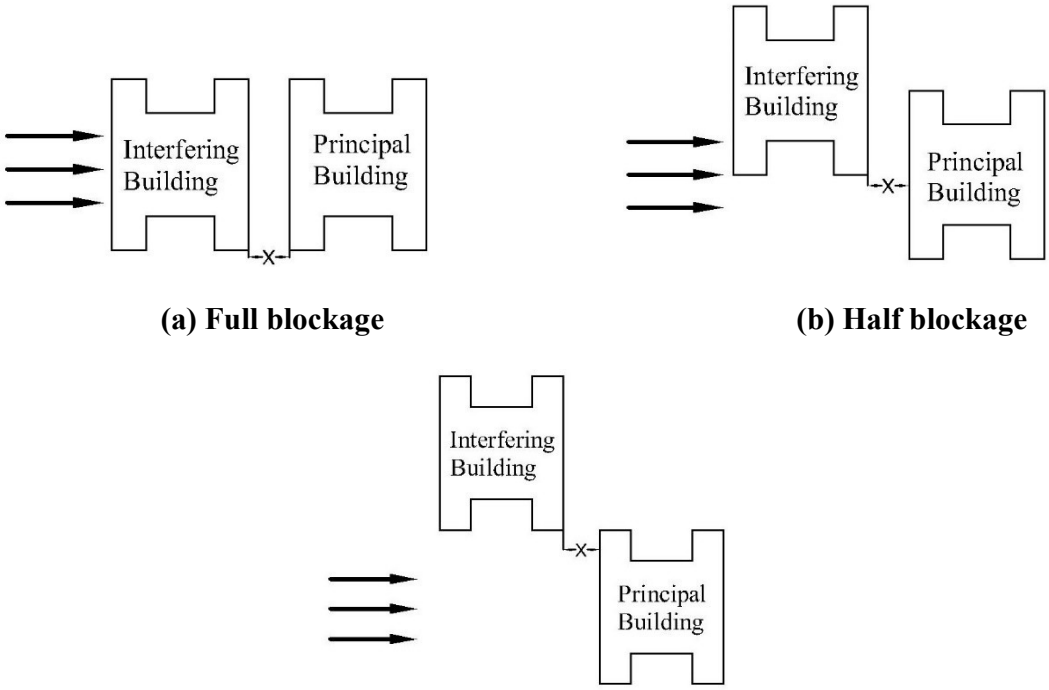

(a) Full blockage **(b) Half blockage**

(b) Half blockage

Fig. 5.25 Various interference conditions – H- model

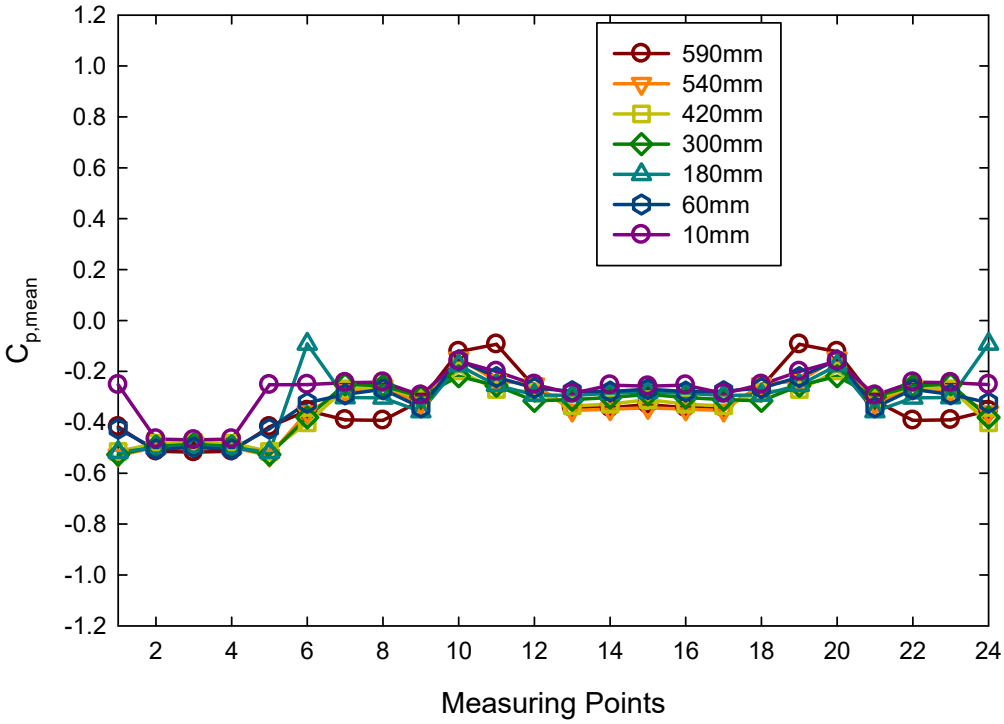

Fig. 5.26 $C_{p,\,mean}$ along perimeter-H-model (Full blockage interference)

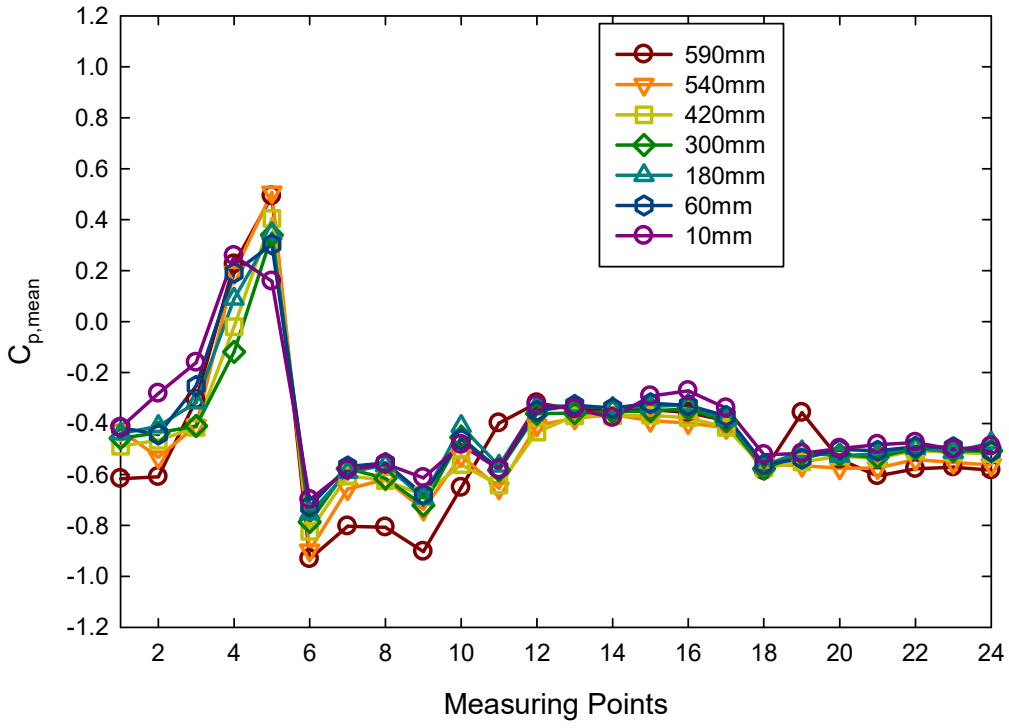

Fig. 5.27 $C_{p,\,mean}$ along perimeter-H-model (Half blockage interference)

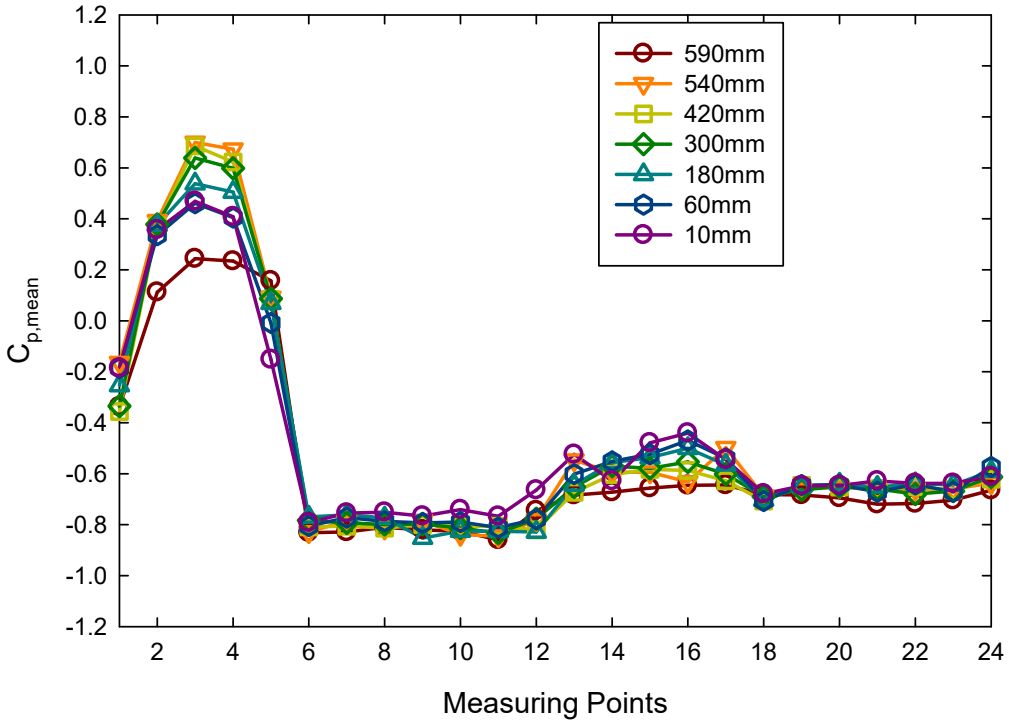

Fig. 5.28 $C_{p,\,mean}$ along perimeter-H-model (No blockage interference)

In no blockage, as upstream building is present at oblique position, flow is not blocked and it cause unfavorable effects due to disturbed vortices. The RIF values of all the faces in the three interference conditions are less than unity. The face A slightly have some increased value of r.m.s pressure coefficients due to interference in half blockage.

The contour plots of MIF and RIF greater than unity for critical faces is shown in Fig. 5.31 and Fig. 5.32 respectively. in full blockage, only front face A have unfavorable locations near the outer edges. The interference is likely to be increased near as we reach near the corners at bottom. In half blockage condition, only front face have significant unfavorable interference effects near the left edge facing the upstream building concentrated at bottom corner. In no blockage, all the faces show the unfavorable locations but the intensity of interference effects is very less. Front face have only very small locations near to the bottom corners. All the other faces have critical locations extended at full face with even distribution of MIF but the larger face have very complex distribution of MIF contours. The MIF is concentrated at bottom of small side faces toward the upstream interfering building.

From Fig. 5.32, The contour lines of RIF ≥ 1 concentrated very near to the edges at bottom up to height level of H/3 at front face in full blockage. In half blockage, the unfavorable location are found to be only on front face, which are concentrated on the half area to the right side of central vertical line with maximum intensity at the middle height. The interference effects are not much significant in case no blockage condition. The front face A have a very small zone of unfavorable effects at top central part.

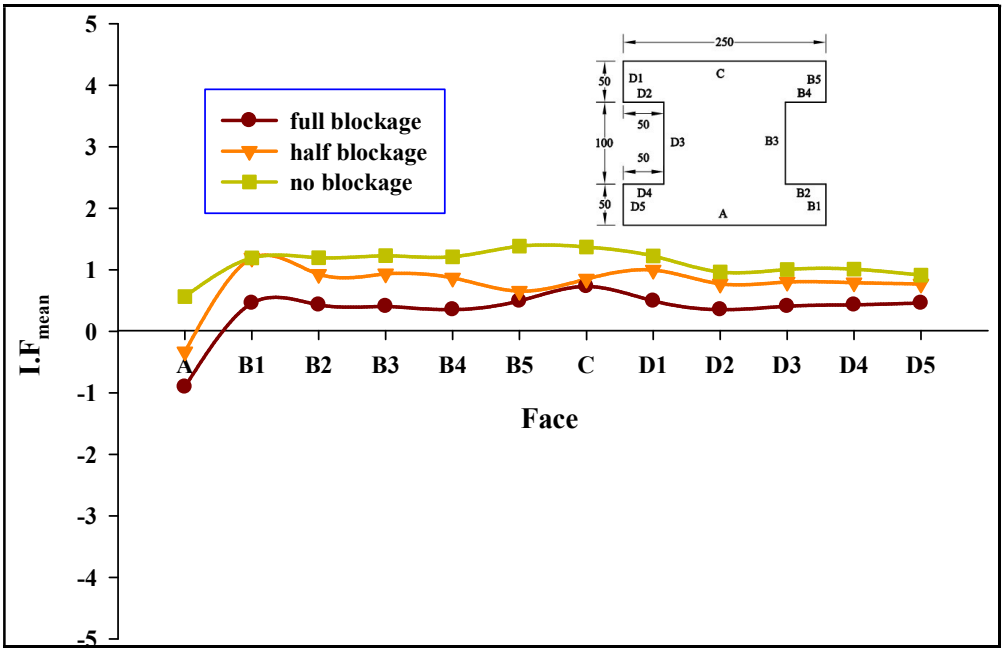

Fig. 5.29 MIF of area average values at faces of H-model

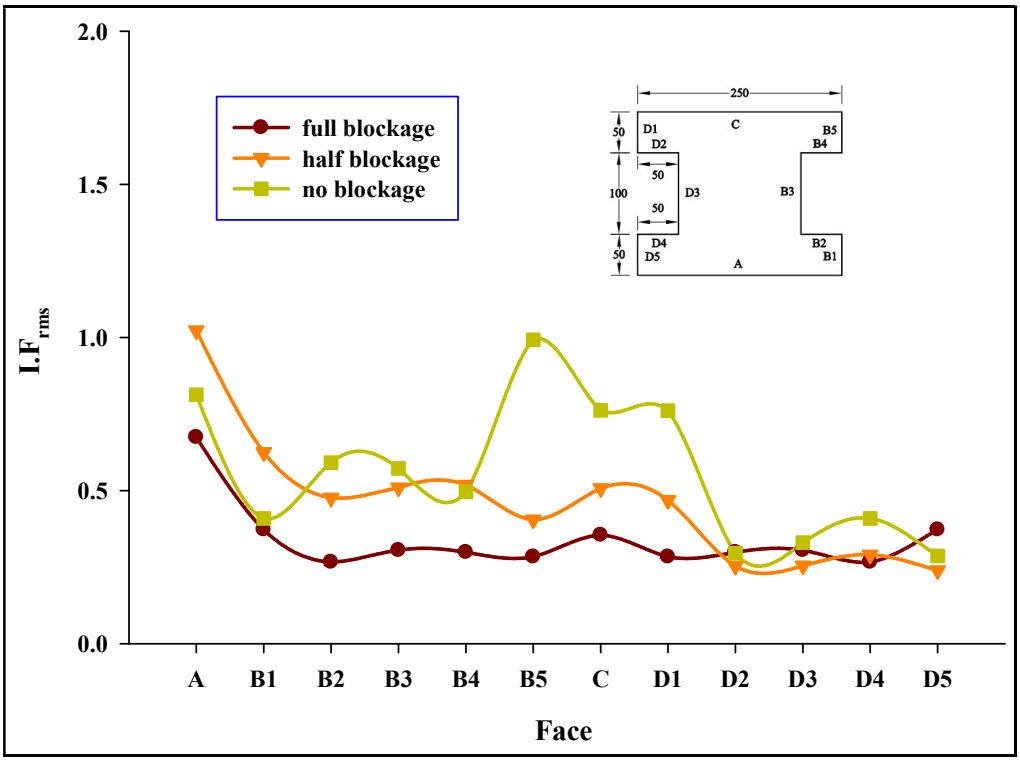

Fig. 5.30 RIF of area average values at faces of H- model

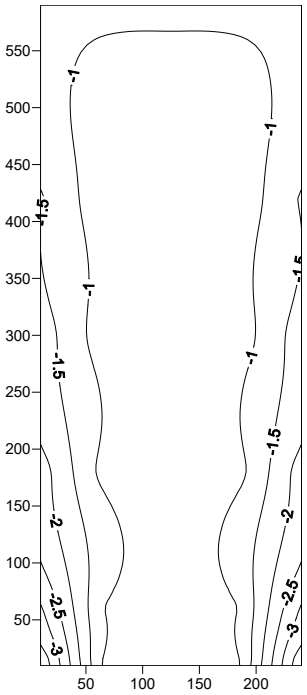

(a) Full blockage (Face A)

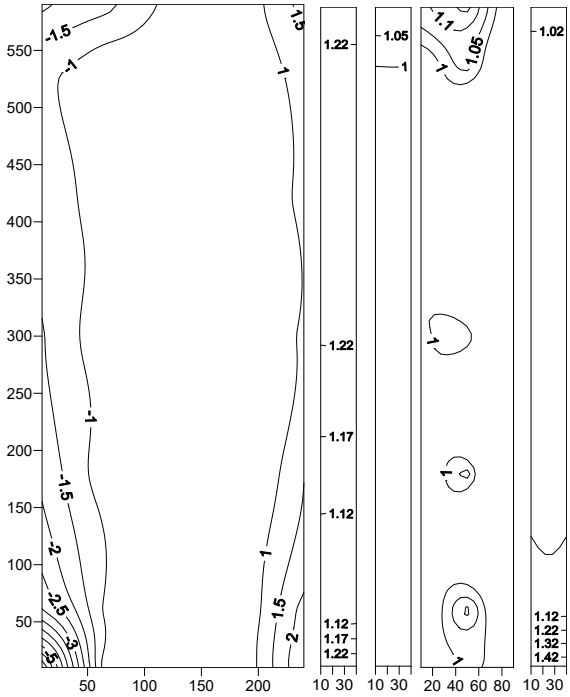

(b) Half blockage (Face A, B1, B2, B3, D1)

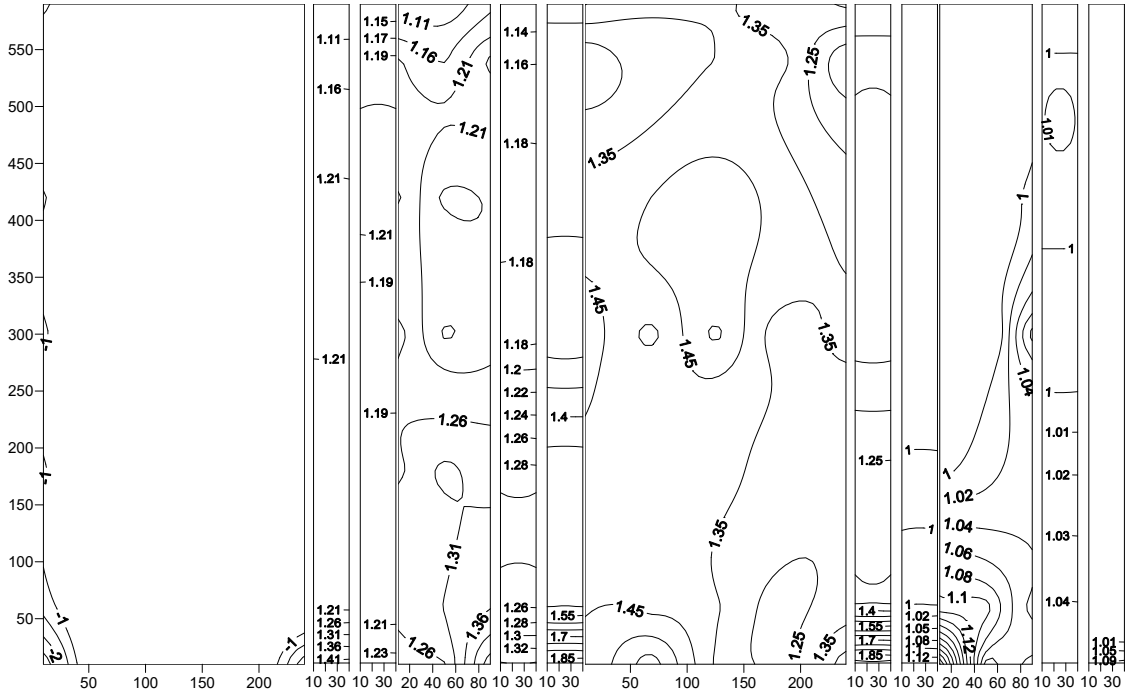

(c) No blockage (Face A, B1, B2, B3,B4,B5,C D1, D2,D3,D4,D5)

Fig. 5.31 MIF (I.F ≥ 1) contour (a) Full (b) Half (c) No blockage- H- model

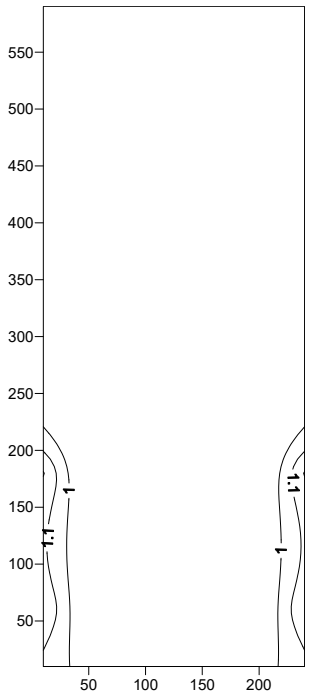

(a) Full blockage (Face A)

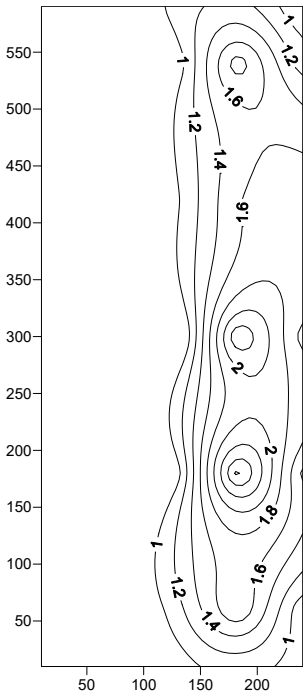

(b) Half blockage (Face A)

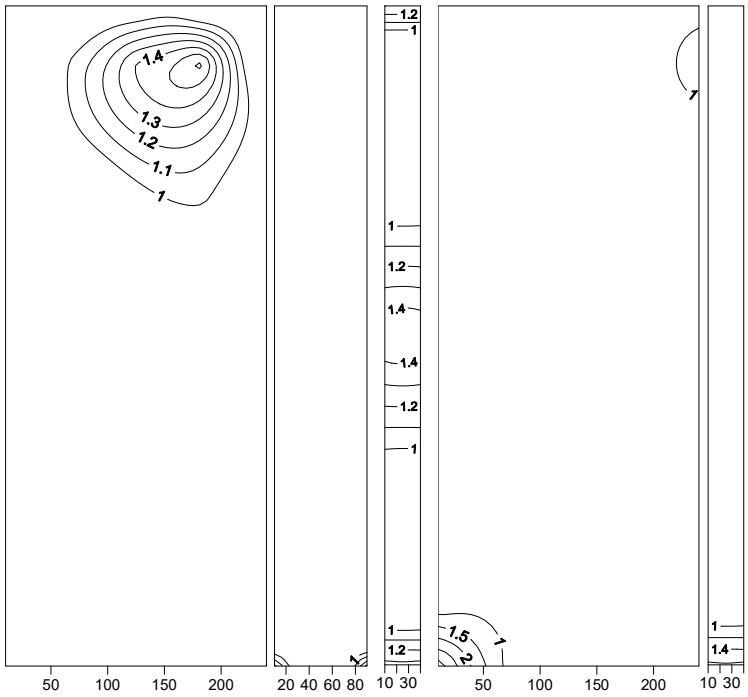

(c) No blockage (Face A, B3, B5, C, D1)

Fig. 5.32 RIF (I.F ≥ 1) contour (a) Full (b) Half (c) No blockage- H- model

6. CHAPTER-6

FORCE MEASUREMENT

6.1. GENERAL

The local wind forces on a bluff body are the function of the wind flow characteristics, building geometry, and elevation levels. The distribution of local wind forces along the elevation of the buildings at various wind flow conditions indicates the physical flow structure around the building. As mentioned earlier, the force coefficients are evaluated by integrating the force coefficients at individual pressure points at various faces of the building model in isolated and interference conditions as described earlier. The local force at each pressure point is calculated by multiplying the pressure and the distributed area of the corresponding pressure point. The local force coefficients at different height levels of the building are calculated by integrating the local forces of all pressure points on all faces at a particular height level. The mean and r.m.s coefficients of local forces at various height levels, the base forces, and the overturning moments are presented in along-wind and across-wind direction.

6.2. SQUARE MODEL

6.2.1. Local wind forces

A detailed study of local wind force coefficients at various height levels of all building models (as shown in chapter 3) has been carried out to investigate the effects of change in wind direction and various blockage conditions of interference as explained in the previous chapter. Fig. 6.1(a) represents the variation of along-wind mean local wind force coefficients ($C_{D(z)}$) for the square model at various wind directions and interfering conditions. The direction of wind flow and blockage condition have pronounced effects. The $C_{D(z)}$ values are likely to be increased along the height at all wind directions and blockage conditions but decreased till mid height and then increase till the top level in half blockage condition. The peak values mostly appear at 0.9H for all wind directions and no blockage condition. The $C_{D(z)}$ values at normal wind incidence are higher than those at

oblique wind incidence. The peak $C_{D(z)}$ values for oblique wind flow are approximately 30% less than those for normal wind flow.

The along-wind forces in all interference conditions decreased significantly from those in isolated condition for 0^0 wind. The full blockage condition generate negative forces at each height level and the reason is the higher negative local wind pressure at front face due to shielding of front face by upstream building. The interference condition with half blockage is the most favorable for along-wind forces as it generate smallest along-wind forces. The $C_{D(z)}$ value for half blockage condition is reduced around by 70% from those in isolated condition.

Fig. 6.1(b) renders the variation of the cross-wind mean local wind force coefficients ($C_{L(z)}$) for various wind flow conditions in isolated as well as in interference. The $C_{L(z)}$ values for all wind flow conditions in isolated and in interference are almost less than 0.5 and keep constant along the height levels. A very minor variation is observed between the $C_{L(z)}$ values at different wind directions and different interference conditions.

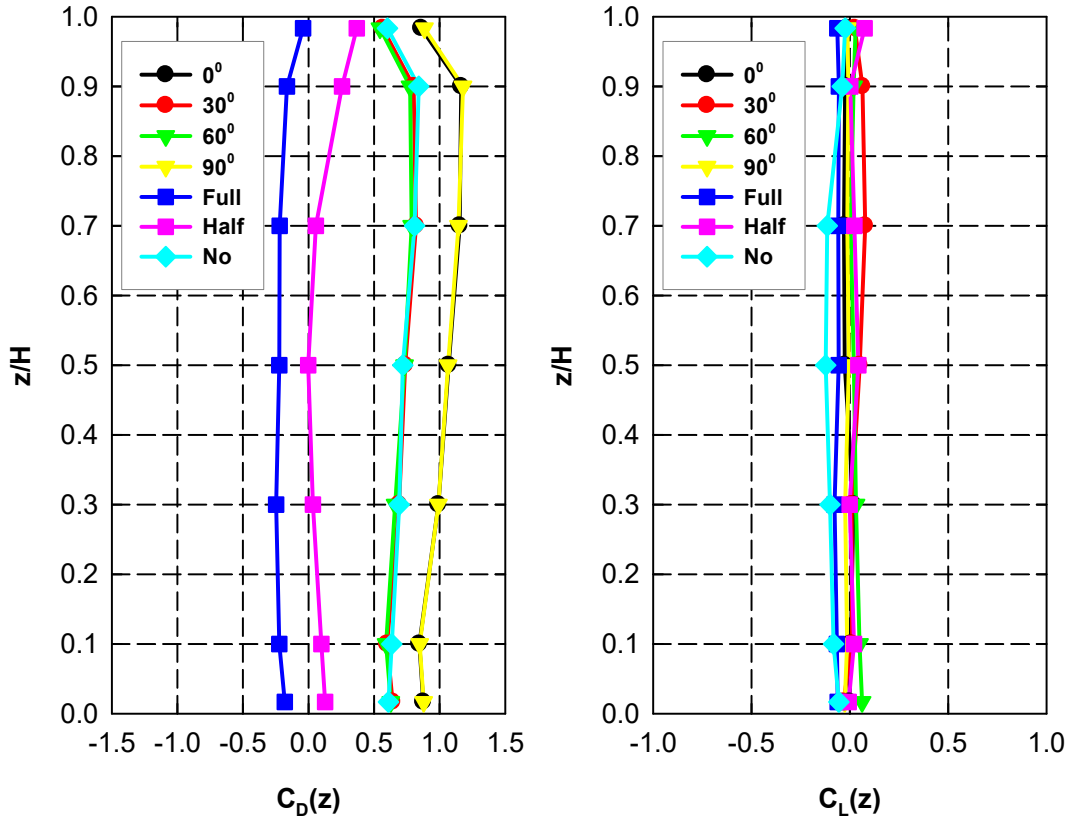

Fig. 6.1 Mean local force coefficient of Sq-model (a) along-wind (b) across-wind

The fluctuating local wind force coefficients are very important to evaluate the dynamic loads on the tall building. The Fig. 6.2 represents the variation of r.m.s of the fluctuating local wind force coefficients in along-wind and in across-wind. The along-wind r.m.s local wind force coefficients ($C^*_{D(z)}$) is very low in isolated conditions at all wind directions and has values less than 0.05. The $C^*_{D(z)}$ values are relatively higher in interference conditions, especially in half blockage. The peak value of $C^*_{D(z)}$ reach up to 0.0787 in half blockage. The distribution pattern along the height is almost similar in all flow conditions of isolated as well as interference and follow the almost straight line path along the height.

The across-wind r.m.s local wind force coefficient ($C^*_{L(z)}$) also keeps constant along the height similar to that of along-wind force in all conditions and have values less than 0.05. The very low values of cross-wind forces indicate low fluctuation in the time varying force data, which may be due to a lower level of turbulence set in the flow inside the tunnel.

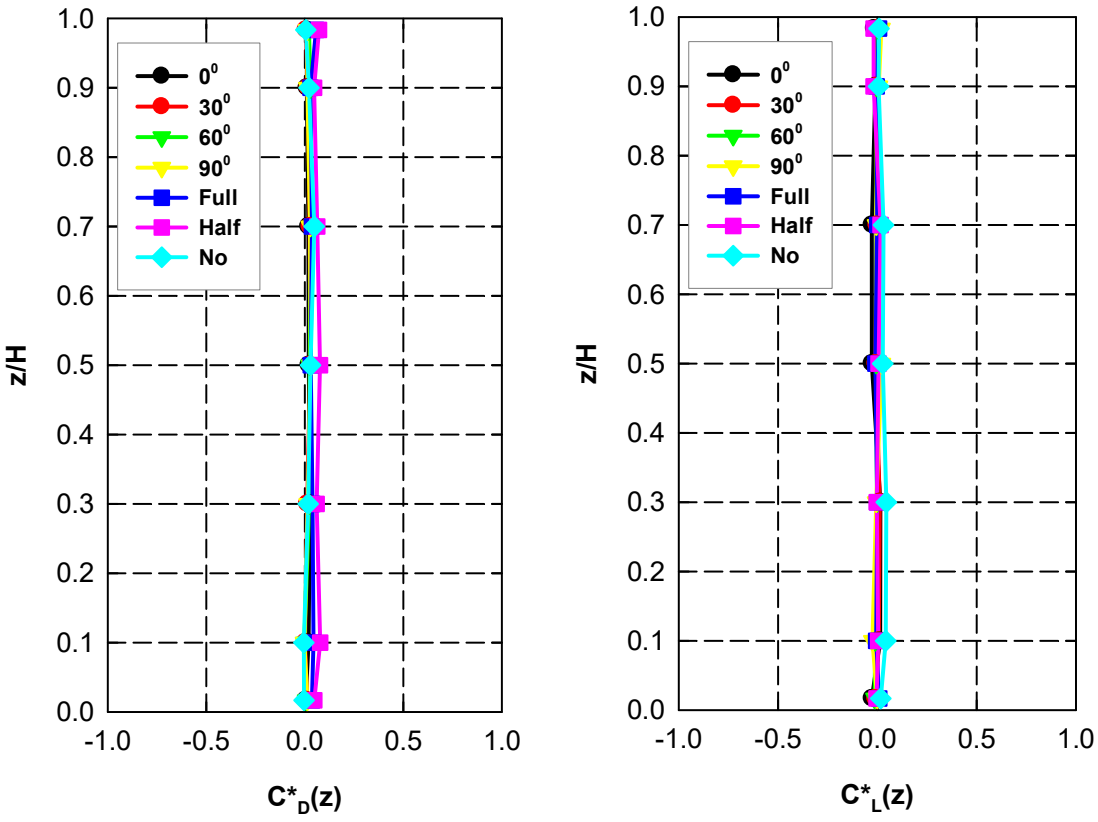

Fig. 6.2 RMS local force coefficients od Sq-model (a) along-wind (b) across-wind

6.2.2. Base force coefficients

The variation of mean drag force coefficients (C_{FD}) , mean lift force coefficients (C_{FL}), mean along-wind OTM coefficient (C_{MD}) and mean across-wind OTM coefficient (C_{ML}) is presented along the wind direction and blockage conditions. The positive and negative direction of drag and lift force and OTM moments have been considered as shown already in Fig. 3.11.

Fig. 6.3 shows the variation of mean base force coefficients in along-wind and across-wind directions. The values of along-wind forces: drag and moment at normal wind incidence of 0^0 and 90^0 angles are larger than those at oblique wind incidence in isolated condition. The C_{FD} and C_{MD} values are likely to be reduced significantly in interference conditions. The full interference condition generates negative drag force on the model because of higher negative pressure at front face due to shielding. As the blockage to the principal building is reduced from full blockage to no blockage, the along wind force and moment coefficients changes from negative to positive and attains values almost similar to oblique wind directions. The building model has its smallest along-wind forces in half blockage condition. The peak value of C_{FD} is 1.029 at normal wind incidence while smallest value is 0.0967 at half blockage. The peak value of C_{MD} is 0.539 at 0 degree while lowest value is 0.065 at half blockage.

The lift force coefficient and the across-wind OTM coefficient have higher values for oblique wind direction of 30^0 and 60^0 unlike along-wind force and moment coefficients. The distribution of lift force coefficient and across-wind OTM coefficients overlap each other. The cross-wind forces have been increased by the presence of upstream building in different blockage conditions. The maximum absolute values are observed at no blockage condition while smallest values are at 0^0 wind angle. The absolute peak values of C_{FL} and C_{ML} are 0.09 and 0.042, respectively at no blockage condition, while smallest values of 0.01 and 0.009, respectively at 0^0 wind direction.

The corresponding r.m.s base force coefficients (C^*_{FD}, C^*_{MD}, C^*_{FL}, and C^*_{ML}) are presented in Fig. 6.4. The distribution of along wind force coefficients is almost straight line for all wind directions in isolated condition but follow a parabolic distribution in interference condition. The values of across-wind force coefficients are almost similar with slightly higher at no blockage condition.

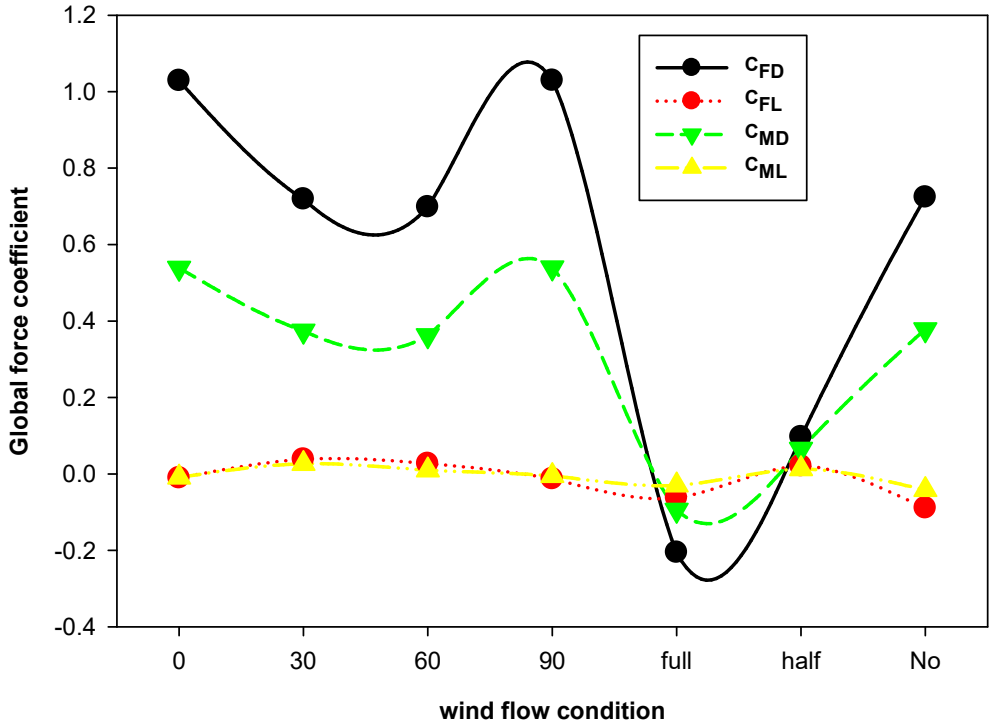

Fig. 6.3 Mean base Force coefficients of Sq-model

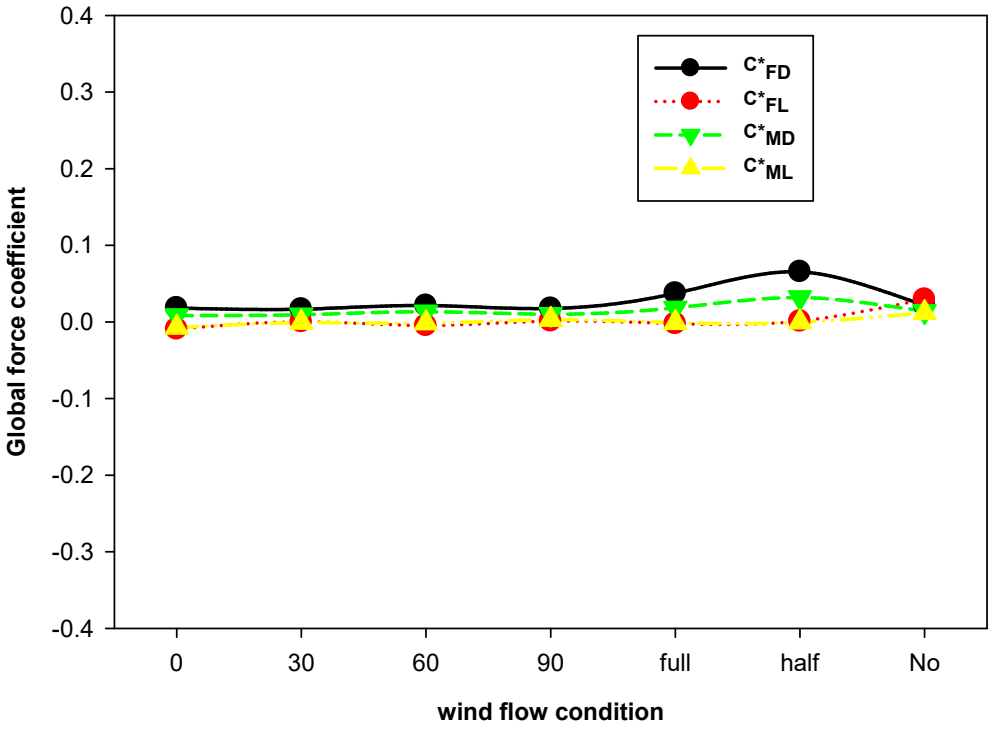

Fig. 6.4 RMS base force coefficients od Sq-model

6.3. PL-1 MODEL

6.3.1. Local wind forces

The distribution of mean and r.m.s coefficients of local wind forces in along-wind and across-wind directions has been presented along the height levels similar to that for square model. The distribution of mean local force coefficients is shown in Fig. 6.5. The distribution of $C_{D(z)}$ in all case is similar and follow the same pattern. The $C_{D(z)}$ values increase with height with peak at approximately 0.9H height in all cases. The effects of change in the wind direction and the presence of upstream building with different blockage are explicitly visible from figure, but the effects are less significant than those on square building. Similar to the square model, the $C_{D(z)}$ values at normal wind direction of 0 and 90 degree are higher than those at oblique wind directions of 30 and 60 degree. The peak $C_{D(z)}$ value of isolated building is maximum at 0 degree wind angle, which is approximately 25% higher than those maximum peak at oblique wind direction. The peak values in full, half and no blockage are around 72%, 18% and 15% less than those in isolated condition at 0^0 wind. The model has absolute minimum values of $C_{D(z)}$ in full blockage condition.

The cross-wind local force coefficient do not change along the height and have almost similar values throughout the height in all case. The effects of change in wind direction and position of interfering upstream building are distinctly visible from Fig. 6.5. The model has negative values of $C_{L(z)}$ at wind direction of 30 and 90 degree. The $C_{L(z)}$ values for 60^0 wind angle are the largest among all the cases of isolated and interference throughout the height. The peak of $C_{L(z)}$ at 60^0 wind is 0.36. The upstream interfering building with full blockage of flow does not affects the $C_{L(z)}$ values of the principal building but have significant effects with half blockage and no blockage condition of flow.

The r.m.s local wind force coefficient variation is shown in Fig. 6.6. The along-wind r.m.s local wind force coefficients ($C^*_{D(z)}$) distribution of Pl-1 model in various case have been overlapped to each other. The distribution in all case follow almost straight line path along the height. The effects of wind direction and position of upstream interfering building does not seems significant. The cross-wind r.m.s local wind force coefficient ($C^*_{L(z)}$) also have similar values in all case with slightly higher values till mid height in 60^0 wind.

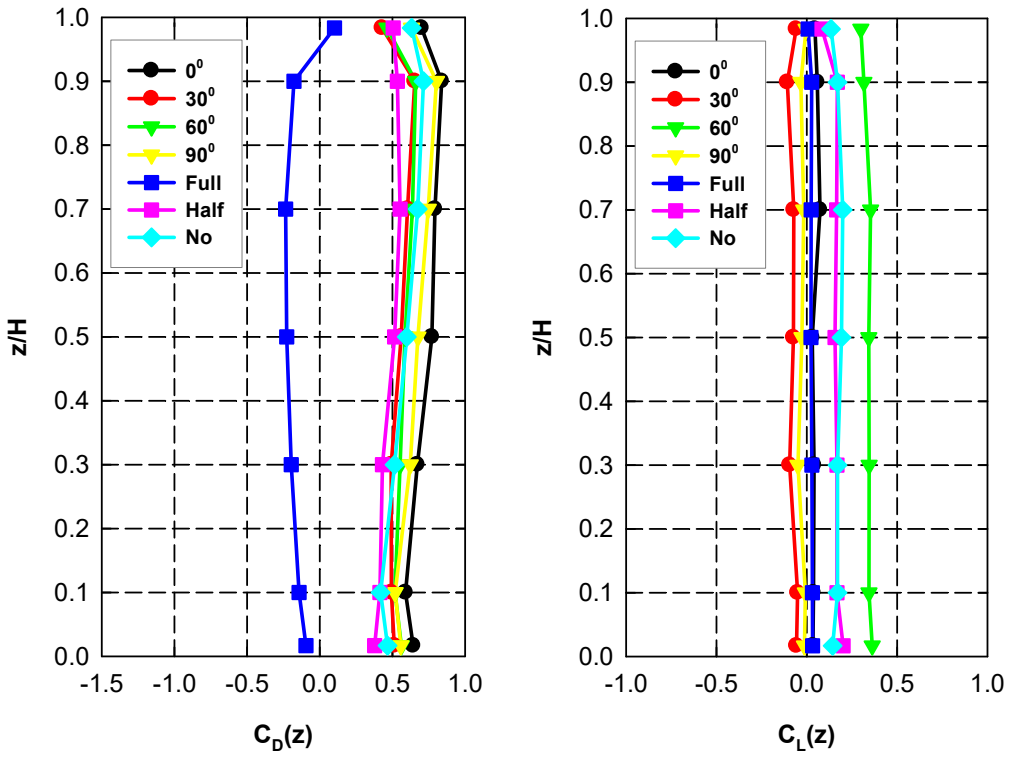

Fig. 6.5 Mean local force coefficient of Pl-1-model (a) along-wind (b) across-wind

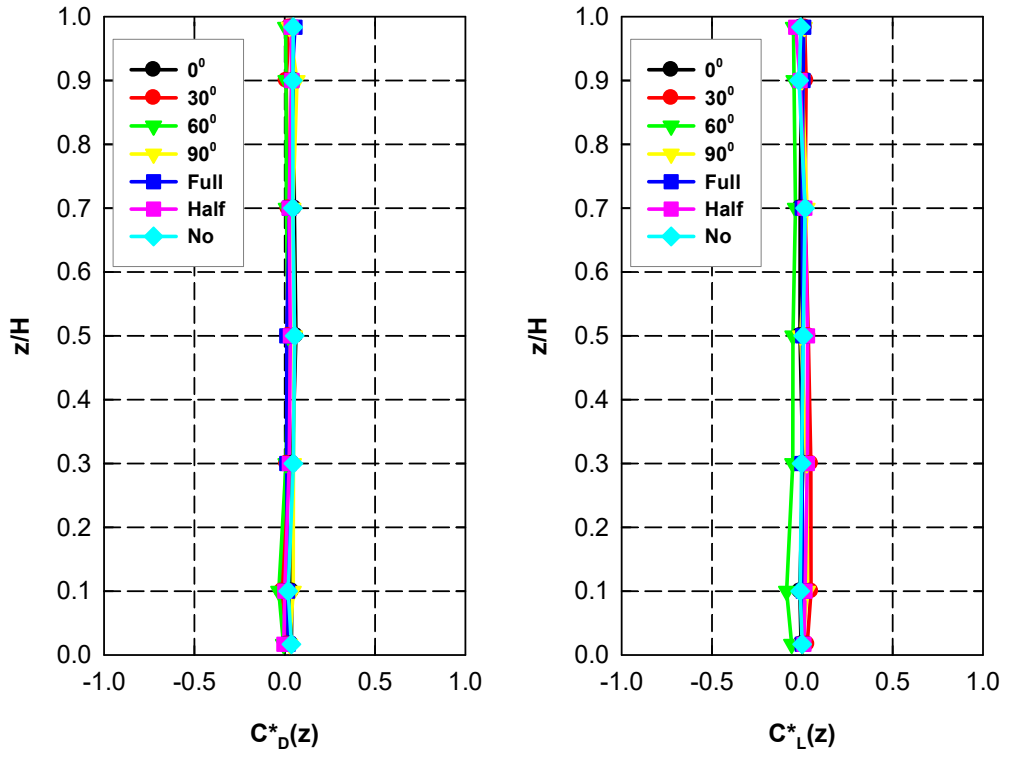

Fig. 6.6 RMS local force coefficient of Pl-1-model (a) along-wind (b) across-wind

6.3.2. Base force coefficients

The mean base force coefficients of Pl-1 model under various wind conditions of isolated building and in interference are shown in Fig. 6.7. It is seen from figure that similar to the square model, the C_{FD} values of Pl-1 model at normal wind incidence are higher than those at oblique wind incidence. The C_{FD} values are not same in case of 0^0 and 90^0 wind angles, because the dimension of front are different in both wind incidences. The higher value in case of 0^0 wind show that wider faces may generate higher drag forces. The models has largest C_{FD} value of 0.73 at wind direction of 0 degree. The mean drag coefficient is negative in full blockage due to shielding and turns positive when blockage to the principal building is reduced to half and attains it maximum value when there is no blockage. The absolute value of C_{FD} in full blockage is approximately 75% lower than isolated case but the direction is opposite and hence a due care must be taken while designing for wind loads.

The effects of change in wind direction and position of interfering building on the along-wind moment coefficient (C_{MD}) is similar to that on C_{FD}. The maximum value of C_{MD} is also observed at 0 degree wind. The absolute lowest value of along-wind moment is observed at full blockage interference condition. The reduction in the C_{MD} value at full blockage condition from isolated condition at 0 degree is around 77%.

Unlike square model, the Pl-1 model has a significant variation between cross-wind forces at various wind directions and interference conditions. The peak values of C_{FL} and C_{ML} are observed at 60^0 wind direction. The model has its maximum value 0.34 of C_{FL} at 60^0 wind angle. The half blockage condition and no blockage condition also have negative effects of interference. The C_{FL} values in these interference conditions are significantly higher than those in isolated 0^0 wind case. The C_{FL} values have been increased to 0.16 and 0.18 in case of half and no blockage conditions, respectively, which is 0.047 in isolated building condition. The variation of C_{ML} is similar to that of C_{FL}. The maximum cross-wind moments is also observed at 60^0 wind direction. The values of C_{FL} and C_{ML} are coincide with each other at wind direction of 0^0 and 90^0 and in full blockage interference condition.

Fig. 6.8 show the variation of corresponding r.m.s coefficients of the base forces. The r.m.s values of various force coefficients do not follow the similar path as seen in case of square building model. The C^*_{FD} values are equal for normal wind angles of 0^0 and 90^0 and

comparatively higher than those at oblique wind angles. The interference effects are also beneficial to some extent as the C^*_{FD} values are reduced in all interference conditions. The variation between the values of C^*_{MD} is small compare to the values of C^*_{FD}. The r.m.s force coefficients in cross-wind direction have a larger effects of change in the direction of wind incidence. The effects of change of blockage condition is very small on the cross-wind r.m.s force coefficients.

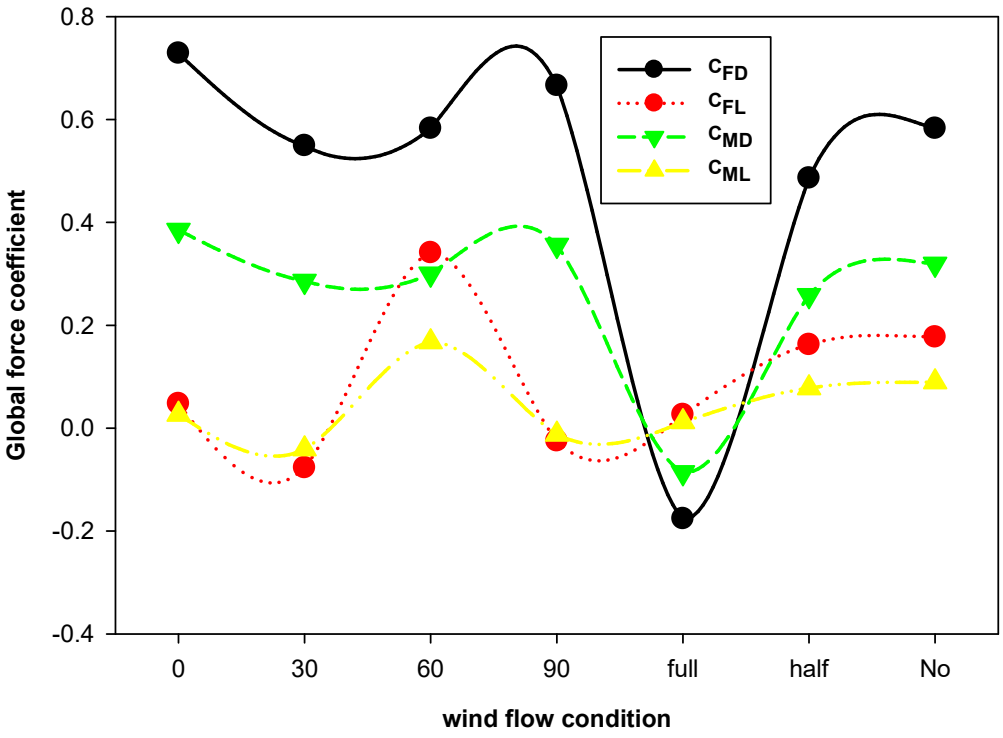

Fig. 6.7 Mean base Force coefficients of Pl-1-model

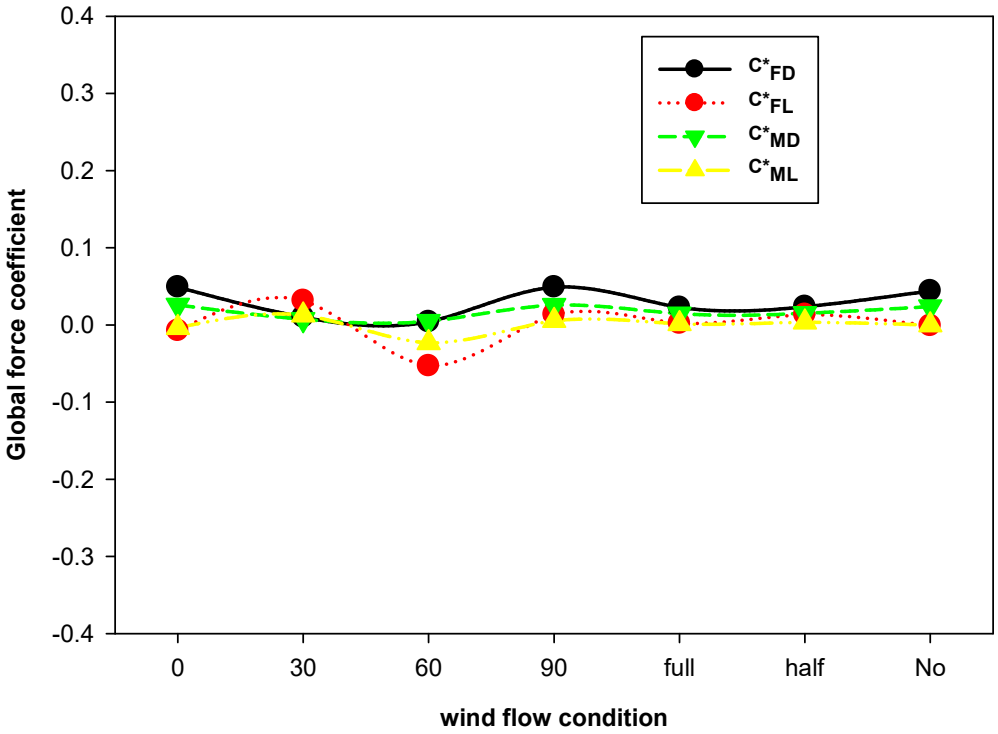

Fig. 6.8 RMS base Force coefficients of Pl-1-model

6.4. PL-2 MODEL

6.4.1. Local wind forces

Similar to the previous model, the along-wind mean local wind force coefficients ($C_{D(z)}$) increase with the elevation height in isolated as well as in interference conditions. The distribution pattern is similar in all cases. The maximum coefficient is observed at around 0.9H height level from the bottom. there is a significant effect of wind angles on the $C_{D(z)}$ values. The along-wind mean coefficient has reduced significantly for wind angles higher than 0 degree. It is very interesting to note the effects of changing size and shape of recessed corners that the $C_{D(z)}$ at 90^0 wind angle is almost 50% of the $C_{D(z)}$ in case of 0^0 wind, which was almost equal in case of similar type of Pl-1 model. The $C_{D(z)}$ values in case of full blockage are negative throughout the height. The absolute value of force coefficient at middle levels is slightly higher in full blockage interference condition, whereas it has higher values at top and bottom levels in case of half blockage interference condition.

The cross-wind mean local wind force coefficient ($C_{L(z)}$) values are less than 0.5 in all case of isolated building as well as interference. In case of 30^0 wind, the $C_{L(z)}$ values are highest among all wind angles. In case of other wind directions, the values are very small comparatively. Out of all interference conditions, the half blockage condition has highest interference effects and the $C_{L(z)}$ values are significantly larger than other interference conditions. The maximum values are observed at 0.7H height level from bottom is case of these critical conditions. The peak values at 30^0 wind direction in isolated condition and at half blockage interference condition are 0.36 and 0.37, respectively.

The Fig. 6.10 show the variation of corresponding r.m.s force coefficients. The along-wind r.m.s local wind force coefficient ($C^*_{D(z)}$) follow the almost similar pattern of straight line path along the height in all conditions. The values are almost similar in all cases throughout the height and thus overlapped with each other. The $C^*_{D(z)}$ values are very small and less than 0.1 in all cases. The cross-wind r.m.s local force coefficient ($C^*_{L(z)}$) values are also very small in all cases and even less than 0.05.

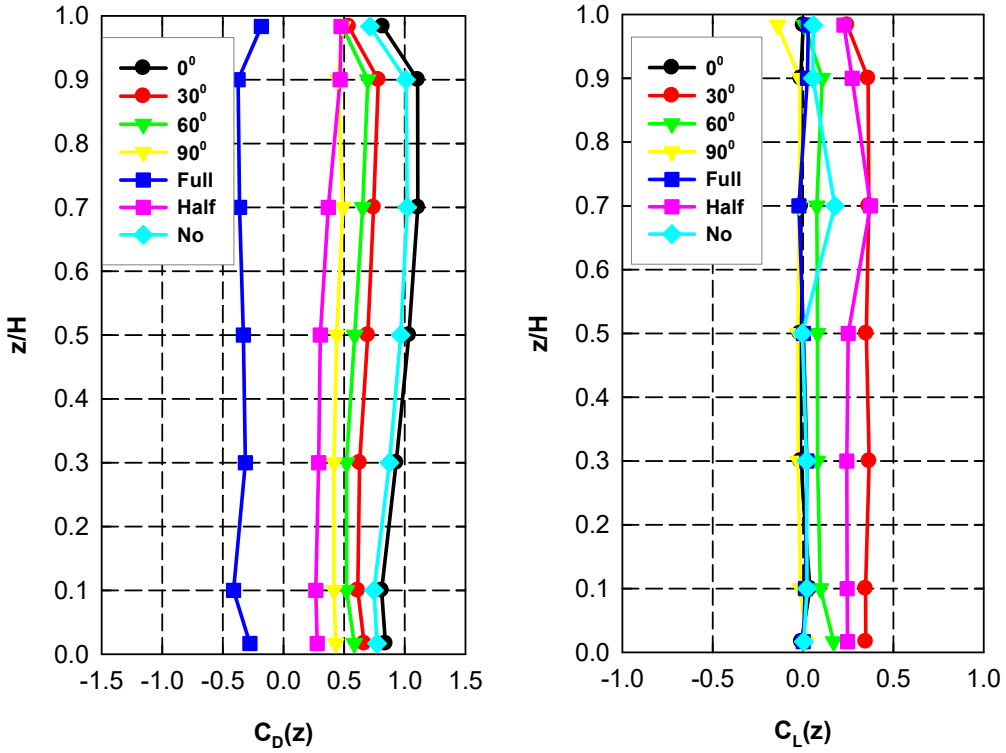

Fig. 6.9 Mean local force coefficient of Pl-2-model (a) along-wind (b) across-wind

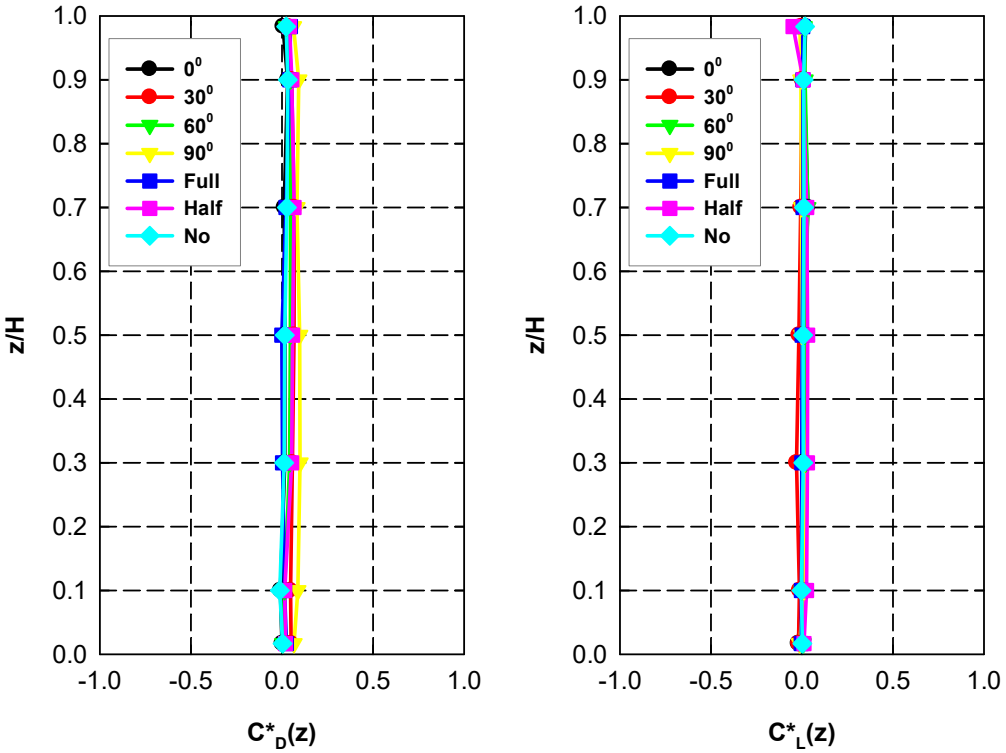

Fig. 6.10 RMS local force coefficient of Pl-2-model (a) along-wind (b) across-wind

6.4.2. Base force coefficients

Fig. 6.11 show the variation of mean base force coefficient and mean OTM coefficient in along-wind and across-wind directions. The mean drag force coefficient (C_{FD}) is significantly affected by the wind incidence angles. The C_{FD} continuously decreases with increase in wind incidence angle between 0^0 to 90^0. The C_{FD} value at 90^0 wind is almost reduced to 45% of the value at 0^0 wind. The full blockage and half blockage interference conditions also affect the mean drag force coefficient. The lowest drag force coefficient is observed at these two interference conditions. The absolute values in full and half blockage interference conditions are almost equal, but the mean drag force coefficient is negative in case of full blockage condition. The mean drag in no blockage is significantly higher than those in two other interference conditions and the value is very near to that in 0^0 wind direction.

The mean along-wind OTM coefficient (C_{MD}) has also similar variation pattern along the flow conditions. In case of full blockage interference condition, the moment is negative but the absolute is less than that is case of half blockage condition. The maximum value of mean OTM coefficient in along-wind direction is observed at 0^0 wind direction.

The mean across-wind coefficients (C_{FL} and C_{ML}) are almost zero at 0^0 wind angle. There is a significant effects of wind direction on mean across-wind force and moment coefficient. The both force and moment coefficients increase at 30^0 wind angle and decrease for higher wind angles. The maximum values of C_{FL} and C_{ML} are 0.35 and 0.17, respectively observed at 30^0 wind directions. The interference conditions also have significant effects on the cross-wind mean force and moment coefficients. The maximum values of both the forces observed at half blockage interference condition.

Fig. 6.12 represent the variation of the corresponding r.m.s coefficients in along-wind and across-wind directions. The r.m.s drag force coefficients (C^*_{FD}) and r.m.s along-wind OTM coefficient (C^*_{MD}) increase and then decrease at alternate wind directions between 0^0 to 90^0. The maximum value of C^*_{FD} and C^*_{MD} are observed at the direction of 60^0 wind in isolated condition. There is slightly higher interference effects in case of half blockage interference condition compare to other interference conditions.

The variation of cross-wind r.m.s coefficients is just opposite to the along-wind coefficients. The C^*_{FL} and C^*_{ML} increase in opposite direction at alternate wind directions.

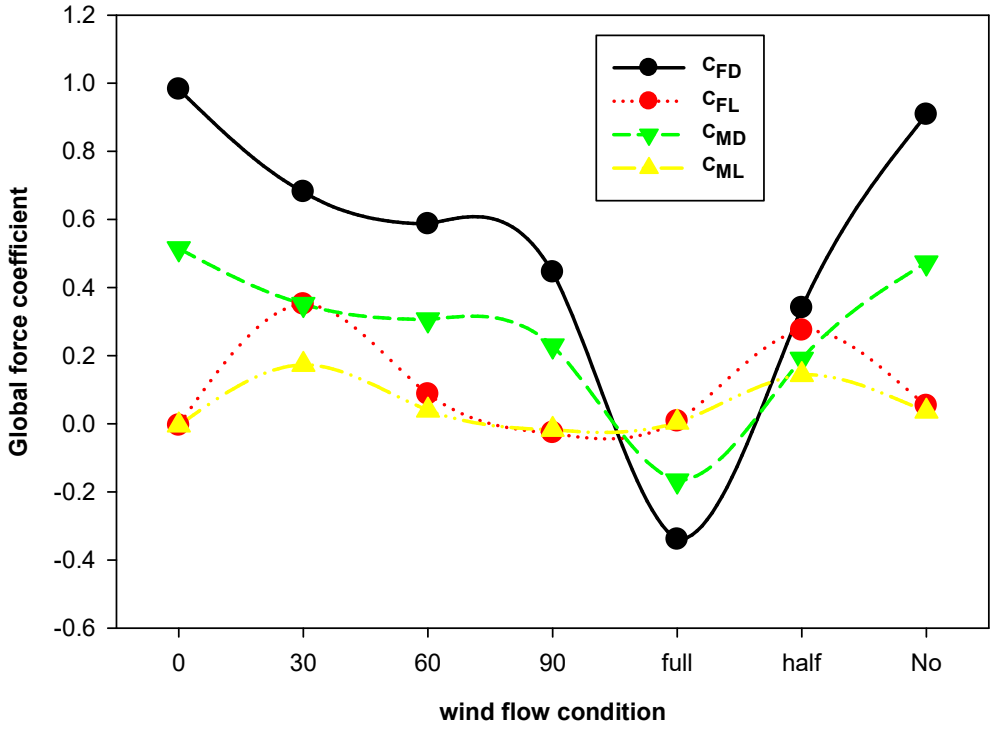

Fig. 6.11 Mean base Force coefficients of Pl-2-model

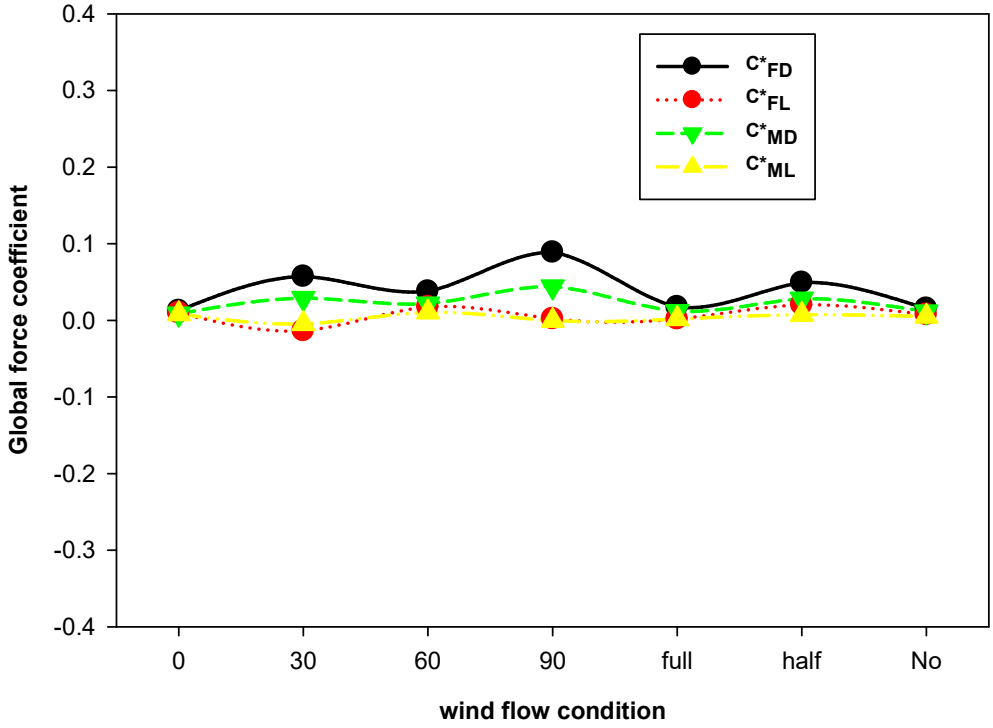

Fig. 6.12 RMS base Force coefficients of Pl-2-model

6.5. H- MODEL

6.5.1. Local wind forces

The mean along-wind local wind force coefficients increase along the height similar to the other models. The Fig. 6.13 renders the variation mean local wind force coefficients in along-wind and across-wind directions. The forces for wind direction at normal incidence are higher than those for the wind directions at oblique angles. The forces for the wind direction at 0^0 are highest at all the levels among all cases of isolated condition whereas for the no blockage interference condition with the presence of interfering building. The across-wind force coefficients at oblique wind directions are significantly higher than those at normal wind directions in isolated condition. Forces in interference condition are highest for upstream building position with no blockage position.

The r.m.s of local wind force coefficients in both direction are very small as shown in Fig. 6.14. In the isolated condition the along-wind forces at 90^0 wind direction are slightly higher at top between height 0.6H to 0.9H whereas forces in interference condition are slightly higher for half blockage interference condition at heigh level between 0.3H to 0.5H. The cross-wind r.m.s forces are also very small compare to the mean forces. Across-wind r.m.s force coefficients are slightly higher at middle levels in half blockage and no blockage interference conditions.

6.5.2. Base force coefficients

The variation of the mean base force and OTM coefficients are shown in Fig. 6.15. The along-wind coefficients are higher at wind directions normal to the surfaces. In the isolated condition, the forces are maximum at 0^0 wind direction. The forces reduces by a large amount in full blockage interference condition compare to the all isolated conditions but increase to almost equal value when upstream building present with no blockage condition. The cross-wind mean forces are maximum at 60^0 wind direction in isolated condition whereas maximum for no blockage in interference condition.

The r.m.s coefficients in along-wind direction are highest at 90^0 wind direction in isolated condition, whereas the across-wind r.m.s coefficients are highest at 60^0 wind direction as shown in Fig. 6.17.

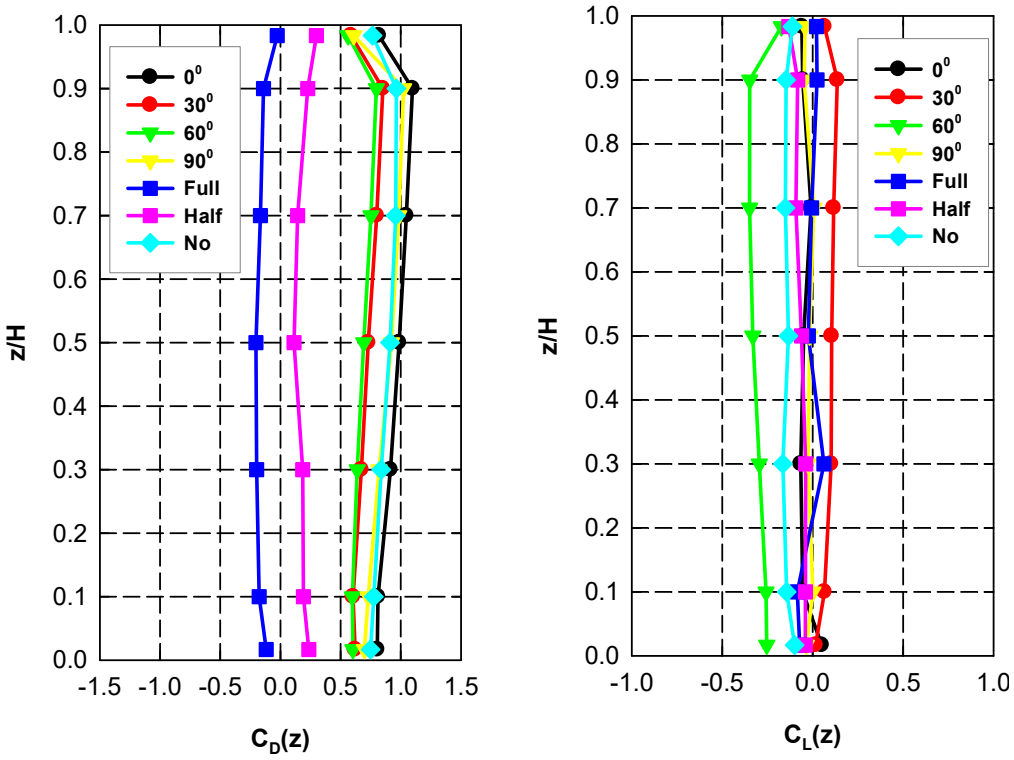

Fig. 6.13 Mean local force coefficient of H-model (a) along-wind (b) across-wind

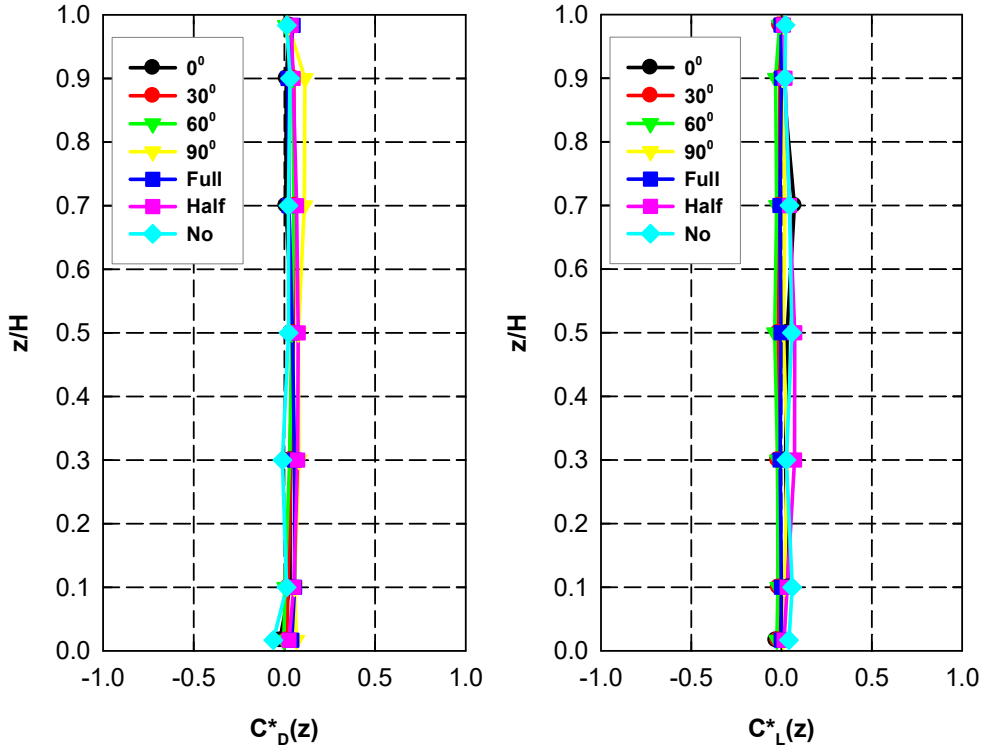

Fig. 6.14 RMS local force coefficient of H-model (a) along-wind (b) across-wind

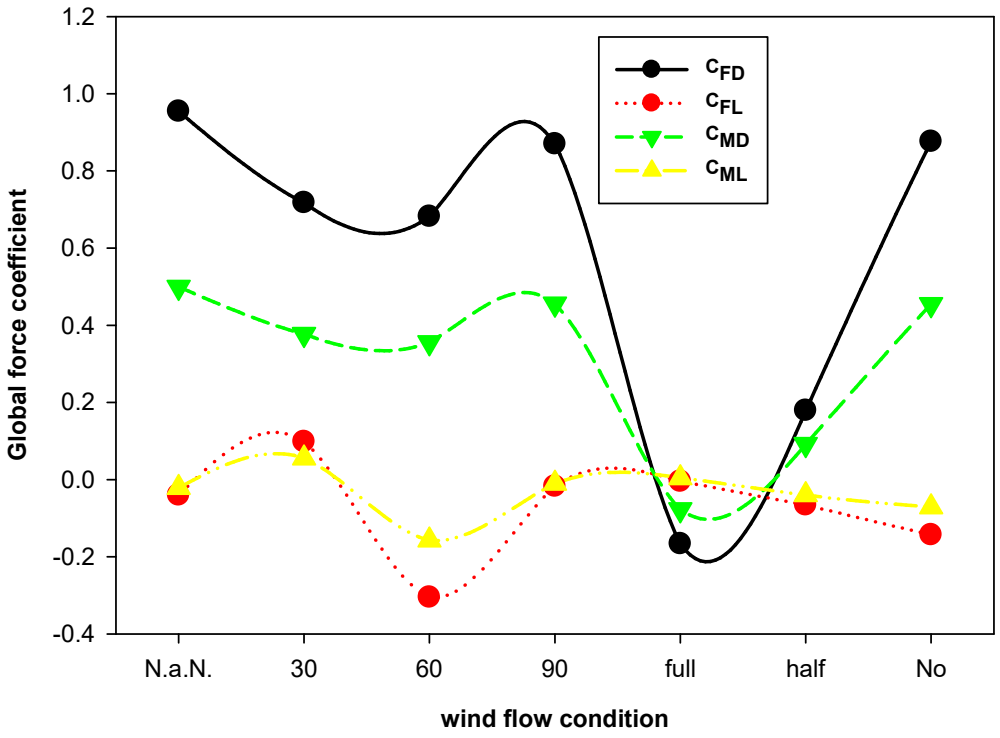

Fig. 6.15 Mean base Force coefficients of H-model

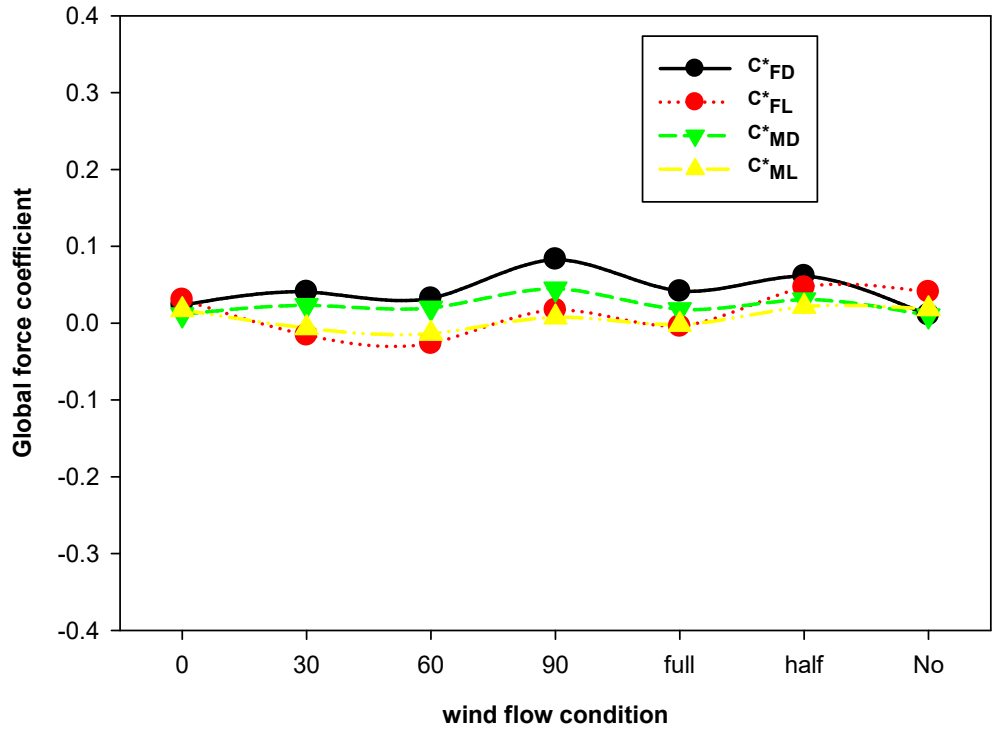

Fig. 6.16 RMS base Force coefficients of H-model

6.6. COMPARISON OF FORCES BETWEEN DIFFERENT SHAPES

To investigate the effects of change in the external shape of the building model on the change of wind loads on high rise buildings, experimental results of the all building model are compared. Based on the experimental results, mean and r.m.s coefficients of base moments of all models in along-wind and crosswind directions are compared to provide the comprehensive assessment of the effect of change of external shape on the wind loads in similar approach wind flow characteristics for all models.

6.6.1. Mean Wind Forces

The comparison of mean along-wind mean OTM coefficients of all models are presented in Fig. 6.17. The distribution pattern is almost similar for all models. The mean along-wind moments for all models are reduced at oblique wind directions from those for wind at normal to the surfaces. All the models have their lowest value of in interference condition of full blockage. In the isolated condition, the square model suffer the maximum drag force whereas Pl-1 model suffer the lowest along-wind force. In the interference condition, the square model show better performance. Fig. 6.18 show the variation of mean across-wind OTM coefficients. The effects of change in cross sectional shape is significant on the across-wind forces. The distribution is completely different for all models. The square model have the lowest values in all case of wind flow in isolated and interference condition. The effects of cross sectional shape are dominant for wind flow at oblique angles in isolated condition while more at half blockage condition of interference.

6.6.2. RMS Wind Forces

The variation of r.m.s along-wind OTM coefficients is shown in Fig. 6.19. The distribution of r.m.s coefficients is different than mean coefficients. The square model show better perforce in isolated condition but with the upstream interfering building at half blockage condition, the $C_{MD,\,rms}$ is highest among all models. All the three modified models have higher values at 90^0 wind direction. All the models show similar performance at full blockage and no blockage interference conditions. The variation of across-wind r.m.s OTM coefficients is shown in Fig. 6.20. At 0^0 wind direction in isolated condition and at half blockage interference condition, the H-model show worst performance, while at oblique angles, the PL-1 model show the worst performance.

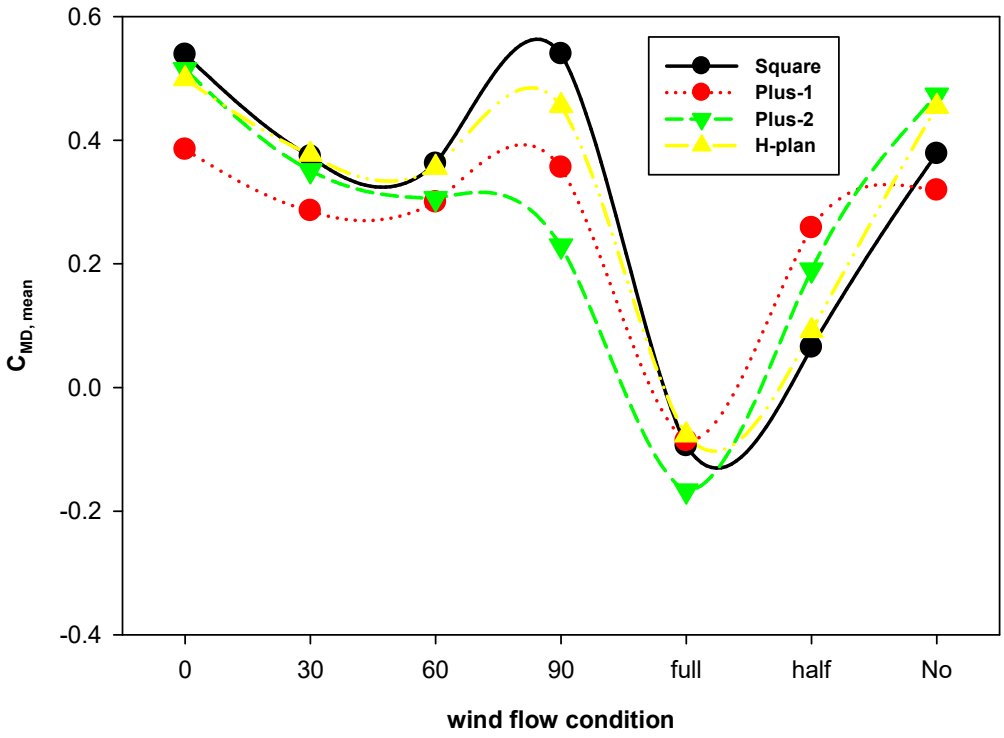

Fig. 6.17 Mean along-wind OTM coefficients

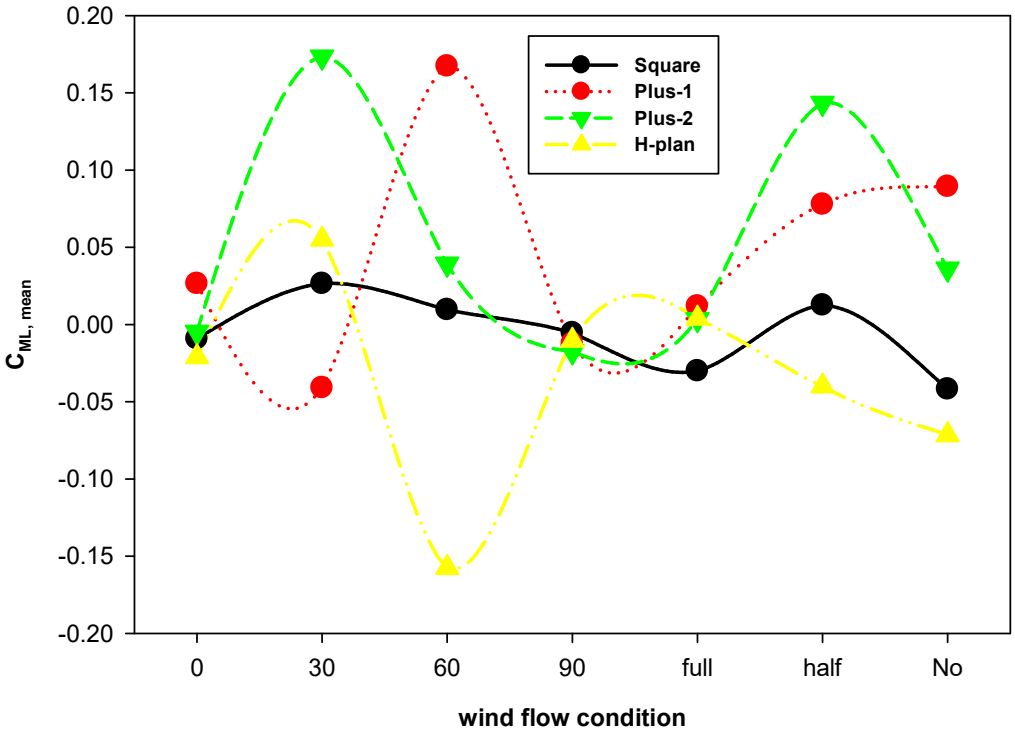

Fig. 6.18 Mean across-wind OTM coefficients

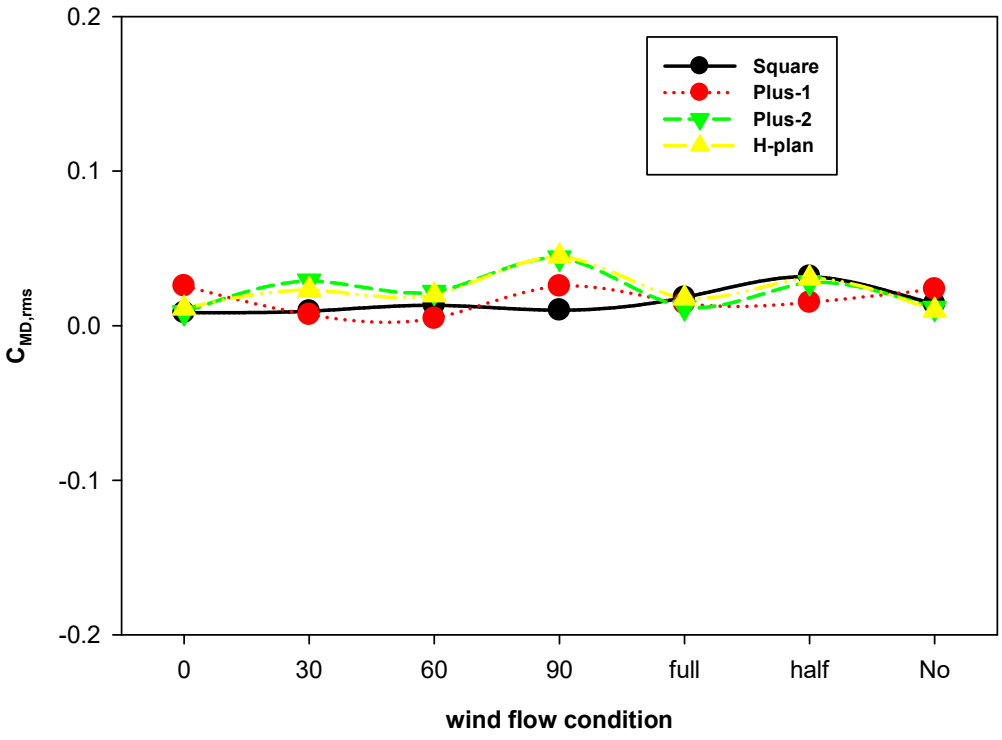

Fig. 6.19 RMS along-wind OTM coefficients

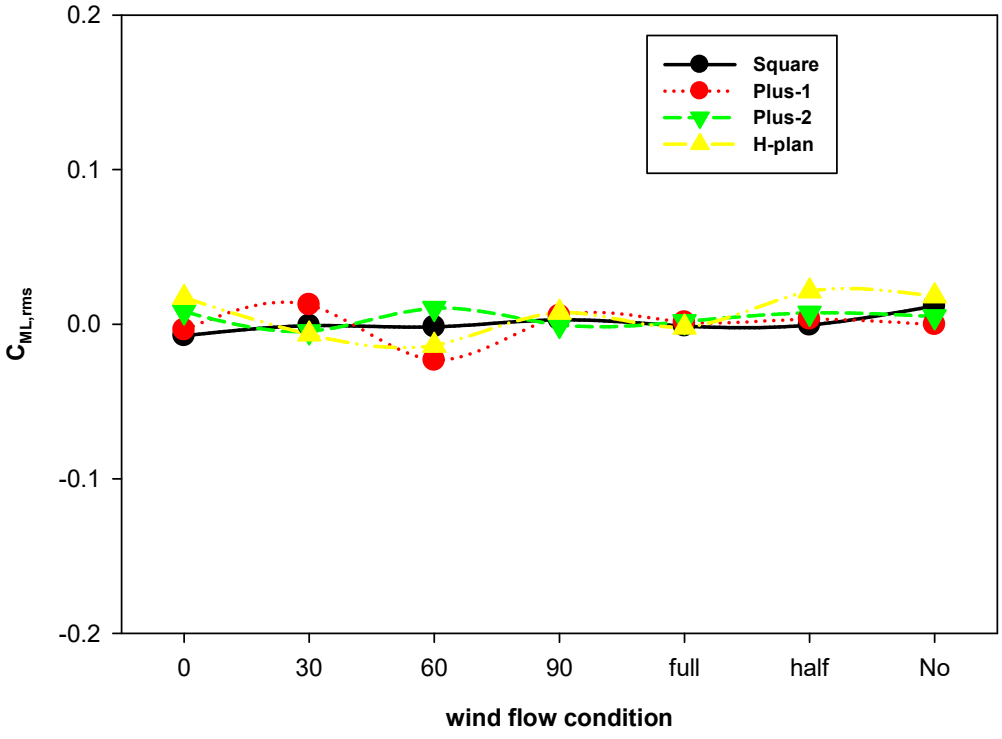

Fig. 6.20 RMS across-wind OTM coefficients

7. CHAPTER-7

RESPONSE STUDY

7.1. GENERAL

This chapter deals with the assessment of the effects of wind directions and presence of upstream interfering building at various locations on the response of the prototype tall buildings with different cross sections due to the experimentally obtained wind loads on the scaled models. The responses of all models are also compared to evaluate the effectiveness of building cross-sectional shapes. All the buildings are analyzed by linear static analysis with help of STAAD.Pro software.

7.2. DETAILS OF BUILDING DIMENSIONS

The dimensions of all the protype buildings are fixed in accordance with the dimensions of the corresponding building models scaled down at geometric scale of 1:300. The height and plan area of buildings are kept 180 m and 3600 m^2 accordingly. The protype buildings are 55-storyed RCC framed building, with height of ground floor as 4.5 m and 3.25 m for the rest of floors. The center to center spacing between grids of all buildings are kept 7.5 m in x-x and z-z directions. The grade of concrete and steel used in prototype buildings is M25 and Fe415, respectively. The details of the structural elements are shown in Table 7.1. The live load of 4 kN/m^2 is considered to act on the floor slab uniformly. Fig. 7.1 to 7.4 show the plan of prototype buildings. Elevation in Y-Z plane and isometric view of buildings are shown in Fig. 7.5 to 7.8.

Table 7.1 Description of structural elements in prototype building

Particulars		Value
Size of beams		300 mm x 300 mm
Size of Columns	Ground to 10^{th} story	1200 mm x 12000 mm
	11^{th} to 20^{th} storey	1000 mm x 1000 mm
	21^{st} to 30^{th} storey	800 mm x 800 mm
	31^{st} to 40^{th} storey	750 mm x 750 mm
	41^{st} to 55^{th} storey	700 mm x 700 mm
Slab thickness		150 mm
Ground storey height		4.50 m
Remaining storey height		3.25 m

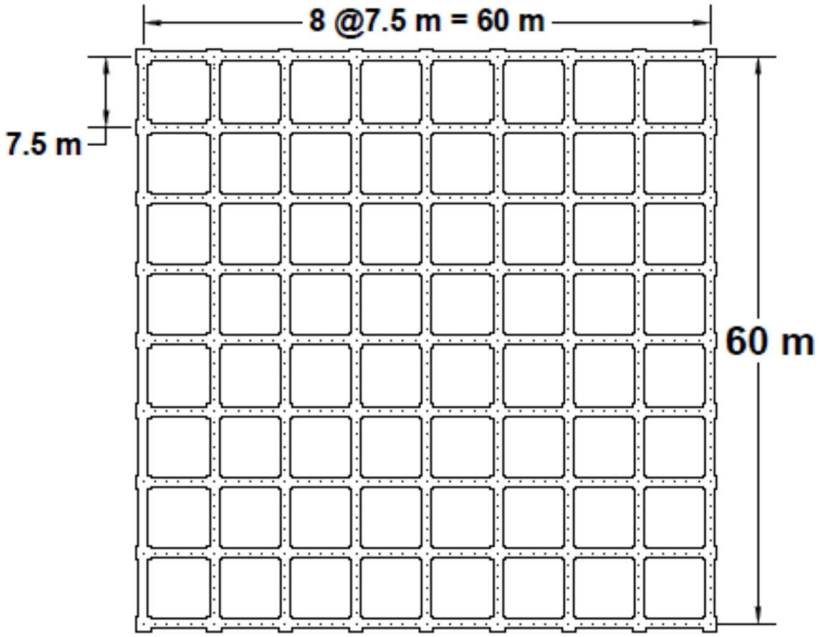

Fig. 7.1 Ground floor plan of Sq building

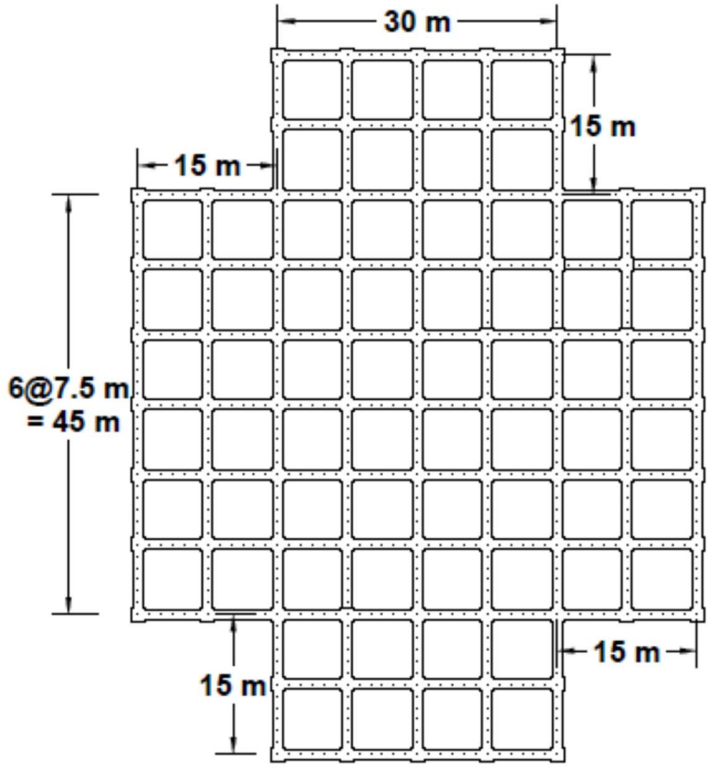

Fig. 7.2 Ground floor plan of PL-1 building

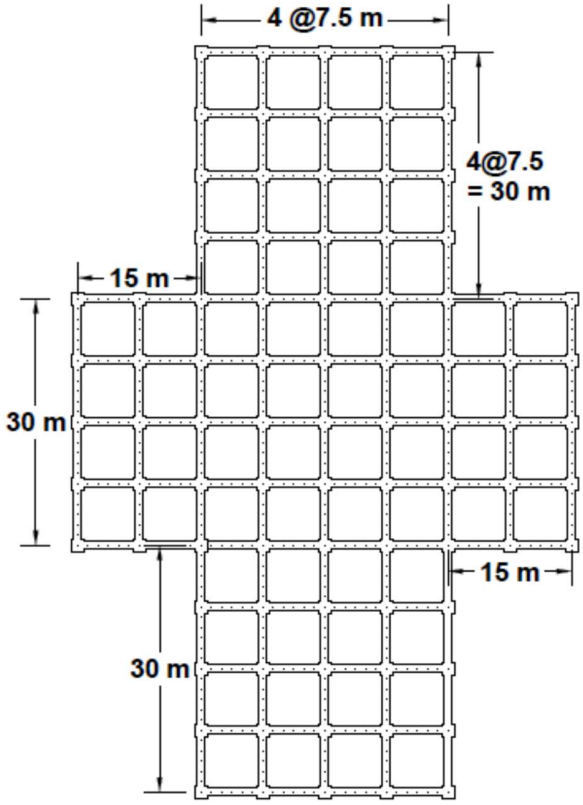

Fig. 7.3 Ground floor plan of PL-2 building

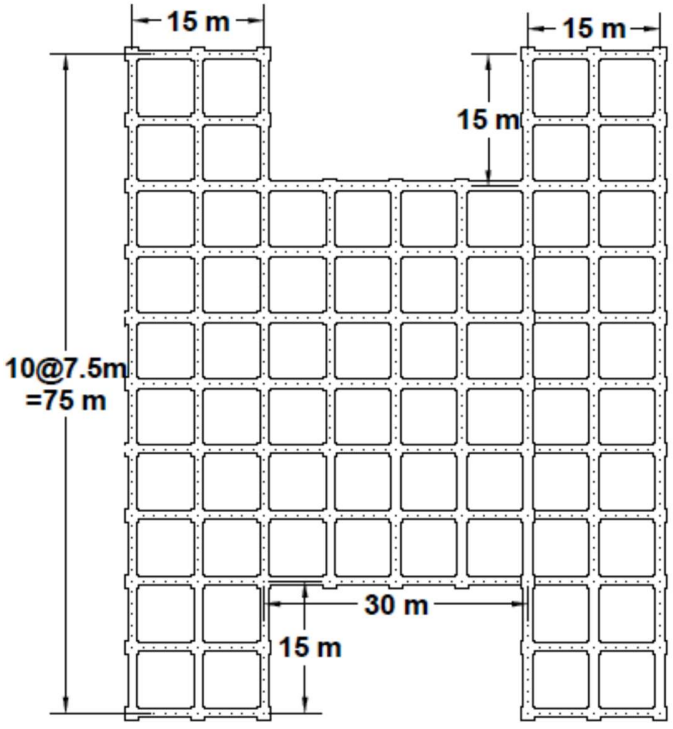

Fig. 7.4 Ground floor plan of H- building

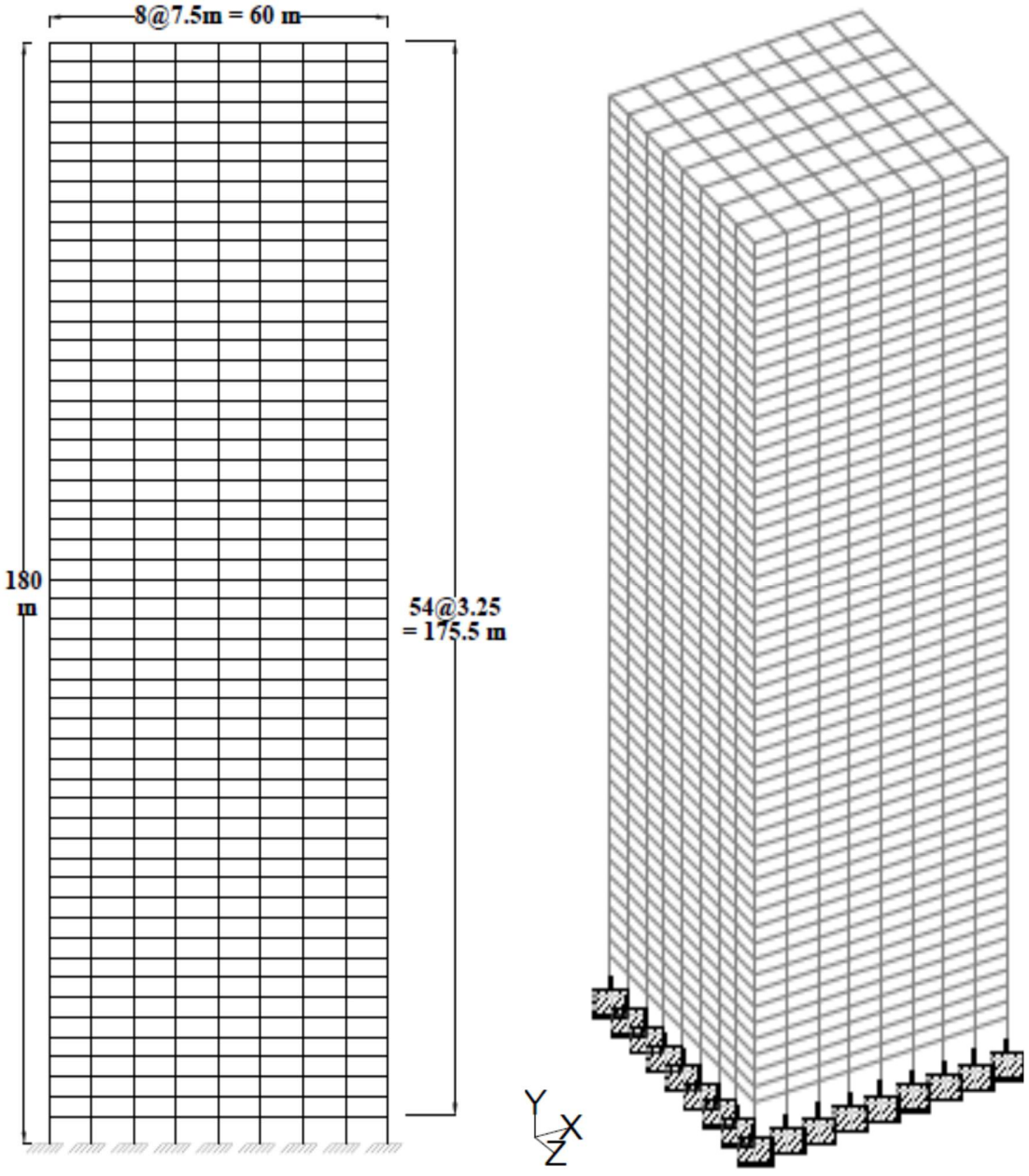

Fig. 7.5 Elevation and isometric view of Sq building

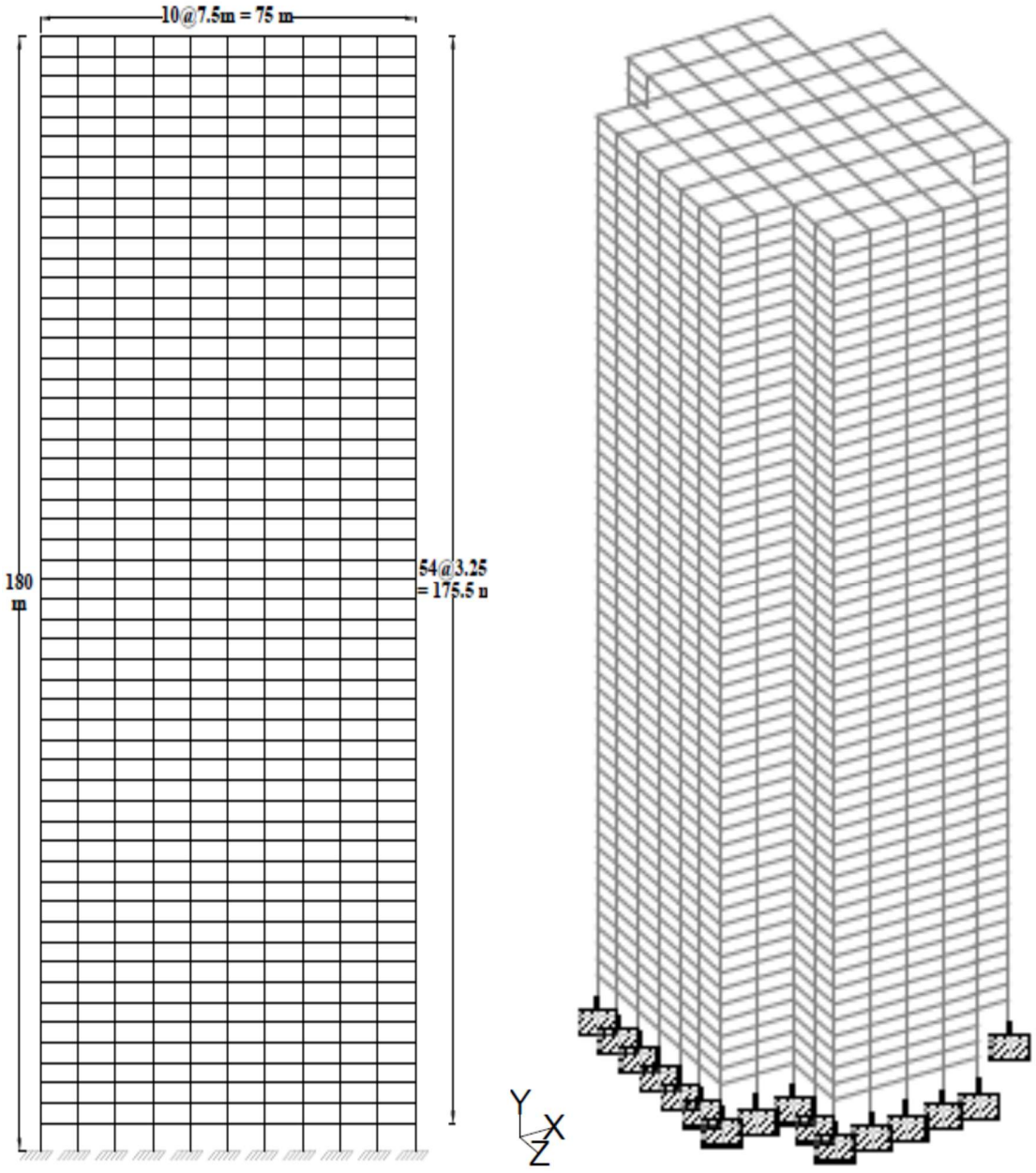

Fig. 7.6 Elevation and isometric view of PL-1 building

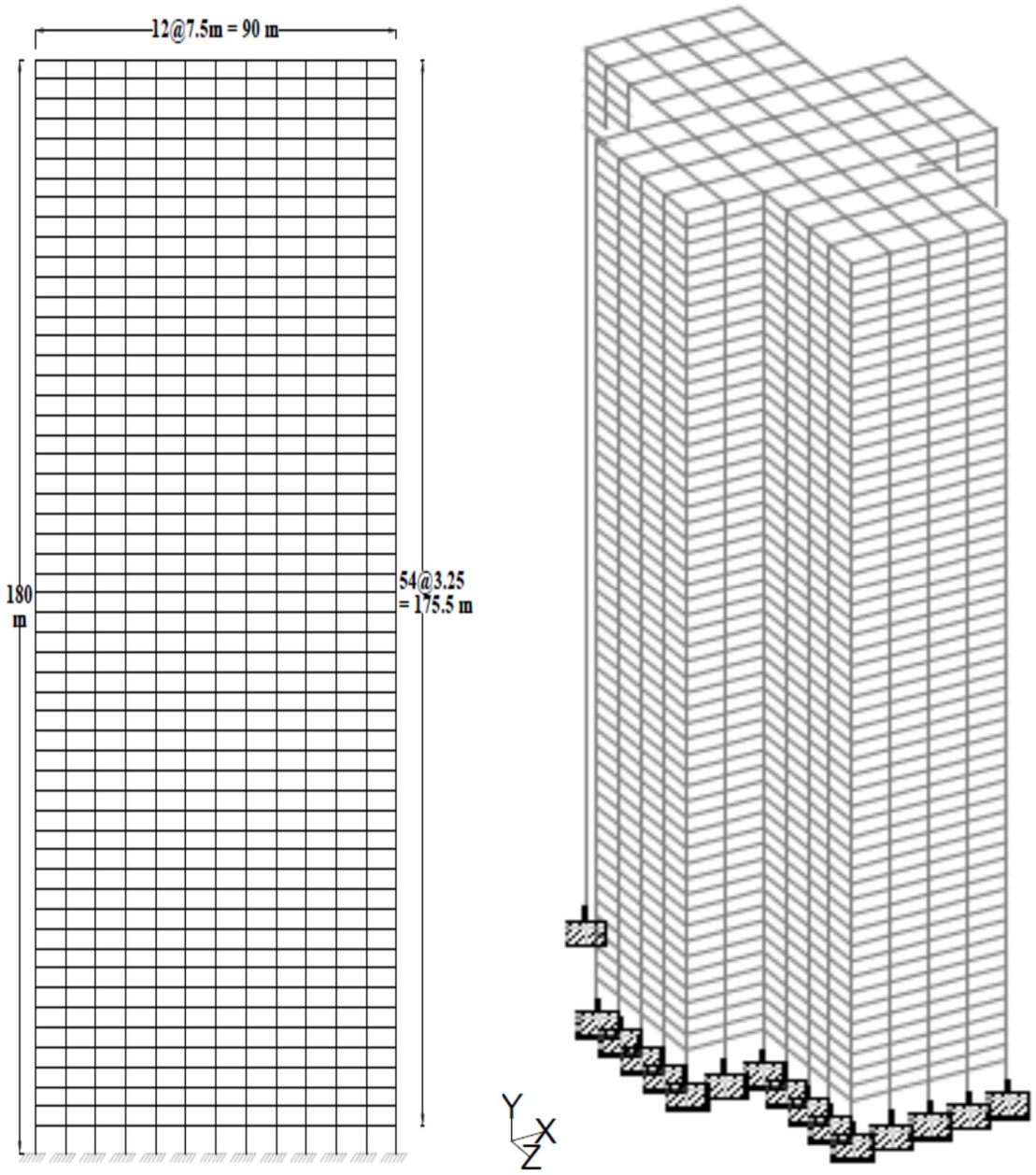

Fig. 7.7 Elevation and isometric view of PL-2 building

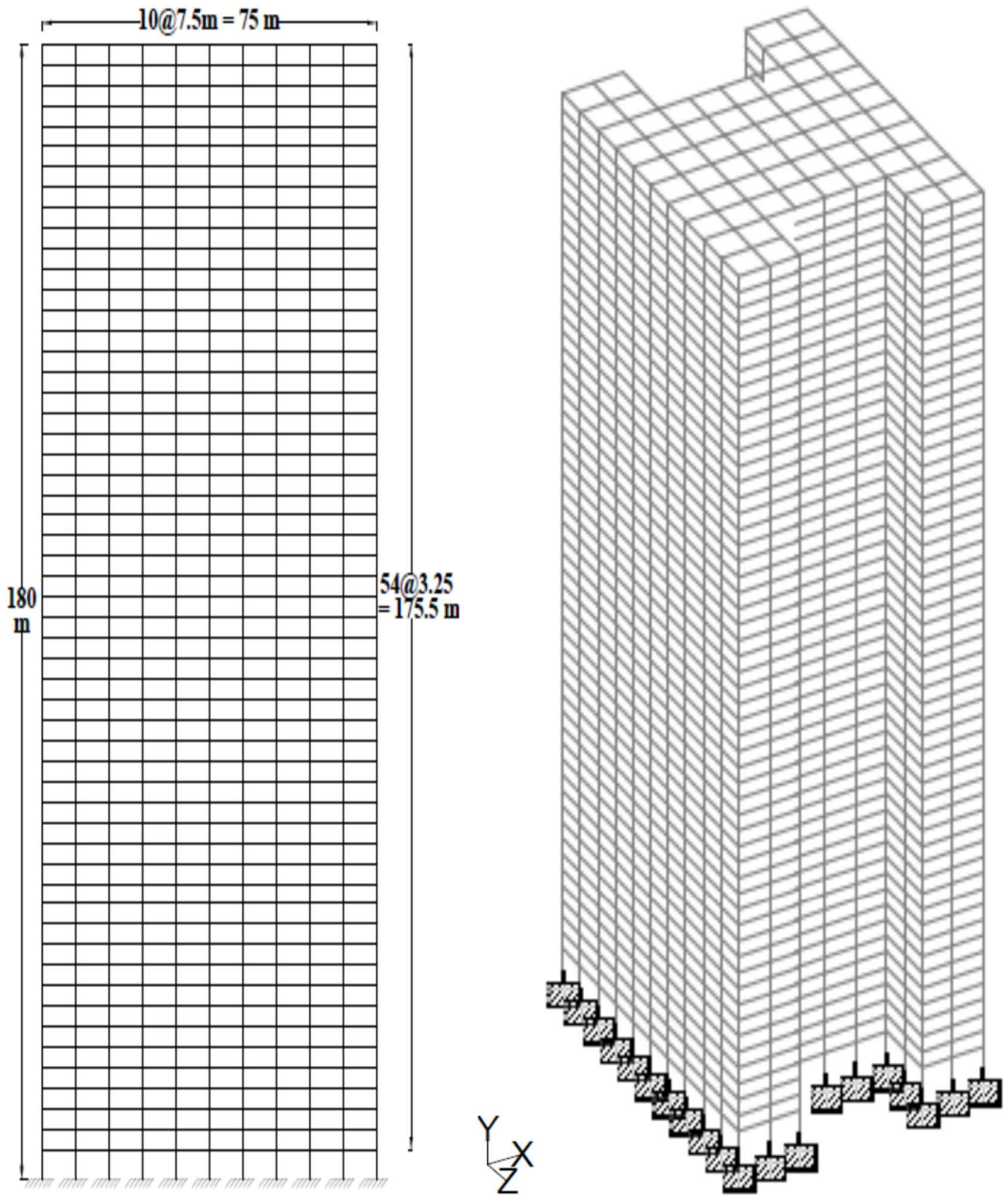

Fig. 7.8 Elevation and isometric view of H-building

7.3. EVALUATION OF WIND LOADS ON PROTOTYPE BUILDINGS

The wind load at each node of the prototype building is calculated in the followed steps

Evaluation of wind velocity at various height level of prototype building given by-

Step-1 Evaluation of wind velocity at various height level of prototype building

$$\frac{u}{u_0} = \left(\frac{y}{y_0}\right)^{\alpha} \quad \text{..... (7.1)}$$

Where,

y_0 = atmospheric boundary layer depth
u_0 = free stream wind velocity corresponding to the boundary layer depth
y = any storey height
u = wind velocity on the structure at any height y
α = power law index

The buildings are assumed to be located in the terrain category-(II) and wind zone-(V). The power law index (α) is 0.22 as calculated in the wind tunnel study of models. The boundary layer depth is 300 m and the basic wind speed at 10 m height is 50 m/s as per IS:875 (part-3), 2015.

Step -2 Evaluation of pressure on prototype as-

$$\frac{P_{r,proto}}{P_{r,model}} = \left(\frac{V_{proto}}{V_{model}}\right)^2 \quad \text{..... (7.2)}$$

Where,

$P_{r,proto}$ = pressure on the building at any height y,
$P_{r,model}$ = pressure on the corresponding model at any height y,
V_{proto} = velocity on the building at any height y,
V_{model} = velocity on the corresponding model at any height y,

Step-3 Finally wind force at various nodal points is calculated as-

$$F_{proto} = P_{r,proto} \text{ x } A_e \quad \text{..... (7.3)}$$

Where,

F_{proto} = static load on the building corresponding to strip area A_e at any height y,

A_e = effective frontal area (strip) area

7.4. THE RESPONSE OF SQUARE BUILDING

7.4.1. Isolated Condition

The response of all buildings is evaluated for wind loads as calculated in previous section of this chapter for wind directions of 0^0, 30^0, 60^0, 90^0. In order to assess the effects of change in wind direction on the response of buildings, the stress resultants including axial force, M_x (global), M_y (global) and twisting moment on the three columns A, B and C (Fig. 7.9 to 7.11) are compared.

The variation of axial force in column A, B and C is shown in Figures 7.9 to 7.11. Axial force in column A increases parabolically from top to bottom for all wind angles. The effect of wind angle is more significant in bottom 75% height of column. Axial force increases with increase of wind incidence angle from 0^0 to 90^0. Axial force at the base of the column for 90^0 wind is almost double of axial force for 0^0 wind. The effects of wind angle on the axial force in column B is not much significant. Axial forces for wind normal to the surface are relatively smaller to that for wind at oblique angles. There is no effect of change in wind direction on the axial force of central column C.

Fig. 7.12 to 7.14 show the variation of moment M_x in column A, B and C respectively. there is a significant effect of change in wind direction on the moment M_x (global) of column A as the moment is reduced largely with change of wind direction from 0^0 to 90^0. The moment for wind at 0^0 is maximum and minimum for wind at 90^0. The moment in column B is almost similar for wind direction between 0^0 to 60^0 while it has reduced significantly for wind at 90^0. The moment in central column C is highest among the three column A, B and C for wind directions of 0^0 to 60^0 and zero for wind at 90^0.

The variation of moment M_y in the three columns are shown in Fig. 7.15 to 7.17, respectively. The moment M_y at the base of column A is maximum for 90^0 wind direction whereas minimum for wind direction of 30^0. The moments at the base for wind directions of 0^0 and 60^0 are almost equal but the distribution along the height is different. The moment M_y in the column B is lowest for wind at 0^0. Effect of change in wind between 30^0 to 90^0 is significant only in bottom 40% height of the column. The effect of wind angles on the moment M_y of the central column is similar to that of M_x due to symmetry.

From Fig. 7.18 to 7.20, the position of column does not have any effect on the twisting moment as the twisting moment is similar in all the columns. The twisting moments in all the three columns is almost zero throughout the height at wind incidence angle of 0^0 and 90^0 due to symmetry. The twisting moments at oblique wind directions have similar variation.

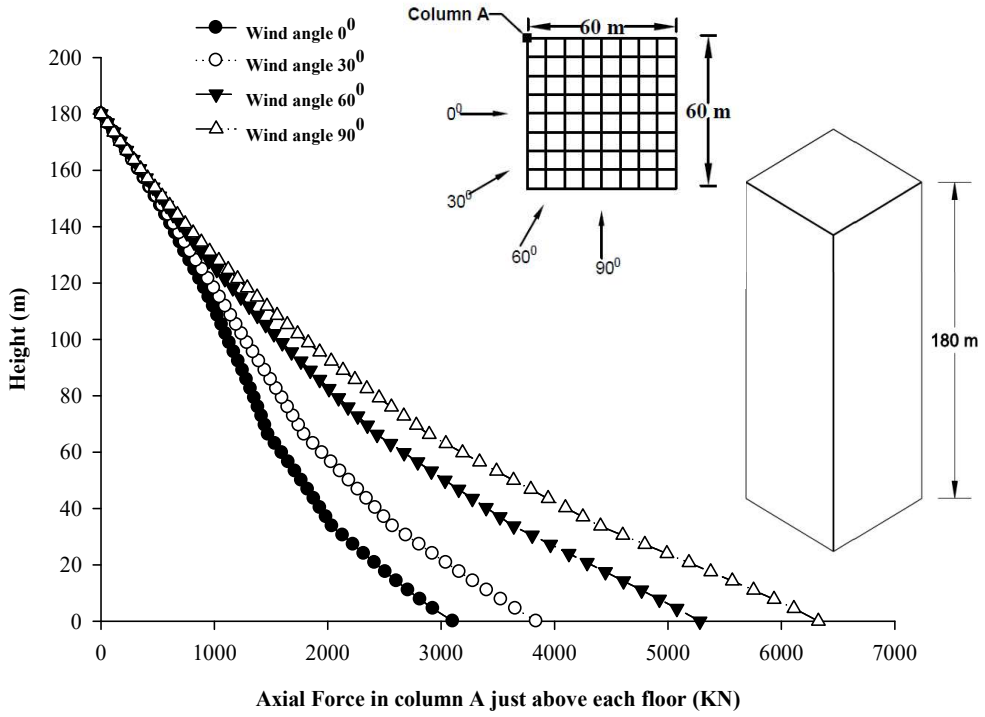

Fig. 7.9 Effect of wind angle on axial force in column-A of Sq building

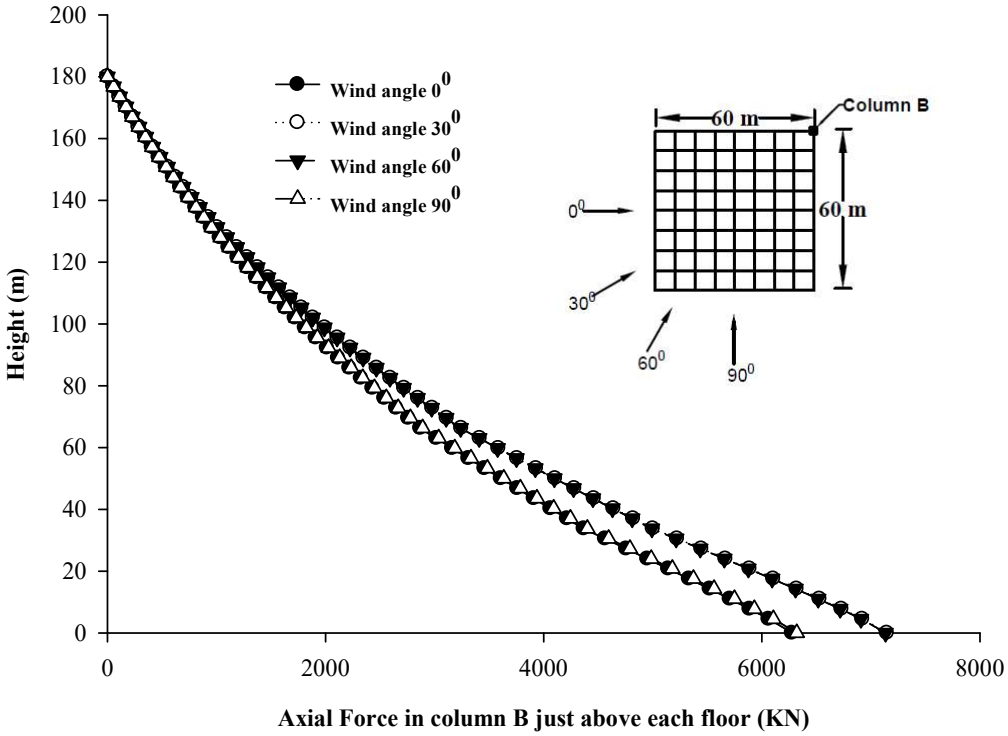

Fig. 7.10 Effect of wind angle on axial force in column-B of Sq building

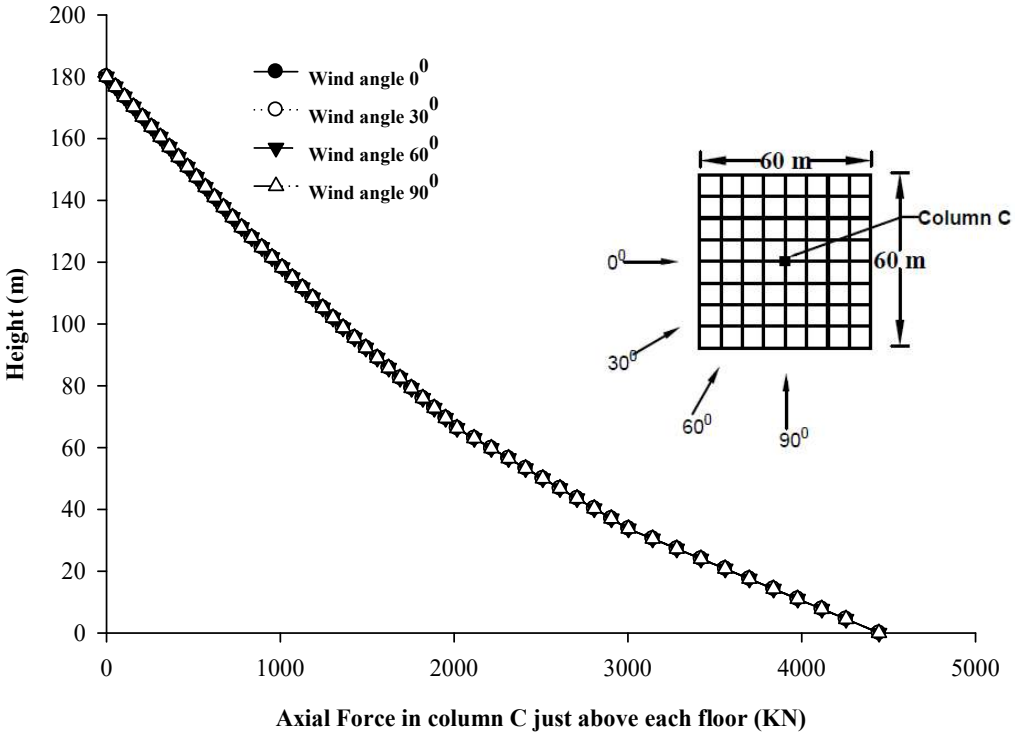

Fig. 7.11 Effect of wind angle on axial force in column-C of Sq building

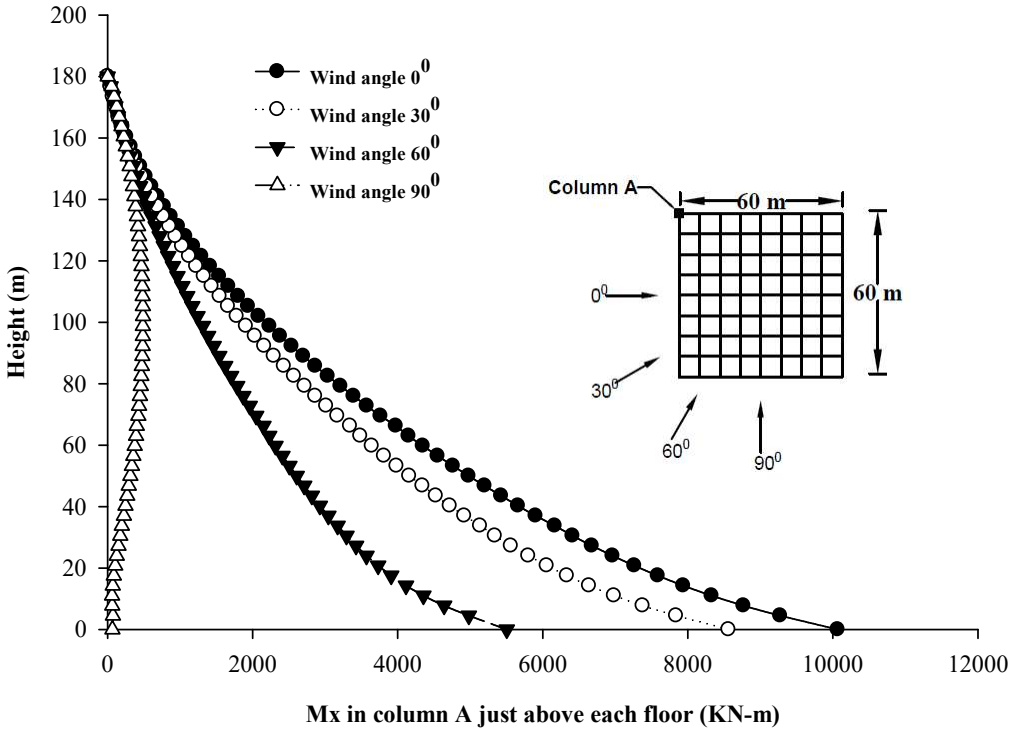

Fig. 7.12 Effect of wind angle on M_x in column-A of Sq building

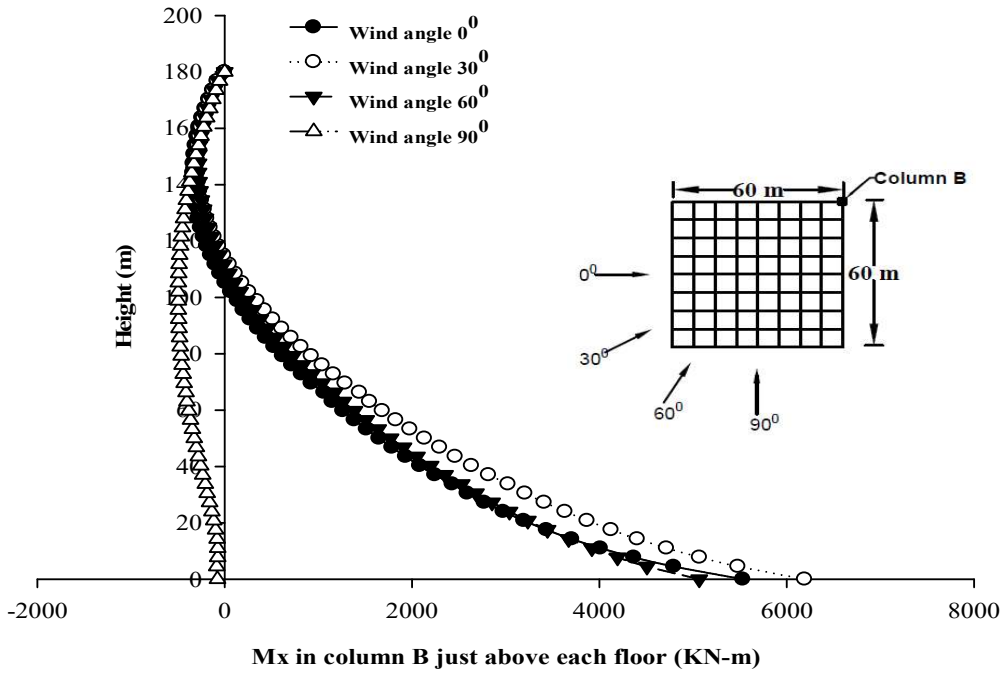

Fig. 7.13 Effect of wind angle on M_x in column-B of Sq building

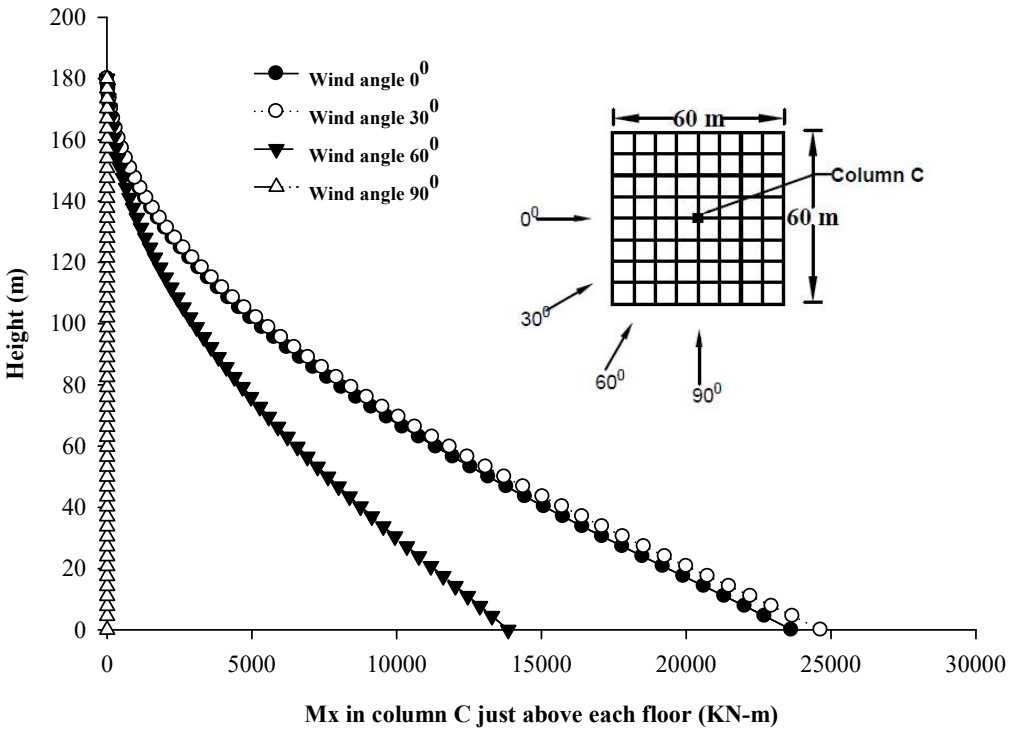

Fig. 7.14 Effect of wind angle on M_x in column-C of Sq building

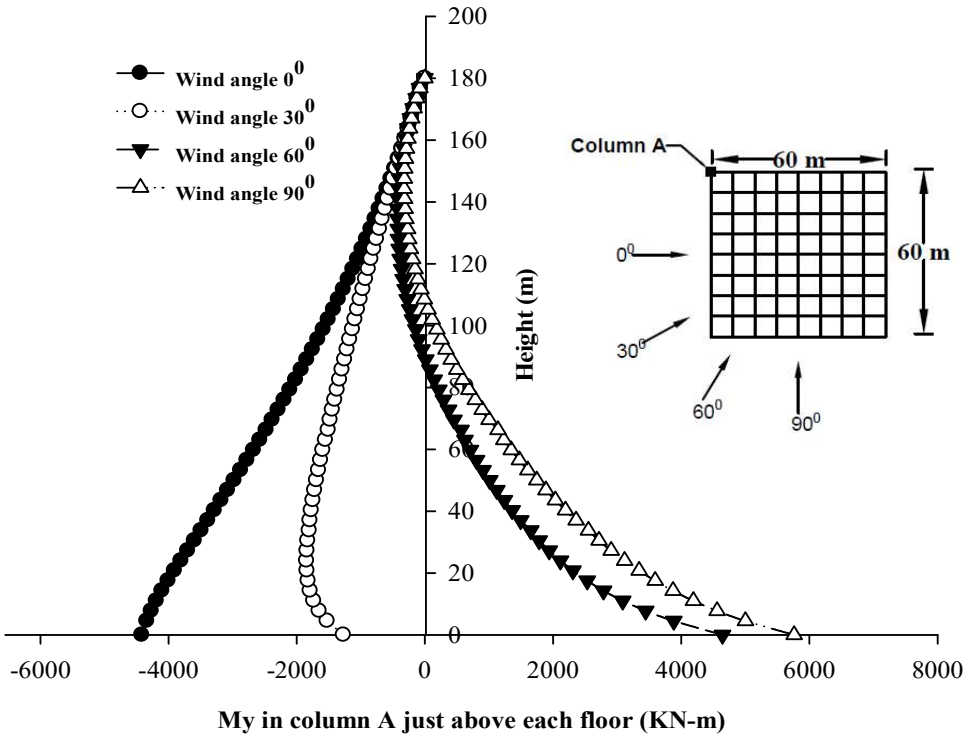

Fig. 7.15 Effect of wind angle on M_y in column-A of Sq building

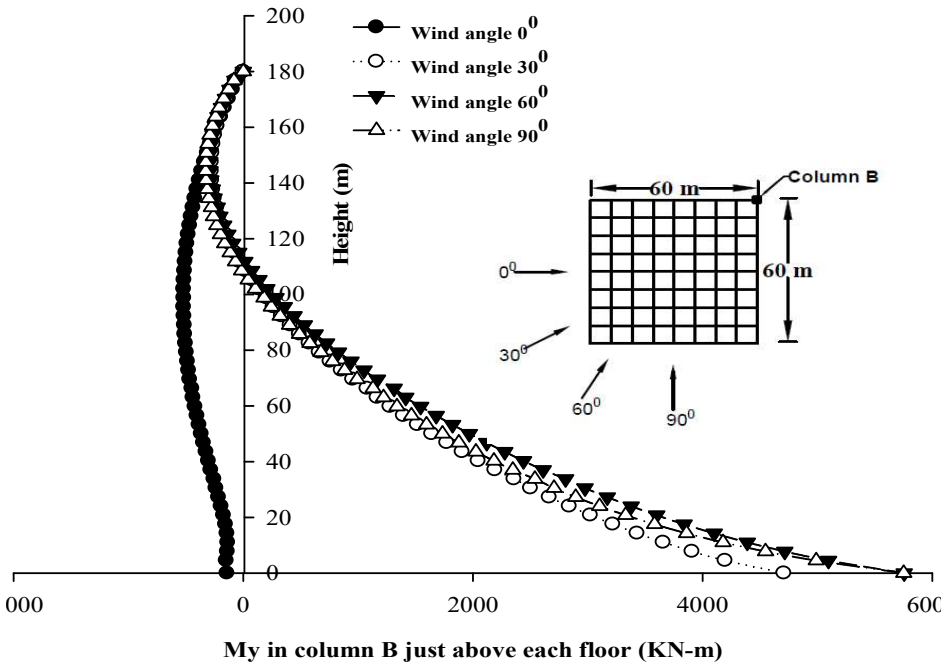

Fig. 7.16 Effect of wind angle on M_y in column-B of Sq building

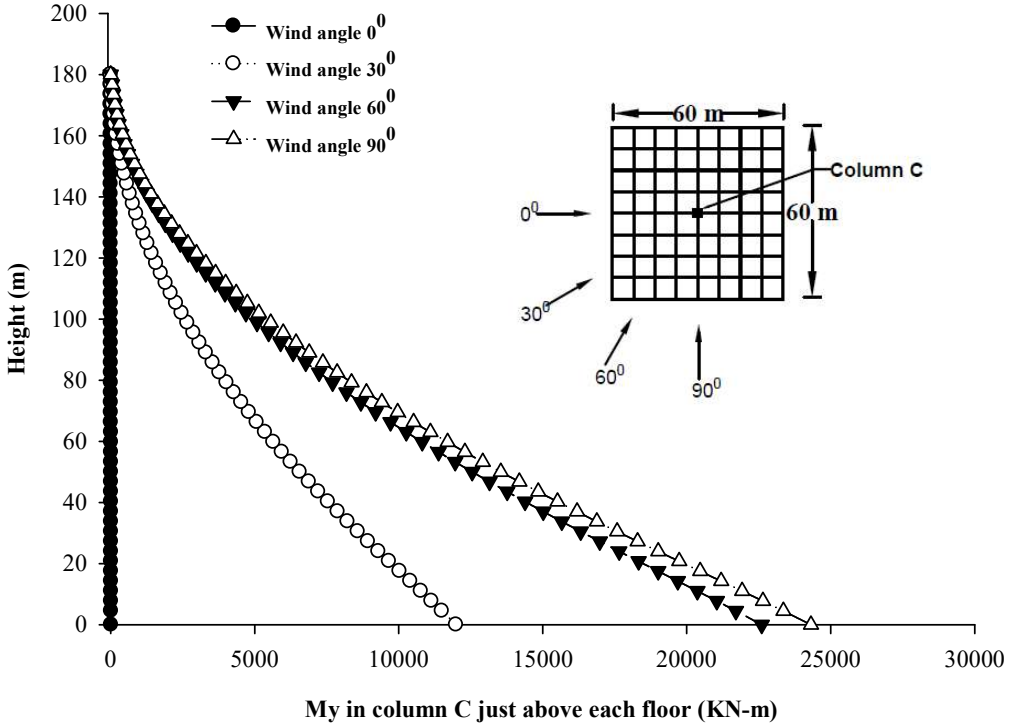

Fig. 7.17 Effect of wind angle on M_y in column-C of Sq building

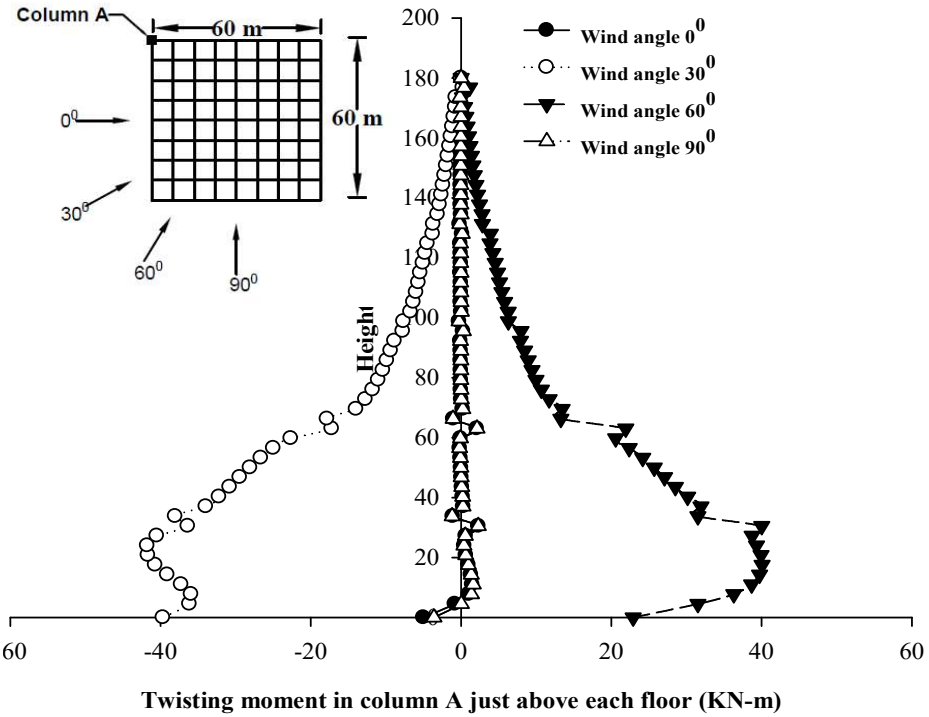

Fig. 7.18 Effect of wind angle on twisting moment M_z in column-A of Sq building

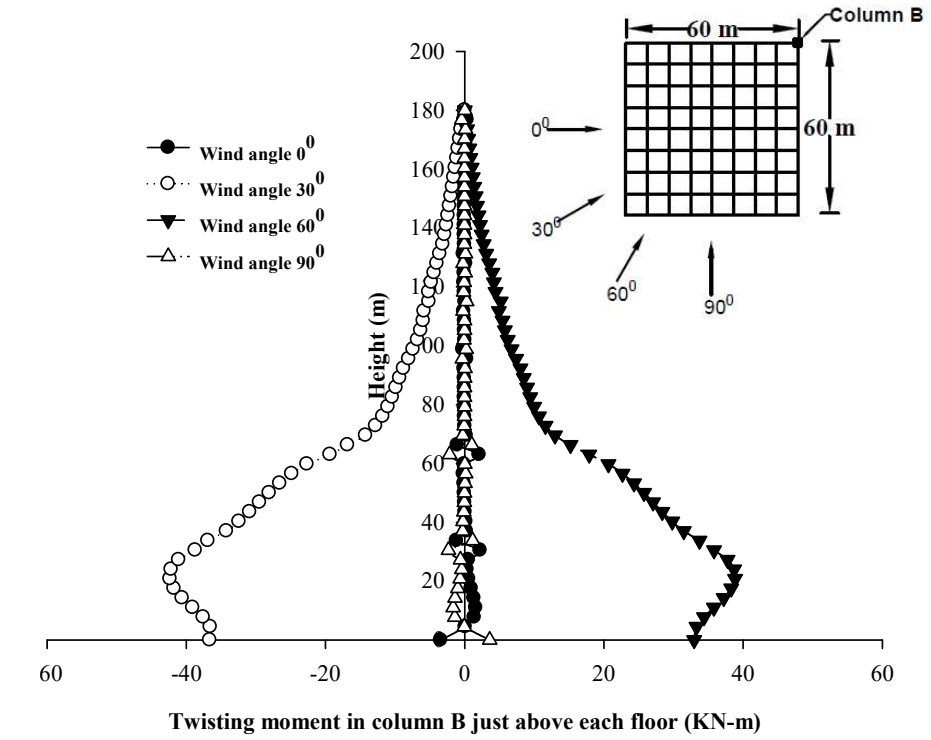

Fig. 7.19 Effect of wind angle on twisting moment M_z in column-C of Sq building

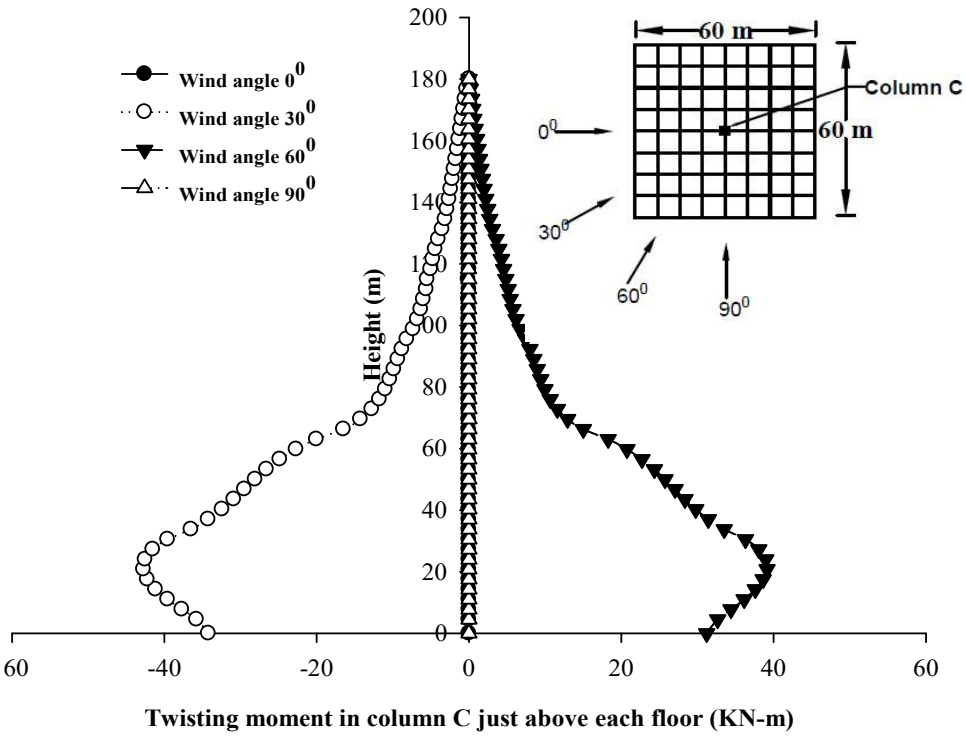

Fig. 7.20 Effect of wind angle on twisting moment M_z in column-C of Sq building

7.4.2. Interference Condition

In order to assess the effects of various interference conditions on the response of the buildings, the stress resultants in the three columns A, B and C are compared for various interference conditions similar to the isolated condition.

The variation of the axial forces in the three columns are presented in then Fig. 7.21 to 7.23, respectively. Similar to the isolated condition, the effects of various interference conditions on axial force are not significant at top 25% height of the column A and B. The axial force of column A in full blockage and half blockage conditions is significantly enlarged compare to that of isolated condition. The axial force in no blockage condition is similar to that of isolated condition. Out of all interference conditions, the full blockage condition has worst unfavorable effects on the axial force of column A. The interference effect on the axial force in column B is favorable in all conditions. The full blockage condition is most beneficial with respect to the axial force in column B. The axial force In column C is not affected by the upstream interfering building in all interference conditions.

From Fig. 7.24, the effect of interference on the moment M_x of column A is beneficial, especially in full blockage and half blockage conditions, as the moment is largely reduced at these two interference conditions. The lowest moment in column A is observed in full blockage interference condition. The moment in Column B and C is also reduced for all interference conditions. The reduction is more significant in half blockage interference condition for both the columns as shown in Fig. 7.25 and 7.26.

The variation of moment M_y in column A, B and C is shown in Fig. 7.27 to 7.29. The moment M_y is also affected by the presence of interfering building and largely depend on the position of interfering building. The moment in column A is reduced significantly in full blockage condition but increased with a great amount in no blockage condition. The half blockage condition has very little effect. The moment of column B is increased by a huge amount in full blockage condition while moment in other interference conditions has changed very slightly. The moment in central column C is zero in full blockage condition due to symmetric flow similar to the isolated condition but does not remain the same in half blockage and no blockage conditions due loss of symmetry of flow.

From Fig. 7.30, the twisting moment is affected by the presence of interfering building in half blockage and no blockage conditions only due to loss of symmetry in the flow. The

half blockage condition has more severe effect compare to the no blockage condition. The twisting moment in all three columns is same and hence only the variation of twisting moment in central column C is presented here.

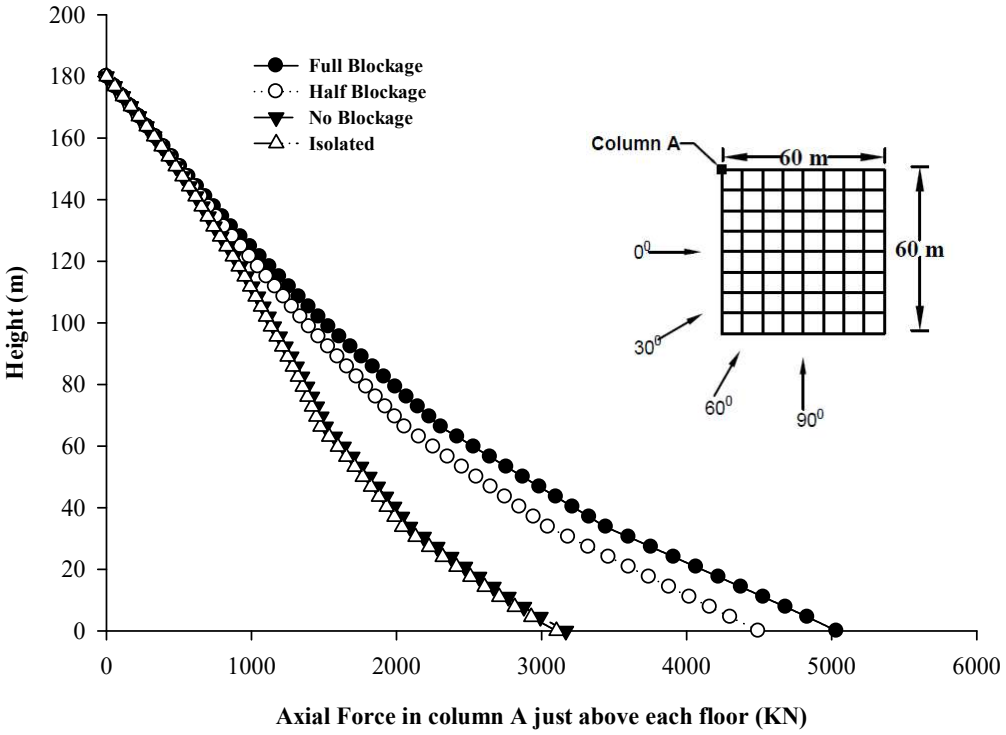

Fig. 7.21 Effect of Interference on axial force in column-A of Sq building

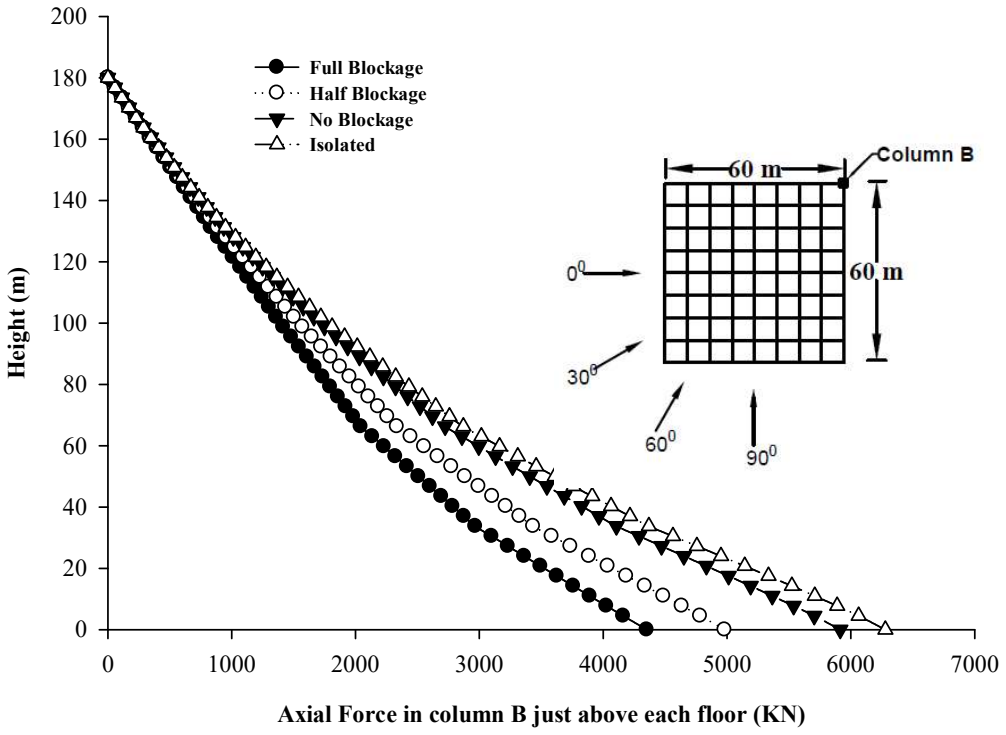

Fig. 7.22 Effect of Interference on axial force in column-B of Sq building

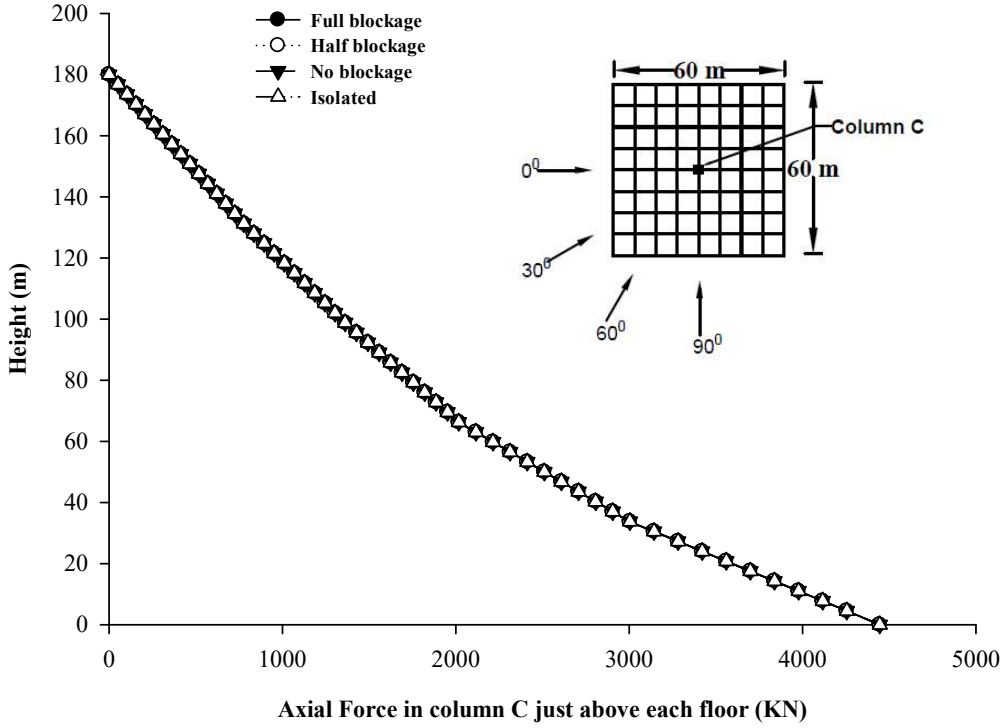

Fig. 7.23 Effect of Interference on axial force in column-C of Sq building

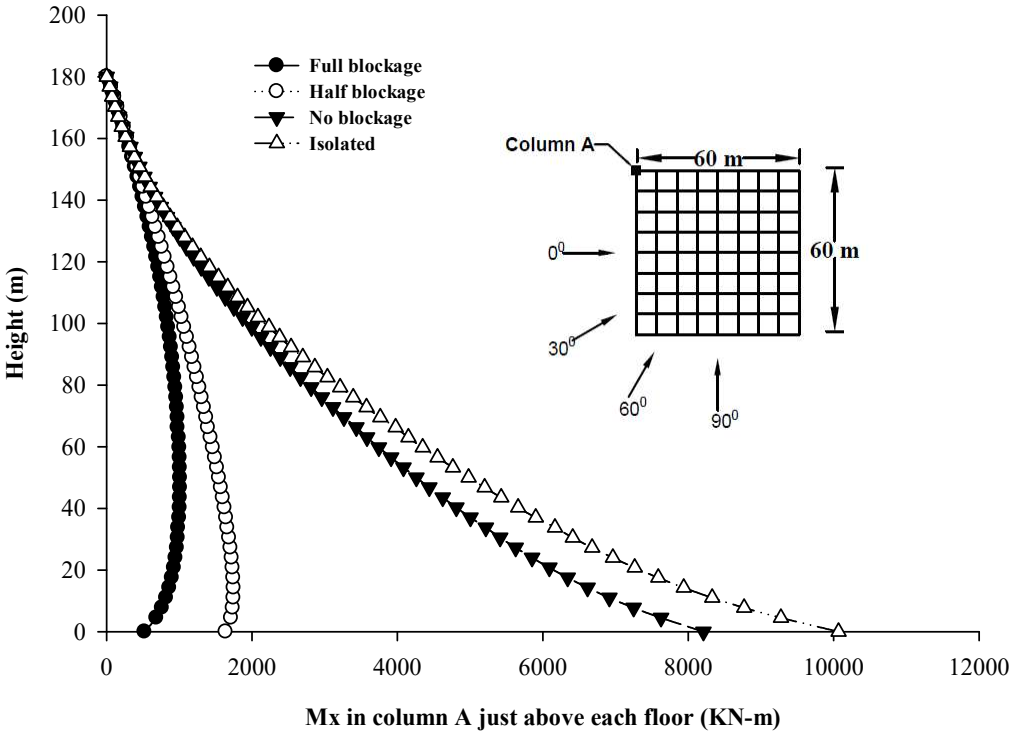

Fig. 7.24 Effect of Interference on M_x in column-A of Sq building

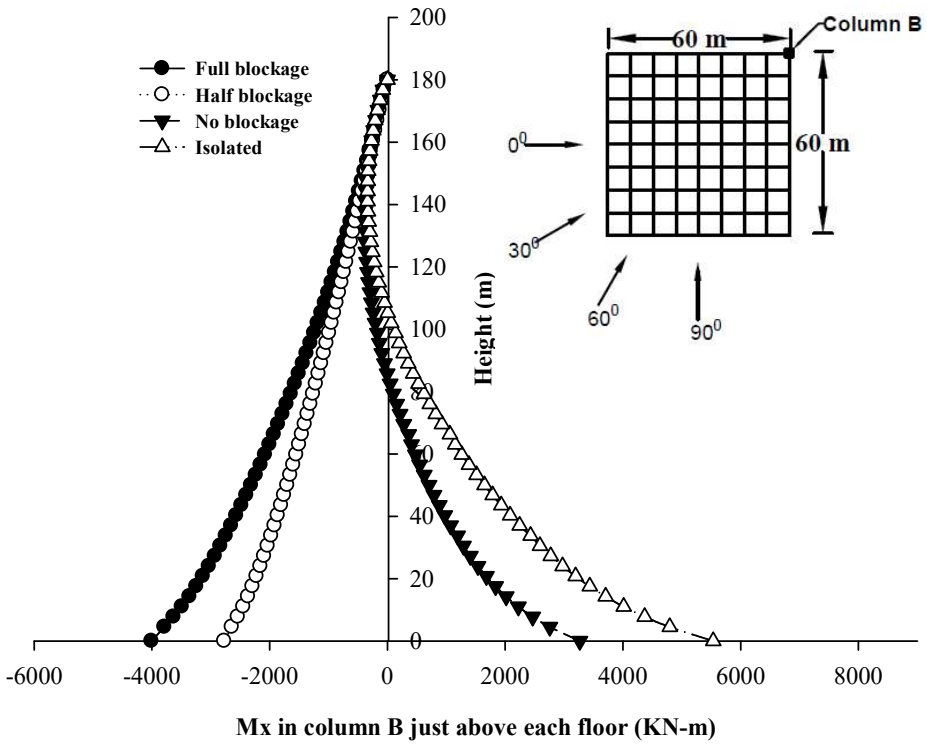

Fig. 7.25 Effect of Interference on M_x in column-A of Sq building

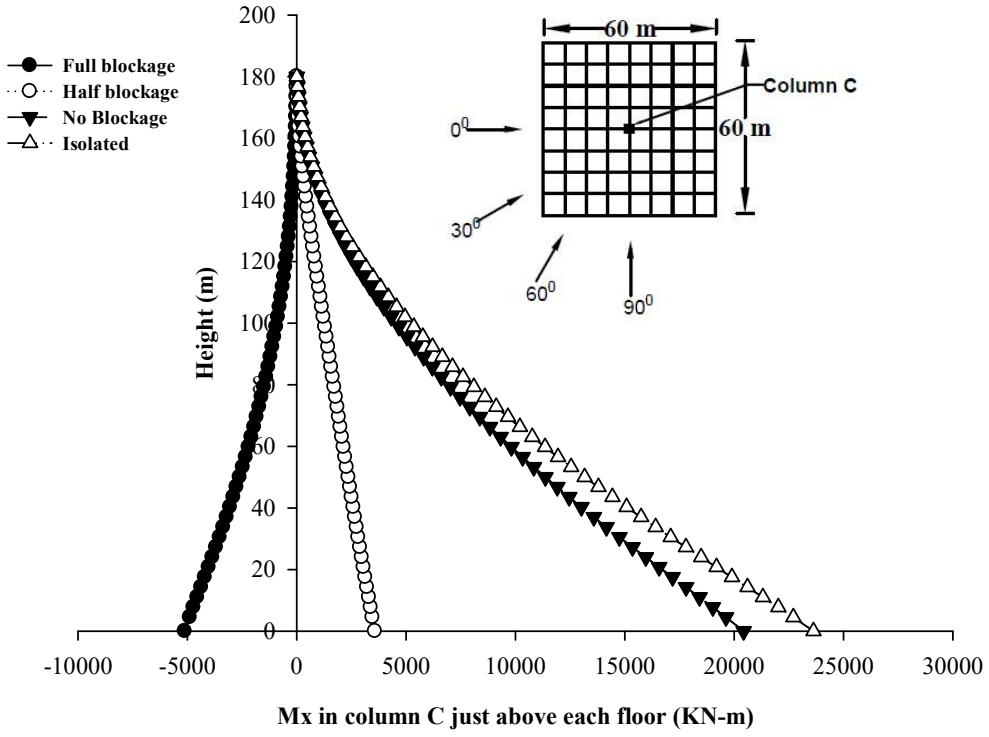

Fig. 7.26 Effect of Interference on M_x in column-C of Sq building

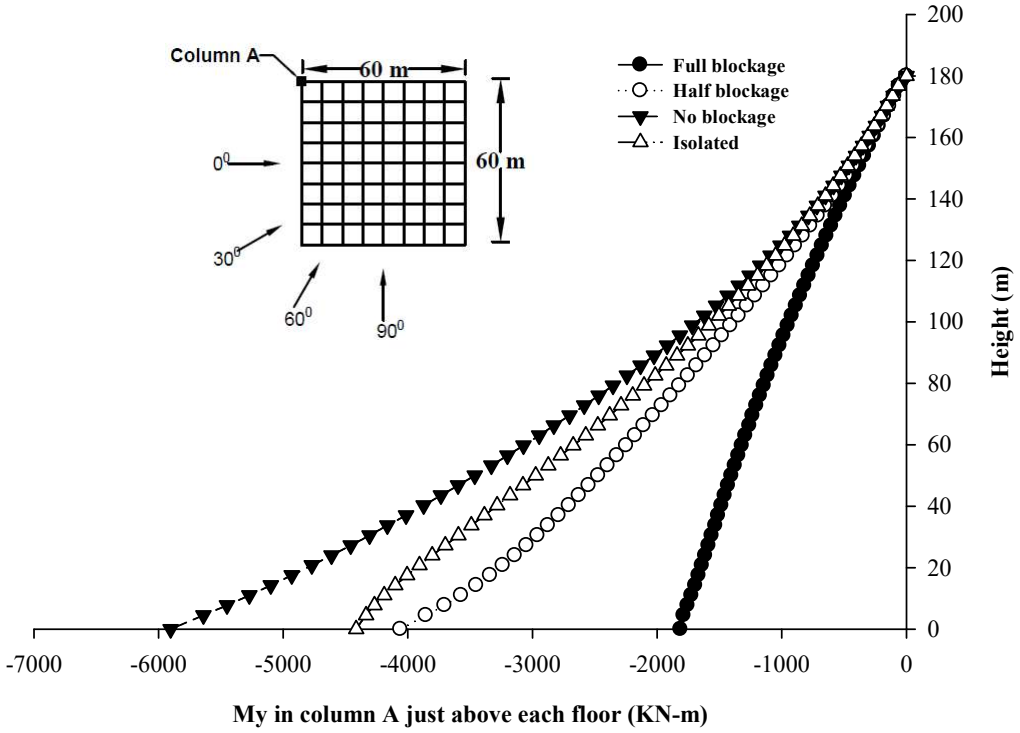

Fig. 7.27 Effect of Interference on M_y in column-A of Sq building

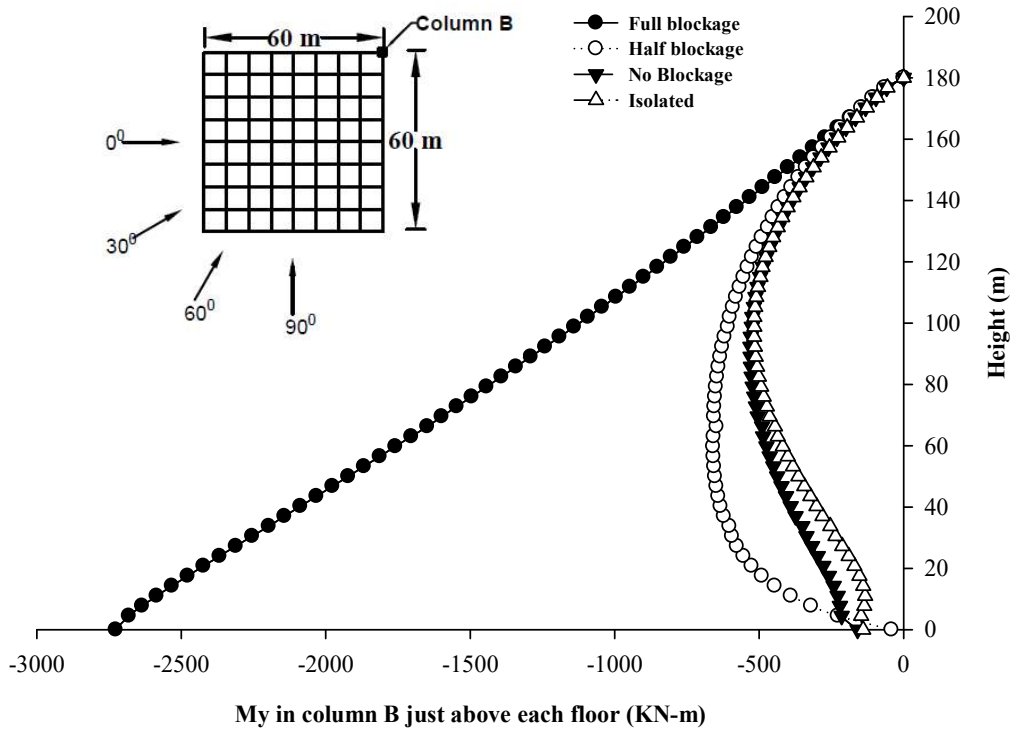

Fig. 7.28 Effect of Interference on M_y in column-B of Sq building

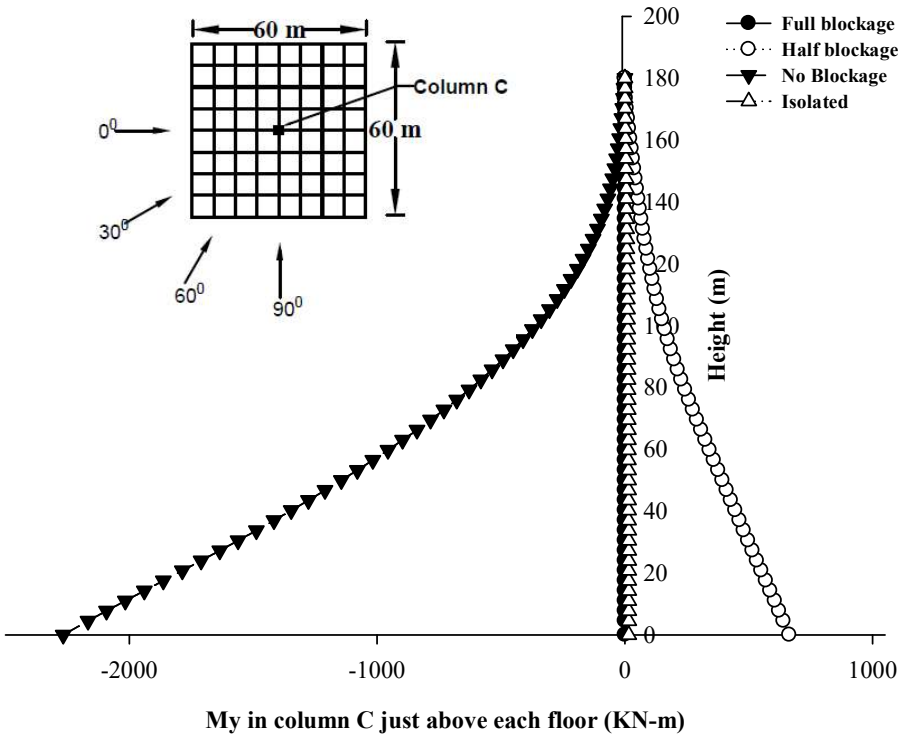

Fig. 7.29 Effect of Interference on M_y in column-C of Sq building

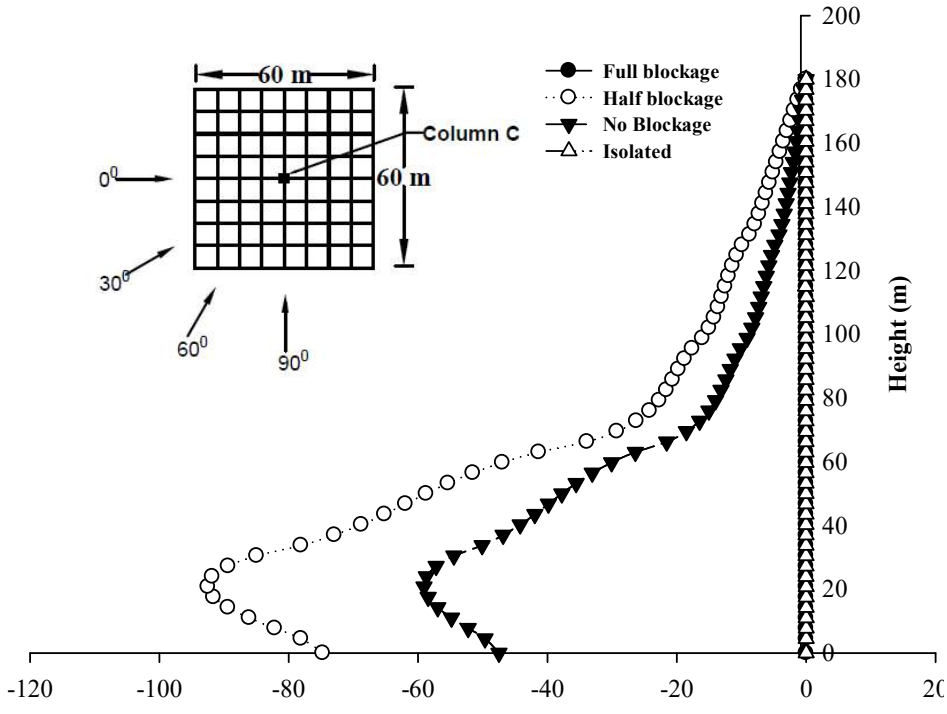

Fig. 7.30 Effect of Interference on M_z in column-C of Sq building

7.5. PL-1 BUILDING

7.5.1. Isolated Condition

In order to assess the effect of wind direction on the response of the PL-1 building, the response due to wind load calculated on the model under the wind direction of 0^0, 30^0, 60^0, 90^0 is compared. Similar to the square building, the stress resultants including axial force, M_x (global), M_y (global) and twisting moment on the three columns A, B and C (Fig. 7.31 to 7.33) are compared.

The variation of the axial forces in column A, B and C are shown in Fig. 7.31 to 7.33. The wind direction has significant effect on the axial force of column A. The axial force is minimum for 0^0 wind and increase with change in wind direction from 0^0 to 90^0. The axial force is maximum at 90^0 wind. The axial force at the base of column at 90^0 wind is reached to the double of the axial force at 0^0 wind. The effect of wind direction on the axial force of column B is not significant. The axial force in column C is not affected by the change of wind direction.

The effect of wind direction on the moment M_x of the three columns are presented in Fig. 7.34 to 7.36, respectively. The effect of wind on moment in column A and B is almost similar. Moments in the both columns reduces with change of wind angle from 0 to 90 degree. Both columns have maximum moments at the wind direction of 0^0 while minimum at wind direction of 90^0. The effect of wind direction on the column C are almost similar to the column A and B for all wind directions except 90^0 wind where the moment is zero in column C due to symmetry.

The Figures 7.37 to 7.39 represent the effect of wind direction on the moment M_y in the three columns of PL-1 building. Moment in column A is greatly affected by the wind direction. Wind at oblique angles i.e. at 30^0 and 60^0 generate less moment M_y compare to that of wind at normal to the building surface. The moment for wind at oblique angle is reduced by approximately 75% . The moment in the column B is also affected by wind direction. The wind at 90^0 wind generate maximum moment while wind at 60^0 generate the minimum M_y in the column B. The effect of wind direction on the moment M_y of column C is similar to that of moment M_x of the same column.

Twisting moment in all the columns have similar distribution and hence only the variation of central column C is presented here. The twisting moment is zero for wind directions of 0^0 and 90^0 due to symmetry in flow. The wind at 30^0 angle generate maximum twisting in all columns. Twisting moment at 60^0 wind is almost half of the moment at 30^0 wind.

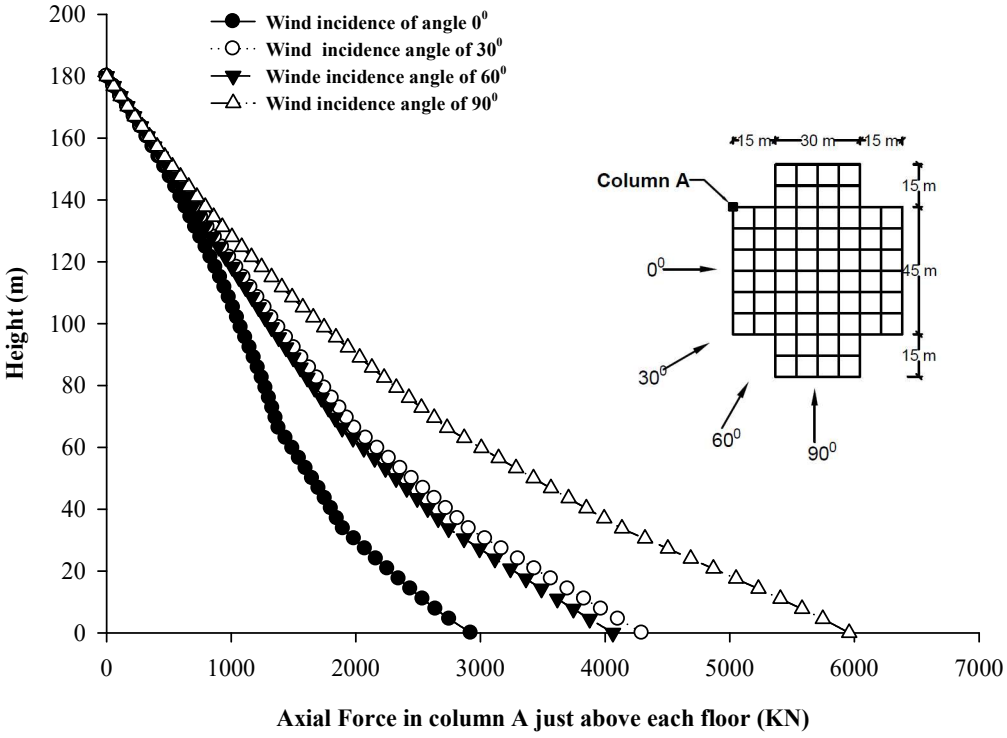

Fig. 7.31 Effect of wind angle on axial force in column-A of PL-1 building

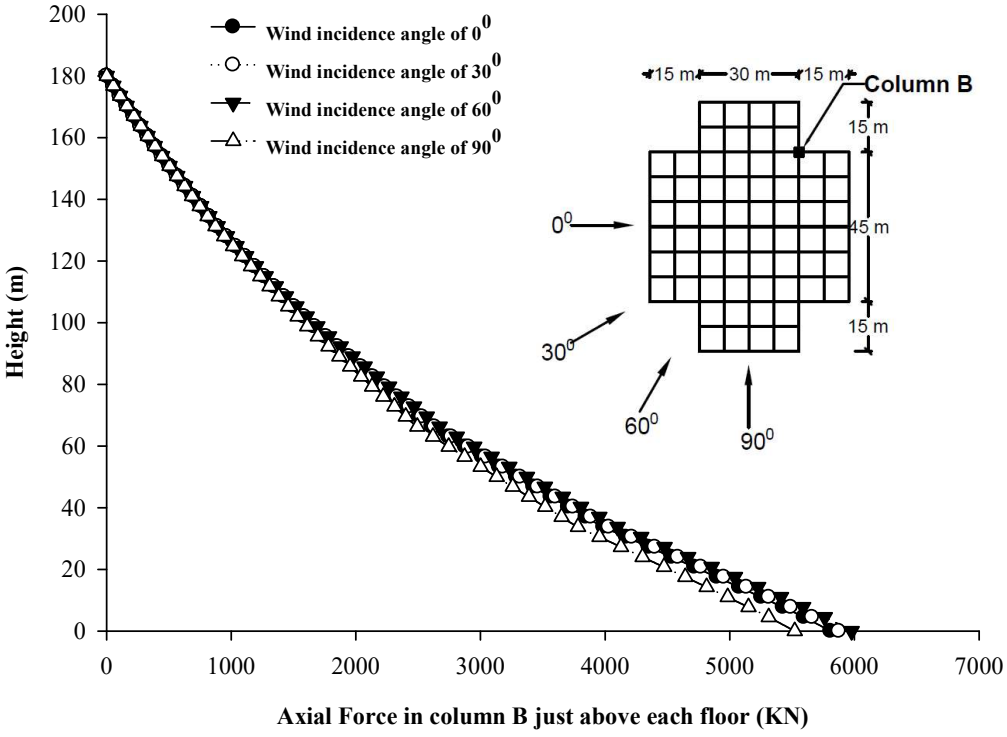

Fig. 7.32 Effect of wind angle on axial force in column-B of PL-1 building

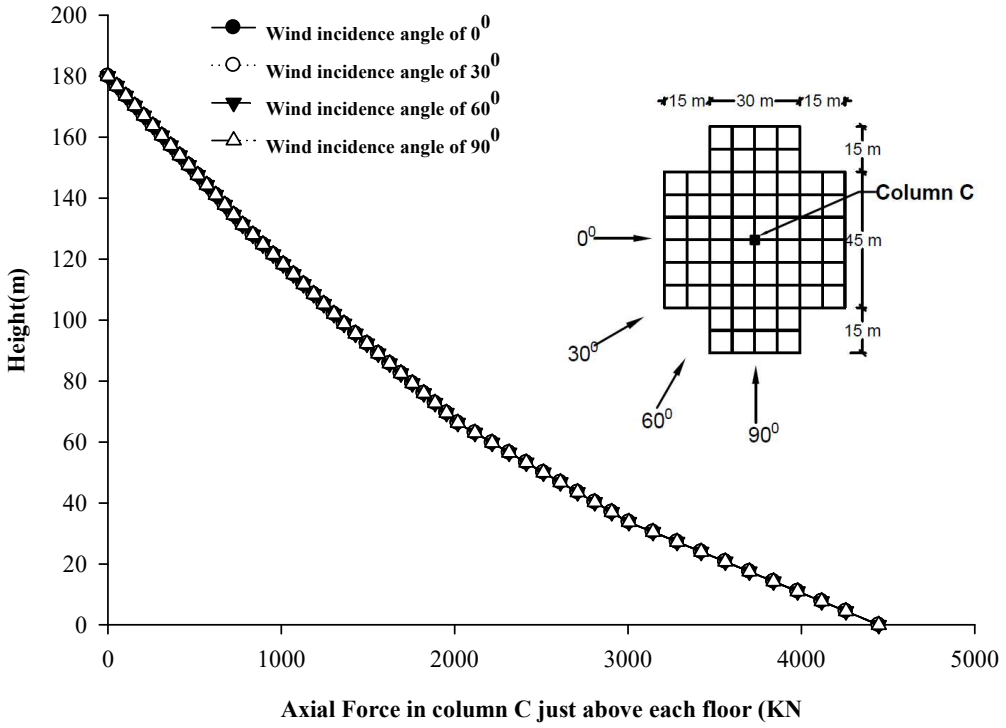

Fig. 7.33 Effect of wind angle on axial force in column-C of PL-1 building

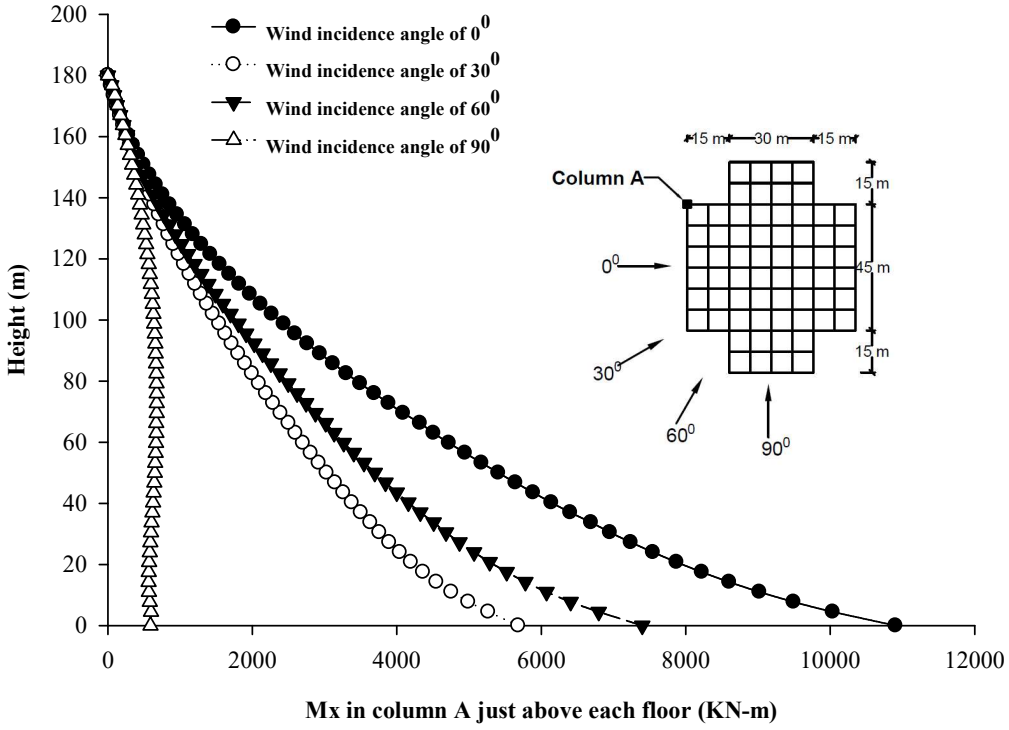

Fig. 7.34 Effect of wind angle on M_x in column-A of PL-1 building

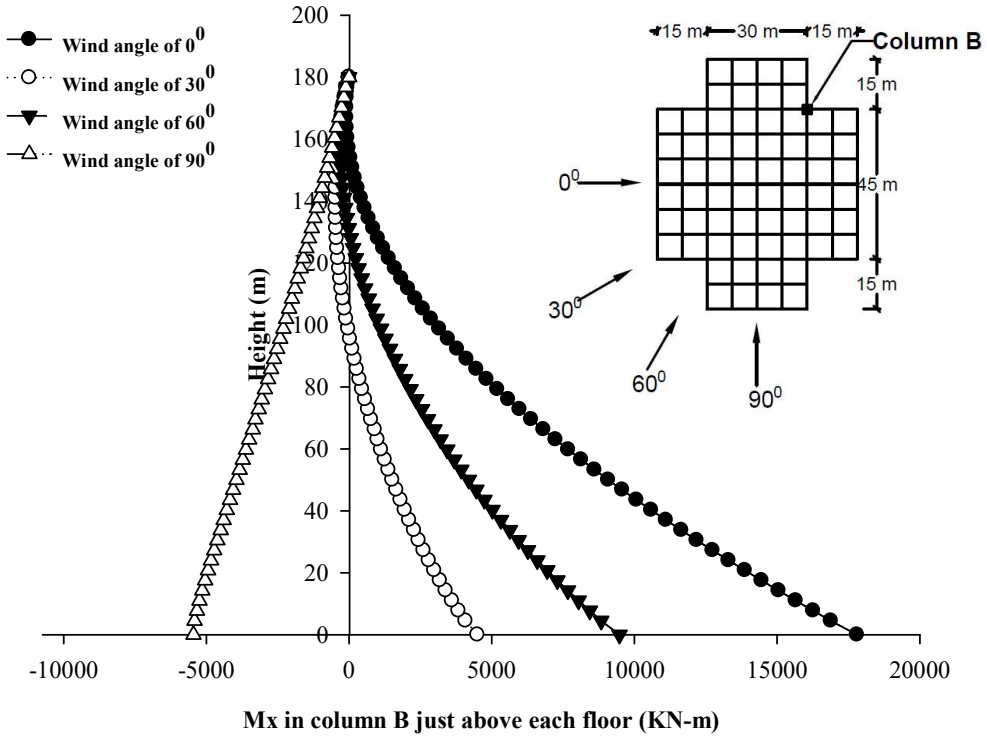

Fig. 7.35 Effect of wind angle on M_x in column-B of PL-1 building

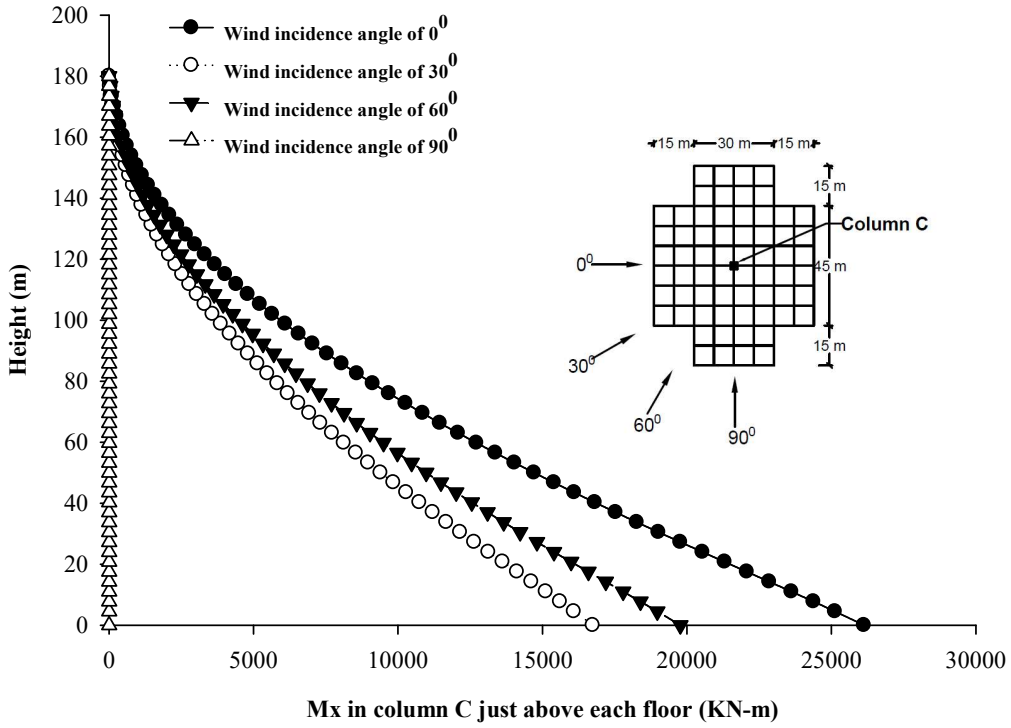

Fig. 7.36 Effect of wind angle on M_x in column-C of PL-1 building

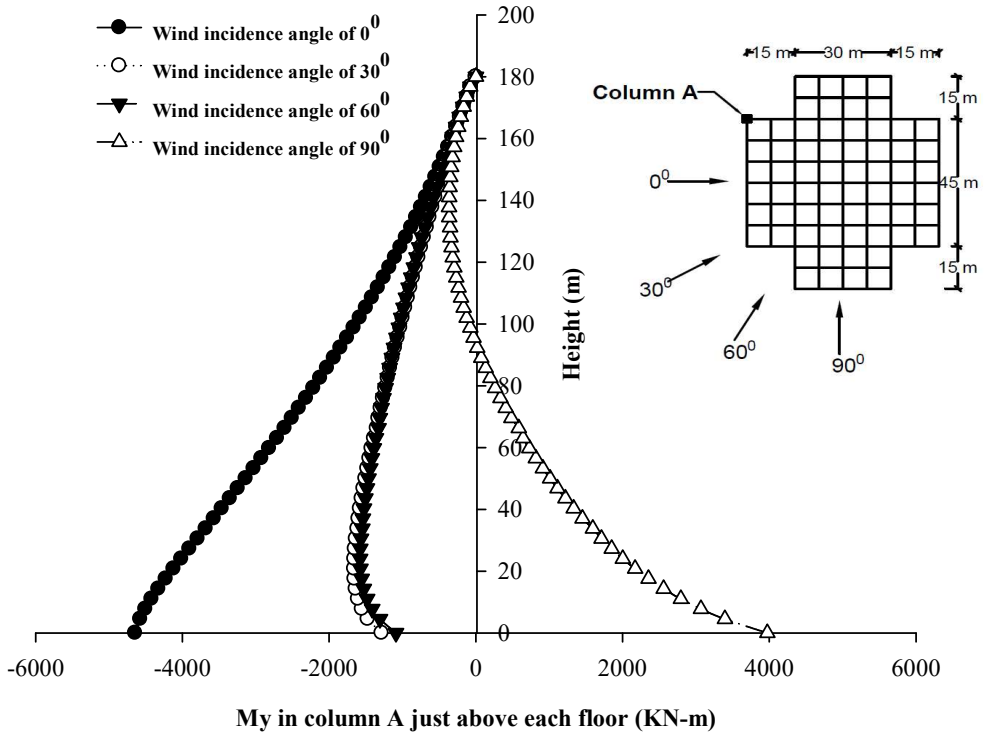

Fig. 7.37 Effect of wind angle on M_y in column-A of PL-1 building

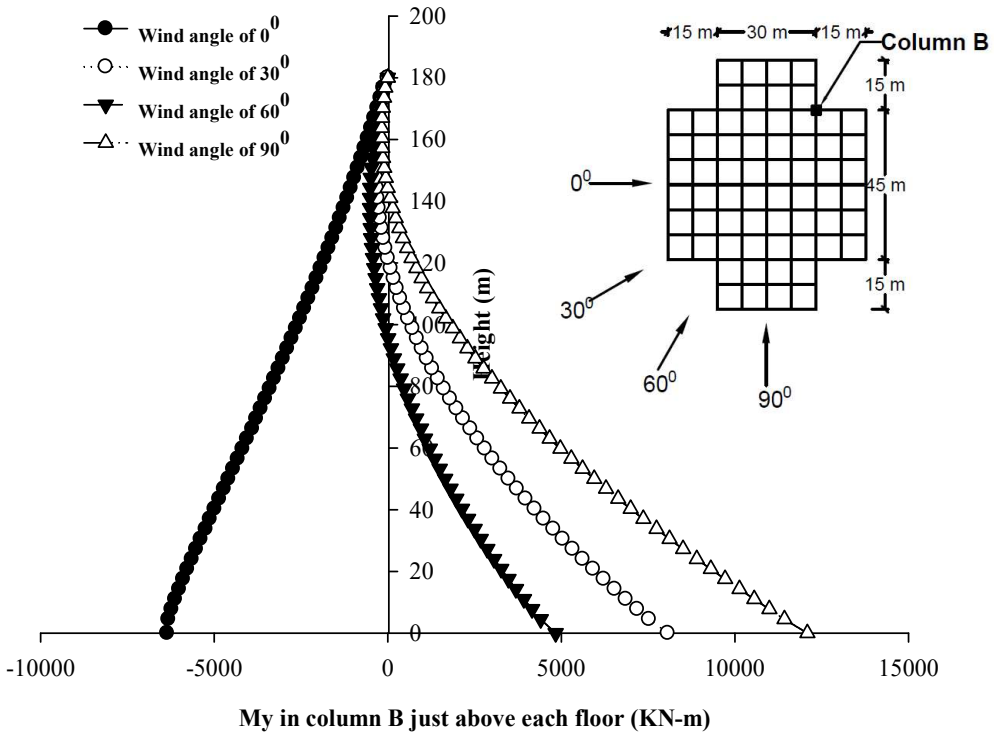

Fig. 7.38 Effect of wind angle on M_y in column-B of PL-1 building

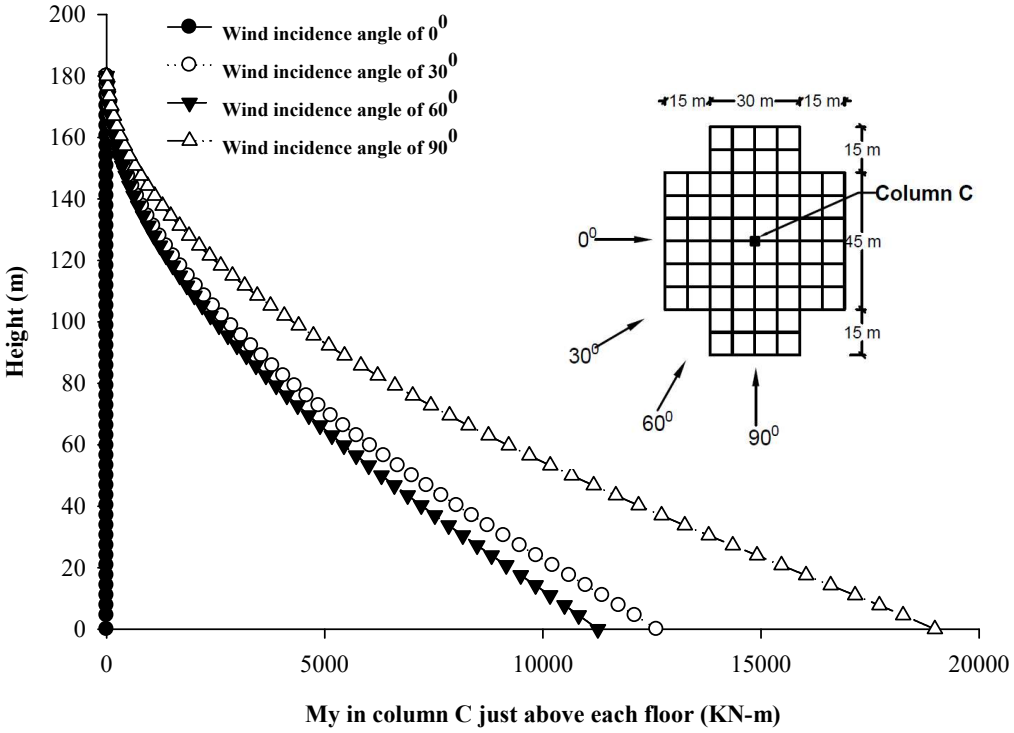

Fig. 7.39 Effect of wind angle on M_y in column-C of PL-1 building

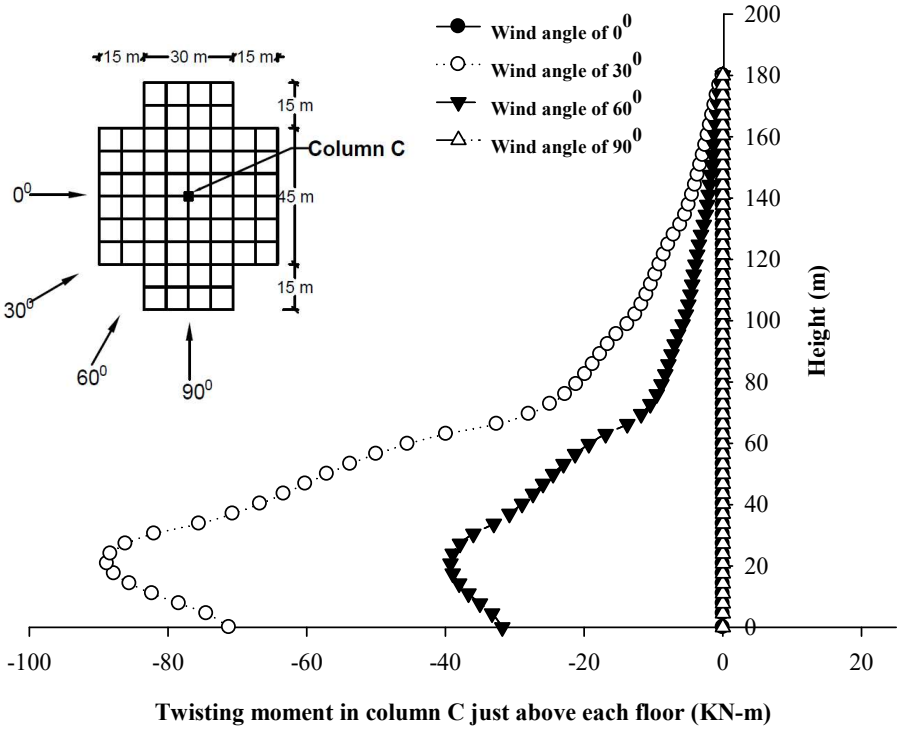

Fig. 7.40 Effect of wind angle on M_z in column-C of PL-1 building

7.5.2. Interference Condition

In order to assess the effects of various interference conditions on the response of the PL-1 buildings, the stress resultants in the three columns A, B and C for three interference conditions as full blockage, half blockage and no blockage are compared with the stress resultants for the isolated condition.

The effect of different interference conditions on the axial forces in three columns is presented through the Fig. 7.41 to 7.43. The axial force in column A affected by the interference building at upstream. The effect is more pronounced at full blockage condition where the axial force is 1.7 time the axial force in isolated condition. The half blockage condition and no blockage condition produce comparatively lesser effects and the axial force is almost 1.2 time the axial force in isolated condition. The effect of interference condition on column B is observed only in full blockage which is beneficial as the axial force is reduced to $3/4^{th}$ of the isolated condition. The axial force of column C is not affected by the interference condition.

From Fig. 7.44 to 7.46, all the interference conditions have beneficial effects on the moment M_x of the three columns. Moment in all the three column is reduced greatly for full blockage interference condition. The moment in column A is almost reduced to zero at base. The reductions for other interference condition are also significant but less than those in full blockage condition.

The variation of moment M_y in the three columns is shown in Fig. 7.47 to 7.49. Similar to the M_x, the full blockage condition has also beneficial effect on the moment in column A. The column A moment is reduced to almost 25% of the isolated condition. The half blockage and no blockage interference conditions have more positive effects compare to the full blockage condition on the moment M_y of the column B. The moment in column C is not affected by the upstream building in full blockage and remain zero as in isolated condition due to symmetry. The moment is maximum in no blockage condition.

The effect of various interference condition on the twisting moment is shown in Fig. 7.50 for column C only because of similar effects on the all three columns. Similar to the square building, there is no effect of the full blockage condition on the twisting moment, whereas the half blockage condition has more sever effect compare to the no blockage condition.

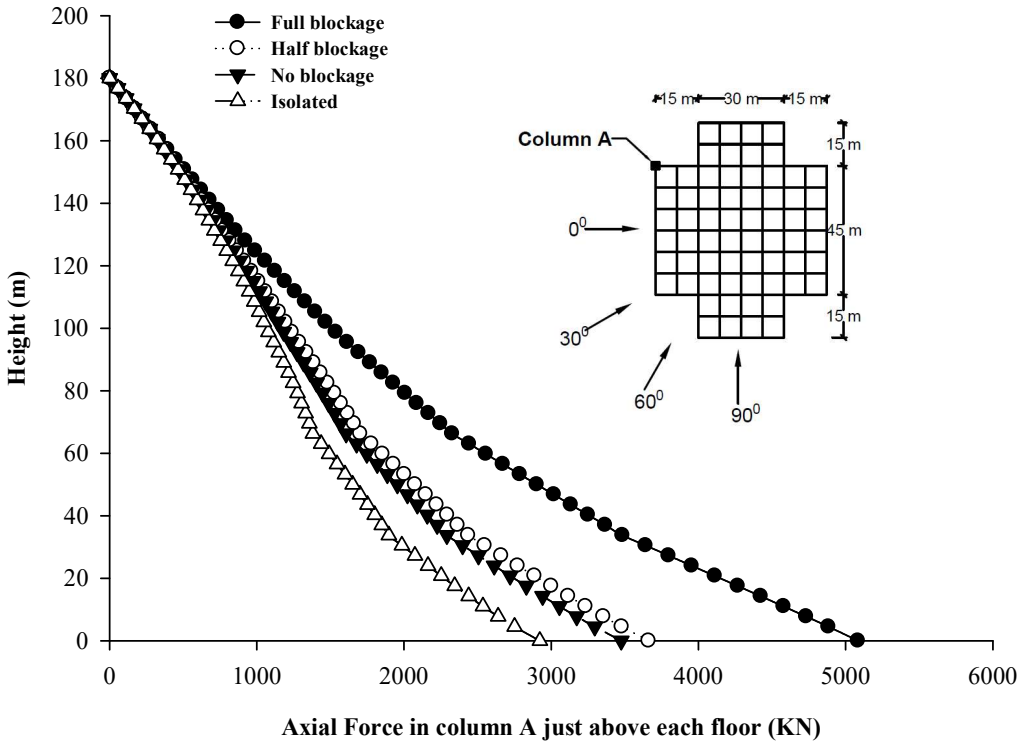

Fig. 7.41 Effect of Interference on axial force in column-A of PL-1 building

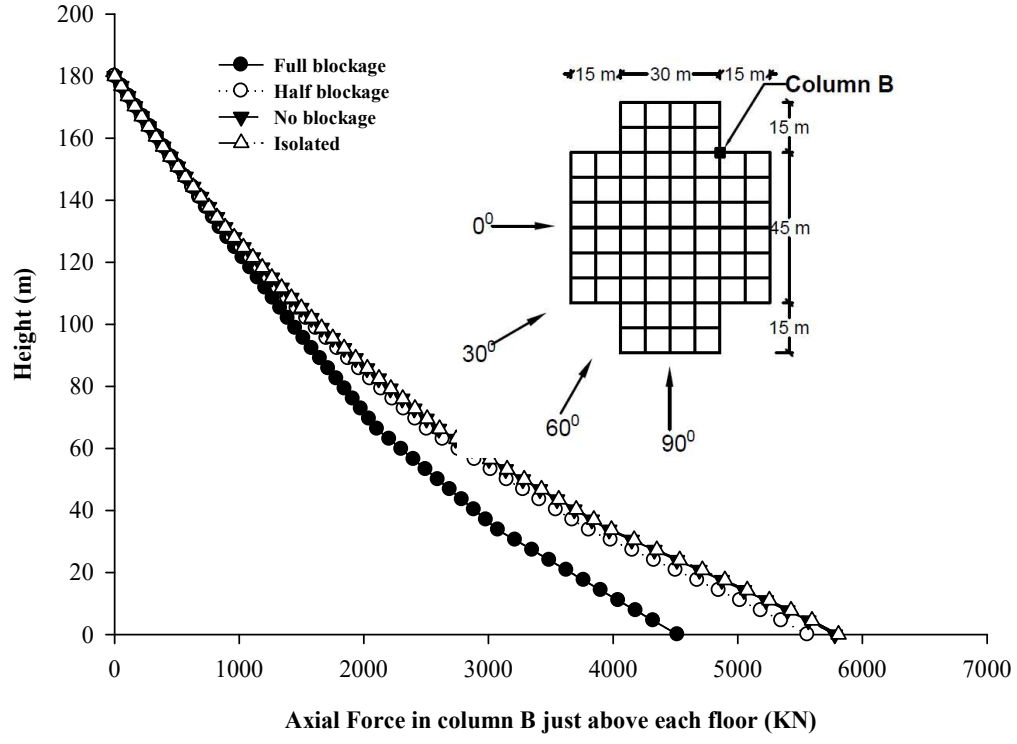

Fig. 7.42 Effect of Interference on axial force in column-B of PL-1 building

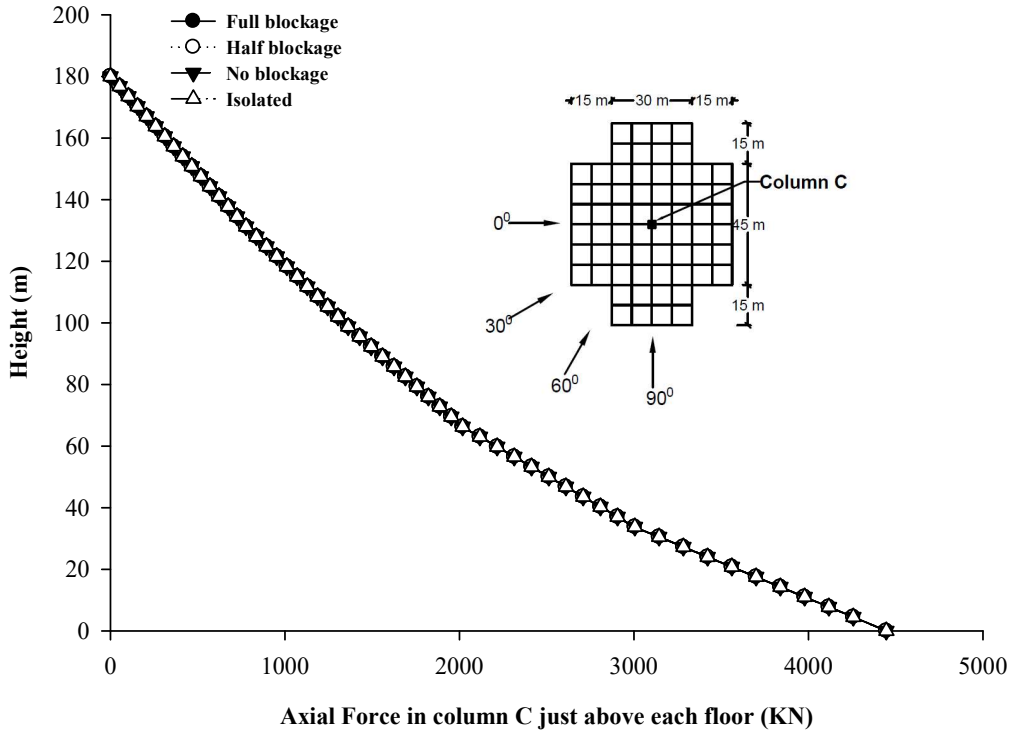

Fig. 7.43 Effect of Interference on axial force in column-C of PL-1 building

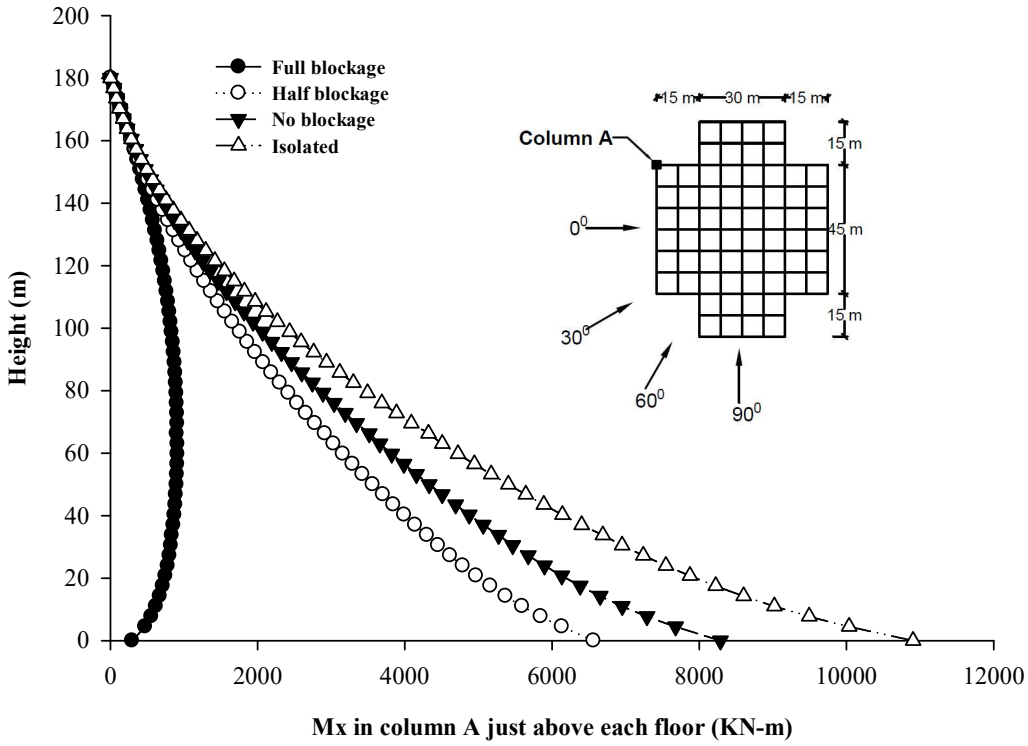

Fig. 7.44 Effect of Interference on M_x in column-A of PL-1 building

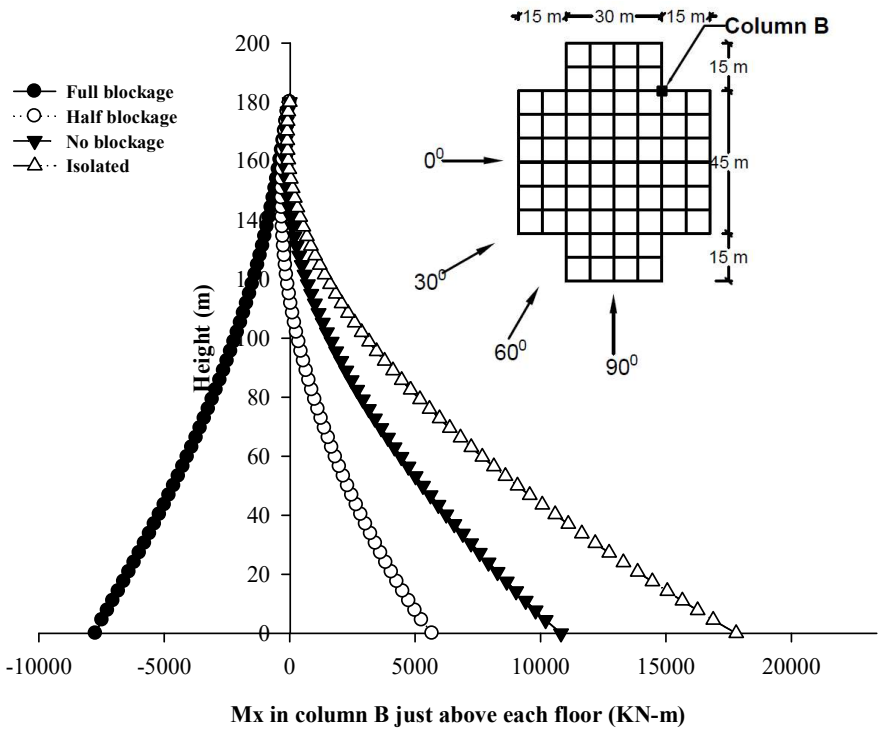

Fig. 7.45 Effect of Interference on M_x in column-B of PL-1 building

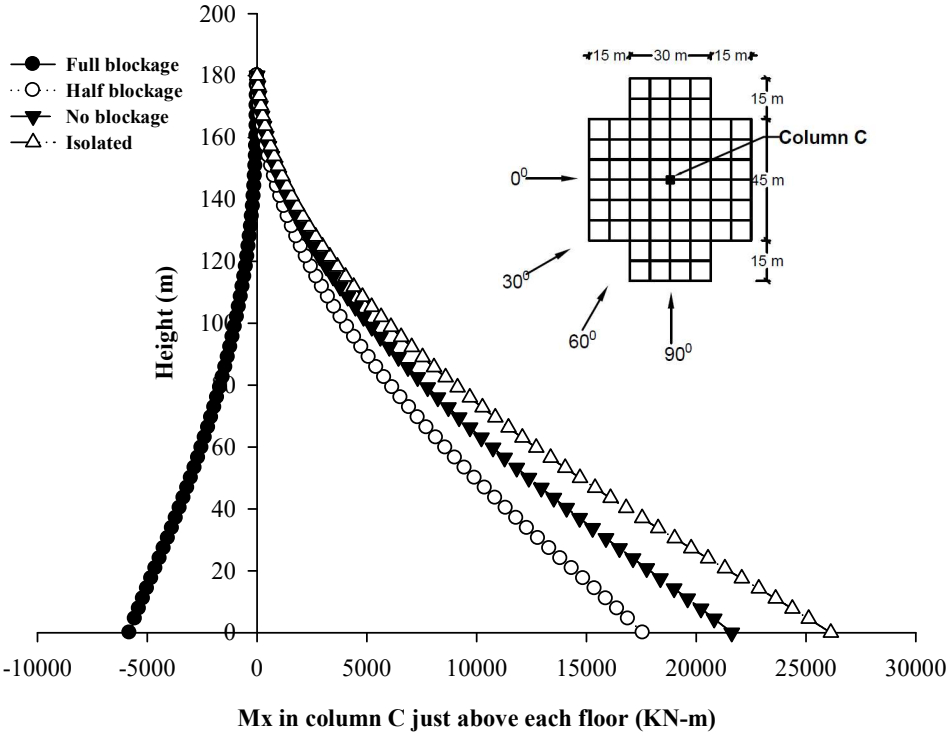

Fig. 7.46 Effect of Interference on M_x in column-C of PL-1 building

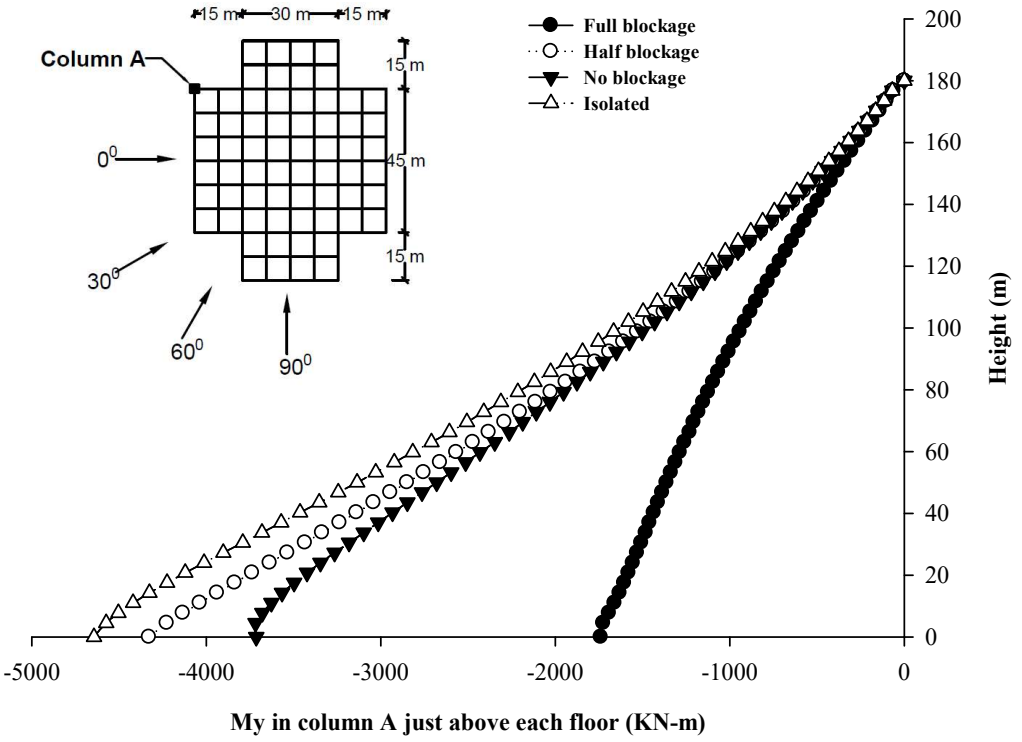

Fig. 7.47 Effect of Interference on M_y in column-A of PL-1 building

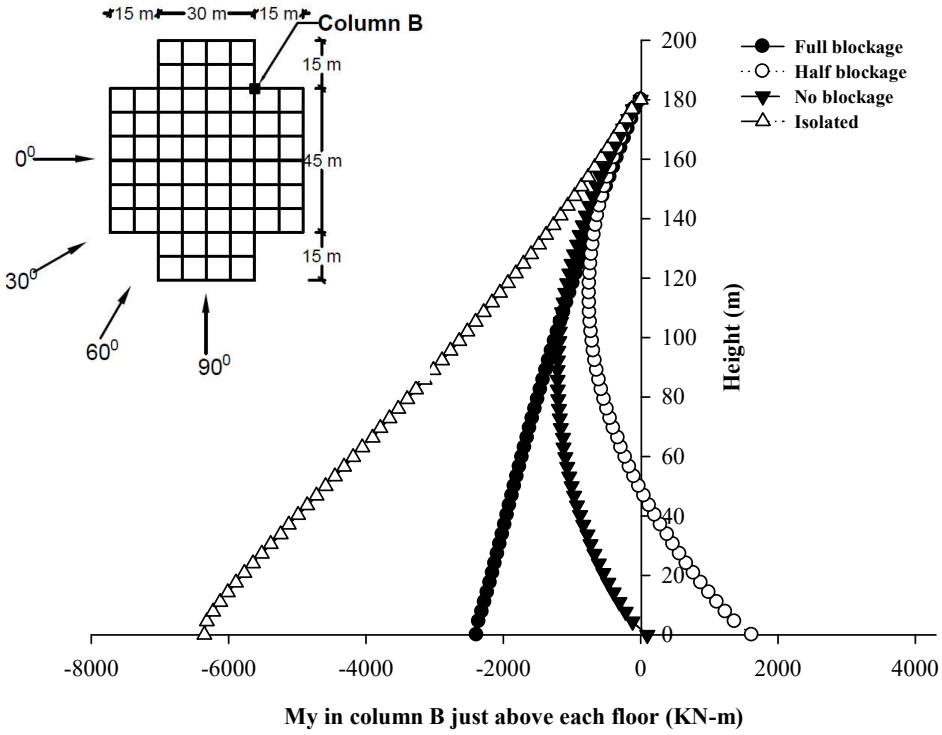

Fig. 7.48 Effect of Interference on M_y in column-B of PL-1 building

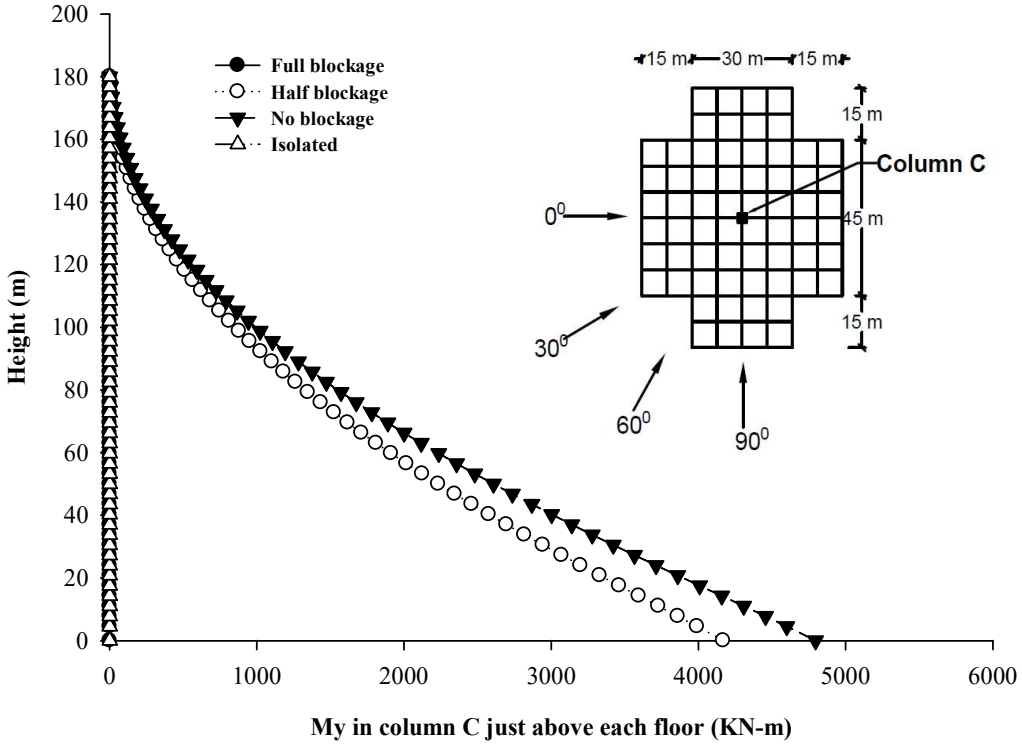

Fig. 7.49 Effect of Interference on M_y in column-C of PL-1 building

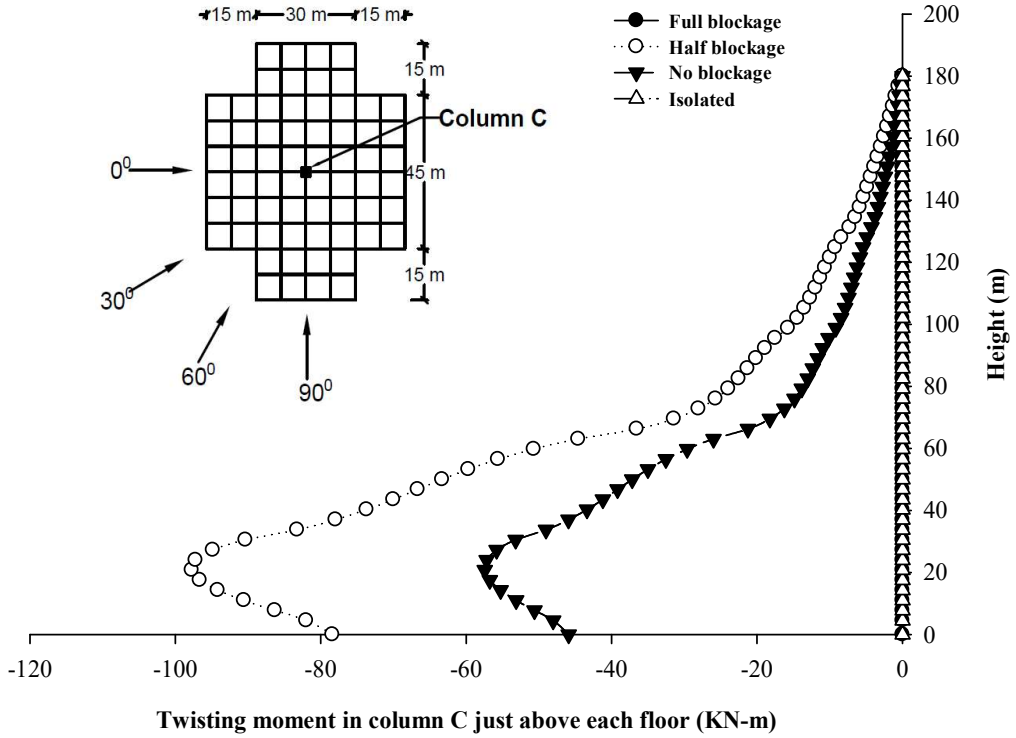

Fig. 7.50 Effect of Interference on M_Z in column-C of PL-1 building

7.6. PL-2 BUILDING

7.6.1. isolated condition

The Fig. 7.51 to 7.53 show the variation of axial forces in column A, B and C, respectively of PL-1 building under the wind directions of 0^0, 30^0, 60^0, 90^0. The wind direction effects the axial force of column A of PL-2 building similar to the PL-1 building. The axial force in column A is increasing with increase of wind angle form 0^0 to 90^0. The axial force for wind at 90^0 is almost 2.8 times the axial for wind at 0^0. The axial force in column B is not much affected by the wind direction. The axial force is slightly reduce for higher wind angles. There is no effect of change of wind incidence angles on the axial force of column C.

The wind direction effects on the moment M_x is shown in Fig. 7.54 to 7.56 for the column A, B and C respectively. The moments in all columns is reduces with increase in wind angle. All the columns have their maximum moment for wind at 0^0 and minimum moment for wind at 90^0. The central column C has zero moment due to symmetry in case of 90^0 wind.

From the Fig. 7.57, the moment M_y in the column A is maximum at 0^0 wind and has negative value. The moment M_y reduces with increase in wind angle till 60^0 wind and increase for 90^0 wind with positive value. The moment in Column B is also maximum with negative value at wind direction of 0^0 and reduces till wind angle 30^0. The moment M_y increase to a positive value at 90^0 wind but has value lower than 60^0 wind as shown in Fig. 7.58. The absolute maximum moment is observed at wind angle of 60^0. As shown in Fig. 7.59, the moment in column C has positive value at all wind directions. Moment M_y is zero at 0^0 wind and maximum at 60^0 wind.

The effects of wind angle on twisting moment M_z are similar on all the three columns as shown in Fig. 7.60. The twisting moment is maximum for wind at 60^0. The twisting moment at 30^0 wind is almost half of that at 60^0 wind. The wind at 0^0 and 90^0 generates zero twisting moments due to symmetric flow.

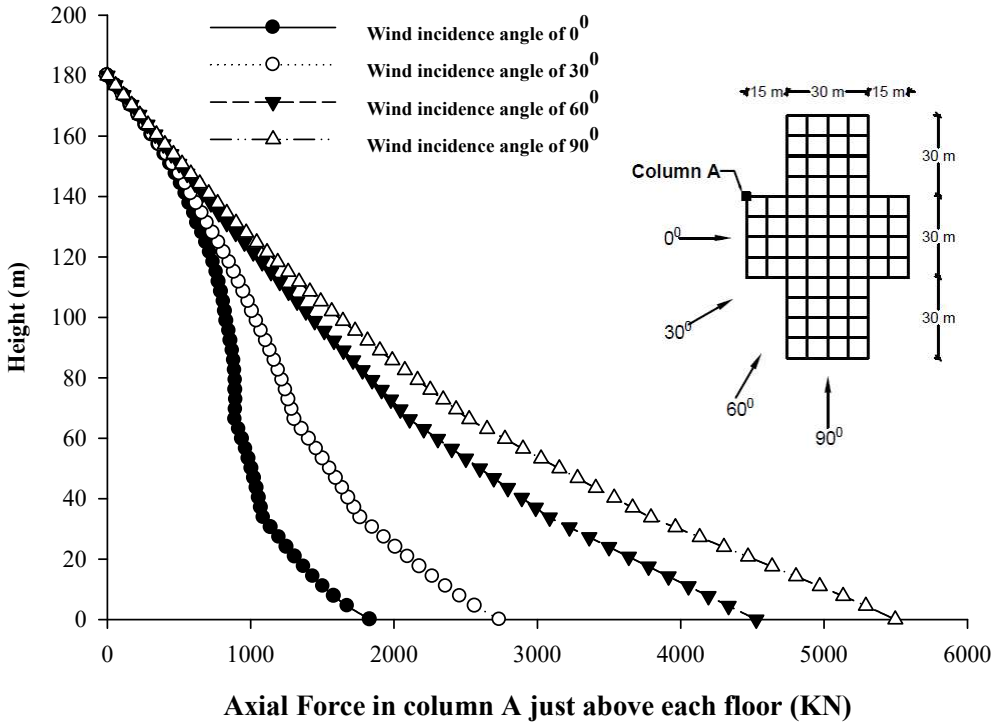

Fig. 7.51 Effect of wind angle on axial force in column-A of PL-2 building

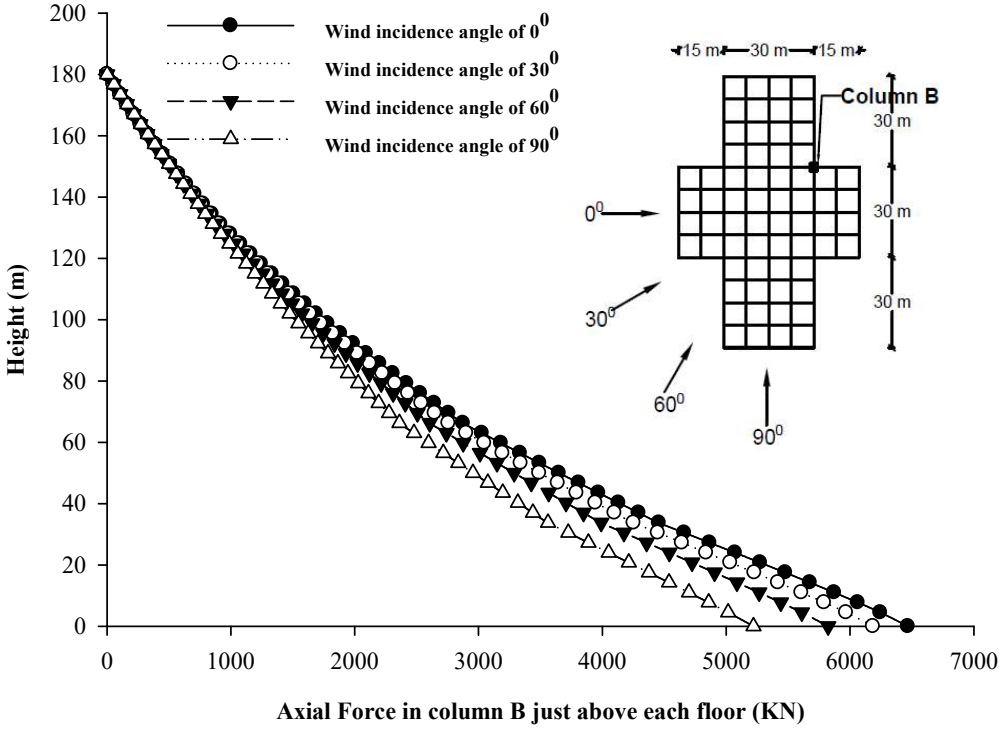

Fig. 7.52 Effect of wind angle on axial force in column-B of PL-2 building

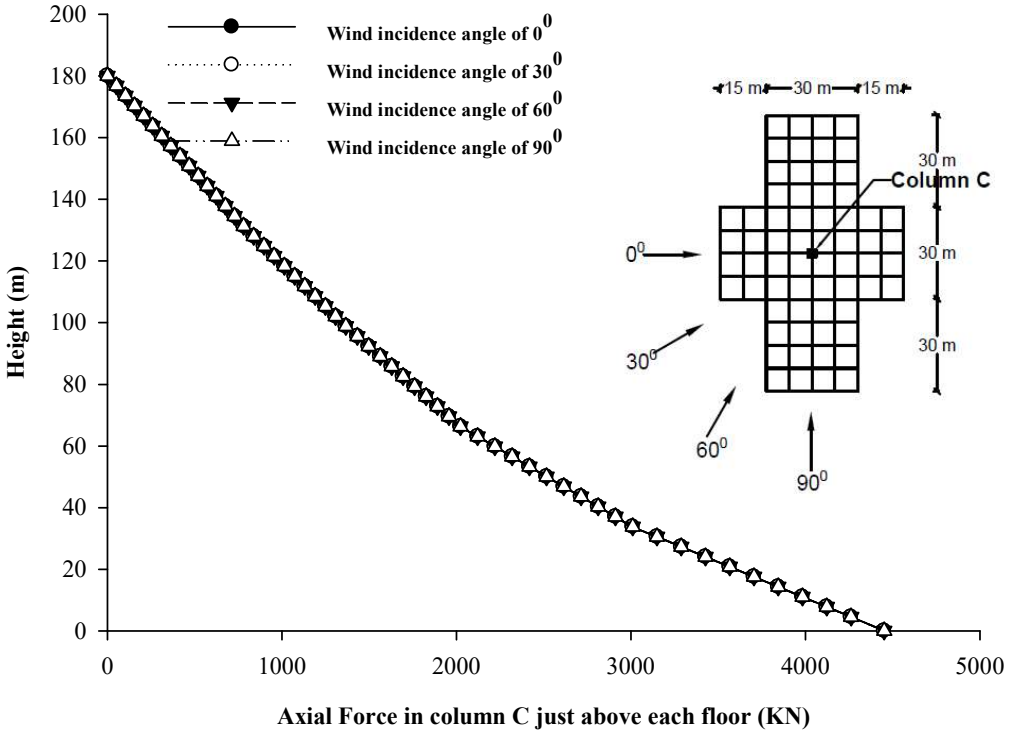

Fig. 7.53 Effect of wind angle on axial force in column-C of PL-2 building

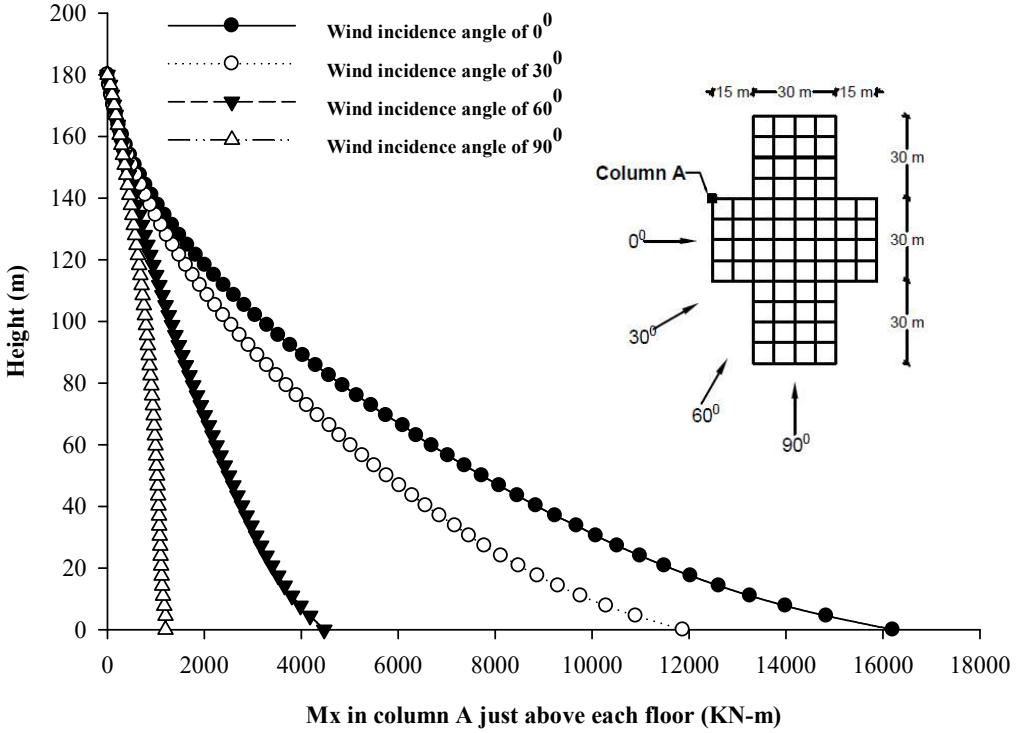

Fig. 7.54 Effect of wind angle on M_x in column-A of PL-2 building

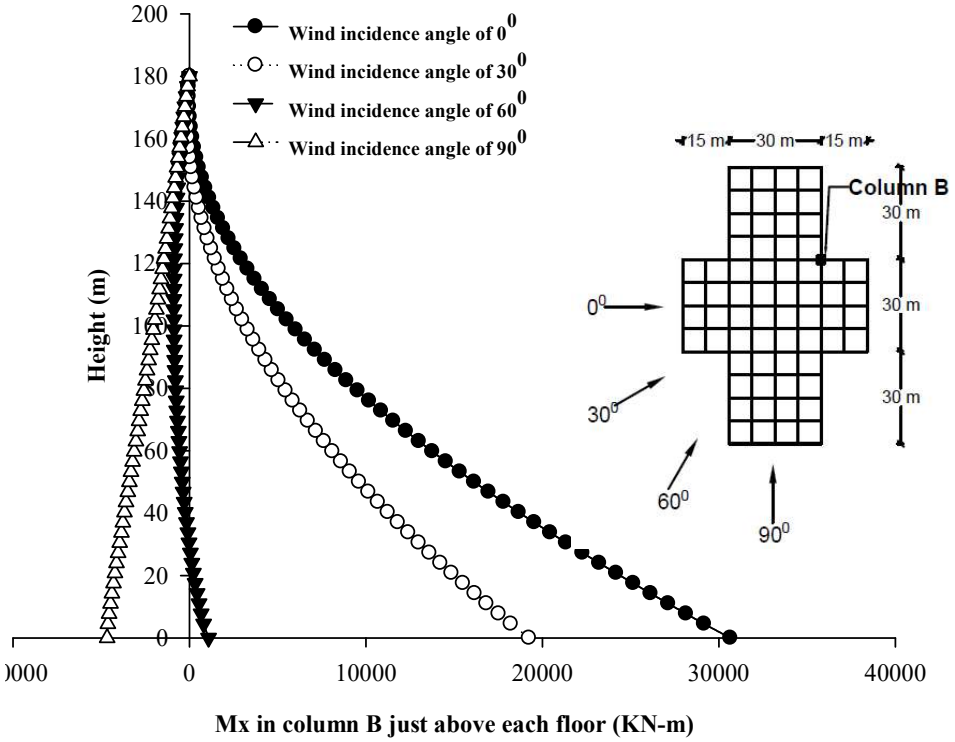

Fig. 7.55 Effect of wind angle on M_x in column-B of PL-2 building

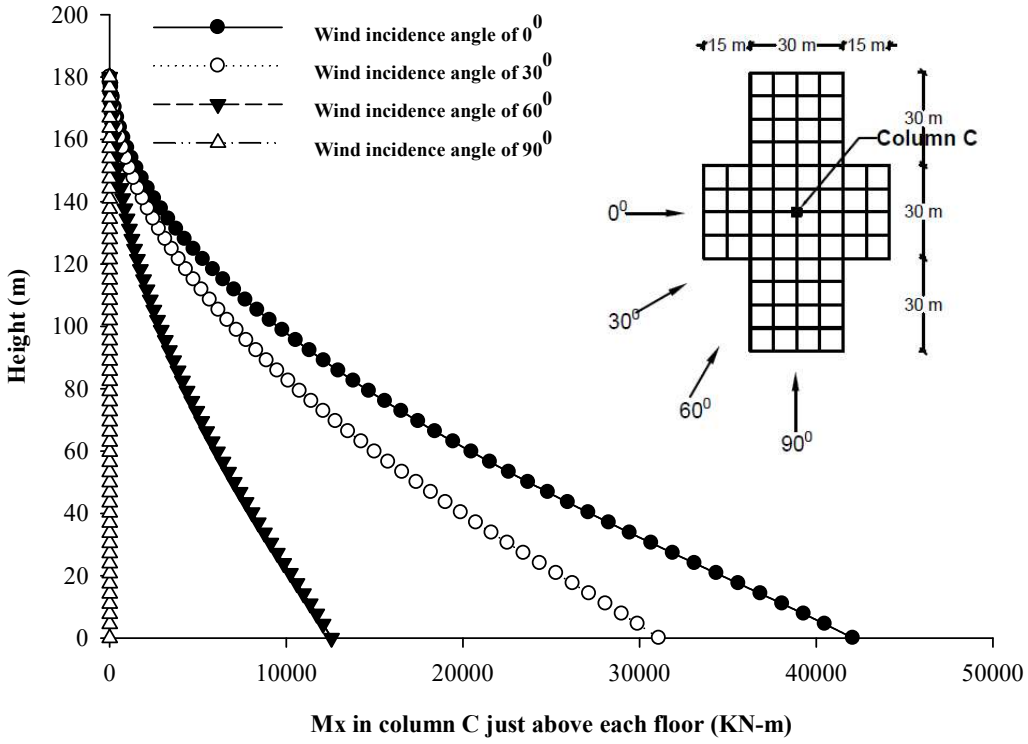

Fig. 7.56 Effect of wind angle on M_x in column-C of PL-2 building

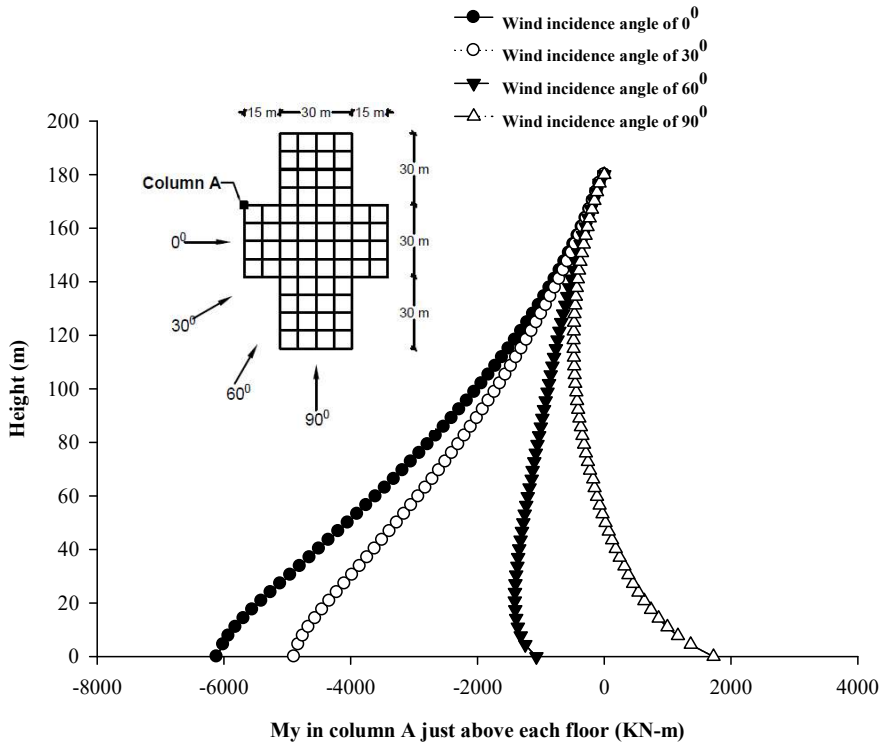

Fig. 7.57 Effect of wind angle on M_y in column-A of PL-2 building

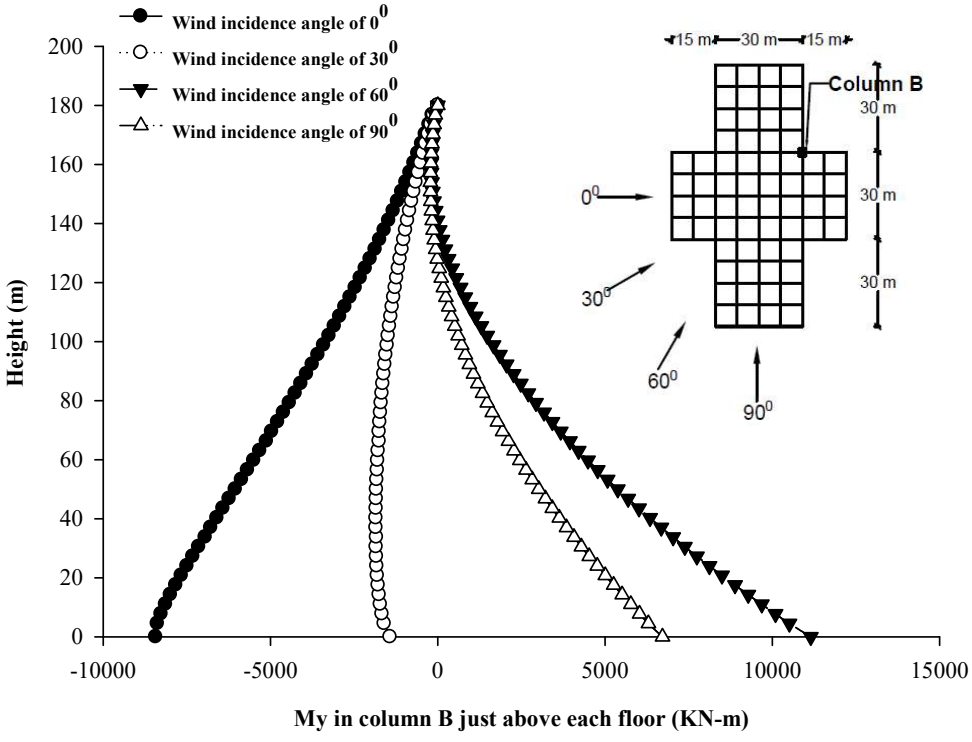

Fig. 7.58 Effect of wind angle on M_y in column-B of PL-2 building

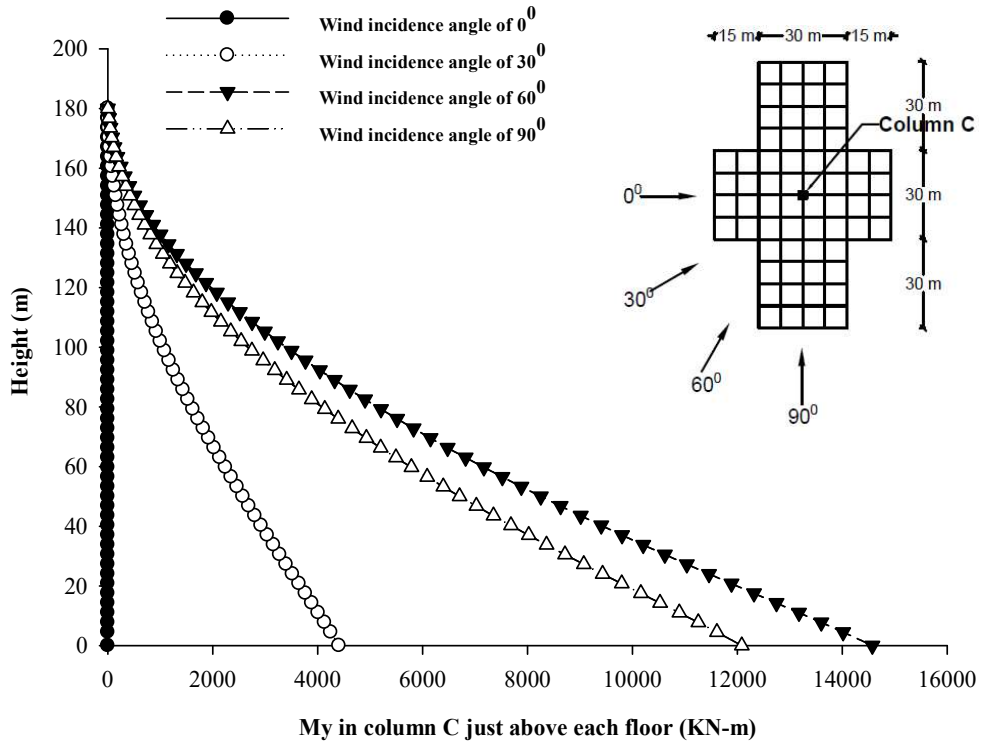

Fig. 7.59 Effect of wind angle on M_y in column-C of PL-2 building

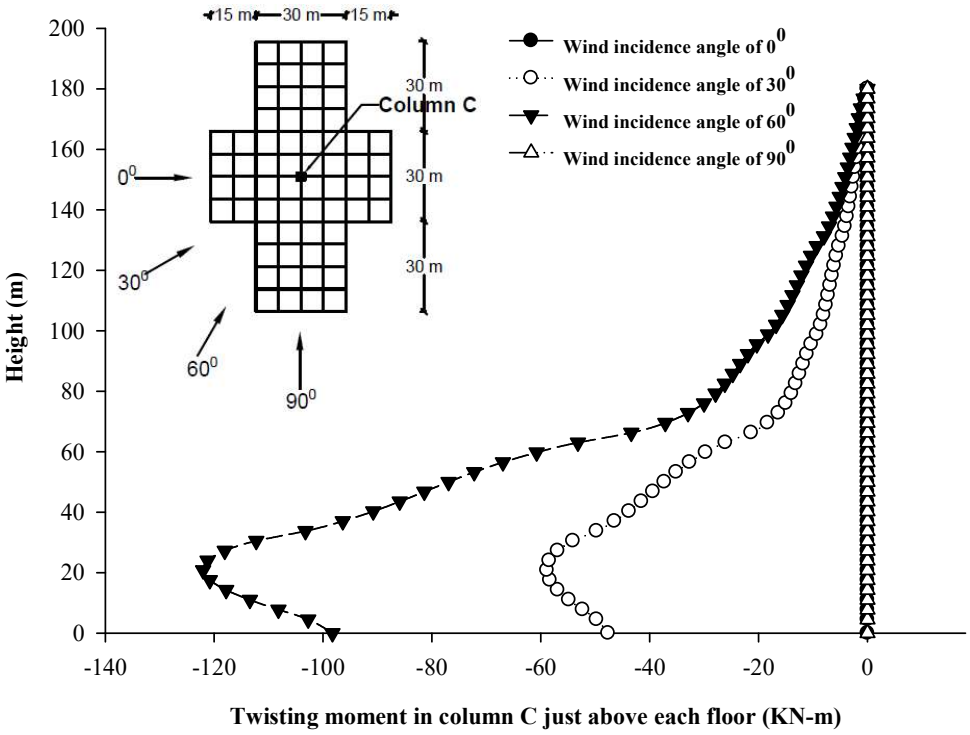

Fig. 7.60 Effect of wind angle on M_z in column-C of PL-2 building

7.6.2. Interference Condition

The influence of the presence of upstream interfering building at various locations with full, half and no blockage conditions on the response of the PL-2 building is assessed through stress parameters of column A, B and C similar to that of Pl-1 building.

The Fig. 7.61 to 7.63 represent the influence of various interference conditions on the axial force of column A, B and C respectively. The upstream building has negative effects on the axial force in column A. the axial forces in full condition are almost 3 time the force in isolated condition. The no blockage condition has minor effect on the axial force. The effects in half blockage condition are less severe than full blockage but more severe than no blockage condition. The interference effects on the column B are beneficial in full blockage condition. The half blockage condition has minor positive effects. The axial force of column B is unaffected by the upstream building in no blockage condition. There is no effect of upstream building on axial force of column C.

The effect of various interference conditions on the moment M_x are shown in Fig. 7.64 to 7.66, respectively for column A, B and C. There is a very minor effect of no blockage condition on the M_x of all the three columns. The full blockage condition and half blockage condition has positive effects on the M_x of all three columns. The moment of column A is minimum in full blockage condition, while the moment of column B is minimum for half blockage condition. The moments in column C for full blockage and half blockage conditions are equal but direction are opposite.

Similar to the M_x, the M_y of column A is also not affected in no blockage condition as shown in Fig. 7.67. Other interference conditions have positive effects. Full blockage condition has largest beneficial effects among all conditions. From Fig. 7.68, the moment M_y in column B is affected by upstream building in all conditions. The M_y is minimum for full blockage condition, and maximum for isolated condition. Due to symmetry in flow, moment in column C at the full blockage condition is zero similar to that of isolated condition as presented in Fig.7.69. The half blockage condition has larger negative effects than no blockage condition.

The effects of various interference conditions on the twisting moment are presented in the Fig. 7.70. The twisting moment M_z is similar in all columns and has similar effects due to interference. The upstream building generates more severe interference effects in half blockage condition and has no effects in no blockage condition.

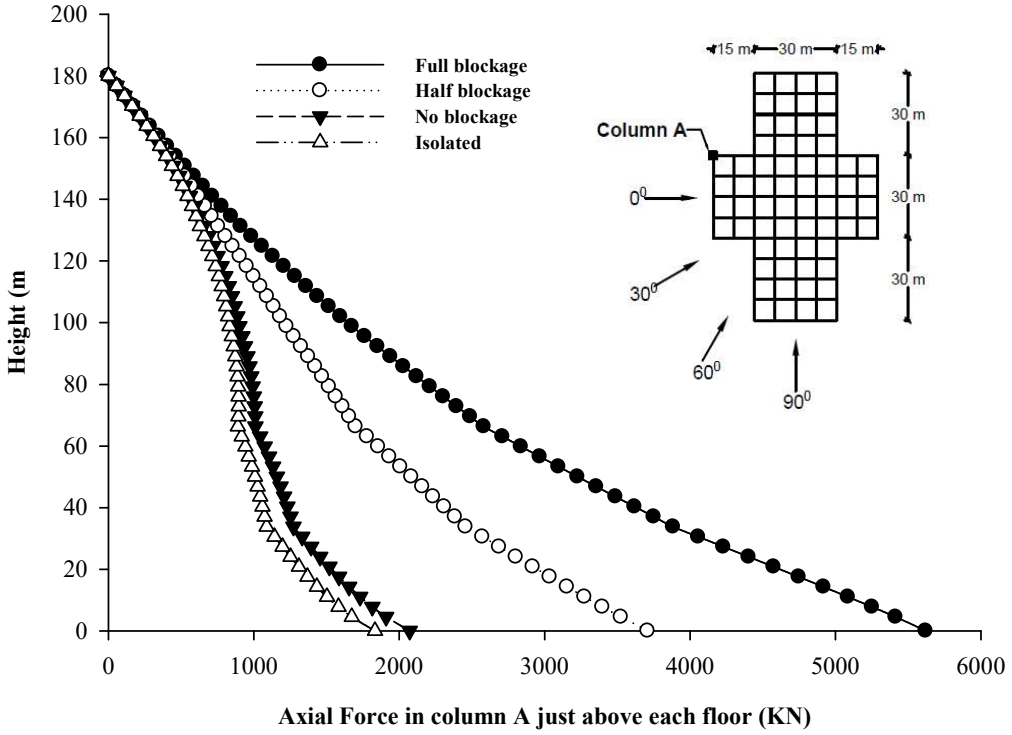

Fig. 7.61 Effect of Interference on axial force in column-A of PL-2 building

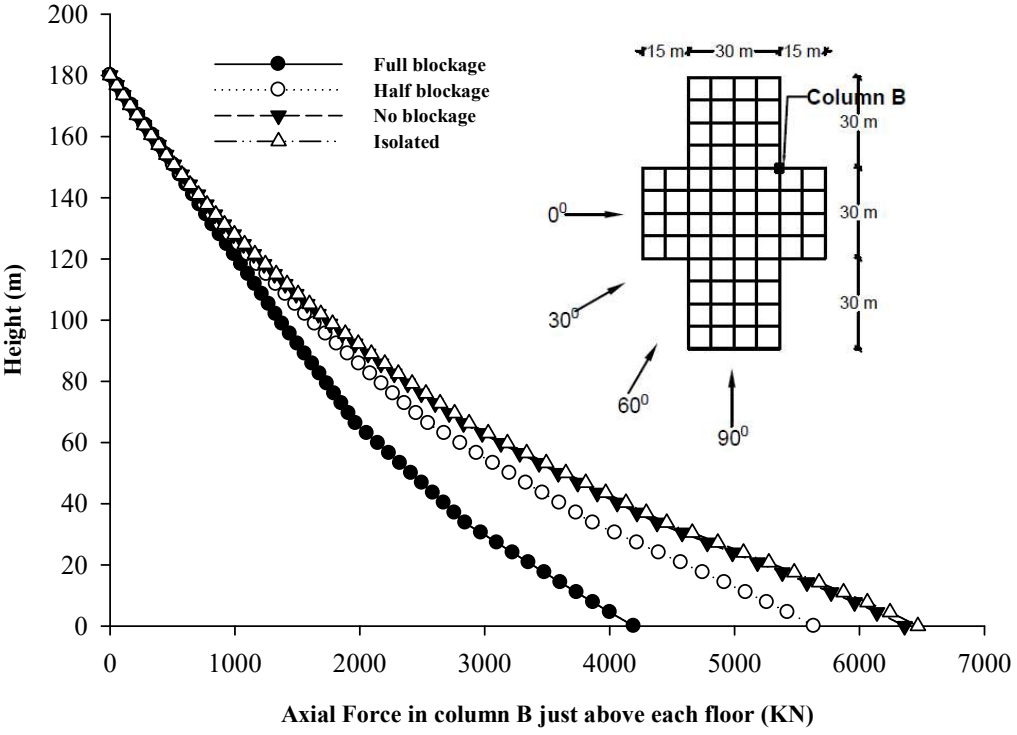

Fig. 7.62 Effect of Interference on axial force in column-B of PL-2 building

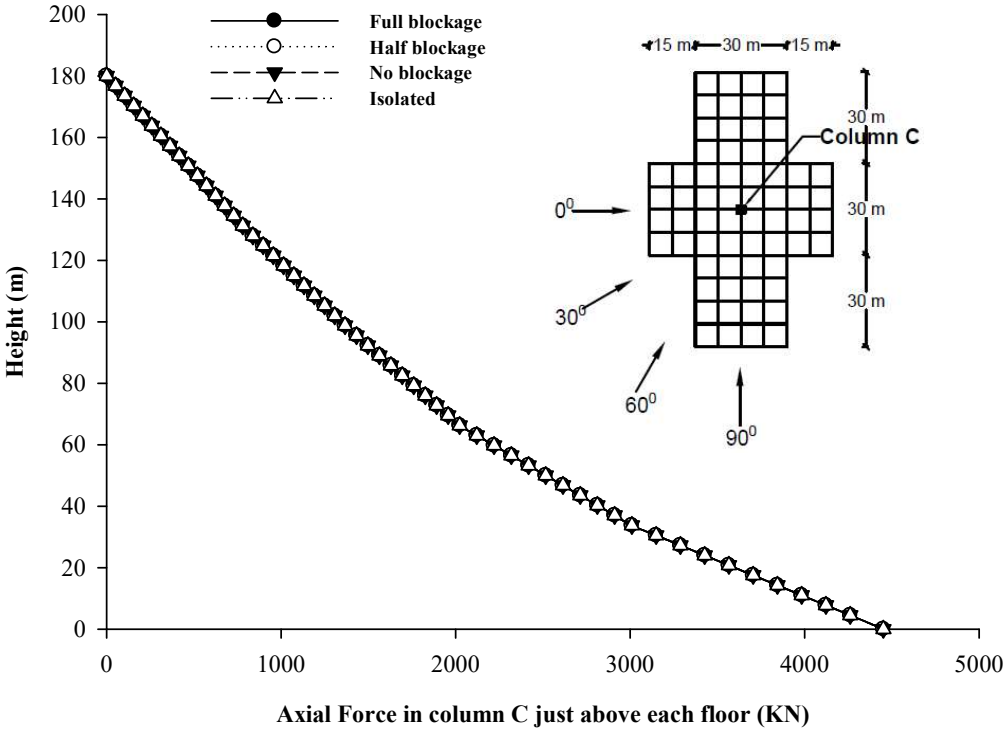

Fig. 7.63 Effect of Interference on axial force in column-C of PL-2 building

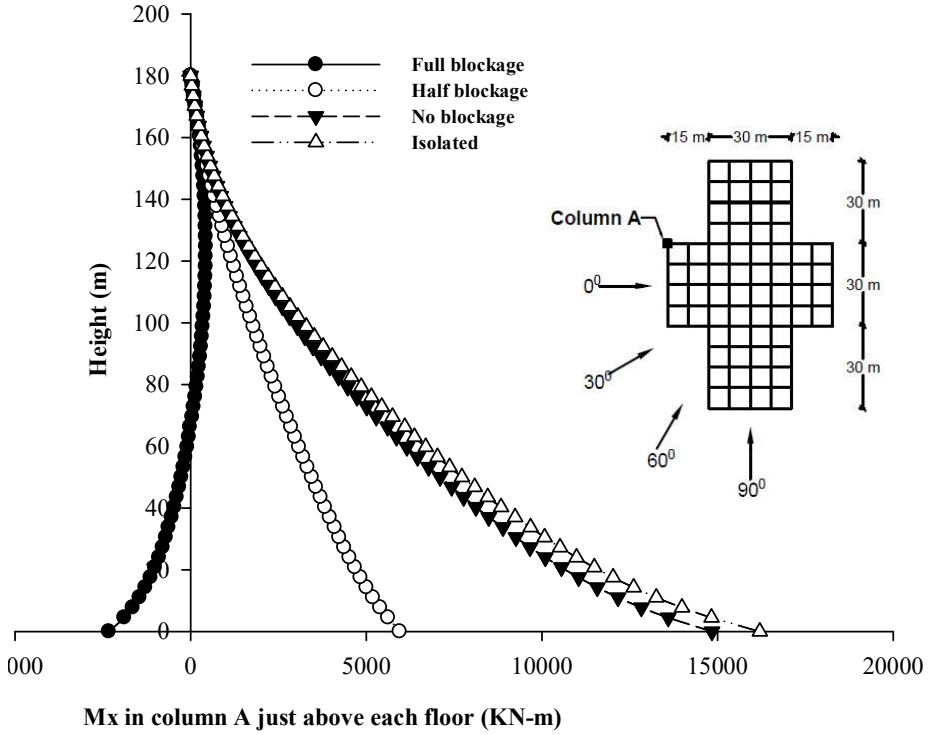

Fig. 7.64 Effect of Interference on M_x in column-A of PL-2 building

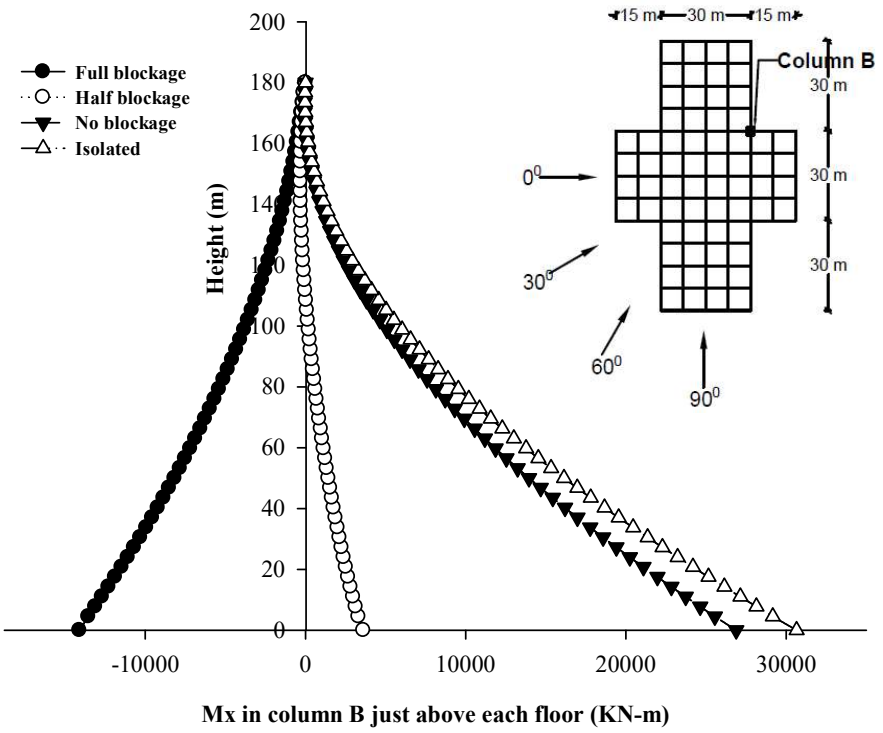

Fig. 7.65 Effect of Interference on M_x in column-B of PL-2 building

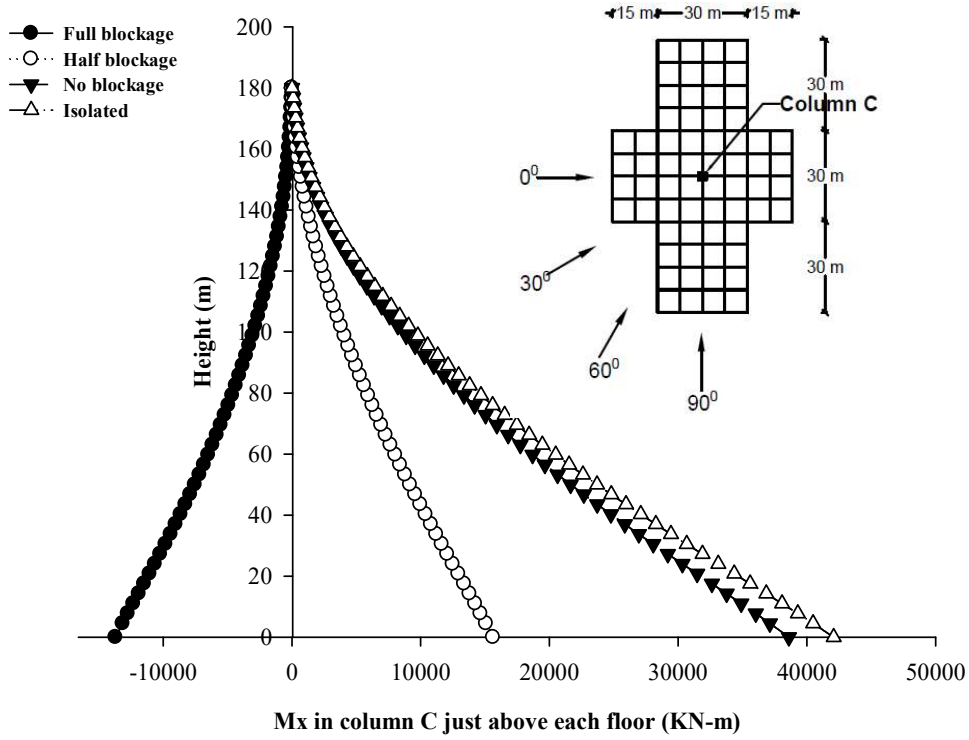

Fig. 7.66 Effect of Interference on M_x in column-C of PL-2 building

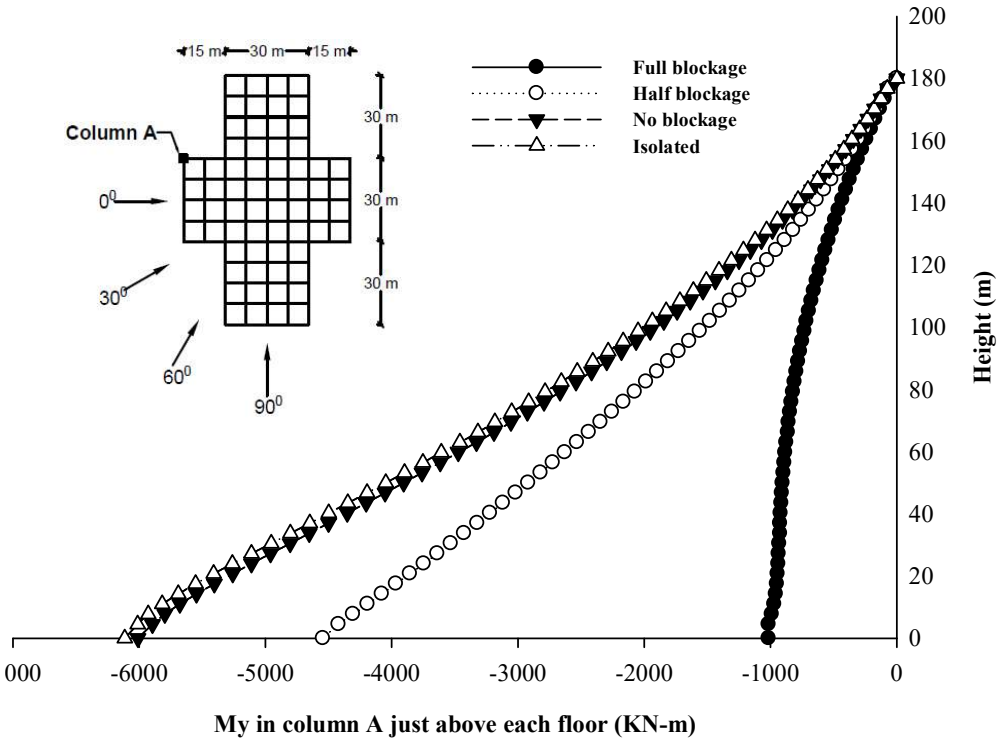

Fig. 7.67 Effect of Interference on M_y in column-A of PL-2 building

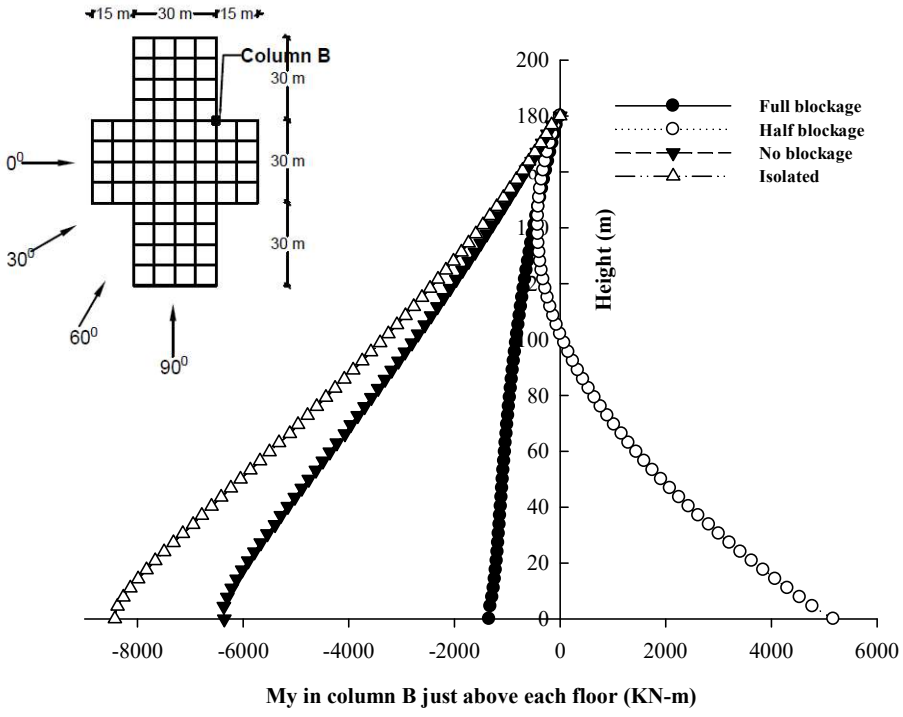

Fig. 7.68 Effect of Interference on M_y in column-B of PL-2 building

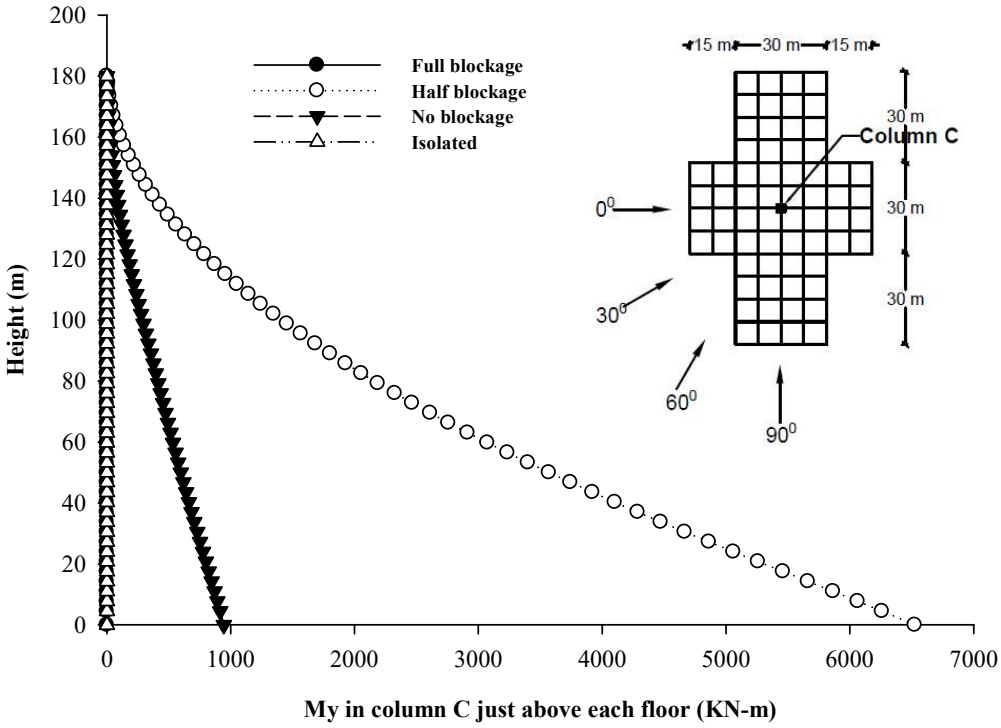

Fig. 7.69 Effect of Interference on M_y in column-C of PL-2 building

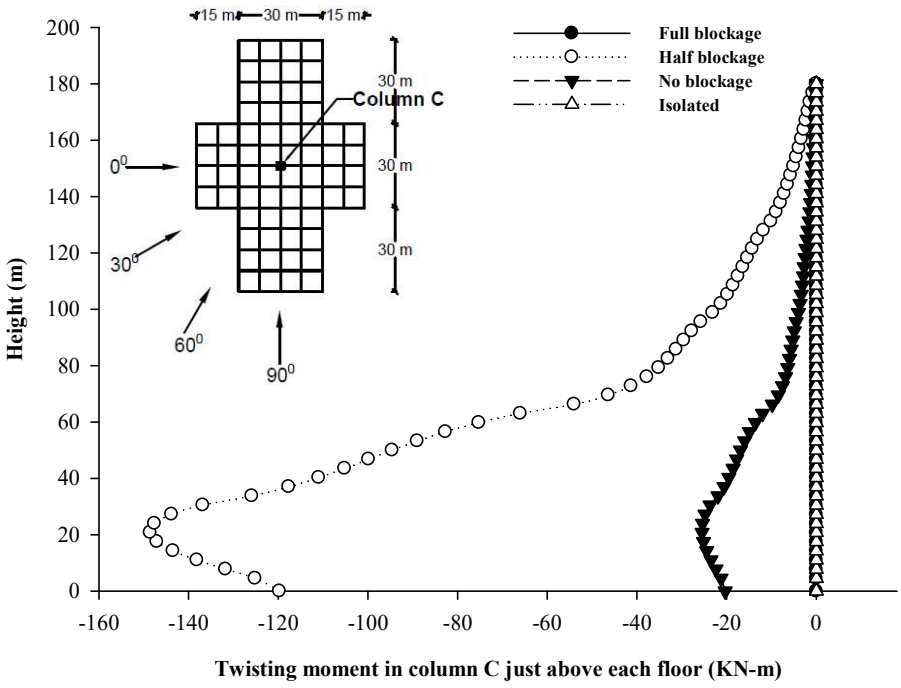

Fig. 7.70 Effect of Interference on M_z in column-C of PL-2 building

7.7. H-BUILDING

7.7.1. Isolated Condition

The effect of wind direction on the response of H-building is assessed similar to the other buildings. Fig. 7.71 to 7.80, represents the effects of wind direction on the various stress parameter of column A, B and C.

The axial force in column A is increases with change of wind direction from 0^0 to 90^0. The axial forces in column A for wind direction of 30^0, 60^0, and 90^0 are approximately 1.4, 2.1 and 2.5 times the axial force for 0^0 wind direction. The effects of wind direction on the axial force in column B are similar to that of column A but the intensity is slightly lower. The axial force of column C is not affected by the change of wind direction.

The moment M_x in all the three column is same for 0^0 and 60^0 wind angles and reduces for 30^0 wind 90^0 wind directions. The moment at base in column A is reduced to almost zero for wind direction of 90^0. The reduction in the moment for 30^0 wind is not as much as for 90^0 wind. Similar to the moment M_x of the three columns, the moment of all the three columns are similar for wind directions of 0^0 and 60^0. The moment in column A for 90^0 wind is also similar to the 0^0 wind but direction is opposite. The moment in column B and C are significantly low at 0 and 60 degree wind directions compare to the 90^0 wind.

Similar to the other buildings, all the three columns of H building have similar effects of wind direction on the twisting moments, hence only the variation of column C is presented here. The wind direction of 30^0 has large negative effects on the twisting moment. The effects are more severe than other wind directions. The wind at 60^0 angle generate very low twisting moment in all columns. The twisting moments in all the three columns are zero at 0^0 and 90^0 wind directions.

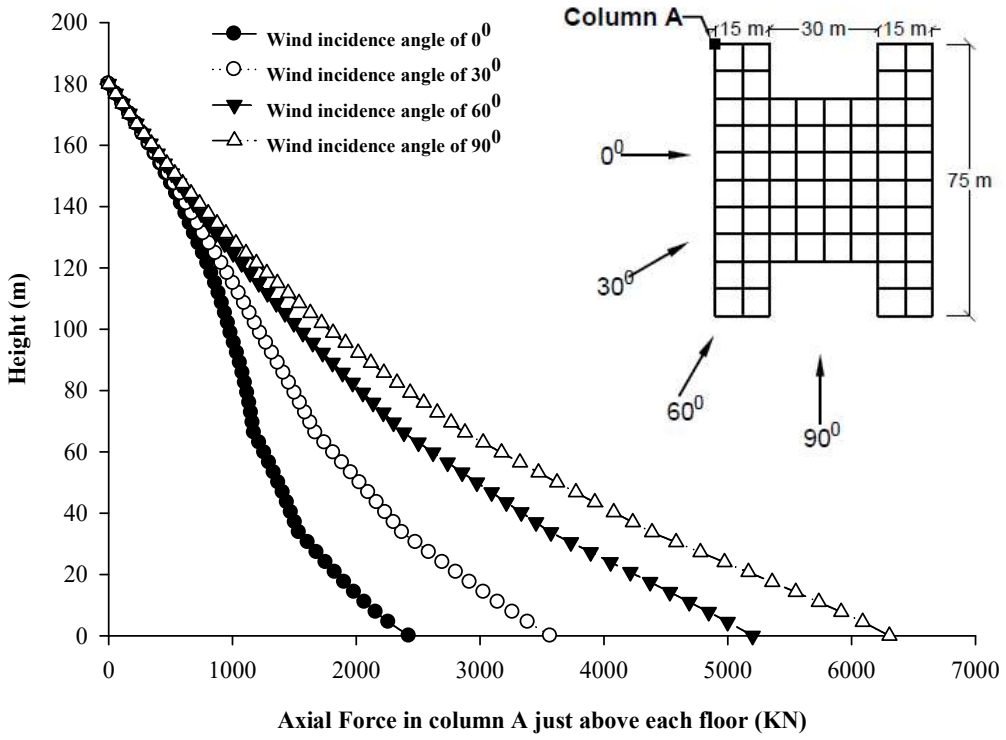

Fig. 7.71 Effect of wind angle on axial force in column-A of H- building

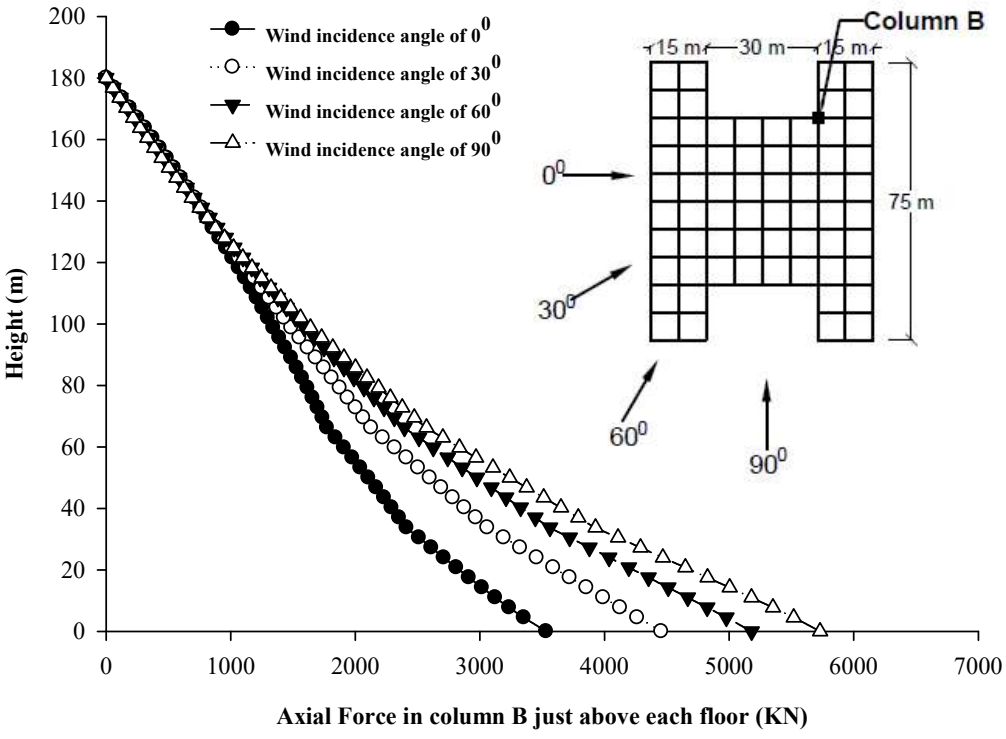

Fig. 7.72 Effect of wind angle on axial force in column-B of H- building

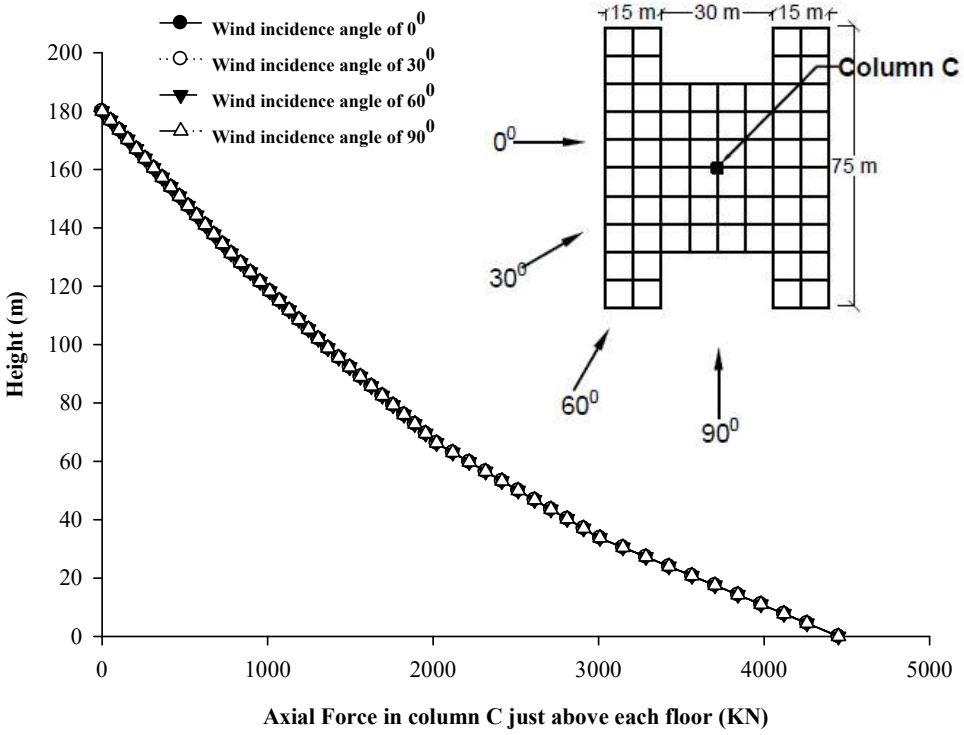

Fig. 7.73 Effect of wind angle on axial force in column-C of H- building

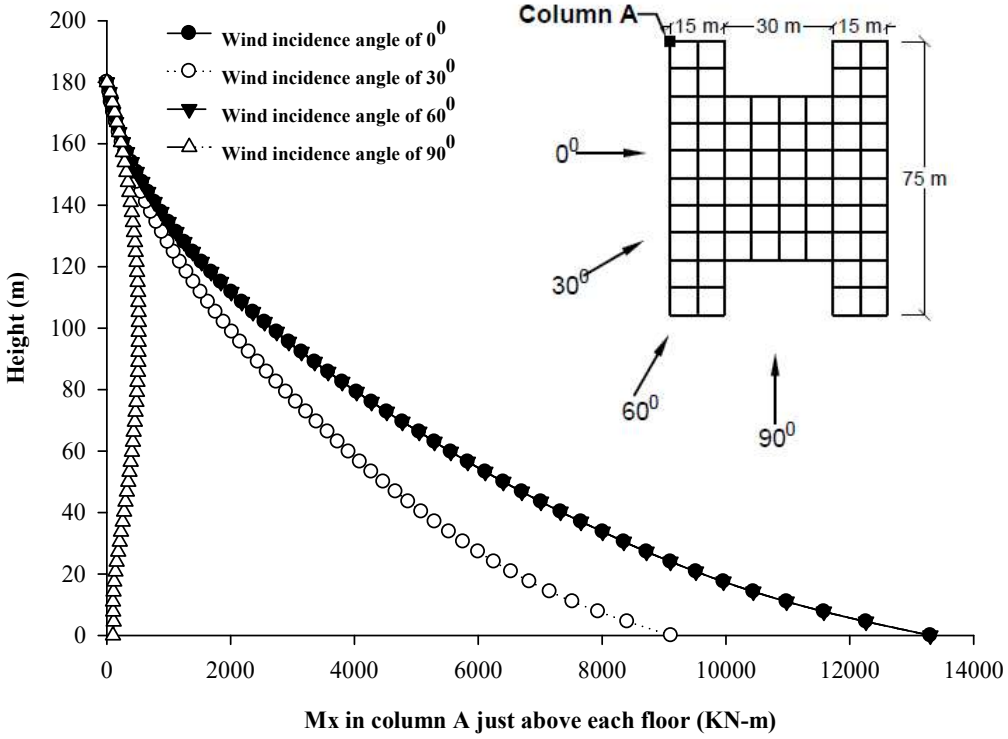

Fig. 7.74 Effect of wind angle on M_x in column-A of H- building

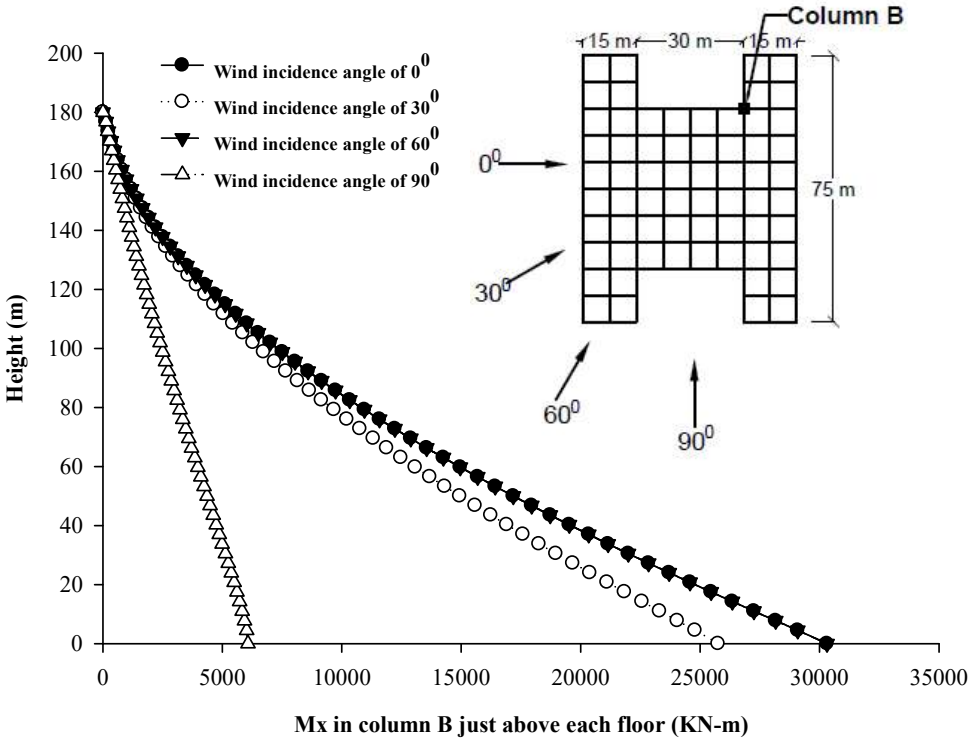

Fig. 7.75 Effect of wind angle on M_x in column-B of H- building

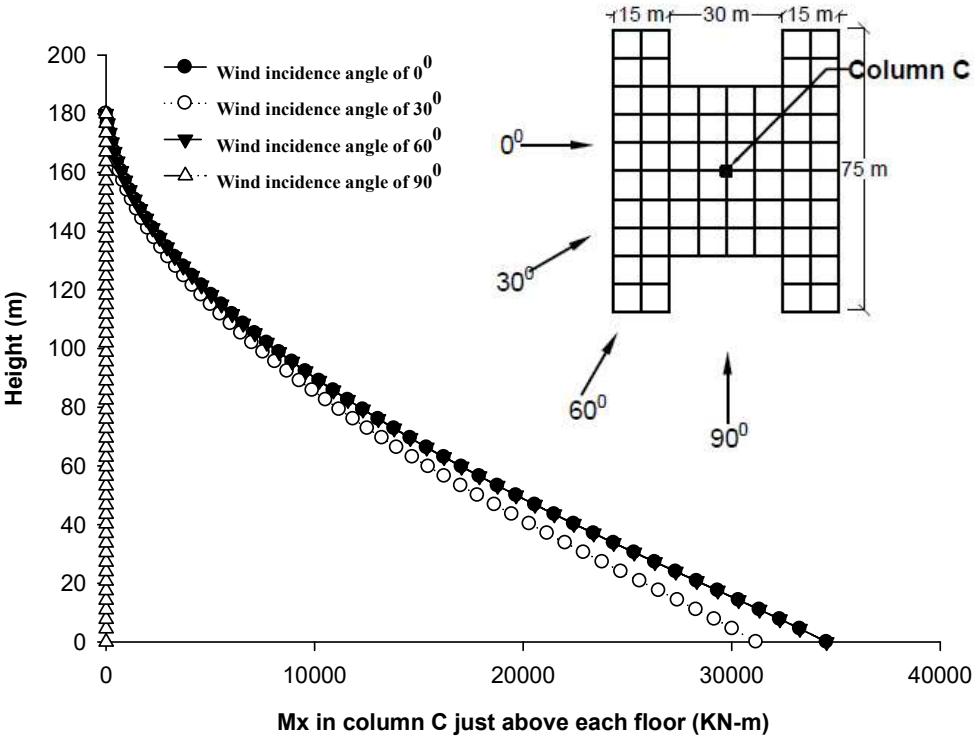

Fig. 7.76 Effect of wind angle on M_x in column-C of H- building

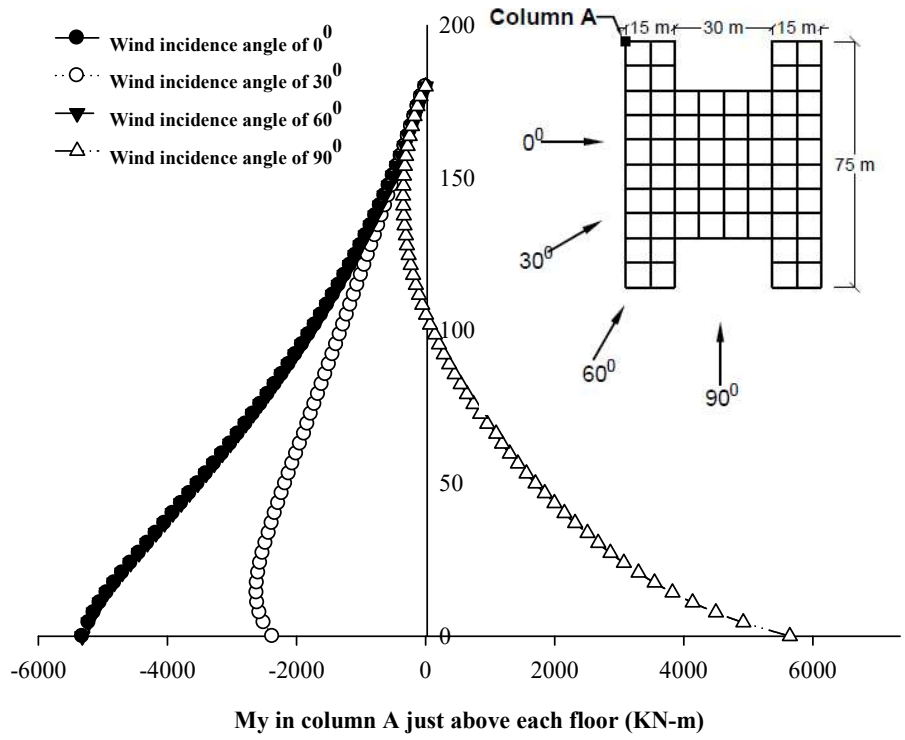

Fig. 7.77 Effect of wind angle on M_y in column-A of H- building

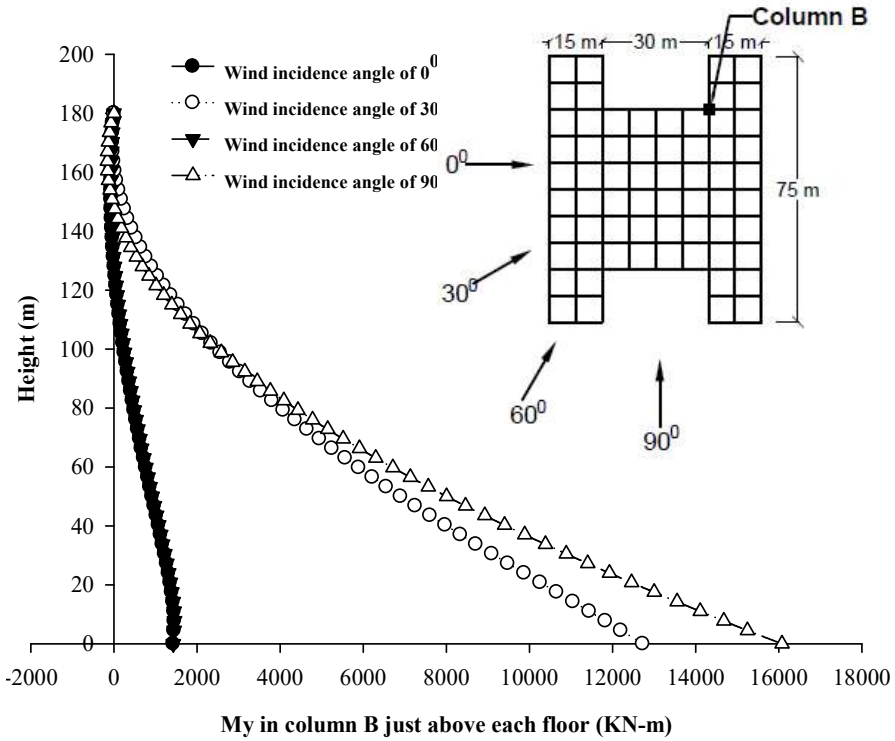

Fig. 7.78 Effect of wind angle on M_y in column-B of H- building

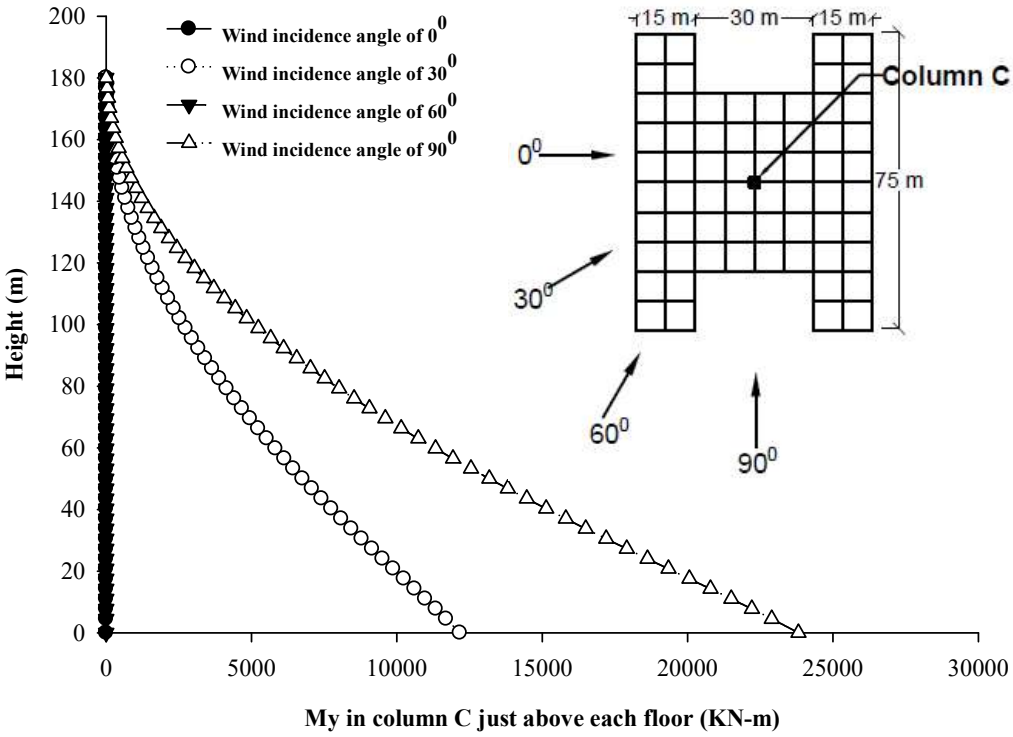

Fig. 7.79 Effect of wind angle on M_y in column-C of H- building

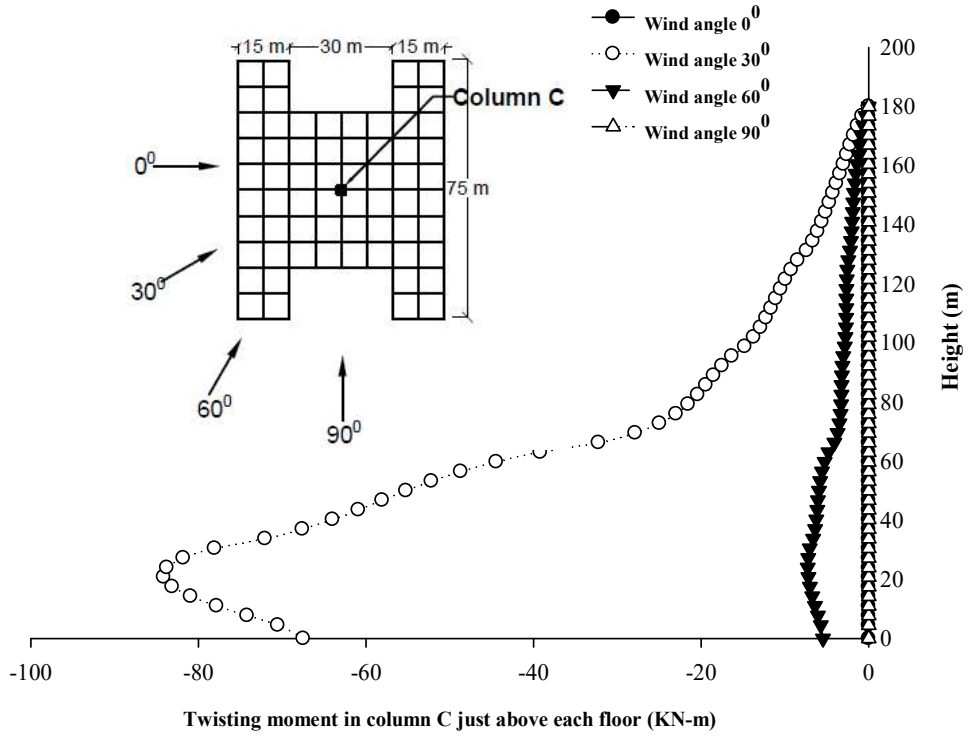

Fig. 7.80 Effect of wind angle on M_z in column-A of H- building

7.7.2. Interference Condition

The effects of various interference conditions on the response of H-building is assessed through the stress resultants similar to the other buildings. The effects of interference on axial force, moment M_x, moment M_y and the twisting moments of three columns are presented through Fig. 7.81 to 7.90.

The axial force in column A for full blockage condition is almost 2 times the axial force of isolated condition. The upstream building at no blockage condition does not affects the axial force of three columns. Axial force in column A for half blockage condition is also increased to almost 1.7 times the isolated condition. The upstream building in full blockage and half blockage conditions generate similar interference effects column B. There is not effect of upstream building on axial force of column C.

The full and half blockage interference conditions has positive effects on the moment M_x of the all three columns. The moment at these conditions is reduced to almost zero in column A and B and reduced by a large amount in column C. The moment M_y in column A and C is maximum for no blockage interference condition whereas maximum for full blockage condition in column B.

The variation of twisting moment in column C is presented here to assess the effect of various interference conditions. The half blockage condition has more severe effects compare to the no blockage condition. twisting moment is zero in full blockage condition similar to the isolated condition.

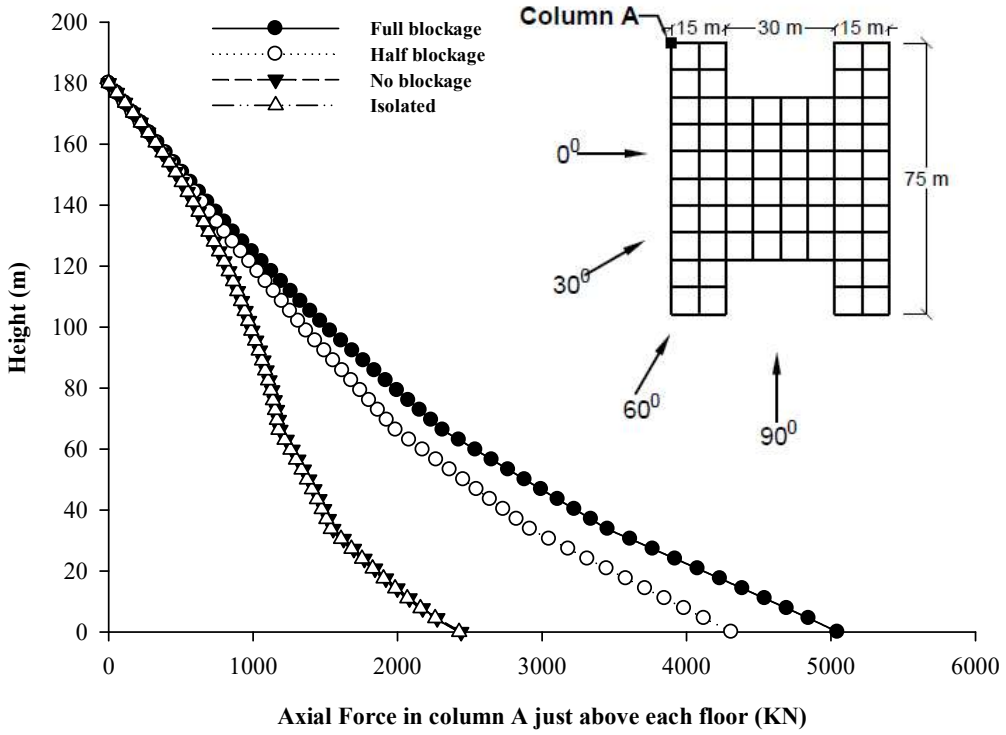

Fig. 7.81 Effect of Interference on axial force in column-A of H- building

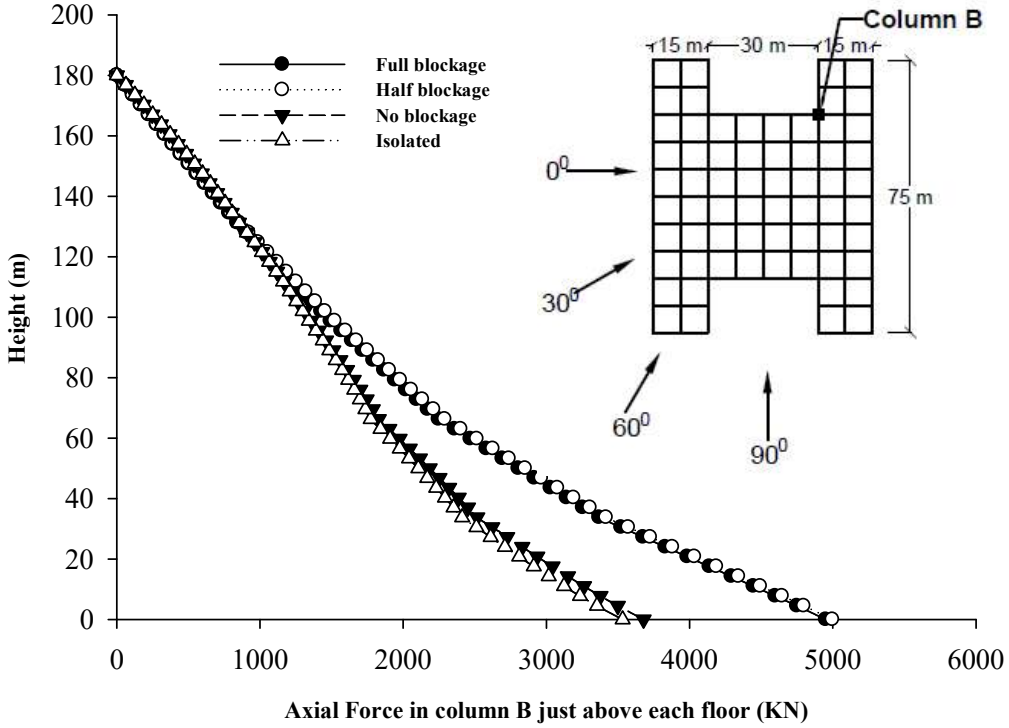

Fig. 7.82 Effect of Interference on axial force in column-B of H- building

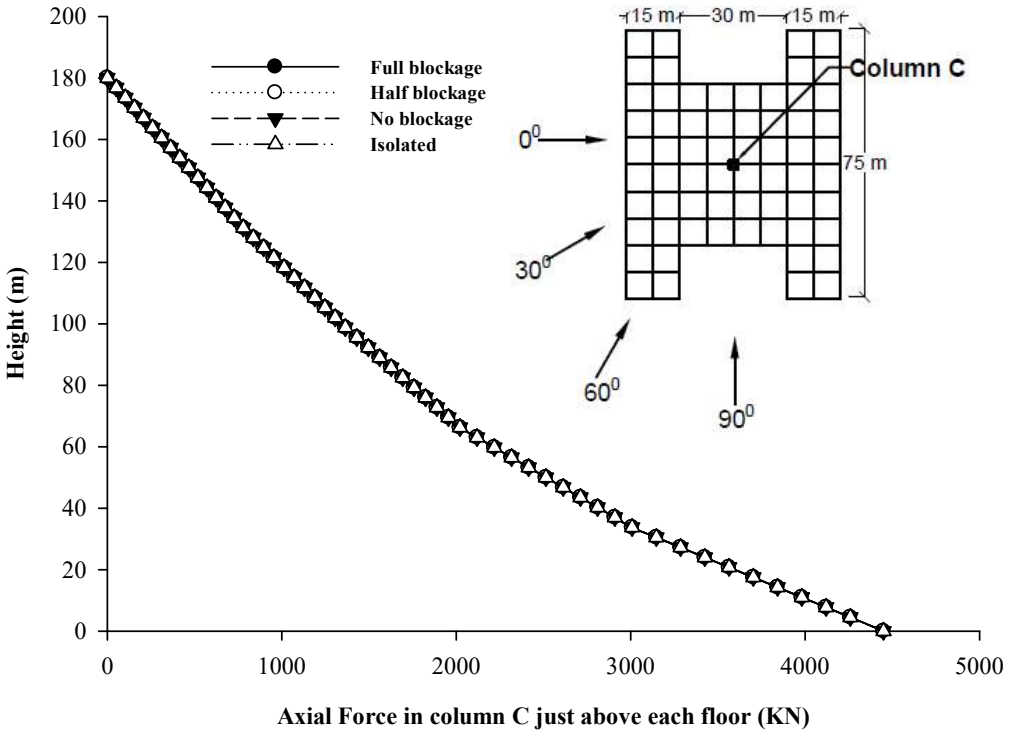

Fig. 7.83 Effect of Interference on axial force in column-C of H- building

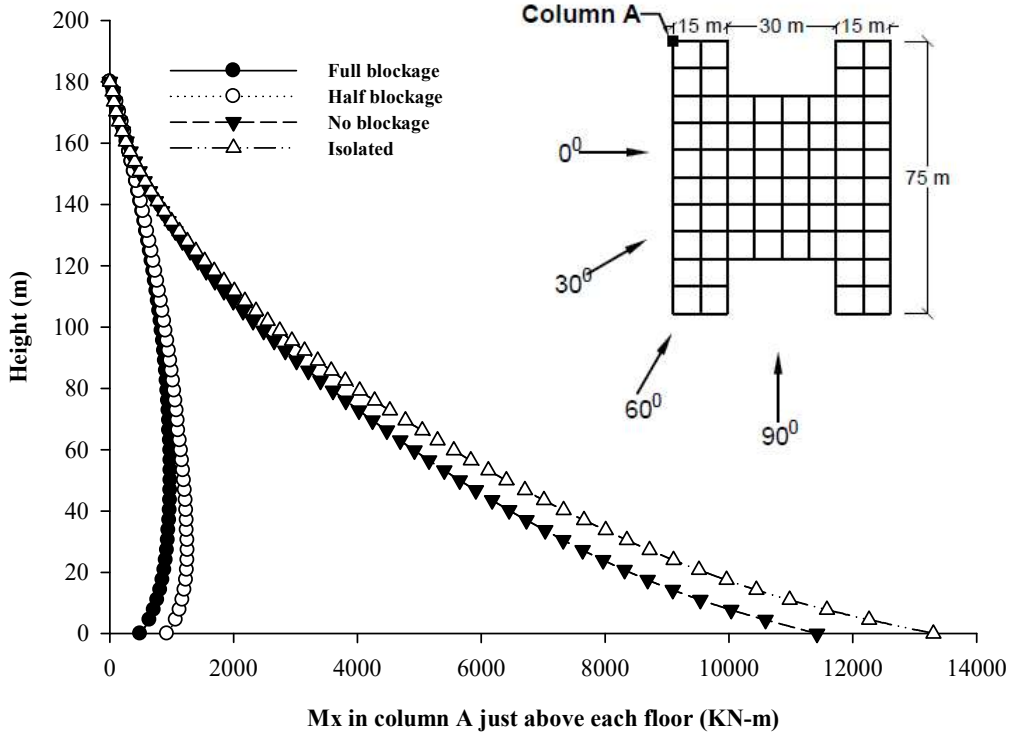

Fig. 7.84 Effect of Interference on M_x in column-A of H- building

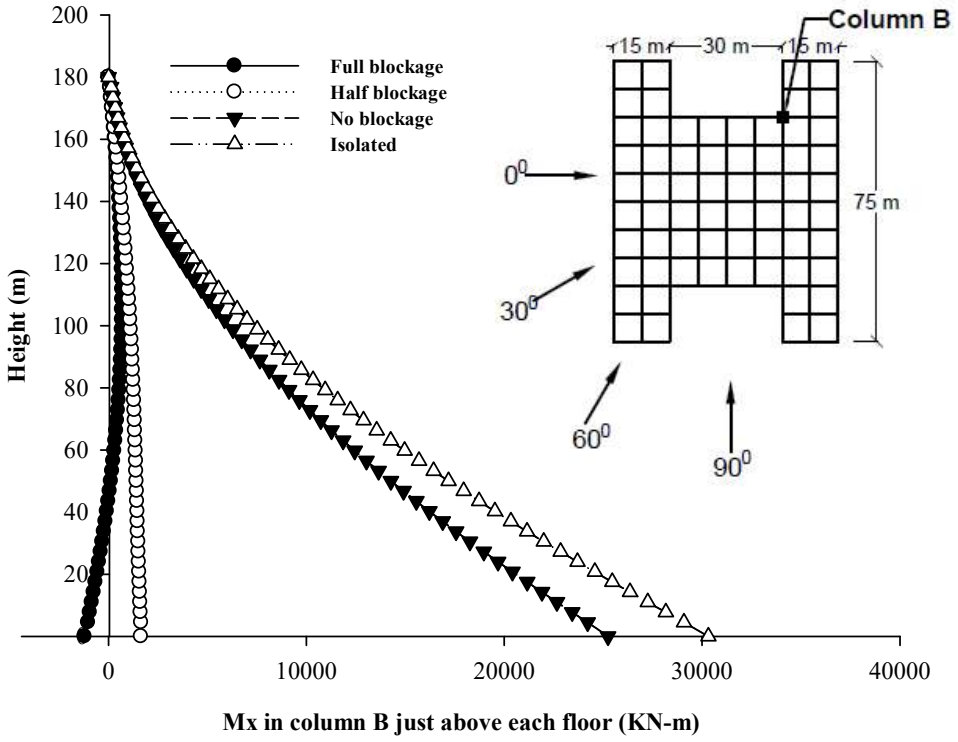

Fig. 7.85 Effect of Interference on M_x in column-B of H- building

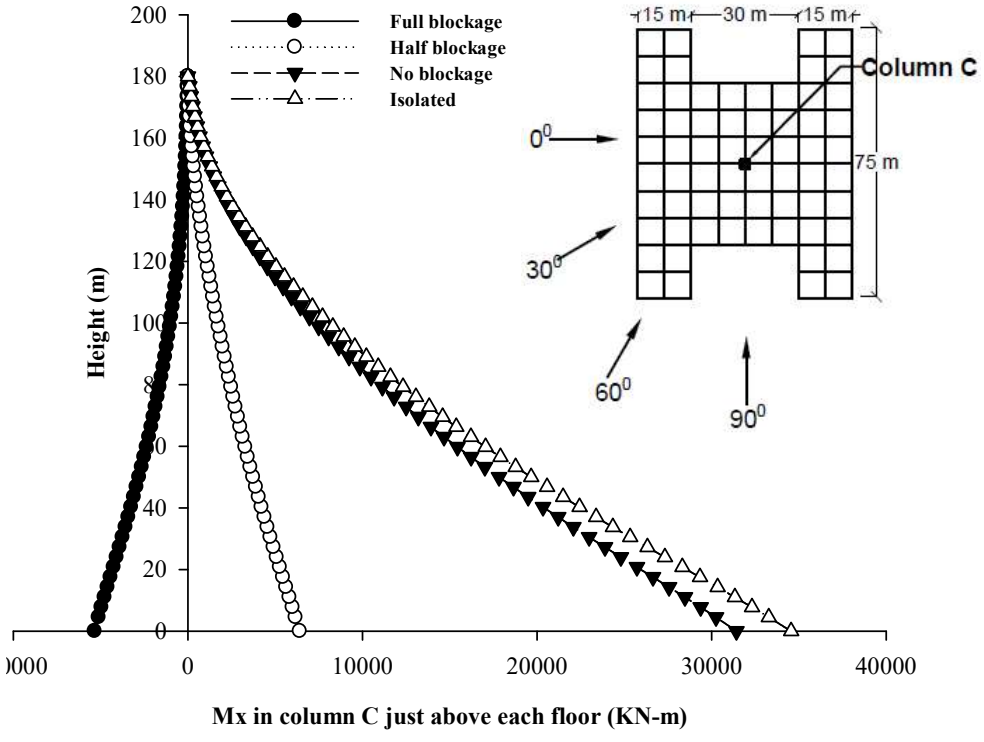

Fig. 7.86 Effect of Interference on M_x in column-C of H- building

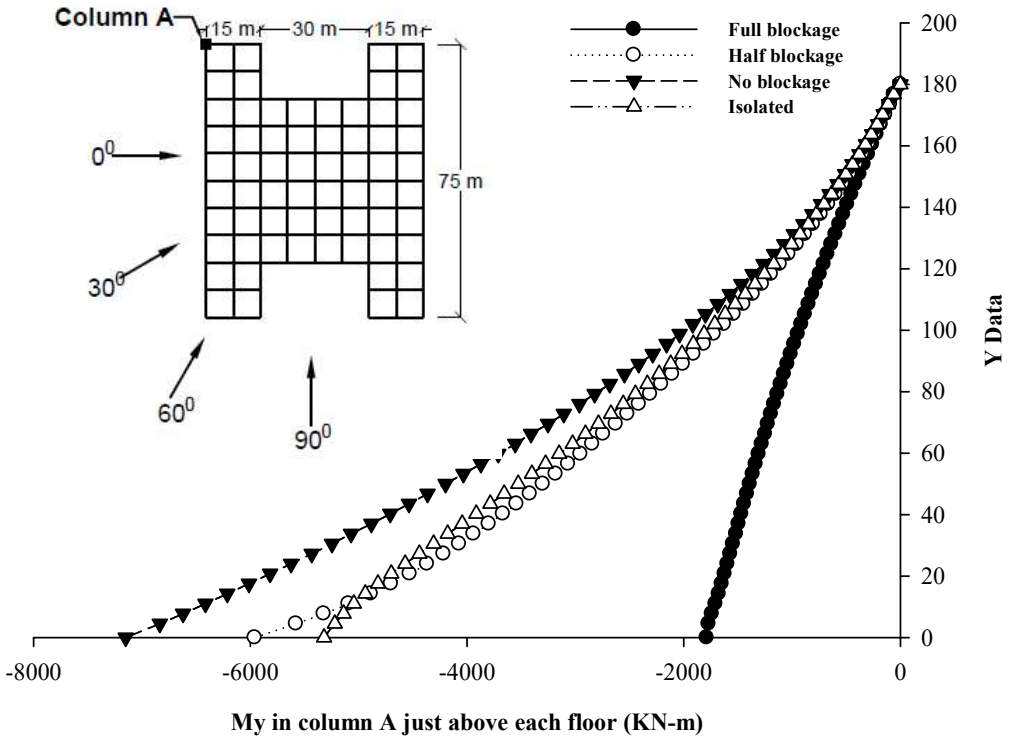

Fig. 7.87 Effect of Interference on M_y in column-A of H- building

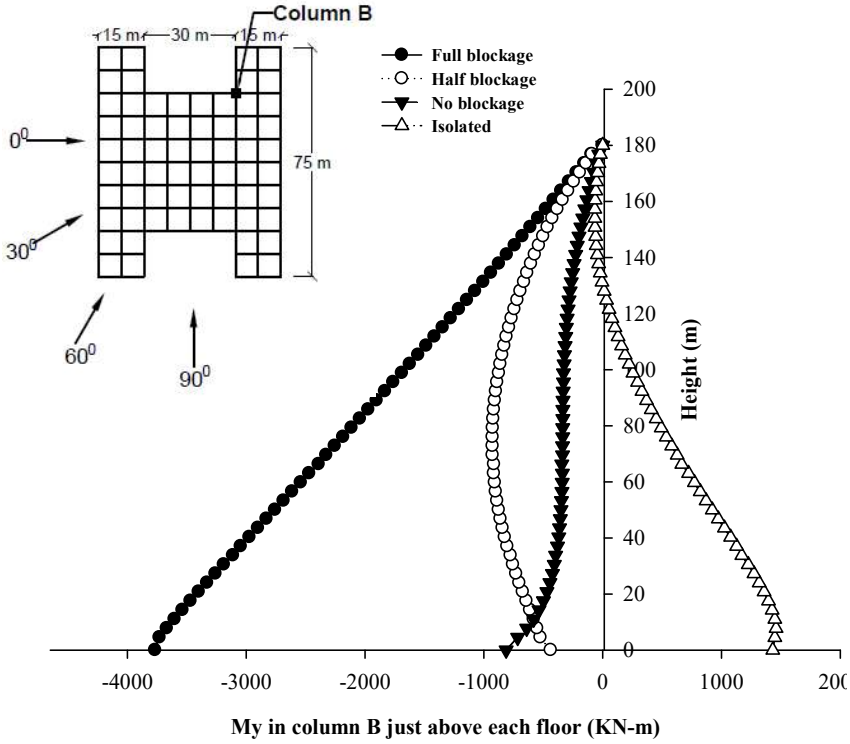

Fig. 7.88 Effect of Interference on M_y in column-B of H- building

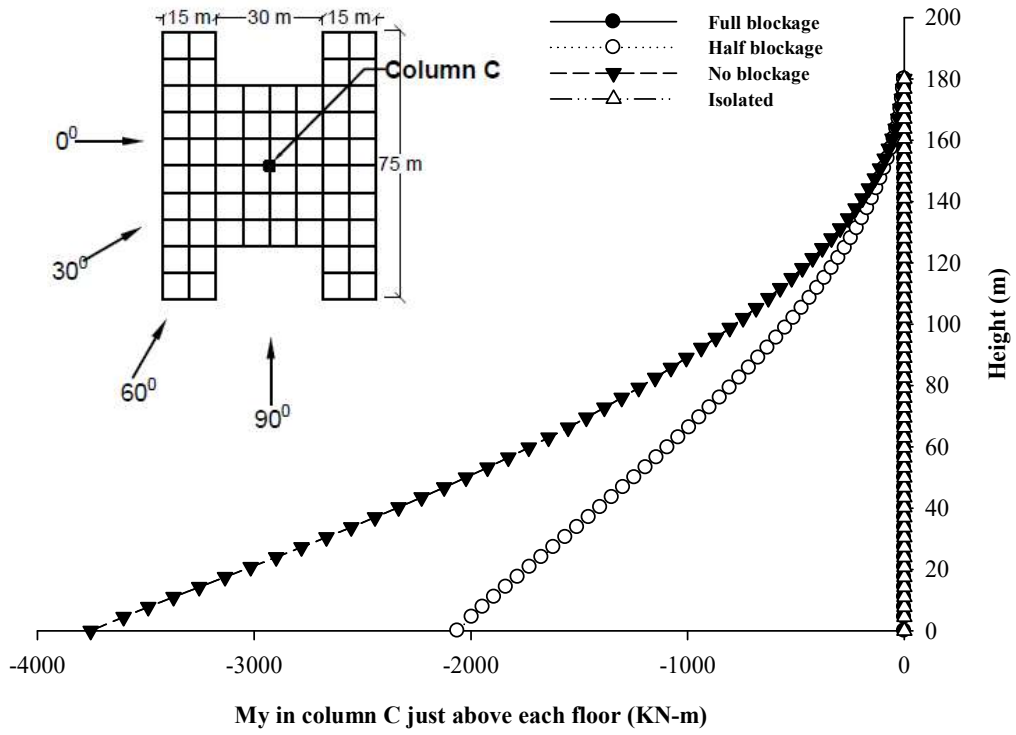

Fig. 7.89 Effect of Interference on M_y in column-C of H- building

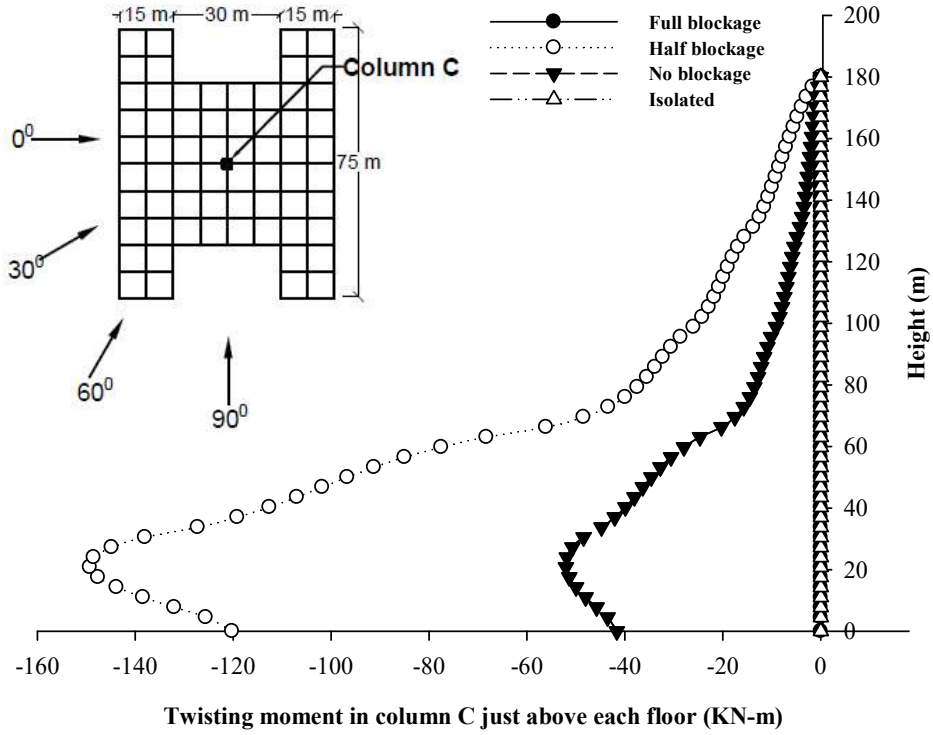

Fig. 7.90 Effect of Interference on M_z in column-C of H- building

7.8. EFFECTS OF BUILDING CROSS-SECTION ON THE RESPONSE

To assess the effects of the cross-sectional shape on the response of tall buildings under wind load, the response parameters of four building as discussed in previous section i.e. axial force, moment M_x, moment M_y and the twisting moments are compared. The stress parameters of central columns of all four buildings are selected.

7.8.1. Axial Force

From the Fig. 7.91, there is no effect of cross-sectional shape on the axial force in column of all four buildings in all wind conditions of isolated as well as interference. As the distribution of axial force in all wind conditions is similar, here only the variation for 0^0 wind in isolated conditions is presented.

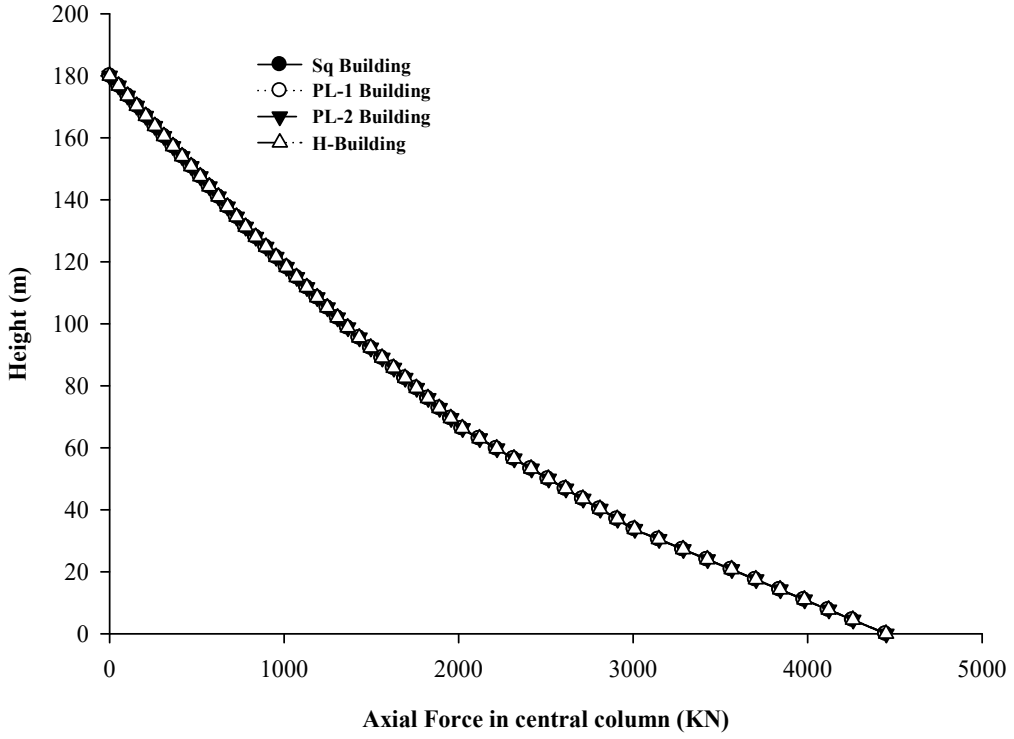

Fig. 7.91 Effect of Building Plan on Axial Force at 0^0 Wind

7.8.2. Moment M_x

Fig. 7.92 to 7.97 show the effects of different building plans on the moment M_x in different wind conditions for isolated and interference cases. The moment at 0^0 wind angle is maximum in PL-2 building. Square building show better performance out of all buildings. At the wind direction of 30^0, the PL-2 building and H-building show the worst performance, and the PL-1 building have least moment. The performance of H-building turns worst while performance of Sq building and PL-2 building improved. The moment in all buildings is zero at 90^0 wind angle due to symmetry. In the all interference conditions, the PL-2 building have largest moment. The moment in PL-2 building is more than double of the building which show minimum moment in all interference condition.

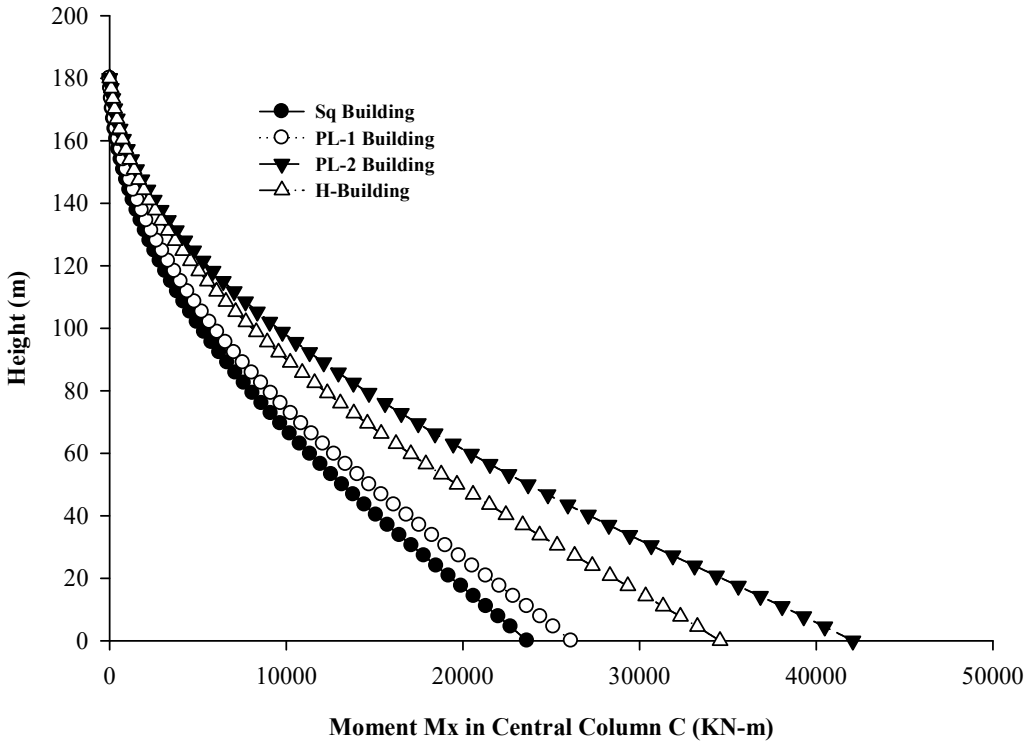

Fig. 7.92 Effect of Building Plan on Moment M_x at 0^0 Wind

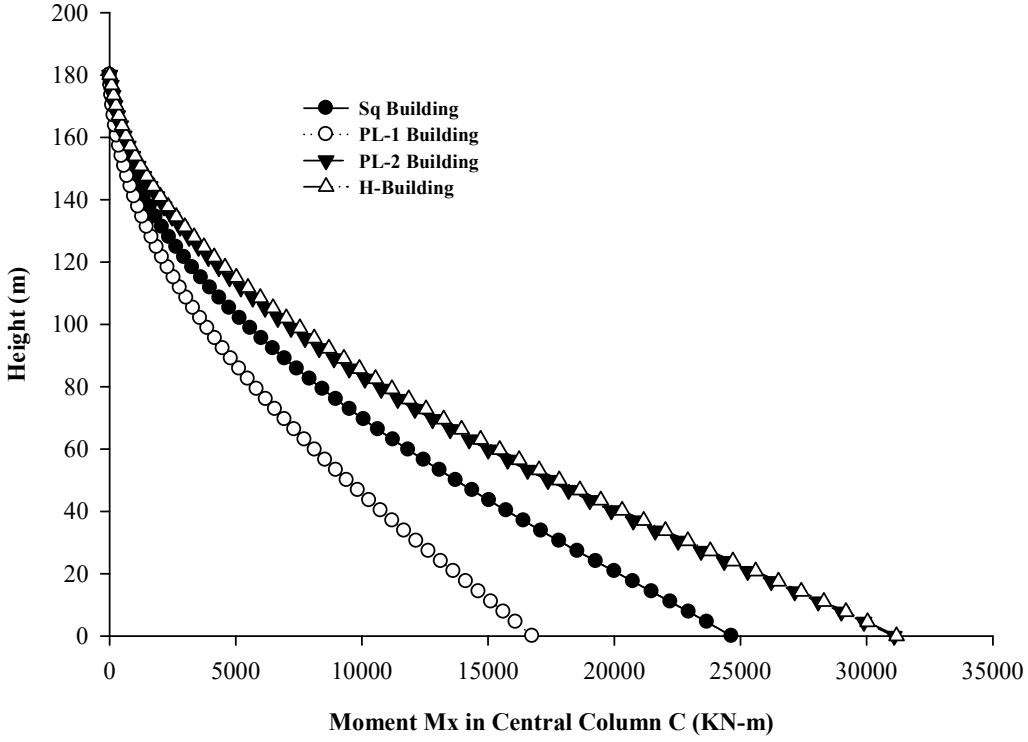

Fig. 7.93 Effect of Building Plan on Moment M_x at 30^0 Wind

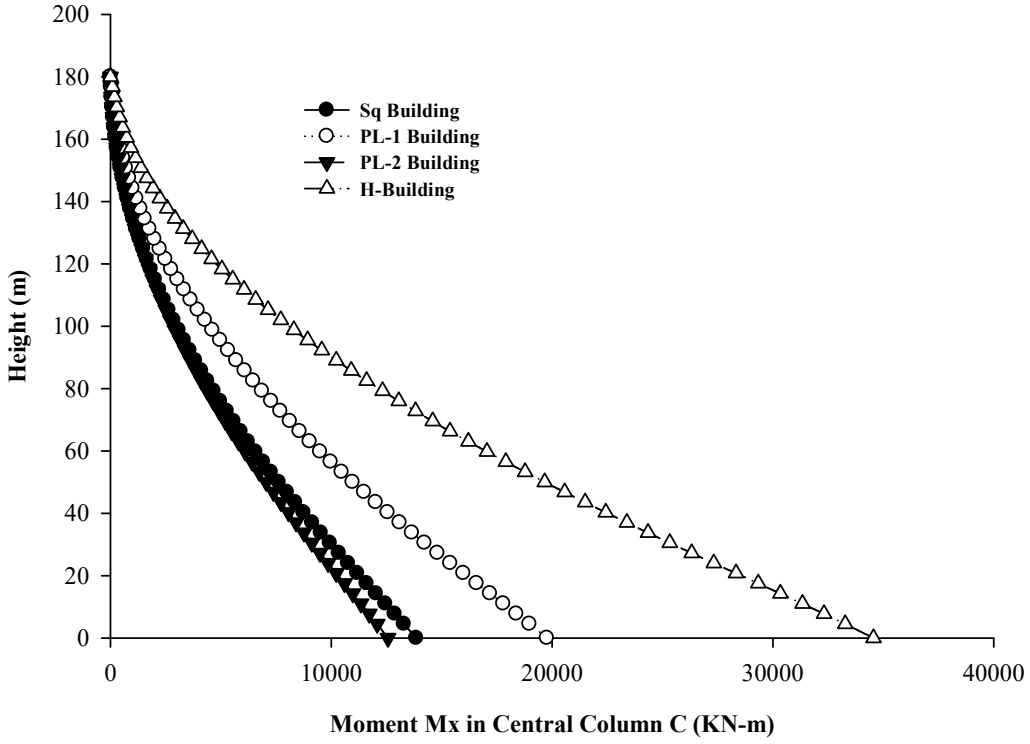

Fig. 7.94 Effect of Building Plan on Moment M_x at 60^0 Wind

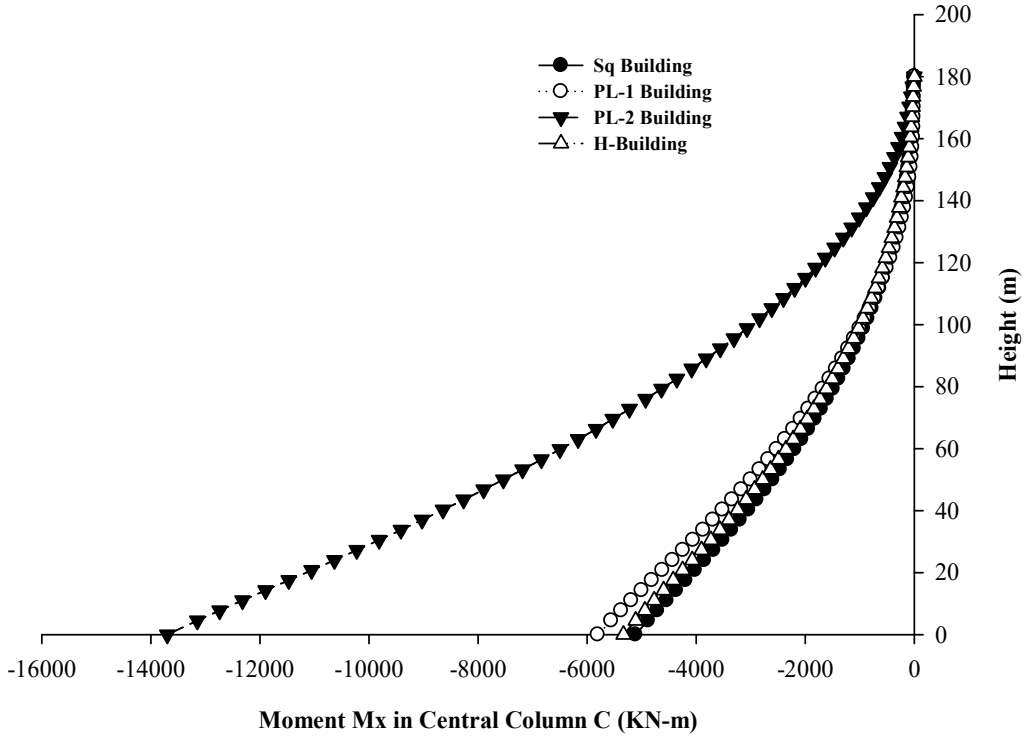

Fig. 7.95 Effect of Building Plan on Moment M_x at Full Blockage

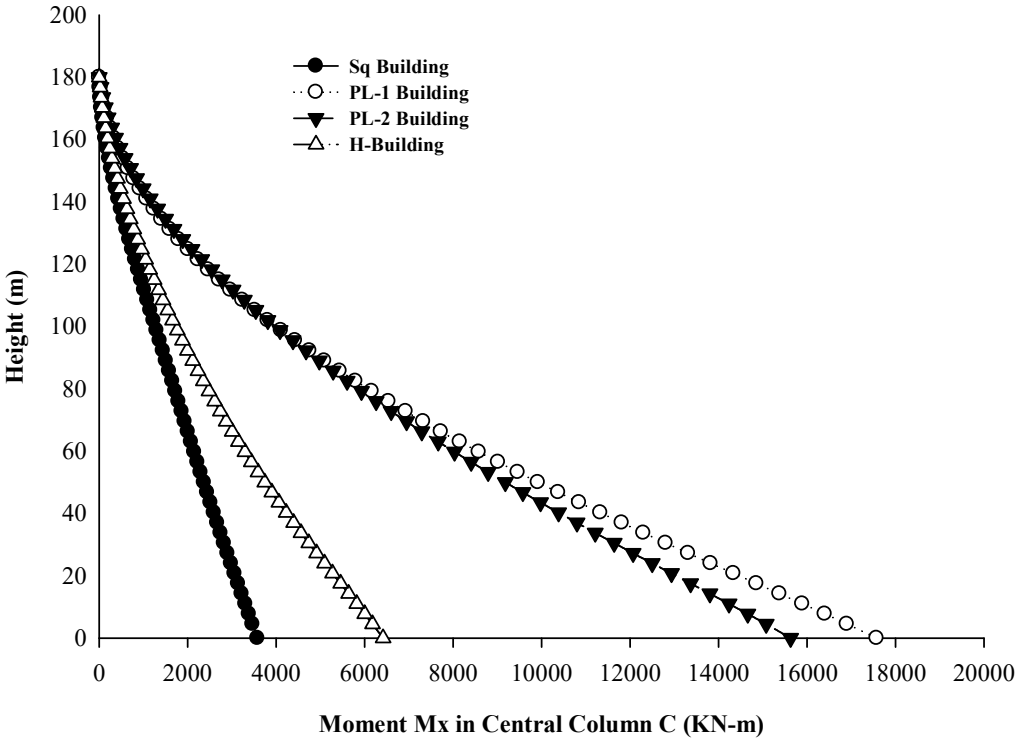

Fig. 7.96 Effect of Building Plan on Moment M_x at Half Blockage

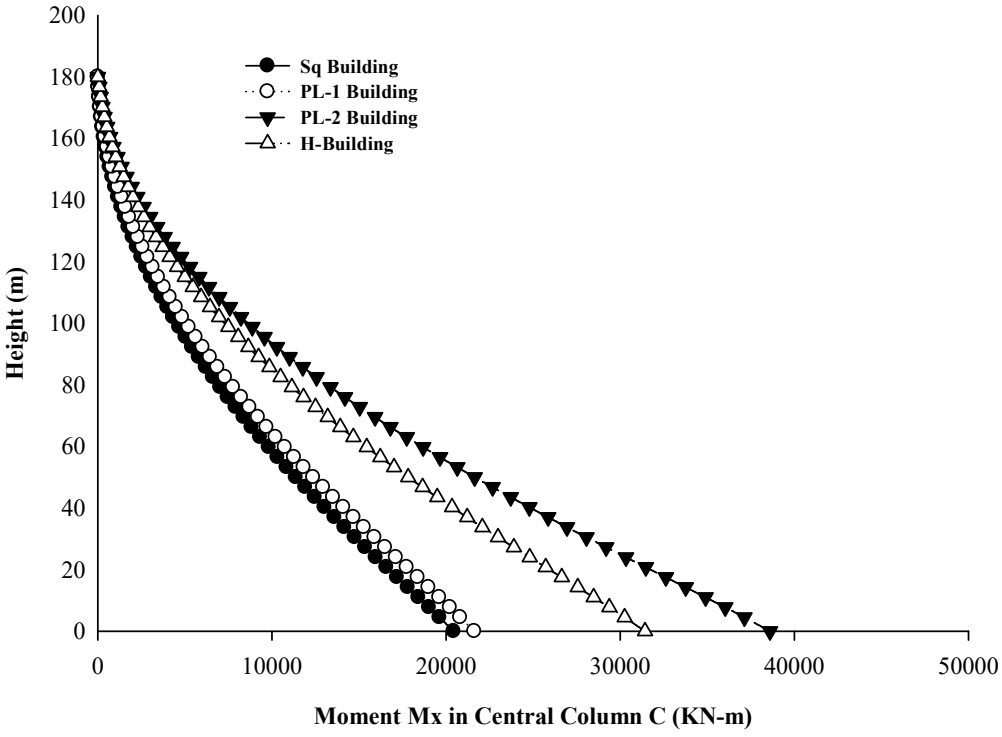

Fig. 7.97 Effect of Building Plan on Moment M_x at No Blockage

7.8.3. Moment M_y

For all the wind direction in isolated building condition, the performance of Sq building is worst as shown in Fig. . While Pl-2 building perform well with lowest moment M_y in isolated condition. The moment is maximum in Pl-2 building while minimum in square building at half blockage condition. In half blockage condition, the PL-1 building has largest moment and the PL-2 building has lowest moment.

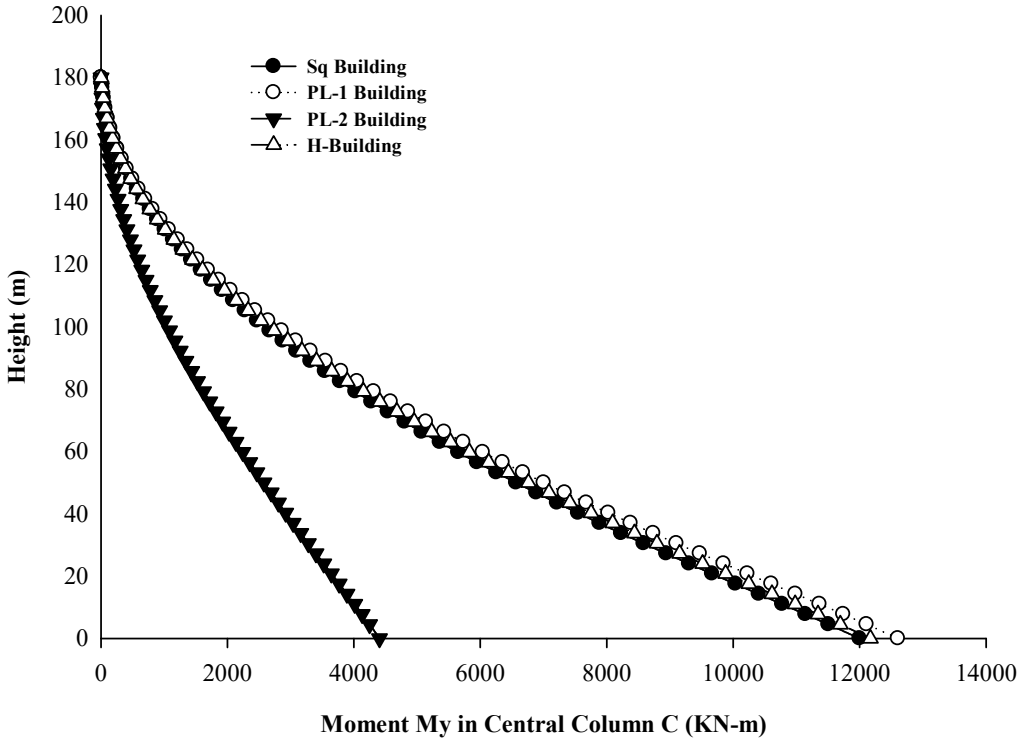

Fig. 7.98 Effect of Building Plan on Moment M_y at 30^0 Wind

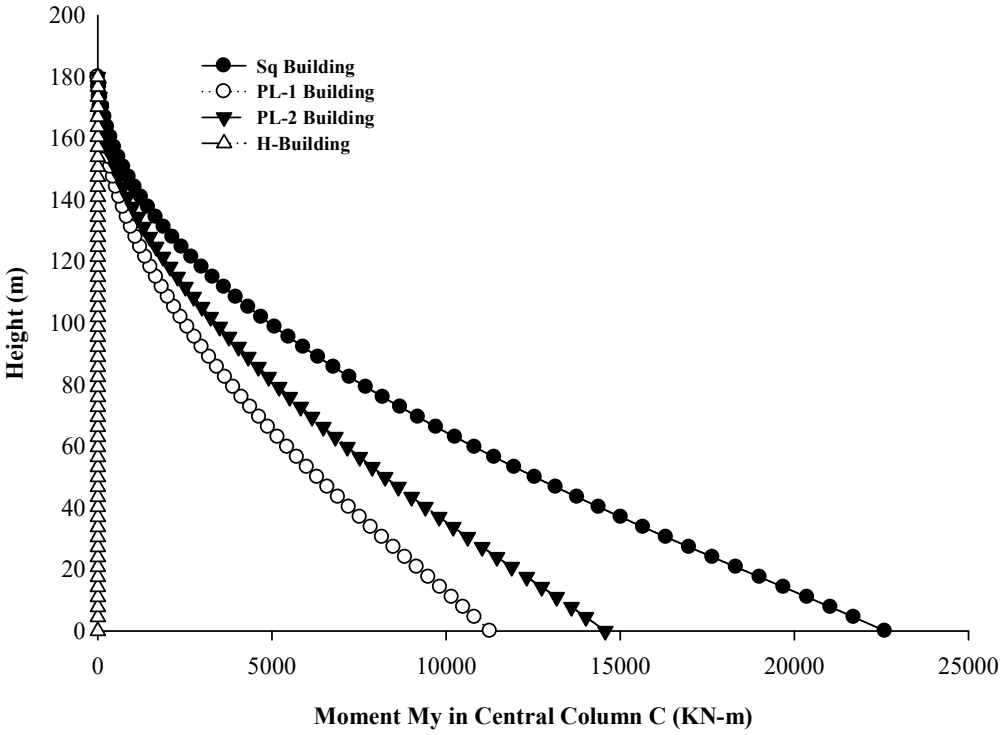

Fig. 7.99 Effect of Building Plan on Moment M_y at 60^0 Wind

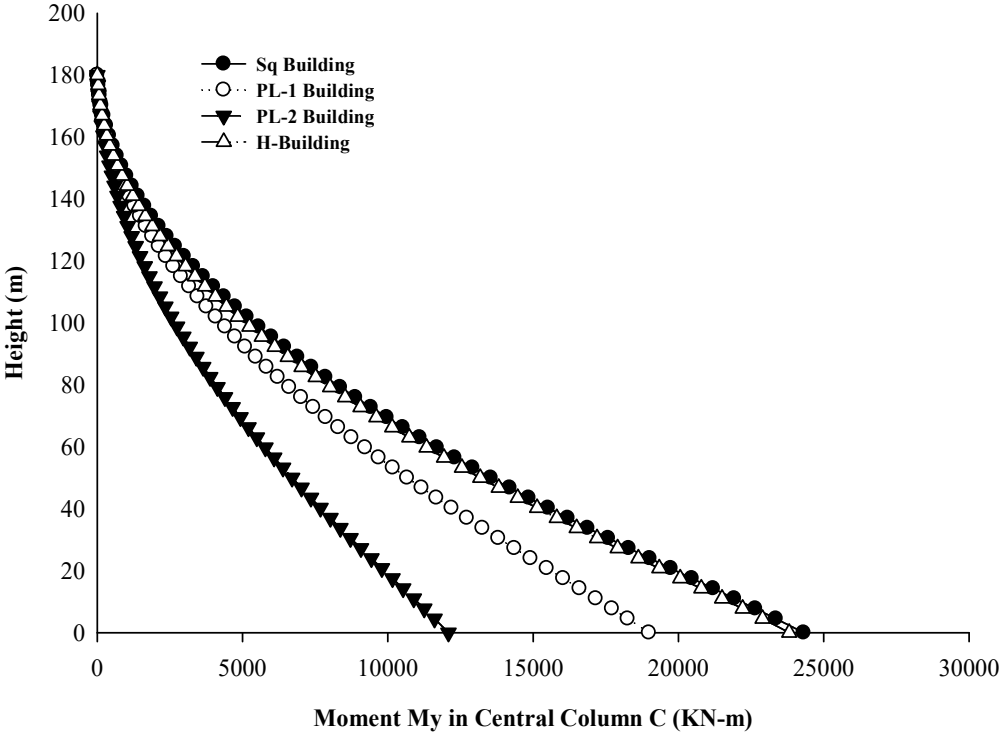

Fig. 7.100 Effect of Building Plan on Moment M_y at 90^0 Wind

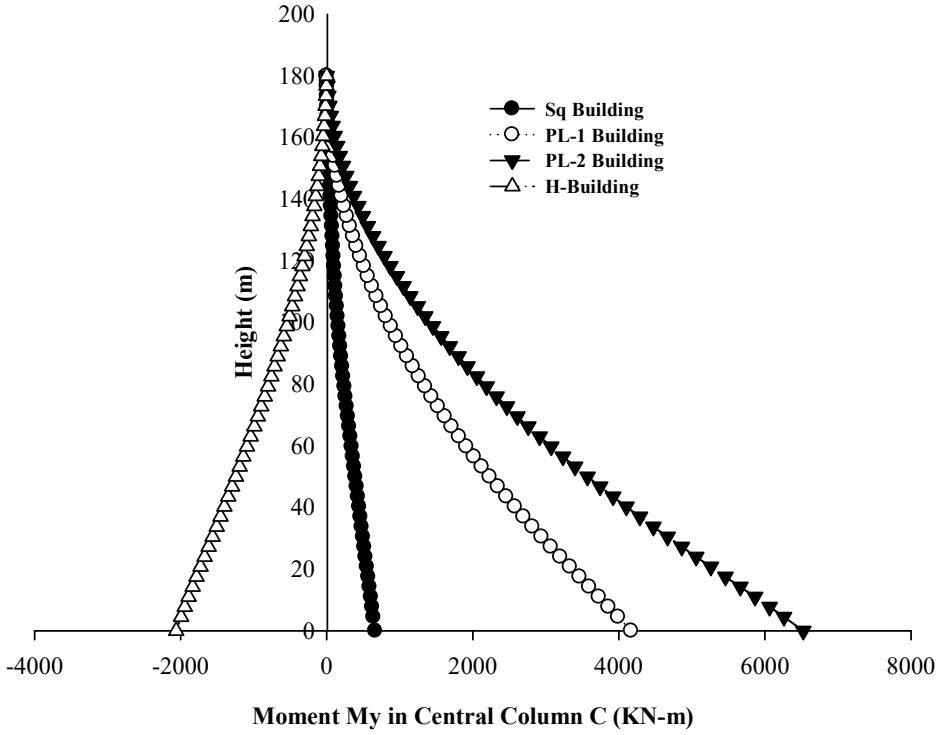

Fig. 7.101 Effect of Building Plan on Moment M_y at Half Blockage

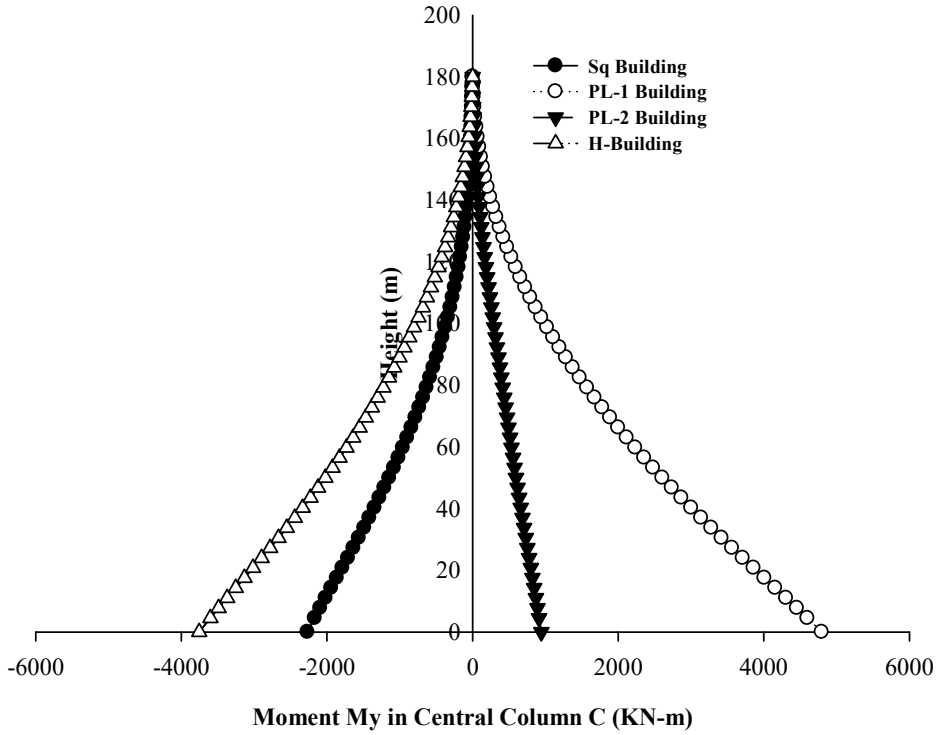

Fig. 7.102 Effect of Building Plan on Moment M_y at No Blockage

7.8.4. Twisting moment

The effects of building plan depend on the wind direction in isolated condition and position of upstream building in interference condition. At 30^0 wind angle, the maximum twisting moment is observed in PL-1 and H-building and minimum is in square building. For 60^0 wind the twisting moment is maximum in the maximum in PL-1 while minimum in H-building. In half blockage condition, the PL-2 and H-plan building suffers the maximum twisting.

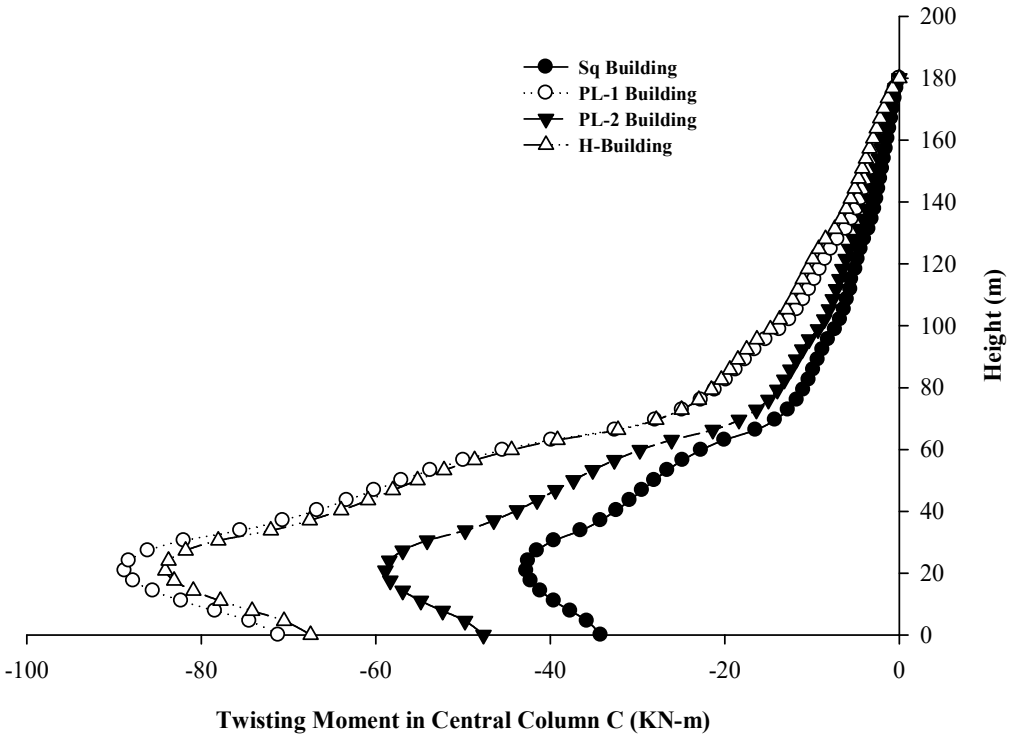

Fig. 7.103 Effect of Building Plan on Twisting Moment at 30^0 Wind

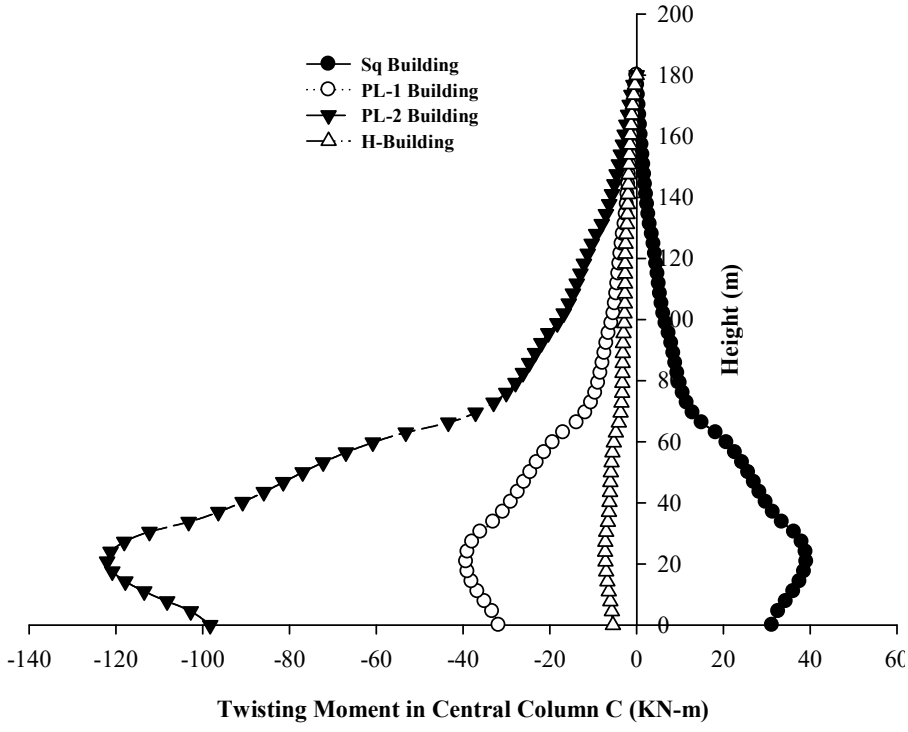

Fig. 7.104 Effect of Building Plan on Twisting Moment at 60^0 Wind

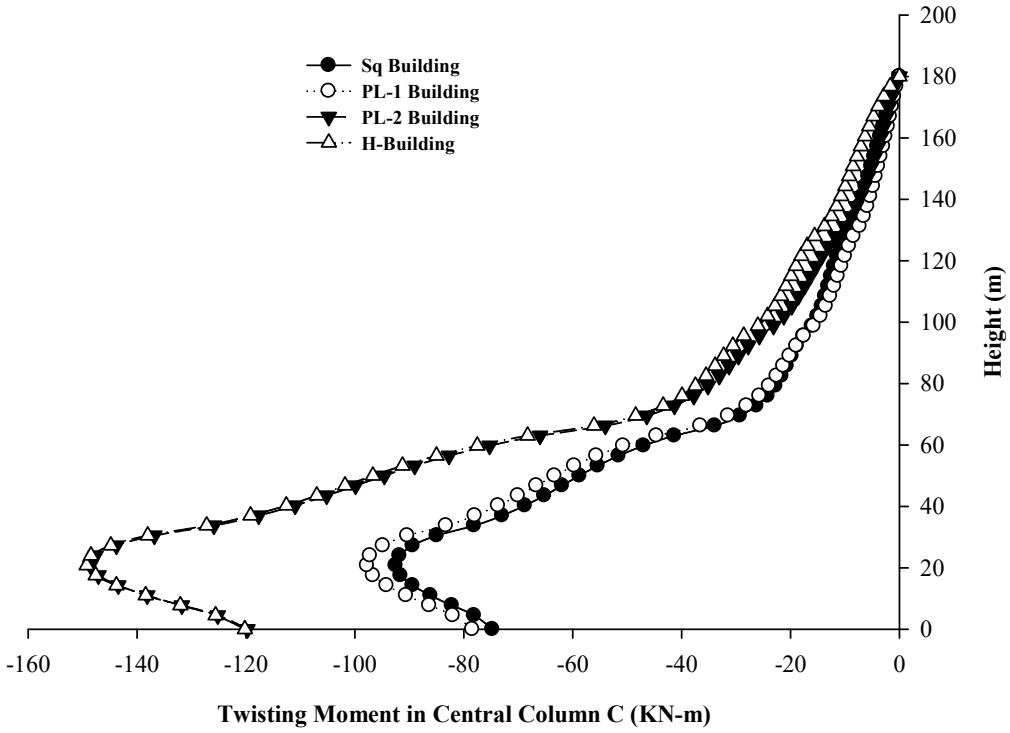

Fig. 7.105 Effect of Building Plan on Twisting Moment at Half Blockage

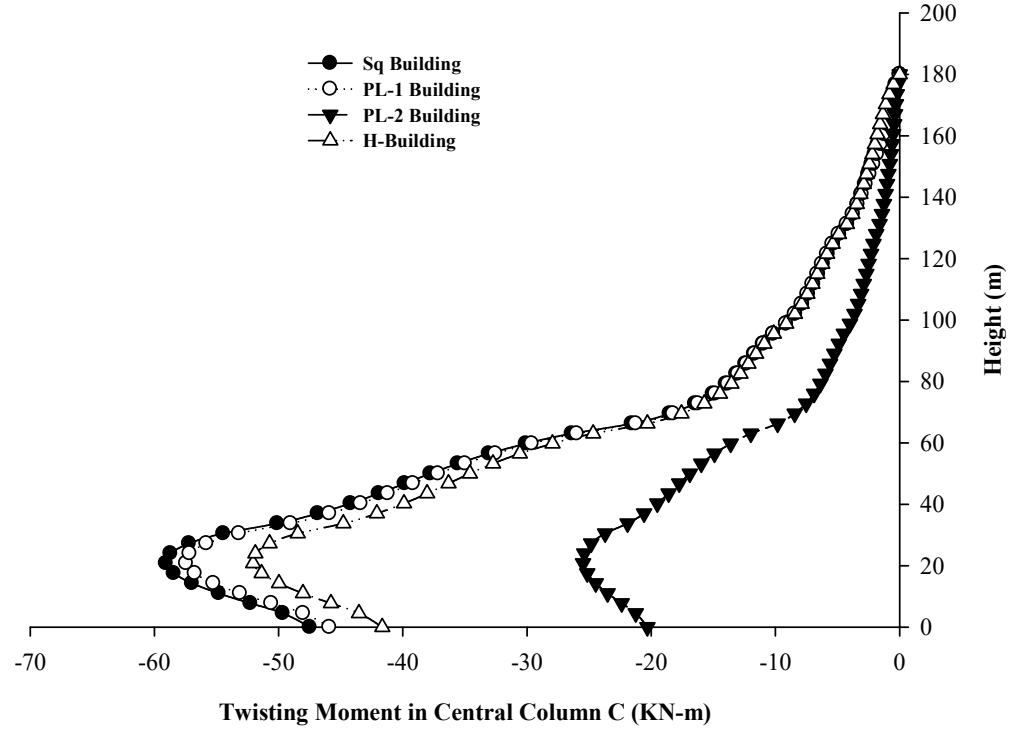

Fig. 7.106 Effect of Building Plan on Twisting Moment at No blockage

8. CHAPTER-8

CONCLUSIONS

8.1. GENERAL

Based on the wind tunnel test results, this study investigated the effects of change in wind direction and various interference conditions on the wind load and response of various buildings. The effects of change in cross-section on the response of buildings are also investigated. The following conclusion can be drawn from this study:

8.2. PRESSURE MEASUREMENT IN ISOLATED CONDITION

8.2.1. Square Model

1. Pressure distribution is symmetric about the vertical central line for wind flow normal to the surface. Pressure increases with height due to an increase in velocity.
2. Wind flow direction has significant effects on the pressure distribution at all surfaces.
3. Wind flow at normal to the surfaces are most critical directions, and designers need to consider local pressure at critical wind direction while designing the cladding elements.
4. Flow at the wind ward is stable, while at leeward, the flow is irregular and disturbed.

8.2.2. PL-1-model

1. The pressure coefficients are highly influenced by the direction of the wind. The effects of wind direction are more severe at windward faces.
2. Effects of the recessed corner are significant on the local pressure. The negative pressure increases by the presence of recessed corners.
3. The pressure at windward and suction at leeward of the plus-1 model has been reduced and thus results in a reduction in along-wind load compare to the square model under similar flow conditions

4. The wind direction 0f 60^0 generates the most critical positive and negative local pressures.

8.2.3. Plus-2 Model (Pl-2)

1. The effects of wind direction are less severe on the PL-2 model compare to the Pl-1 model.
2. The positive mean pressure does not change much with the change of wind direction but suction depends on wind direction.
3. The wind direction of 0^0 is the most critical direction in respect of local pressure.

8.2.4. H-Model

1. Local pressure changes significantly with wind direction especially positive pressure at windward surfaces.
2. The wind flow at 90^0 angle generates critical positive pressure while the wind flow at 0^0 generates critical negative pressure.
3. The presence of recessed cavities affects the Local pressure. Positive pressure increases due to recessed cavities, whereas negative pressure reduces.
4. The variation of $C_{p,mean}$, is almost similar to the square models at the front face for all wind incidence angles, but the H-plan model has a slightly higher pressure coefficient.
5. The difference between the two peaks is higher at side faces due to the disturbed flow.

8.3. PRESSURE MEASUREMENT IN INTERFERENCE CONDITION

8.3.1. Sq-model

1. Pressure distribution at the front face is completely different than those in case of isolated building. Windward face suffers higher negative wind pressure as it immerse in the wake of upstream building.
2. The pressure distribution on the side and leeward faces is similar to the isolated building case, but the suction intensity is likely to be reduced, especially on the side faces.

3. The interference effects on mean pressure coefficients at all surfaces of the square model are beneficial in full and half blockage interference conditions.
4. The MIF values for area average of mean surface pressure are less than unity, which indicates the overall reduction in the mean pressure coefficients.
5. The influence of the upstream building on the r.m.s pressure coefficients is not beneficial at front face in no blockage condition.

8.3.2. PL-1 MODEL

1. Strong interference effects are generated on front faces because it immersed in the wake of interfering building,
2. The high suction zone is located at a height between .75H to 0.85H.
3. The surfaces towards the interfering building, which come under the wake region of the interfering building, are under suction, whereas the opposite side has positive pressure.
4. The interference effects are significant for face A1, B1, and D3 only.
5. The fluctuating component of pressure coefficient is not much affected by the presence of an interfering building at three positions

8.3.3. PL-2 MODEL

1. The interference effects in full and half blockage are significant only at the surfaces on the windward side
2. The pressure distribution at surfaces on the windward side is found to be critically affected by the upstream interfering building
3. The shielding is favorable at side faces and leeward in full blockage.
4. In the half blockage interference condition, the shielding effects are more severe at half vertical area towards the interfering building of faces on the windward side
5. In no blockage, the pressure points on the walls toward the interfering building are only affected by the upstream building.

8.3.4. H-model

1. In the interference full blockage condition, the front face A experience suction and distribution is symmetric about the vertical centerline, whereas for other

blockage conditions symmetry is lost, and higher variation of mean pressure coefficients is noticed.

2. In full blockage, the MIF at all faces is less than unity which represent the beneficial effects of interference through shielding by upstream building.
3. The interference effects are also beneficial in half blockage at all other faces but face A suffers the some unfavorable effects

8.4. EVALUATION OF WIND FORCES

8.4.1. Local wind forces

8.4.1.1. Square model

1. The along-wind mean local wind forces are likely to be increased along the height
2. The along-wind mean local wind forces at normal wind incidence are higher than those at oblique wind incidence. The peak values for oblique wind flow are approximately 30% less than those for normal wind flow.
3. The along-wind forces in all interference conditions decreased significantly from those in isolated condition
4. A very minor variation is observed between the across-wind mean local wind forces values at different wind directions and different interference conditions
5. The along-wind r.m.s local wind force coefficients is very low in isolated conditions at all wind directions and relatively higher in interference conditions

8.4.1.2. PL-1 Model

1. The distribution of along-wind mean local wind forces in all case is similar and follow the same pattern.
2. Effects of wind directions are less significant than those on square building.
3. The cross-wind local force coefficient do not change along the height and have almost similar values throughout the height in all case.
4. The upstream interfering building have significant effects with half blockage and no blockage condition of flow.

8.4.1.3. Pl-2 Model

1. The along-wind mean coefficient has reduced significantly for wind angles higher than 0 degree.
2. In case of 30^0 wind, the across-wind mean coefficient values are highest among all wind angles.
3. Out of all interference conditions, the half blockage condition has highest interference effects and the across-wind mean coefficient values are significantly larger than other interference conditions.

8.4.1.4. H-model

1. The along-wind mean local force coefficients are highest for wind angles of 0 degree and lowest in half blockage interference.
2. Wind direction at oblique angle generate higher cross-wind mean local forces at each level.
3. The mean along wind force coefficient are highest at 0 degree wind and lowest at full blockage interference condition
4. The r.m.s forces in along-wind and across-wind are very low.

8.4.2. Base forces

1. The values of along-wind forces: drag and moment at normal wind incidence of 0^0 and 90^0 angles are larger than those at oblique wind incidence in isolated condition. The C_{FD} and C_{MD} values are likely to be reduced significantly in interference conditions.
2. The C_{FD} values of Pl-1 model at normal wind incidence are higher than those at oblique wind incidence
3. The absolute lowest value of along-wind moment is observed at full blockage interference condition
4. The C_{FD} continuously decreases with increase in wind incidence angle between 0^0 to 90^0.
5. The maximum value of mean OTM coefficient in along-wind direction is observed at 0^0 wind direction.

6. The mean across-wind coefficients (C_{FL} and C_{ML}) increase at 30^0 wind angle and decrease for higher wind angles.
7. The r.m.s drag force coefficients (C^*_{FD}) and r.m.s along-wind OTM coefficient (C^*_{MD}) increase and then decrease at alternate wind directions between 0^0 to 90^0.

8.4.3. Comparison between models

1. In the isolated condition, the square model suffers the maximum along-wind force whereas Pl-1 model suffer the lowest along-wind force. In the interference condition, the square model show better performance.
2. The effects of change in cross sectional shape are significant on the across-wind forces.
3. The square model have the lowest values in all case of wind flow in isolated and interference condition. The effects of cross sectional shape are dominant for wind flow at oblique angles in isolated condition while more at half blockage condition of interference.
4. The square model show better perforce in isolated condition but with the upstream interfering building at half blockage condition, the CMD, rms is highest among all models.
5. For across-wind r.m.s OTM coefficients At 0^0 wind direction in isolated condition and at half blockage interference condition, the H-model show worst performance, while at oblique angles, the PL-1 model show the worst performance.

8.5. RESPONSE STUDY

1. The effects of wind direction on the response of all building are not uniform and depends largely on the location of columns. The influence in more on axial force in the windward columns compare to the leeward columns. The axial force in central column does not influenced by wind direction.
2. The windward columns have higher moment for respective wind directions compare to the leeward columns. Wind direction normal to any surface produce higher M_y.

3. The effects of wind direction on the twisting moment are independent of the location of columns. All the models have zero twisting for symmetric flow.
4. The wind at 60^0 angle is the most critical for twisting in columns of Pl-2 building where as 30^0 wind is the most crucial for other buildings.
5. The effects of interference are not beneficial on windward columns but beneficial for leeward columns and largely depends on the column location. The effects of interference are positive on windward column in full blockage whereas no blockage condition has some negative effects on the M_y.
6. The half blockage condition is most critical for twisting moment in all buildings.
7. The axial force is independent of the building cross section. All the buildings have same axial force in central columns.
8. The Pl-2 building suffers the maximum moment M_x for most of the flow conditions in isolated as well as interference condition whereas the Square building suffers the minimum M_x.
9. The square building have largest moment M_y in isolated conditions whereas PL-1 building have largest M_y in interference condition.
10. The maximum twisting moment is observed in PL-2 Building in isolated as well as in interference condition. The H-building show the best performance in isolated condition.

8.6. RECOMMENDATIONS FOR FUTURE STUDY

Although a large amount of experiments have been carried out in the presents study in isolated and interference conditions still there is a need of detailed study in some areas as-

1. The present study is carried out at an interval of 30^0 wind angles. Future study may be carried out with small interval for better understanding of critical wind incidence angle directions.
2. The interference effects in the present study have been identified for the wind direction in line of the buildings. It is recommended to study the interference effects for all wind directions.

REFERENCES

[1] G. Solari, “Wind Loading of Structures: Framework, Phenomena, Tools and Codification,” *Structures*, vol. 12, no. September, pp. 265–285, 2017.

[2] P. A. Irwin, “Bluff body aerodynamics in wind engineering,” *J. Wind Eng. Ind. Aerodyn.*, vol. 96, no. 6–7, pp. 701–712, 2008.

[3] M. Shirzadeh Germi and H. Eimani Kalehsar, “Numerical investigation of interference effects on the critical wind velocity of tall buildings,” *Structures*, vol. 30, no. January, pp. 239–252, 2021.

[4] K. Wijesooriya, D. Mohotti, A. Amin, and K. Chauhan, “An uncoupled fluid structure interaction method in the assessment of structural responses of tall buildings,” *Structures*, vol. 25, no. October 2019, pp. 448–462, 2020.

[5] C. Zheng, Y. Xie, M. Khan, Y. Wu, and J. Liu, “Wind-induced responses of tall buildings under combined aerodynamic control,” *Eng. Struct.*, vol. 175, no. January, pp. 86–100, 2018.

[6] H. Tanaka, Y. Tamura, K. Ohtake, M. Nakai, and Y. Chul, “Experimental investigation of aerodynamic forces and wind pressures acting on tall buildings with various unconventional configurations,” *Jnl. Wind Eng. Ind. Aerodyn.*, vol. 107–108, pp. 179–191, 2012.

[7] K. C. S. Kwok, “Cross-wind response of tall buildings,” *Eng. Struct.*, vol. 4, no. 4, pp. 256–262, 1982.

[8] M. Ã. Gu and Y. Quan, “Across-wind loads of typical tall buildings,” *J. Wind Eng. Ind. Aerodyn.*, vol. 92, pp. 1147–1165, 2004.

[9] G. U. Ming and Q. Yong, “Across-wind loads and effects of super-tall buildings and structures,” *Sci. China Technol. Sci.*, vol. 54, no. 10, pp. 2531–2541, 2011.

[10] H. Kawai, “Effect of corner modifications on aeroelastic instabilities of tall buildings,” *J. Wind Eng. Ind. Aerodyn.*, vol. 74–76, pp. 719–729, 1998.

[11] Y. Chul and J. Kanda, “Wind pressures on tapered and set-back tall buildings,” *J. Fluids Struct.*, vol. 39, pp. 306–321, 2013.

[12] Y. Kim and K. You, “Dynamic responses of a tapered tall building to wind loads,” *J. Wind Eng. Ind. Aerodyn.*, vol. 90, pp. 1771–1782, 2002.

[13] B. 6399-2:1997, “BS 6399-2: 1997 Loading for Buildings Part 2: Code of pravtice for wind loads,” *Br. Stand. Inst.*, vol. 3, no. July, p. , 1997.

[14] A. 7-02, *Internal corrosion direct assessment of gas transmission pipelines*, vol. 27, no. 10. 2002, pp. 513–517.

[15] AS/NZS, *AS-NZS 1170-2 (2011) (English): Structural design actions - Part 2 : Wind actions*, vol. 2. 2011.

[16] I. IS 875 Part 3, *Design loads (other than Earthquake) for Buildings and Structures - Code of Practice*, vol. 875, no. April. 2015.

[17] E. 1991-1-4, *Actions on structures - Part 1-4: General actions - Wind actions*, no. 5. 2005, pp. 18-22+95.

[18] A. C. Khanduri, T. Stathopoulos, and C. Bédard, “Wind-induced interference effects on buildings - A review of the state-of-the-art,” *Eng. Struct.*, vol. 20, no. 7, pp. 617–630, 1998.

[19] B. S. Taranath, *Reinforced Tall Buildings Design of Concrete*. New York: CRC Press, Taylor & Francis Group, 2010.

[20] A. G. Davenport, “The Response of six building shapes to turbulent wind,” *Phil Trans Roy Soc London Ser A. Math Phys Sci*, vol. 269, no. 1199, pp. 385–394, 1971.

[21] K. C. S. Kwok, “effect of building shape on wind-induced response of tall building,” *J. Wind Eng. Ind. Aerodyn.*, vol. 28, pp. 381–390, 1988.

[22] H. Hayashida and Y. Iwasa, “Aerodynamic shape effects of tall building for vortex induced vibration,” *J. Wind Eng. Ind. Aerodyn.*, vol. 33, no. 1–2, pp. 237–242, 1990.

[23] G. R. Lythe and D. Surry, “Wind-induced torsional loads on tall buildings,” *J. Wind Eng. Ind. Aerodyn.*, vol. 36, no. PART 1, pp. 225–234, 1990.

[24] K. T. Tse, P. A. Hitchcock, K. C. S. Kwok, S. Thepmongkorn, and C. M. Chan, “Economic perspectives of aerodynamic treatments of square tall buildings,” *Jnl. Wind Eng. Ind. Aerodyn.*, vol. 97, no. 9–10, pp. 455–467, 2009.

[25] M. Gu, “Wind-resistant studies on tall buildings and structures,” *Sci. China Technol. Sci.*, vol. 53, no. 10, pp. 2630–2646, 2010.

[26] Y. Li, X. Tian, K. Fah, Q. Li, and Y. Li, “Aerodynamic treatments for reduction of wind loads on high-rise buildings,” *J. Wind Eng. Ind. Aerodyn.*, vol. 172, no. September 2017, pp. 107–115, 2018.

[27] Y. Li, Y. G. Li, Q. S. Li, and K. F. Tee, “Investigation of wind effect reduction on square high-rise buildings by corner modification,” *Adv. Struct. Eng.*, vol. 22, no. 6, pp. 1488–1500, 2019.

[28] Z. N. Xie and M. Gu, “Simplified formulas for evaluation of wind-induced interference effects among three tall buildings,” *J. Wind Eng. Ind. Aerodyn.*, vol. 95, no. 1, pp. 31–52, 2007.

[29] X. F. Yu, Z. N. Xie, J. B. Zhu, and M. Gu, “Interference effects on wind pressure distribution between two high-rise buildings,” *J. Wind Eng. Ind. Aerodyn.*, vol. 142, pp. 188–197, 2015.

[30] X. F. Yu, Z. N. Xie, X. Wang, and B. Cai, “Interference effects between two high-rise buildings on wind-induced torsion,” *J. Wind Eng. Ind. Aerodyn.*, vol. 159, no. February, pp. 123–133, 2016.

[31] Y. Hui, Y. Tamura, and Q. Yang, “Analysis of interference effects on torsional moment between two high-rise buildings based on pressure and flow field measurement,” *J. Wind Eng. Ind. Aerodyn.*, vol. 164, no. February, pp. 54–68, 2017.

[32] X. Yu, Z. Xie, and M. Gu, “Interference effects between two tall buildings with different section sizes on wind-induced acceleration,” *J. Wind Eng. Ind. Aerodyn.*, vol. 182, no. August 2017, pp. 16–26, 2018.

[33] Z. N. Xie and M. Gu, “Mean interference effects among tall buildings,” *Eng. Struct.*, vol. 26, pp. 1173–1183, 2004.

[34] K. M. Lam, M. Y. H. Leung, and J. G. Zhao, “Interference effects on wind loading of a row of closely spaced tall buildings,” *J. Wind Eng. Ind. Aerodyn.*, vol. 96, no. 5, pp. 562–583, 2008.

[35] M. Gu and Z. N. Xie, “Interference effects of two and three super-tall buildings under wind action,” *Acta Mech. Sin. Xuebao*, vol. 27, no. 5, pp. 687–696, 2011.

[36] W. Kim, Y. Tamura, and A. Yoshida, “Interference effects on local peak pressures between two buildings,” *Jnl. Wind Eng. Ind. Aerodyn.*, vol. 99, no. 5, pp. 584–600, 2011.

[37] W. Kim, Y. Tamura, and A. Yoshida, “Interference effects on aerodynamic wind forces between two buildings,” *J. Wind Eng. Ind. Aerodyn.*, vol. 147, pp. 186–201, 2015.

[38] Y. Hui, Y. Tamura, A. Yoshida, and H. Kikuchi, “Pressure and flow field investigation of interference effects on external pressures between high-rise buildings,” *J. Wind Eng. Ind. Aerodyn.*, vol. 115, pp. 150–161, 2013.

[39] Y. Hui, A. Yoshida, and Y. Tamura, “Interference effects between two rectangular-section high-rise buildings on local peak pressure coefficients,” *J. Fluids Struct.*, vol. 37, pp. 120–133, 2013.

[40] T. G. Mara, B. K. Terry, T. C. E. Ho, and N. Isyumov, “Aerodynamic and peak response interference factors for an upstream square building of identical height,” *J. Wind Eng. Ind. Aerodyn.*, vol. 133, pp. 200–210, 2014.

[41] C. K. C. Cheng, K. M. Lam, Y. T. A. Leung, K. Yang, H. W. Li Danny, and C. P. Cheung Sherman, “Wind-induced natural ventilation of re-entrant bays in a high-rise building,” *J. Wind Eng. Ind. Aerodyn.*, vol. 99, no. 2–3, pp. 79–90, 2011.

[42] S. Y. Wong and K. M. Lam, “Effect of recessed cavities on wind-induced loading and dynamic responses of a tall building,” *Jnl. Wind Eng. Ind. Aerodyn.*, vol. 114, pp. 72–82, 2013.

[43] L. Cheng, K. M. Lam, and S. Y. Wong, “POD analysis of crosswind forces on a tall building with square and H-shaped cross sections,” *Wind Struct. An Int. J.*, vol. 21, no. 1, pp. 63–84, 2015.

[44] Y. Zhou, T. Kijewski, and A. Kareem, “Aerodynamic Loads on Tall Buildings: Interactive Database,” *J. Struct. Eng.*, vol. 129, no. 3, pp. 394–404, 2003.

[45] D. L. Beneke and K. C. S. Kwok, “Aerodynamic effect of wind induced torsion on tall buildings,” *J. Wind Eng. Ind. Aerodyn.*, vol. 50, pp. 271–280, 1993.

[46] J. A. Amin and A. K. Ahuja, “Experimental study of wind pressure on irregular-plan shape buildings,” in *BBAA VI International Colloquium on: Bluff Bodies Aerodynamics & Applications Milano, Italy, July, 20-24 2008*, 2008, pp. 20–24.

[47] A. Yoshida, E. K. Bandi, Y. Tamura, Y. Chul Kim, and Q. Yang, “Experimental investigation on aerodynamic characteristics of various triangular-section high-rise buildings,” in *The Seventh International Colloquium on Bluff Body Aerodynamics and its Applications, Shanghai, China*, 2012, pp. 849–856.

[48] Y. Li, Q. S. Li, and F. Chen, “Wind tunnel study of wind-induced torques on L-shaped tall buildings,” *J. Wind Eng. Ind. Aerodyn.*, vol. 167, no. September 2016, pp. 41–50, 2017.

[49] K. S. Kumar, “Wind loading on tall buildings: Review of Indian Standards and recommended amendments,” *J. Wind Eng. Ind. Aerodyn.*, vol. 204, no. May, p. 104240, 2020.

[50] M. Gu, X. Wang, and Y. Quan, “Wind tunnel test study on effects of chamfered corners on the aerodynamic characteristics of 2D rectangular prisms,” *J. Wind Eng. Ind. Aerodyn.*, vol. 204, no. October 2019, p. 104305, 2020.

[51] Y. Li, C. Li, Q. S. Li, Q. Song, X. Huang, and Y. G. Li, “Aerodynamic performance of CAARC standard tall building model by various corner chamfers,” *J. Wind Eng. Ind. Aerodyn.*, vol. 202, no. April, p. 104197, 2020.

[52] K. C. S. Kwok and P. A. Bailey, “Aerodynamic devices for tall buildings and structures,” *J. Eng. Mech.*, vol. 113, no. 3, pp. 349–365, 1987.

[53] K. Miyashita *et al.*, “Wind-induced response of high-rise buildings Effects of corner cuts or openings in square buildings,” *J. Wind Eng. Ind. Aerodyn.*, vol. 50, no. C, pp. 319–328, 1993.

[54] Y. C. Kim, J. Kanda, and Y. Tamura, “Wind-induced coupled motion of tall buildings with varying square plan with height,” *Jnl. Wind Eng. Ind. Aerodyn.*, vol. 99, no. 5, pp. 638–650, 2011.

[55] Y. M. Kim, K. P. You, and N. H. Ko, “Across-wind responses of an aeroelastic tapered tall building,” *J. Wind Eng. Ind. Aerodyn.*, vol. 96, no. 8–9, pp. 1307–1319, 2008.

[56] K. You, Y. Kim, and N. Ko, “The evaluation of wind-induced vibration response to a tapered tall building,” *Struct. Des. Tall Spec. Build.*, vol. 17, pp. 655–667, 2008.

[57] Y. Kim and J. Kanda, “Characteristics of aerodynamic forces and pressures on square plan buildings with height variations,” *Jnl. Wind Eng. Ind. Aerodyn.*, vol. 98, no. 8–9, pp. 449–465, 2010.

[58] K. B. Rajasekarababu, G. Vinayagamurthy, and S. Selvi Rajan, “Experimental and computational investigation of outdoor wind flow around a setback building,” *Build. Simul.*, vol. 12, no. 5, pp. 891–904, 2019.

[59] A. Sharma, H. Mittal, and A. Gairola, “Wind tunnel and delayed detached eddy simulation investigation of interference between two tall buildings,” *Adv. Struct. Eng.*, vol. 22, no. 9, pp. 2163–2178, 2019.

[60] Y. C. Kim and J. Kanda, “Wind pressures on tapered and set-back tall buildings,” *J. Fluids Struct.*, vol. 39, pp. 306–321, 2013.

[61] J. Xie, “Journal of Wind Engineering Aerodynamic optimization of super-tall buildings and its effectiveness assessment,” *Jnl. Wind Eng. Ind. Aerodyn.*, vol. 130, pp. 88–98, 2014.

[62] S. Liang, S. Liu, Q. S. Li, L. Zhang, and M. Gu, “Mathematical model of acrosswind dynamic loads on rectangular tall buildings,” *J. Wind Eng. Ind. Aerodyn.*, vol. 90, no. 12–15, pp. 1757–1770, 2002.

[63] N. Lin, C. Letchford, Y. Tamura, and B. Liang, “Characteristics of wind forces acting on tall buildings,” *J. Wind Eng. Ind. Aerodyn.*, vol. 93, pp. 217–242, 2005.

[64] J. Zhang and M. Gu, “Distribution of background equivalent static wind load on high-rise buildings,” *Front. Arch. Civ. Eng. China*, vol. 3, no. 3, pp. 241–248, 2009.

[65] J. A. Amin and A. K. Ahuja, “Characteristics of wind forces and responses of rectangular tall buildings,” *Int. J. Adv. Struct. Eng.*, vol. 6, no. 3, pp. 1–14, 2014.

[66] V. Guzmán-Solís, A. Pozos-Estrada, and R. Gómez, “Experimental study of wind-induced shear, bending, and torsional loads on rectangular tall buildings,” *Adv. Struct. Eng.*, vol. 23, no. 14, pp. 2982–2995, 2020.

[67] R. Dutton and N. Isyumov, “Reduction of tall bilding motion by aerodynamic treatments,” *J. Wind Eng. Ind. Aerodyn.*, vol. 36, pp. 739–747, 1990.

[68] K. R. Cooper, M. Nakayama, Y. Sasaki, A. A. Fediw, S. Resende-Ide, and S. J. Zan, “Unsteady aerodynamic force measurements on a super-tall building with a tapered cross section,” *J. Wind Eng. Ind. Aerodyn.*, vol. 72, no. 1–3, pp. 199–212, 1997.

[69] M. G. Gomes, A. Moret Rodrigues, and P. Mendes, “Experimental and numerical study of wind pressures on irregular-plan shapes,” *J. Wind Eng. Ind. Aerodyn.*, vol. 93, no. 10, pp. 741–756, 2005.

[70] S. Liang, Q. S. Li, L. Zou, and J. R. Wu, “Simplified formulas for evaluation of across-wind dynamic responses of rectangular tall buildings,” *Wind Struct. An Int. J.*, vol. 8, no. 3, pp. 197–212, 2005.

[71] G. Huang and X. Chen, “Wind load effects and equivalent static wind loads of tall buildings based on synchronous pressure measurements,” *Eng. Struct.*, vol. 29, no. 10, pp. 2641–2653, 2007.

[72] M. Gu, “Study on wind loads and responses of tall buildings and structures,” *7th Asia-Pacific Conf. Wind Eng. APCWE-VII*, 2009.

[73] Y. Tamura, H. Tanaka, K. Ohtake, M. Nakai, and Y. Kim, “Aerodynamic characteristics of tall buildings with unconventional configurations,” in *In Structural Congress, 2010 ASCE*, 2010, vol. 2, pp. 3104–3113.

[74] Y. Kim and J. Kanda, “Effects of taper and set-back on wind force and wind-induced response of tall buildings,” *Wind Struct. An Int. J.*, vol. 13, no. 6, pp. 499–517, 2010.

[75] W. Lou, M. Huang, H. Jin, G. Shen, and C. M. Chan, “Three-dimensional wind load effects and wind-induced dynamic responses of a tall building with X-shape,” *Struct. Des. Tall Spec. Build.*, vol. 19, no. 8, pp. 885–900, 2010.

[76] J. Amin and A. Ahuja, “Experimental study of wind-induced pressures on buildings

of various geometries," *Int. J. Eng. Sci. Technol.*, vol. 3, no. 5, pp. 1–19, 2011.

[77] F. Cluni, V. Gusella, S. M. J. Spence, and G. Bartoli, "Wind action on regular and irregular tall buildings: Higher order moment statistical analysis by HFFB and SMPSS measurements," *J. Wind Eng. Ind. Aerodyn.*, vol. 99, no. 6–7, pp. 682–690, 2011.

[78] J. A. Amin and A. K. Ahuja, "Effects of Side Ratio on Wind-Induced Pressure Distribution on Rectangular Buildings," *J. Struct.*, vol. 2013, pp. 1–12, 2013.

[79] E. K. Bandi, Y. Tamura, A. Yoshida, Y. C. Kim, and Q. Yang, "Experimental investigation on aerodynamic characteristics of various triangular-section high-rise buildings," *Jnl. Wind Eng. Ind. Aerodyn.*, vol. 122, pp. 60–68, 2013.

[80] Y. C. Ha, "Empirical formulations for evaluation of across-wind dynamic loads on rectangular tall buildings," *Wind Struct. An Int. J.*, vol. 16, no. 6, pp. 603–615, 2013.

[81] S. Mukherjee, S. Chakraborty, S. K. Daluf, and A. K. Ahuja, "Wind induced pressure on 'Y' plan shape tall building," *Wind Struct. An Int. J.*, vol. 19, no. 5, pp. 523–540, 2014.

[82] S. Chakraborty, S. K. Dalui, and A. K. Ahuja, "Wind load on irregular plan shaped tall building – a case study," *Wind Struct. An Int. J.*, vol. 19, no. 1, pp. 59–73, 2014.

[83] J. D. Holmes, "Along- and cross-wind response of a generic tall building: Comparison of wind-tunnel data with codes and standards," *J. Wind Eng. Ind. Aerodyn.*, vol. 132, pp. 136–141, 2014.

[84] B. Bhattacharyya, S. K. Dalui, and A. K. Ahuja, "Wind Induced Pressure on ' E ' Plan Shaped Tall Buildings," *Jordan J. Civ. Eng.*, vol. 8, no. 2, pp. 120–134, 2014.

[85] B. Bhattacharyya and S. K. Dalui, "Investigation of mean wind pressures on 'E' plan shaped tall building," *Wind Struct. An Int. J.*, vol. 26, no. 2, pp. 99–114, 2018.

[86] T. Deng, X. Yu, and Z. Xie, "Aerodynamic measurements of across-wind loads and responses of tapered super high-rise buildings," *Wind Struct. An Int. J.*, vol. 21, no. 3, pp. 331–352, 2015.

[87] B. Bhattacharyya and S. K. Dalui, "Along and Across Wind Effects on Irregular

Plan Shaped Tall Building," *Adv. Struct. Eng.*, pp. 1445–1460, 2015.

[88] Y. C. Kim, Y. Tamura, and S. W. Yoon, "Effect of taper on fundamental aeroelastic behaviors of super-tall buildings," *Wind Struct. An Int. J.*, vol. 20, no. 4, pp. 527–548, 2015.

[89] G. Hu, K. T. Tse, K. C. S. Kwok, and Z. S. Chen, "Pressure measurements on inclined square prisms," *Wind Struct. An Int. J.*, vol. 21, no. 4, pp. 383–405, 2015.

[90] Y. C. Kim, E. K. Bandi, A. Yoshida, and Y. Tamura, "Response characteristics of super-tall buildings - Effects of number of sides and helical angle," *J. Wind Eng. Ind. Aerodyn.*, vol. 145, pp. 252–262, 2015.

[91] Y. Li and Q. Li, "Across-wind dynamic loads on L-shaped tall buildings," *Wind Struct. An Int. J.*, vol. 23, no. 5, pp. 385–403, 2016.

[92] Y. Quan, H. L. Cao, and M. Gu, "Effects of turbulence intensity and exterior geometry on across-wind aerodynamic damping of rectangular super-Tall buildings," *Wind Struct. An Int. J.*, vol. 22, no. 2, pp. 185–209, 2016.

[93] Y. Guan, A. Li, Y. Zhang, C. Jiang, and Q. Wang, "Experimental and numerical investigation on the distribution characteristics of wind pressure coefficient of airflow around enclosed and open-window buildings," *Build. Simul.*, vol. 9, no. 5, pp. 551–568, 2016.

[94] A. Elshaer, G. Bitsuamlak, and A. El Damatty, "Enhancing wind performance of tall buildings using corner aerodynamic optimization," *Eng. Struct.*, vol. 136, pp. 133–148, 2017.

[95] D. Zhao and B. He, "Effects of architectural shapes on surface wind pressure distribution : Case studies of oval-shaped tall buildings," *J. Build. Eng.*, vol. 12, no. May, pp. 219–228, 2017.

[96] J. W. Zhang and Q. S. Li, "Wind tunnel test and field measurement study of wind effects on a 600-m-high super-tall building," *Struct. Des. Tall Spec. Build.*, vol. 26, no. 17, pp. 1–17, 2017.

[97] W. Yuan, N. Yu, and Z. Wang, "The effects of grooves on wind characteristics of

tall cylinder buildings," *Wind Struct. An Int. J.*, vol. 26, no. 2, pp. 89–98, 2018.

[98] T. Deng, J. Y. Fu, Z. N. Xie, Y. L. Pi, and B. Q. Shi, "An experimental study on the wind pressure distribution of tapered super high-rise buildings," *Struct. Des. Tall Spec. Build.*, vol. 27, no. 13, pp. 1–11, 2018.

[99] R. Sheng, L. Perret, I. Calmet, F. Demouge, and J. Guilhot, "Wind tunnel study of wind effects on a high-rise building at a scale of 1:300," *J. Wind Eng. Ind. Aerodyn.*, vol. 174, no. September 2017, pp. 391–403, 2018.

[100] M. Mallick, A. Mohanta, A. Kumar, and V. Raj, "Modelling of Wind Pressure Coefficients on C-Shaped Building Models," *Model. Simul. Eng.*, vol. 2018, 2018.

[101] Y. Liu, G. A. Kopp, and S. fu Chen, "Effects of plan dimensions on gust wind loads for high-rise buildings," *J. Wind Eng. Ind. Aerodyn.*, vol. 194, no. September, p. 103980, 2019.

[102] Z. Liu, C. Zheng, Y. Wu, R. G. J. Flay, and K. Zhang, "Investigation on the effects of twisted wind flow on the wind loads on a square section megatall building," *J. Wind Eng. Ind. Aerodyn.*, vol. 191, no. January, pp. 127–142, 2019.

[103] S. L. Li, L. L. Liu, H. Wu, N. Jiang, S. Y. Zheng, and P. Guo, "New Test Method of Wind Pressure Coefficient Based on CAARC Standard Model Determined Using Vehicle Driving Wind," *Exp. Tech.*, vol. 43, no. 6, pp. 707–717, 2019.

[104] G. Hu, J. Song, S. Hassanli, R. Ong, and K. C. S. Kwok, "The effects of a double-skin façade on the cladding pressure around a tall building," *J. Wind Eng. Ind. Aerodyn.*, vol. 191, no. June, pp. 239–251, 2019.

[105] N. Khodaie, "Vibration control of super-tall buildings using combination of tapering method and TMD system," *J. Wind Eng. Ind. Aerodyn.*, vol. 196, no. November 2019, p. 104131, 2020.

[106] G. Lamberti, L. Amerio, G. Pomaranzi, A. Zasso, and C. Gorlé, "Comparison of high resolution pressure measurements on a high-rise building in a closed and open-section wind tunnel," *J. Wind Eng. Ind. Aerodyn.*, vol. 204, no. May, p. 104247, 2020.

[107] Y. Li, J. Yan, X. Chen, Q. Li, and Y. Li, “Investigation of surface pressures on CAARC tall building concerning effects of turbulence,” *Wind Struct. An Int. J.*, vol. 31, no. 4, pp. 287–298, 2020.

[108] D. Li, B. Liu, X. Zhou, and Z. Wang, “Size effects of area extreme pressure for large-scale cladding,” *Structures*, vol. 29, no. October 2020, pp. 408–415, 2021.

[109] B. Bhattacharyya and S. K. Dalui, “Experimental and Numerical Study of Wind-Pressure Distribution on Irregular-Plan-Shaped Building,” *J. Struct. Eng.*, vol. 146, no. 7, p. 04020137, 2020.

[110] Y. Li, Q. S. Li, and K. L. Ju, “Experimental investigation of the wind pressure distribution and wind interference effects on a typical tall building,” *Adv. Mater. Res.*, vol. 639–640, no. 1, pp. 444–451, 2013.

[111] P. A. Bailey and K. C. S. Kwok, “Interference excitation of twin tall buildings,” *J. Wind Eng. Ind. Aerodyn.*, vol. 21, no. 3, pp. 323–338, 1985.

[112] M. Yahyai, K. Kumar, P. Krishna, and P. K. Pande, “Aerodynamic interference in tall rectangular buildings,” *J. Wind Eng. Ind. Aerodyn.*, vol. 41, no. 1–3, pp. 859–866, 1992.

[113] Y. Taniike, “Interference mechanism for enhanced wind forces on neighboring tall buildings,” *J. Wind Eng. Ind. Aerodyn.*, vol. 42, no. 1–3, pp. 1073–1083, 1992.

[114] W. J. Zhang, Y. L. Xu, and K. C. S. Kwok, “Interference effects on aeroelastic torsional response of structurally asymmetric tall buildings,” *J. Wind Eng. Ind. Aerodyn.*, vol. 57, no. 1, pp. 41–61, 1995.

[115] A. C. Khanduri, T. Stathopoulos, and C. Bédard, “Generalization of wind-induced interference effects for two buildings,” *Wind Struct. An Int. J.*, vol. 3, no. 4, pp. 255–266, 2000.

[116] S. Thepmongkorn, G. S. Wood, and K. C. S. Kwok, “Interference effects on wind-induced coupled motion of a tall building,” *J. Wind Eng. Ind. Aerodyn.*, vol. 90, no. 12–15, pp. 1807–1815, 2002.

[117] Z. N. Xie and M. Gu, “A correlation-based analysis on wind-induced interference

effects between two tall buildings," *Wind Struct. An Int. J.*, vol. 8, no. 3, pp. 163–178, 2005.

[118] J. Lim and B. Bienkiewicz, "Wind-induced response of structurally coupled twin tall buildings," *Wind Struct. An Int. J.*, vol. 10, no. 4, pp. 383–398, 2007.

[119] J. Zhao and K. M. Lam, "Interference effects in a group of tall buildings closely arranged in an L- or T-shaped pattern," *Wind Struct. An Int. J.*, vol. 11, no. 1, pp. 1–18, 2008.

[120] M. M. Tavakol and M. Yaghoubi, "Experimental and numerical analysis of turbulent air flow around a surface mounted hemisphere," *Sci. Iran.*, vol. 17, no. 6 B, pp. 480–491, 2010.

[121] Y. Hui, Y. Tamura, and A. Yoshida, "Mutual interference effects between two high-rise building models with different shapes on local peak pressure coefficients," *Jnl. Wind Eng. Ind. Aerodyn.*, vol. 104–106, pp. 98–108, 2012.

[122] B. Yan and Q. S. Li, "Wind tunnel study of interference effects between twin super-tall buildings with aerodynamic modifications," *J. Wind Eng. Ind. Aerodyn.*, vol. 156, pp. 129–145, 2016.

[123] H. Dongmei, Z. Xue, H. Shiqing, H. Xuhui, and H. Hua, "Characteristics of the aerodynamic interference between two high-rise buildings of different height and identical square," *Wind Struct. An Int. J.*, vol. 24, no. 5, pp. 501–528, 2017.

[124] B. Kim and K. T. Tse, "POD analysis of aerodynamic correlations and wind-induced responses of two tall linked buildings," *Eng. Struct.*, vol. 176, no. September, pp. 369–384, 2018.

[125] B. Kim, K. T. Tse, and Y. Tamura, "POD analysis for aerodynamic characteristics of tall linked buildings," *J. Wind Eng. Ind. Aerodyn.*, vol. 181, no. August, pp. 126–140, 2018.

[126] G. B. Zu and K. M. Lam, "Shielding effects on a tall building from a row of low and medium rise buildings," *Wind Struct. An Int. J.*, vol. 27, no. 6, pp. 439–449, 2018.

[127] A. Flaga, A. Kocoń, R. Kłaput, and G. Bosak, "The environmental effects of

aerodynamic interference between two closely positioned irregular high buildings," *J. Wind Eng. Ind. Aerodyn.*, vol. 180, no. August, pp. 276–287, 2018.

[128] L. Zhang, W. Cheng, and Z. Xie, "Wind effect of a twin-tower super high-rise building with weak connection," *Structural Design of Tall and Special Buildings*, vol. 27, no. 15. 2018.

[129] B. Kim, K. T. Tse, A. Yoshida, Z. Chen, P. Van Phuc, and H. S. Park, "Investigation of flow visualization around linked tall buildings with circular sections," *Build. Environ.*, vol. 153, no. February, pp. 60–76, 2019.

[130] X. Li and Q. S. Li, "Wind-induced interference effects between twin tapered skyscrapers," *Structural Design of Tall and Special Buildings*, vol. 28, no. 6. 2019.

[131] W. Jing, J. Wang, and X. Cheng, "Dynamic responses of oil storage tank considering wind interference effect," *Eng. Fail. Anal.*, vol. 104, no. December 2018, pp. 1053–1063, 2019.

[132] J. Chen, Y. Quan, and M. Gu, "Aerodynamic interference effects of a proposed super high-rise building on the aerodynamic forces and responses of an existing building," *J. Wind Eng. Ind. Aerodyn.*, vol. 206, no. July, p. 104312, 2020.

[133] Y. Quan, J. Chen, and M. Gu, "Aerodynamic interference effects of a proposed taller high-rise building on wind pressures on existing tall buildings," *Structural Design of Tall and Special Buildings*, vol. 29, no. 4. 2020.

[134] Q. S. Liang, J. Y. Fu, Z. Li, B. W. Yan, Z. R. Shu, and Y. C. He, "Bimodal distribution of wind pressure on windward facades of high-rise buildings induced by interference effects," *J. Wind Eng. Ind. Aerodyn.*, vol. 200, no. October 2019, 2020.

[135] Y. Sun, Z. Li, X. Sun, N. Su, and S. Peng, "Interference effects between two tall chimneys on wind loads and dynamic responses," *J. Wind Eng. Ind. Aerodyn.*, vol. 206, no. May, pp. 1–17, 2020.

[136] S. Behera, D. Ghosh, A. K. Mittal, Y. Tamura, and W. Kim, "The effect of plan ratios on wind interference of two tall buildings," *Struct. Des. Tall Spec. Build.*, vol. 29, no. 1, pp. 2–11, 2020.

[137] B. S. Chauhan, A. Chakrabarti, and A. K. Ahuja, “Investigation of wind load alteration on rectangular cross-section tall building due to change in relative orientation of interfering building,” *Structures*, vol. 31, no. March, pp. 970–981, 2021.

[138] J. Revuz, D. M. Hargreaves, and J. S. Owen, “On the domain size for the steady-state CFD modelling of a tall building,” *Wind Struct. An Int. J.*, vol. 15, no. 4, pp. 313–329, 2012.

[139] R. Kar and S. K. Dalui, “Wind interference effect on an octagonal plan shaped tall building due to square plan shaped tall buildings,” *Int. J. Adv. Struct. Eng.*, vol. 8, no. 1, pp. 73–86, 2016.

[140] K. Roy and A. Kumar Bairagi, “Wind pressure and velocity around stepped unsymmetrical plan shape tall building using CFD simulation- a case study,” *Asian J. Civ. Eng.*, vol. 17, no. 8, pp. 1055–1075, 2016.

[141] R. Paul and S. K. Dalui, “Wind effects on ‘ Z ’ plan-shaped tall building : a case study,” *Int. J. Adv. Struct. Eng.*, vol. 8, pp. 319–335, 2016.

[142] A. Mukherjee and A. K. Bairagi, “Wind pressure and velocity pattern around ‘N’ plan shape tall building-A case study,” *Asian J. Civ. Eng.*, vol. 18, no. 8, pp. 1241–1258, 2017.

[143] Q. Xing and J. Qian, “CFD analysis of wind interference effects of three high-rise buildings,” *J. Asian Archit. Build. Eng.*, vol. 17, no. 3, pp. 487–494, 2018.

[144] Q. H. Chen, H. T. Hu, C. Z. Qian, and C. P. Chen, “Analysis of wind environmental characteristics around a square building,” *IOP Conf. Ser. Earth Environ. Sci.*, vol. 146, no. 1, 2018.

[145] P. Sanyal and S. K. Dalui, “Effect of corner modifications on Y’ plan shaped tall building under wind load,” *Wind Struct. An Int. J.*, vol. 30, no. 3, pp. 245–260, 2020.

[146] R. Raj, “Effects of Cross-Sectional Shapes on Response of Tall Buildings Under Wind Loads,” vol. 247667, 2015.

[147] J. D. Holmes, *Wind loading on structures.* New York: Spon Press, Taylor & Francis

Group, 2004.

[148] J. A. Amin, “Effects of Plan Shape on Wind Induced Response of Tall Buildings,” Indian Institute of Technology, Roorkee, India, 2008.

[149] F. Q. Meng, B. J. He, J. Zhu, D. X. Zhao, A. Darko, and Z. Q. Zhao, “Sensitivity analysis of wind pressure coefficients on CAARC standard tall buildings in CFD simulations,” *J. Build. Eng.*, vol. 16, no. October 2017, pp. 146–158, 2018.

[150] G. W. Alminhana, A. L. Braun, and A. M. Loredo-Souza, “A numerical-experimental investigation on the aerodynamic performance of CAARC building models with geometric modifications,” *J. Wind Eng. Ind. Aerodyn.*, vol. 180, no. July, pp. 34–48, 2018.

[151] X. Du, H. Xu, W. Ma, C. Dai, and Q. Liu, “Experimental study on aerodynamic characteristics of two square cylinders at various incidence angles,” *J. Wind Eng. Ind. Aerodyn.*, vol. 191, no. December 2018, pp. 154–169, 2019.

[152] L. D. Sy, H. Yamada, and H. Katsuchi, “Interference effects of wind-over-top flow on high-rise buildings,” *J. Wind Eng. Ind. Aerodyn.*, vol. 187, no. February, pp. 85–96, 2019.

[153] B. H. L. Gowda and R. A. Kumar, “Flow-induced oscillations of a square cylinder due to interference effects,” *J. Sound Vib.*, vol. 297, no. 3–5, pp. 842–864, 2006.

[154] G. B. Zu and K. M. Lam, “Across-wind excitation mechanism for interference of twin tall buildings in staggered arrangement,” *J. Wind Eng. Ind. Aerodyn.*, vol. 177, no. December 2017, pp. 167–185, 2018.